Material Science of Rydberg Excitons in Cuprous Oxide

This dissertation is submitted for the degree of

Doctor of Philosophy

by

Aisha Sheded Albeladi

School of Physics and Astronomy - Cardiff University

UK

Sep 2024

Abstract

Cu_2O is a promising material for quantum technologies due to its ability to host Rydberg excitons with high principal quantum numbers. These excitons are particularly interesting because their large Bohr radius allows them to behave as microscale objects which can be manipulated and transported over longer distances within the material. This is essential for integration of quantum technologies into larger scale system.

A key question motivating this research is: why do synthetic Cu_2O crystal exhibit poorer excitonic properties compared to natural, especially when high principal quantum number excitons are only observed in natural material? The objective of this thesis is to investigate sub-bandgap defect states, considering them as a factor preventing the creation of high principal quantum number excitons in synthetic Cu_2O therefore, limiting its technological use. This is based on one of the hypotheses that high concentrations of charge impurities in synthetic material introduce internal electric field that distort the exciton wave function, limiting the highest observable quantum number excitons.

This thesis addresses the defect detection through a combination of electrical and optical techniques of synthetic single crystal Cu_2O. These techniques include temperature dependent Hall measurements, room temperature spectrally resolved photoconductive response to pulsed nanosecond infrared laser light and mid-infrared (MIR) and Terahertz (THz) spectroscopy across a wide temperature range. In the electrical characterization phase, Ohmic contacts with low specific contact resistance were successfully optimized and fabricated, allowing precise Hall measurements and photoconductivity measurements and hence assessing the intrinsic properties of Cu_2O accurately. Therefore, the specific contact resistance (ρ_c) was tested between different metallization schemes using a unique CTLM design and Au-Cu_2O without adhesion layer was chosen as an optimal contact with specific contact resistance of $1.698\times10^{-2}\Omega cm^{-2}$. Then the Hall-measurement device was fabricated using a Van der Pauw configuration and Au contacts. The temperature dependence Hall-measurements revealed key insights into material's conductivity, activation energy, and Hall mobility. The temperature dependent conductivity analysis indicates two different

activation energies at 0.2 and 0.1 eV corresponding to different conduction mechanisms across the temperature range which could indicate presence of different defect states in sub-bandgap. Also, carrier concentration measurements confirmed that the material has two activation energies and the two acceptor states occur at approximately the same value as the previously obtained from conductivity measurements. Hall mobility showed minimal variation across the studied temperature range. Phonon scattering and neutral impurities were found to be the dominated mechanisms limiting Hall mobility.

Our photoconductivity study used a novel technique to investigate the sub-bandgap defect states in sub-bandgap. This measurement was performed using pulsed wavelength-tuned laser photoconductivity spectroscopy, at room temperature. This time-resolved measurement was key to distinguishing between different optical process in Cu_2O by analysing the time-dependent photoresponse, which showed two different photoconductance recovery timescales, of the order of nanoseconds and microseconds. Different excitation-wavelength dependent resonance photoresponse was observed in the sub-bandgap photoconductivity spectrum at 820nm, 900nm, 930nm, and 980nm which is consistence with known impurity features such as copper and oxygen vacancies.

We present a detailed investigation of the infrared and terahertz spectral properties of Cu_2O. By comparing our experimental measurements with the calculated phonon spectrum, we identify and explain, for the first time, the mid-infrared (MIR) absorption features observed between 100–115 meV and 135–155 meV as higher-order replicas of the Reststrahlen bands. Furthermore, no additional absorption features were detected in the MIR or THz spectra of both synthetic and natural samples, suggesting the absence of shallow impurity states in this material. Our findings provide new insights into the fundamental optical properties of Cu_2O.

Declaration

I hereby declare that the work presented in this thesis is my own, original research, conducted independently unless otherwise stated. All sources of information and data have been properly acknowledged. This thesis has not been submitted for any degree or qualification at any other university or institution.

Aisha Albeladi

Sep 2024

List of publications

- "Photoconductivity Measurement as a Proposed Technique to Monitor Defect States in Cu2O Crystals at Room Temperature." Presented at SIOE Conference, 2023.

- "Sub-Bandgap Photoconductivity Response of Synthetic Cu2O to Pulsed Laser Exciton at IR Wavelengths." UK Semiconductor Conference, 2023.

- **Aisha S. Albeladi**, Craig P. Allford, Chris Hodges, Ravi P. Singh, Wolfgang W. Langbein, and Stephen A. Lynch1, " Transient Photoconductive Response of Synthetic Cuprous Oxide (Cu_2O) to Sub-bandgap Infrared Wavelength Tunable Pulsed Laser Excitation." To be Submitted to IOP

- “Unlocking the Hidden Power: Unravelling Sub-Bandgap Photoconductivity in Synthetic Cu2O under Pulsed Laser Excitation at IR wavelength”. Presented at CMQM 2023.

Content

List of figures

Chapter 1 Introduction

1.1 Context

The expression Quantum Technologies covers a broad range of applications which seek to exploit the quantum properties of electromagnetic radiation and matter to achieve enhanced functionality. As one of the fastest-growing research and development fields, these technologies hold the potential to revolutionize areas such as computing, cryptography, sensing, and communication. In recent years, there has been significant investment in quantum technologies across the globe, particularly in the UK and Europe. The UK government has committed over £1 billion to quantum technology research and development through initiatives like the UK National Quantum Technologies Programme. This program, launched in 2014, includes the establishment of four Quantum Technology Hubs, each focusing on different aspects of broad quantum science and technology, such as quantum sensing and imaging, quantum communications, quantum computing, and quantum metrology [1]. Also, in Europe, the EU has allocated around €1 billion through the Quantum Flagship initiative and the QuantERA network, which supports research across 31 organizations in 26 countries. These investments highlight the growing interest and belief in the transformative potential of quantum technologies [2].

1.1.1 Quantum Technologies

The expression covers a wide range of technology areas, each with different quantum requirements. Loosely these areas can be broadly categorised under quantum sensing, quantum computing and quantum communications.

Quantum sensing seeks to exploit that electromagnetic radiation can be described in terms of discreet packets (or quanta) of energy called photons. This is true regardless of whether we mean conventional light or longer wave radiation with terahertz or microwave

frequencies. Normally when sensing using light, we are concerned with the intensity of radiation falling on a sensor, such as individual pixels of a camera. However, when the intensity falls to a level of a few photons, the statistics can change. This can be exploited in several ways to result in enhanced sensitivity or accuracy. For example, a quantum effect called squeezing is now routinely used to achieve displacement measurements with precisions of a fraction of the diameter of a proton, in the Laser Interferometric Gravitational-Wave Observatory (LIGO) measures gravitational disturbances caused by the merging of black holes and neutron star [3]. Single photon detectors can achieve extraordinary sensitivity, especially in situations where the photons are heralded. Quantum Computing seeks to fundamentally change the way electronic operations are performed on-chip. While conventional computing involves the serial manipulation of bits of information synchronised to a clock pulse, quantum computing has the potential to achieve speed-up by exploiting quantum coherence across multiple quantum bits (qubits) and quantum gates for certain types of well-defined computing problems like prime factorisation (Shor's algorithm) [4] and searching and sorting (Grover's algorithm) [5]. Quantum Communication exploits the properties of quantum measurement for secure encryption and transfer of data. Any quantum measurement leaves behind a trace (collapsed wavefunctions), and so it becomes possible to ascertain whether there has been an eavesdropper listening in [4].

1.2 Why Cu_2O for quantum technology

For each application within the broad range of quantum technologies, there are leading materials or architectures that show great promise or where proof-of principal quantum manipulations have been demonstrated. However, all current technology approaches suffer from the same problem, scale-up. The scale-up problem means that it is difficult to see how to technologically achieve coherence across tens of thousands of qubits, which is the approximate order of magnitude of qubits needed for a quantum computer (with error correction) to compete with a conventional computer.

Arguably, two of the leading technologies are Ion Traps [6] and Superconducting qubits.

Trapped-ion quantum computers face major challenges, such as the necessity of needing advanced hardware such as ultra-high vacuum chambers and cryogenic systems to isolate the ions from external particles. Decoherence remains a problem: It occurs when qubits interact undesirably with their environment, disrupting their quantum states and affecting the computer's performance [6]. In addition, there is the complexity of trap design, where this structure use both radiofrequency RF and static electric field to confine and manipulate ion in three dimensions which must be precisely manufactured and aligned. Ion cooling and manipulating process is done by using stable and precise laser system. Integrating ion traps with necessary control electrical, optical (using to focus and direct the laser beams onto the ions) and cooling is also challenging. Superconducting qubits also show promise, but "physical footprint" may lead to scaling problems. The area occupied by a single superconducting qubit on chip ranges of tens squared micrometre [7]. However, the qubit itself is just a part of total area as additional space is required for control and readout circuity as well as for interconnect between qubits. As the number of qubits increases, the space required for interconnects and control lines also grows. This added complexity can lead to issues like crosstalk, where signals interfere with each other, making it harder to maintain precise control over each qubit. As a result, the overall footprint needed per qubit expands to ensure the system remains stable and functional. The system should be in the cryogenic atmosphere typically in dilution refrigerators at millikelvin temperatures.

1.2.1 Rydberg Exciton in Cu_2O

Cu_2O has real potential to be a breakthrough material that could lead to a disruptive quantum technology, due to the unique properties of its exciton spectrum. This became immediately obvious with the publication in 2014 of Kazimierczuk's paper in the journal *Nature* [8]. In a simplistic picture an exciton can be understood as bound electron and hole pair. This electronic system is an analogue of the hydrogen atom and shares many of the hydrogen atom's quantum properties. This work showed that Cu_2O hosted an extraordinarily rich excitonic spectrum, revealing principal quantum numbers up to n = 25, which possess a notably large radius in order of um. This large Bohr radius means that the

exciton is nanoscale object which is interesting because it allows the exciton to be compatible with nanoscale fabrication techniques. Also, such excitons could be manipulated and transported over longer distances within a material which is essential for the integration of quantum technologies into larger-scale systems. Although this observation is remarkable on its own, the detection of hints of a phenomenon called Rydberg blockade added even more excitement. Rydberg blockade is a well-established concept in cold atom physics[9]. Observing it in a solid-state material opens up the possibility of developing single photon sources, which are crucial for advancing quantum technologies[10]. This is because Rydberg blockade prevents multiple atoms from being simultaneously excited to high-energy states, ensuring that only one atom in an ensemble can emit a photon at a time. This suppression of multiple excitations makes it possible to produce a single, well-defined photon, crucial for realizing single-photon sources.

1.3 Technological Pathway Towards Exploitation

So far, many of the proof-of-principle experiments have been performed in a small number of “hero” samples. This means there is a danger that Cu_2O could be viewed as a lab curiosity. For Cu2O to be considered as a serious technological material, there needs to be a pathway towards largescale manufacture and fabrication.

1.3.1 Natural Material

The best Cu_2O samples so far have been of natural origin. There are two stable oxides of copper that occur in nature. Copper(ii) oxide (CuO) is found naturally as the mineral tenorite. However, the more interesting form is Copper(i) oxide (Cu_2O), which occurs much less commonly in nature as the mineral cuprite. Large single crystals have been found in a small number of mines around the world (the Ural Mountains (Russia), Altai Mountains (mountain range in Central Asia and Eastern Asia), Sardinia, and in more isolated locations in Cornwall (UK), France, Arizona (USA), Chile, Bolivia, and Namibia [11]). The best samples have historically come from the Tsumeb mine in Namibia [8]. These single crystals have sometimes been used as gemstones, although they are not ideal for this purpose because the softness of the material causes it to scratch easily. All the experiments which

demonstrate exemplary quantum properties have been performed on natural single crystals to date, and this has greatly limited the interest of technologists in the wider quantum technologies community.

1.3.2 Current Limitations of Synthetic Material

For the industrial application there needs to be a way to manufacture synthetic single crystal material of similar quality to the natural gemstone samples and there are many possible routes to manufacturing synthetic material. These include furnace annealing, Czochralski method (CZ), and Floating-zone method (FZ) [12]. However, as scientists began to attempt to replicate the work of the Dortmund group, it became clear that the quality of natural samples was significantly higher than the best available synthetic single crystal material. One immediately obvious quantitative measure of quality is the maximum principal quantum number observable in the exciton spectrum at low temperature. To date, natural materials have demonstrated excitons with principal quantum numbers up to n=30 [13], whereas synthetic materials have only reached n=10 [14]. This notable disparity in exciton principal quantum numbers between natural and synthetic materials highlights a limitation of synthetic Cu_2O, affecting its attractiveness as a technological quantum material. Understanding the factors that supress higher quantum number excitons in synthetic Cu_2O is crucial for unlocking its full potential, driving ongoing investigations in this field.

1.4 Understanding the Role of Defects

Scientists have speculated as to why synthetic material doesn't currently match the quality of natural material (as judged by the highest principal quantum number exciton observable). Indeed, some synthetic material is elementally purer than natural material, and there is no discernible difference in the X-ray diffraction spectra of comparable single crystals.

However, nature has the advantage that crystals form over millions of years with an abundance of time to anneal out defects. Typical growth times of synthetic single crystals range from hours to days, which leaves the possibility of atomic scale defects not visible in X-ray diffraction spectra. Recent theoretical calculations show that localised electric fields associated with various types of defects a can result in distortions of the exciton wave-function, thus limiting the maximum principal quantum number observable. The rationale behind the work in this thesis is to try to understand what defects might be present, and whether there might be easily measurable signatures of these defects that could be used to design a feedback optimisation loop to track changes due to post growth treatment of crystals.

1.5 Structure of the Thesis

This thesis is structured into seven chapters. **Chapter 2** contains the background material needed to help understand the main results. This explores the fundamental properties of Cu_2O, growth methods, intrinsic defects, and both the electrical and optical properties, particularly excitons and their interactions with crystal imperfections. **Chapter 3** discusses the preparation of Cu_2O single crystals, including the cutting and polishing processes, as well as the fabrication of various devices for different experiments. The chapter then outlines the electrical setup used for Hall measurements to characterize the material. Additionally, a detailed explanation is provided for the design and implementation of a novel experiment to investigate impurities that could affect the Rydberg spectrum. This investigation involves spectrally resolved photoconductivity measurements in the NIR region. Another experiment is then described using an FTIR spectrometer to explore the mid-infrared (MIR) and terahertz (THz) regions. **Chapter 4** explores the formation of efficient ohmic contacts for synthetic Cu_2O single crystal, focusing on achieving low specific contact resistance ρ_c. Gold (Au) is evaluated as the optimal metallization material due to its low resistivity and stability, with circular transmission line measurement (CTLM) used to determine contact resistance. Then systematically examines the Hall properties, impurity levels, charge carrier concentration, and the dominant hole scattering mechanisms in Cu_2O single crystals that

impact Hall mobility. **Chapter 5** presents the results of spectrally resolved photoconductivity measurements using a wavelength-tunable nanosecond laser. This approach allowed for precise illumination of Cu_2O bulk synthetic single crystals, enhancing the detection of subtle spectral features linked to various defect states. Notably, several sharp spectral peaks were identified within the sub-bandgap region, revealing specific defect-related states at room temperature. **Chapter 6** presents the results of transmission spectra for natural and synthetic Cu_2O, investigating impurities that could influence the Rydberg spectrum. The chapter focuses on MIR and THz measurements aimed at detecting shallow bound states. **Chapter 7** provides the conclusions and the future perspective of the work on Cu_2O.

Chapter 2 Background

2.1 Introduction

This chapter presents the fundamental background on the crystal structure and electronic band structure of Cu_2O, as these characteristics play a crucial role in determining the material's optical, electrical, and mechanical properties. The presence of defects, such as vacancies, dislocations, and interstitials within the lattice, is an important factor, as these imperfections have a direct impact on the material's behaviour and performance. An overview of the Cu-O phase diagram, with a particular focus on Cu_2O, is also provided, outlining the key challenges associated with the synthesis of Cu_2O in different growth environments. Understanding the conditions necessary for producing high-purity Cu_2O is essential, as this directly influences the material's quality and its effectiveness in various applications.

The chapter will also introduce the optical floating zone technique, a crucible-free method used to grow high-quality Cu_2O crystals with minimal defects. This method has proven effective in producing material suitable for high-performance applications. Furthermore, the key parameters used to assess the quality of Cu_2O, including electrical properties and carrier mobility, will be discussed to highlight the importance of these measurements in evaluating material quality. This chapter also will introduce the optical absorption characteristics of Cu_2O, including the formation of ortho and para excitons, as well as the study of Rydberg excitons. The influence of defects on the behaviour and visibility of Rydberg excitons, which are highly sensitive to material quality, will also be covered, emphasizing their significance in understanding Cu_2O's optical properties.

2.2 General Material Properties of Cu_2O

Cu_2O has been known for a very long time. In crystalline form it is optically transparent at wavelengths longer than 570 nm, giving it a deep red colour. Arguably it is the first material found to exhibit semiconducting properties, with a bandgap of 2.17 eV at 10K.

2.2.1 Crystal Structure

The crystal structure of Cu_2O is different from the more familiar elemental semiconductors like silicon and germanium (which have a diamond lattice), or the III-V compound semiconductors, such as GaAs (which have a zinc blende crystal structure). Instead Cu_2O has a cubic crystal structure, which is relatively unusual.

2.2.1.1 Cubic Lattices and Reciprocal Vectors

In 3D space, there are 14 Bravais possible lattices, of which 3 are cubic. These lattices are shown in Figure 2.1 along with their lattice vectors. All three lattices are useful when describing the crystal structure of Cu_2O.

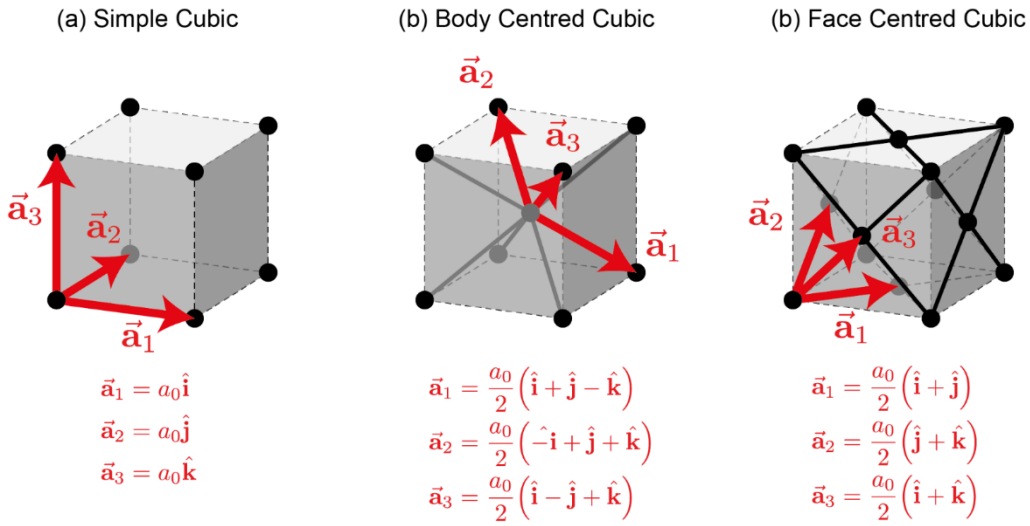

Figure 2.1: Three cubic lattice structure: (a) SC lattice has 8 lattice points located at the vertices of the cube, with 3 mutually orthogonal lattice vectors lying along the conventional Cartesian axes. (b)BCC lattice includes an additional lattice point at the centre of the cube body, from which the 3 lattice vectors originate. (c) FCC lattice has 6 additional lattice points at the centres of each cube face, with its lattice vectors extending from a cube corner to the centres of the closest three cube faces.

The most fundamental lattice is the Simple Cubic (SC), which has 8 lattice points located at the vertices of the cube. The 3 lattice vectors are mutually orthogonal, lying along the convention cartesian axes. Closely related to the Simple Cubic is the Body Centred Cubic (BCC) lattice. This has an additional lattice point in the centre of the body of the cube. The 3 lattice vectors start from this point. The third cubic lattice is the Face Centred Cubic (FCC). There is no lattice point in the centre of the cube body. Instead, there are 6 additional lattice points at the centre of each cube face. The corresponding lattice vectors start at one of the cube corners and end at the lattice points in the centre of the closest three cube faces.

There is no requirement for atoms to be located at lattice points. The repeating unit cell of the crystal is usually defined by this lattice, filling space without any gaps. The pattern of atoms inside the unit cell is known as the basis. Sometimes it is convenient to use more than one lattice to specific the atomic positions. So, for example, the atomic sites in the diamond structure of silicon, or the zinc blende structure of III-V compound semiconductors are often described using two interpenetrating FCC lattice offset by $\frac{a_0}{4}$ (1,1,1) where a_0 is the lattice constant. The atoms located at the lattice points of each FCC lattice. The atomic sites for Cu2O can be conveniently described by using similar trick. However, for Cu_2O the

atomic sites are best described by interpenetrating BCC and FCC lattices, offset by $\frac{a_0}{4}$ $(1,1,1)$ are shown in Figure 2.2. The Cu atoms are located at the lattice point of the FCC, while the oxygen are located at the lattice point of BCC [15].

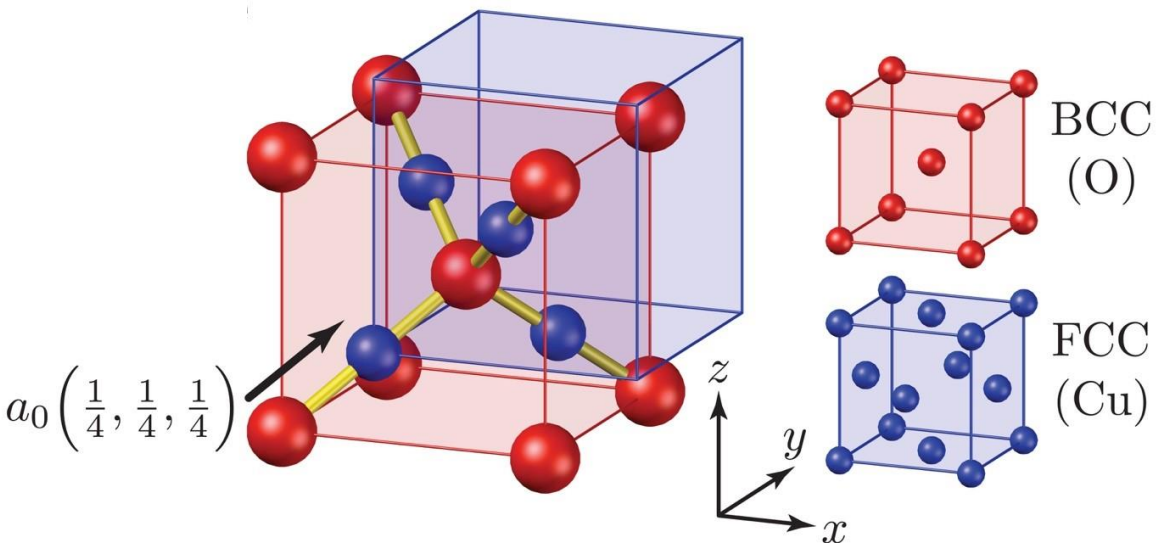

Figure 2.2: Cu_2O features an interleaved lattice structure composed of BCC and FCC sub-lattices. Oxygen (O) atoms occupy the lattice positions of the body-centered cubic (BCC) cell, while copper (Cu) atoms are positioned at the lattice points of a face-centered cubic (FCC) cell with the same lattice constant (a_o). The two cells are shifted by $\frac{a_0}{4}$ $(1,1,1)$.

2.2.1.2 Unit cell

It is useful to consider the simplest repeating element needed to reproduce the periodic crystal structure. This is the SC primitive cell below. The basis requires 2 oxygen atoms, one located at the corner of the cubic cell and one at the centre of the cube, and four copper atoms arranged as shown in Figure 2.3. This is sufficient to reproduce the periodic crystal structure, without double counting any of the atoms (as shown of the right of this figure).

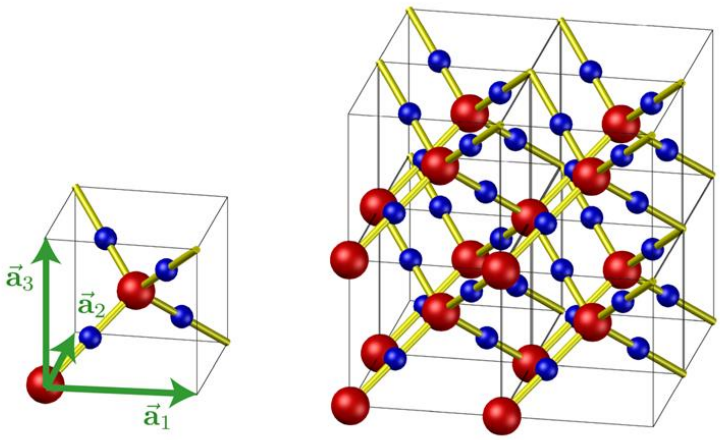

Figure 2.3: Left: *the SC primitive cell of Cu_2O, containing two oxygen atoms—one at the corner and one at the center—and four copper atoms. Right: this unit replicates the full periodic crystal structure without atom duplication.*

The SC cubic cell can be used to calculate basic material properties like the density of the material. So, assuming the lattice constant for Cu_2O is a_0=4.2696 *Å*, Then the cell volume is 77.8A^0. The unit cell contain are 2 oxygen atoms and 4 copper atoms, with atomic masses 63.55 g/mol and 16 g/mol respectively. This gives a density of 6.10 g/cm^3.

2.2.1.3 Reciprocal Lattice and Brillouin Zone

This primitive unit cell can also be used to calculate the reciprocal lattice vectors $\vec{b}_i$ using the transformations (see Figure 2.4),

$$\overrightarrow{b_1} = 2\pi \frac{\overrightarrow{a_2} \times \overrightarrow{a_3}}{\overrightarrow{a_1}.(\overrightarrow{a_2} \times \overrightarrow{a_3})},$$

$$\overrightarrow{b_2} = 2\pi \frac{\overrightarrow{a_3} \times \overrightarrow{a_1}}{\overrightarrow{a_2}.(\overrightarrow{a_3} \times \overrightarrow{a_1})},$$

$$\overrightarrow{b_3} = 2\pi \frac{\overrightarrow{a_1} \times \overrightarrow{a_2}}{\overrightarrow{a_3}.(\overrightarrow{a_1} \times \overrightarrow{a_2})} \quad .$$

where the $\vec{a}_i$ are the real-space SC Bravais lattice vectors. Calculating the cross and dot products of real-space lattice vectors gives,

$$\overrightarrow{a_2} \times \overrightarrow{a_3} = (a_0^2) \begin{vmatrix} \hat{\imath} & \hat{\jmath} & \hat{k} \\ 0 & 1 & 0 \\ 0 & 0 & 1 \end{vmatrix} = a_0^2(1,0,0)$$

$$\overrightarrow{a_1}.(\overrightarrow{a_2} \times \overrightarrow{a_3}) = a_0(1,0,0).a_0^2(1,0,0) = a_0^3$$

We note here that this also gives the correct volume for the primitive SC cell. Thus, we see that the Brillouin Zone in reciprocal space is also cubic, with,

$$\overrightarrow{b_1} = 2\pi \frac{\overrightarrow{a_2} \times \overrightarrow{a_3}}{\overrightarrow{a_1}.(\overrightarrow{a_2} \times \overrightarrow{a_3})} = 2\pi \frac{a_0^2(1,0,0)}{a_0^3} = \frac{2\pi}{a_0}(1,0,0)$$

and similarly for the other two reciprocal lattice vectors

$$\overrightarrow{b_2} = \frac{2\pi}{a_0}(0,1,0) \text{ and } \overrightarrow{b_3} = \frac{2\pi}{a_0}(0,0,1)$$

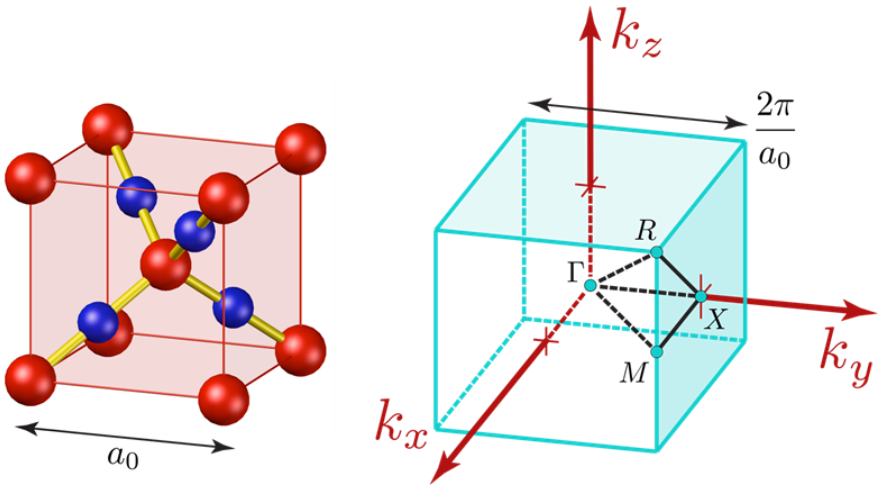

Figure 2.4: Left: Representation of the Cu_2O crystal structure, with copper atoms (red) and oxygen atoms (blue) arranged in a face-centered cubic configuration. Right: Schematic of the reciprocal lattice,

2.2.2 Electronic Band Structure and Effective Mass

The Cu^+ ion electronic structure ends $3d^{10}4s^0$, with the 4*s* orbitals only slightly higher in energy than the 3*d* levels. The Cu 3*d* levels form the valence band of Cu_2O and the empty Cu 4*s* levels form the conduction band [16]. These means also that the bands have the same parity. It can be shown that Cu_2O is a semiconductor with a direct gap at the centre of the Brillouin zone (Γ point).

The spatial wave function part of the highest valence band is triple degenerate with symmetry Γ_{25}^+ and is six-fold degenerate if electron spin is included $\Gamma_{25}^+ \otimes \Gamma_6^+$. The lowest of the conduction band is single and transforms with Γ_1^+ if the electron spin is included the total wave function belongs to Γ_6^+. Spin orbit coupling lifts the degeneracy of the six degenerate valence bands, separating two Γ_7^+ states from four Γ_8^+ states with an energy split of $\Delta_{so} = 133.8\, mev$ independent of temperature[17]. (Formally the direct product of the representations of the spatial and spin wave functions are reducible: $\Gamma_{25}^+ \otimes \Gamma_6^+ = \Gamma_7^+ \otimes \Gamma_8^+$). Experiments on exciton absorption showed that Γ_7^+ is higher in energy. Another conduction band higher in energy, with a spatial part belonging to Γ_2^- and with a total wave function to Γ_8^-, is formed by Cu 4*p* orbitals. See Figure 2.32.

The measured energy gap is $\Delta E = \Gamma_7^+ - \Gamma_6^+ = E_g = 2.1720\, eV$ at 4.2K, obtained as the limit of the yellow exciton series [17], [18]. As usual it decreases with temperature and its dependence on the temperature is showed in Figure 2.5. The expression used to fit the data, based on the Toyozawa model, is [19]:

$$E_g(T) = E_0(0) + S\hbar\omega - S\hbar\omega \coth\left(\frac{\hbar\omega}{2kT}\right) \qquad (2.1)$$

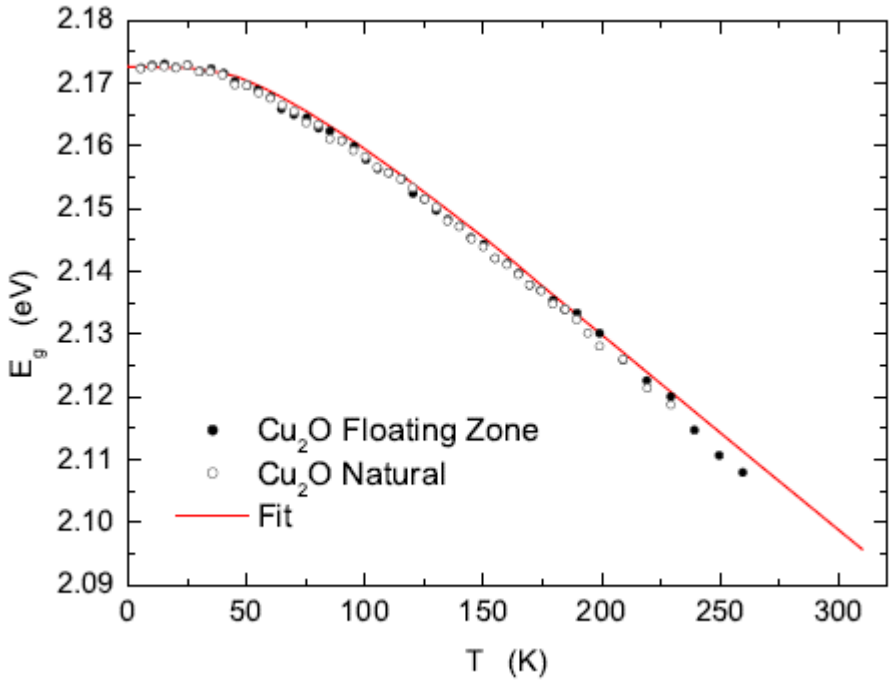

Figure 2.5: Eg as a function of temperature for two different Cu2O samples, after [19]. The data are obtained by luminescence experiments, observing the threshold energy of lower edge of the $X_o - \Gamma_{12}^-$ phonon replica, where XO indicates the orthoexciton emission line. The solid lines is a fit of the experimental data by the expression $Eg\mathcal{T}\square = E_0(0) + S\hbar\omega - S\hbar\omega\, coth(\frac{\hbar\omega}{2kT})$ (2.1).[19]

where $Eg\ (0) = 2.173\ eV$ is the energy gap value at *T* = 0K, *S* = 1.89 is a constant related to the material and $\hbar\omega = 13.6mev$ is the phonon energy of the emitted phonon, Γ_{12}^- in this case.

Table 2-1: Effective masses of carriers in Cu_2O, expressed in unit of the free electron mass m_0. The experimental data are taken from [20] while theoretical predictions from [21].

band		theory			experiment
		ΓX	ΓM	ΓR	
$\boldsymbol{m_e}$	Γ_6^+	0.92	0.92	0.92	0.99
$\boldsymbol{m_h^{LH}}$	Γ_7^+	0.36	0.36	0.36	0.58
$\boldsymbol{m_h^{HH}}$	Γ_7^+	2.83	0.91	0.72	

m_h^{SPH}	Γ_7^+	0.21	0.25	0.27

At intermediate and high temperature, the variation of the gap with temperature can be described by the empirical formula proposed by Varshni:

$$E_g(T) = E_g(0) + \frac{\alpha T^2}{T+\beta} \qquad (2.2)$$

Where $\alpha \; and \; \beta$ are two empirical constants which consider the effect of thermal expansion and electron-phonon interaction. In the case of Cu_2O [22], [23] from the experimental fit of exciton luminescence the constants are $\alpha = 4.8 \times 10^{-4} eV/k$ and $\beta = 275k$.

Other inter-band transition energies at 4.2K are: $\Delta E(\Gamma_8^+ - \Gamma_6^+) = 2.304ev$

obtained as the limit of the green exciton series [18], $\Delta E(\Gamma_7^+ - \Gamma_8^+) = 2.624ev$

obtained as the limit of the blue exciton series [24], $\Delta E(\Gamma_8^+ - \Gamma_8^-) = 2.755ev$

obtained as the limit of the indigo exciton series [24].

The effective hole masses are labelled with LH (Light Hole) for the $\Gamma_7^+$and HH (Heavy Hole) and SPH (spin-orbit SPlit-off Hole) for the Γ_8^+(an explanation of the acronyms can be found in [25]). The effective masses of the free carriers are measured by experiments of cyclotronic resonance [20] and the results are reported in Table 2-1 together with the best available theoretical predictions [25]. For symmetry reasons m_e and m_h^{LH} have to be isotropic whereas m_h^{HH} and m_h^{SPH} have to be anisotropic. These symmetry considerations were confirmed by calculations [25] and experiments [26]. The effective masses are polaron effective masses. Indeed, being the Cu_2O partly ionic, the free carriers are surrounded in their motion by a cloud of phonons which increases their mass. Bare effective masses, strictly related to the curvature of the bands are few per cent points smaller [20].

Using the experimental values of m_e andm_h^{LH} we obtain the values of the effective density of states, N_c and N_v, of the lowest conduction band and the higher valence band of Cu_2O respectively:

$$N_c(T) = 2(\frac{2\pi m_e kT}{h^2})^{\frac{2}{3}} = 4.76 \times 10^{15}\, T^{\frac{3}{2}}\, cm^{-3} \qquad (2.3)$$

$$N_v(T) = 2(\frac{2\pi m_h^{LH} kT}{h^2})^{\frac{2}{3}} = 2.13 \times 10^{15}\, T^{\frac{3}{2}}\, cm^{-3} \qquad (2.4)$$

where the temperature *T* is expressed in kelvin. At room temperature we have:

$$N_c(300K) = 2.47 \times 10^{19} cm^{-3}$$
$$N_v(300K) = 1.11 \times 10^{19} cm^{-3}$$

Finally, the values of n_i^2:

$$n_i^2(T) = 1.014 \times 10^{31} T^3 e^{-\frac{E_g(T)}{kT}}\, cm^{-6}$$
$$n_i^2(300k) = \ 2.12 \times 10^3 cm^{-6}$$

where we have used E_g (300 K) = 2.09 eV in the last expression.

From the theoretical point of view, several ab-initio calculations of the Cu_2O electronic structure have been performed, by several different techniques. We have to remember that the self-consistent techniques based on Local Density Approximation (LDA) or Generalized Gradient Approximation (GGA) underestimate the energy of the excited states (i.e., the conduction bands) whereas those based on the Hartree-Fock approximation overestimate it. However, the shape of the conduction bands are qualitatively correct and therefore they can give an idea of the real conduction bands simply shifting them in the energy. The only calculations with correct estimation of the band gap are semi-empirical rather than self-consistent. For a brief review see [27]–[29]. In *Figure 2.6*Figure 2.7 self-consistent [30] and semi-empirical [31] bands calculation are shown.

The correctness of band calculations was investigated by several kind of spectroscopic experiments (X-ray Photoemission Spectroscopy (XPS), X-ray Absorption Spectroscopy

(XAS), X-ray Emission Spectroscopy (XES), Ultraviolet Photoemission Spectroscopy (UPS), Resonant Photoemission Spectroscopy (RPES), Angle Resolved Photoelectron Spectroscopy (ARPES) Auger Electron Spectroscopy (AES) and Bremsstrahlung Ssochromat Spectroscopy (BIS, also called inverse photoemission); Low-energy Electron-Diffraction (LEED); predictions on absorption coefficient). See [28], [29] for a review.

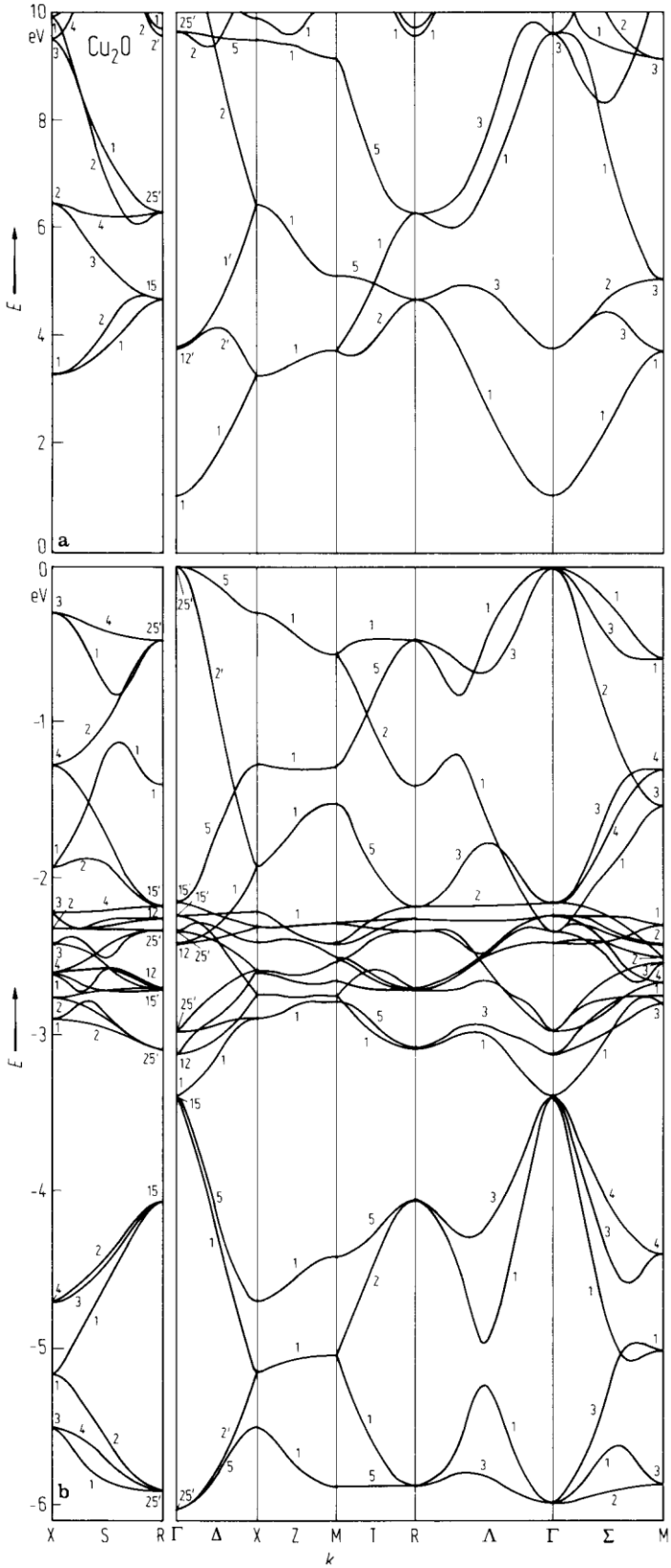

Figure 2.6: Electronic bands calculated by a self-consistent LDA approach with localized Gaussian basis and Slater exchange. a) Conduction bands. b) Valence bands. Notice the typical underestimation of the band gap due to the Local Density Approximation[30].

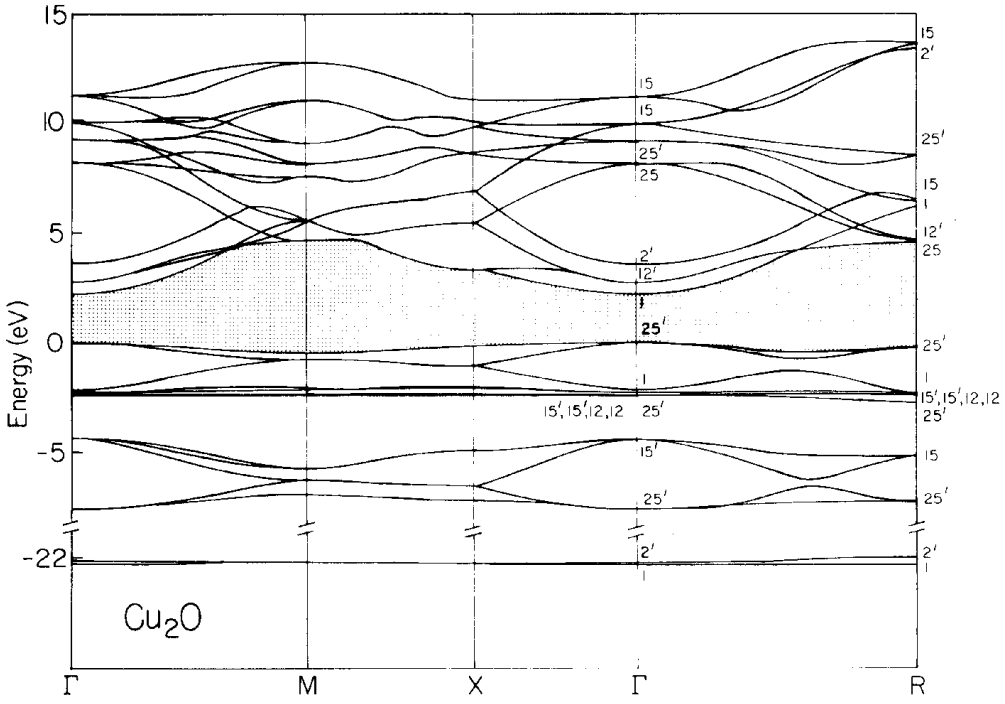

Figure 2.7: Electronic bands calculated by parameterized semiempirical tight-binding method [31]

A good agreement between the calculated bands and the experiments has been found and the ionic-covalent character of the bonds was experimentally seen. In contrast with some other transition metal oxides, the electronic correlation is expected to be relatively small, thanks to the closed shell (*d*10 configuration, in a pure ionic model Cu^{+},O_2^{-}). Indeed, the valence band calculations are not affected by many body effects (one-electron band theory is enough) and this was confirmed by the experiments. Finally, as we have seen, Cu2O shows an unusual linear coordination O−Cu−O of copper atoms. This coordination, and therefore the cuprite structure, cannot be explained by simple ionic forces which, instead, predict an unstable structure. The cited experiments found that the hybridization between orbitals O2*p*–Cu4*sp* exists, confirming a long-time hypothesis for cuprite stability. For the sake of completeness, in Table 2-2 we report the characteristic energy values of Cu2O near the surface (see Figure 2.8 for an explanation). Electron affinity χ is taken from [32]. According to these values, near the surface an electron can be excited up to the fourth conduction band before escaping from the material.

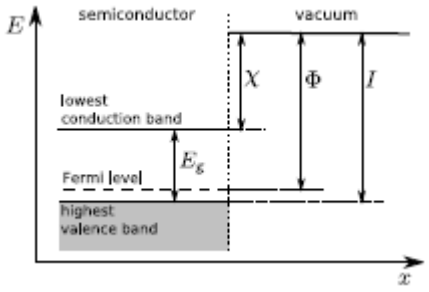

Figure 2.8: Schematic band diagram of a semiconductor near the surface.χ is the electron affinity, ϕ is the work function, I is the photo-threshold energy, E_g is the band gap and $\mu = \chi + E_g - \phi$ is the electron chemical potential. Even if μ is improperly called Fermi energy (E_F), according to the tradition we will use this wrong term along this thesis.

Table 2-2: Surface potential values for Cu_2O at 300K. *I* and Φ are calculated from the experimentally values of χ, E_g and E_F. Remember that χ does not depend on temperature whereas ϕ, *I*, E_g, and consequently E_F,do. E_F andϕdepend on doping concentration also.

quantity	value (eV)
χ	3.20
Φ	≈ 4.90
I	5.25
E_g	2.09
E_F	≈ 0.35

A recent attempted to model the electronic band structure was done by our calibrators, Alistair Brewin and prof Stewert Clark at the university of Durham, using the CASTEP modelling code[33]. Their electronic band structure (see Figure 2.9) shows the electronic dispersion curves along different paths for the cubic 1st Brillouin zone described in the previous diagram. This band structure illustrates that Cu_2O is a direct band semiconductor because the minimum of the conduction band is located at the same point in k-space as both the light- and heavy-hole valance band maxima. We can also fit parabolas around the band maxima and minima and use the curvatures to estimate the effective masses. This gives $m^* = 0.94\ m_e$ for the conduction band, and $m^* = 0.36\ m_e$ and $m^* = 3.22\ m_e$ for the light- and heavy-hole bands respectively.

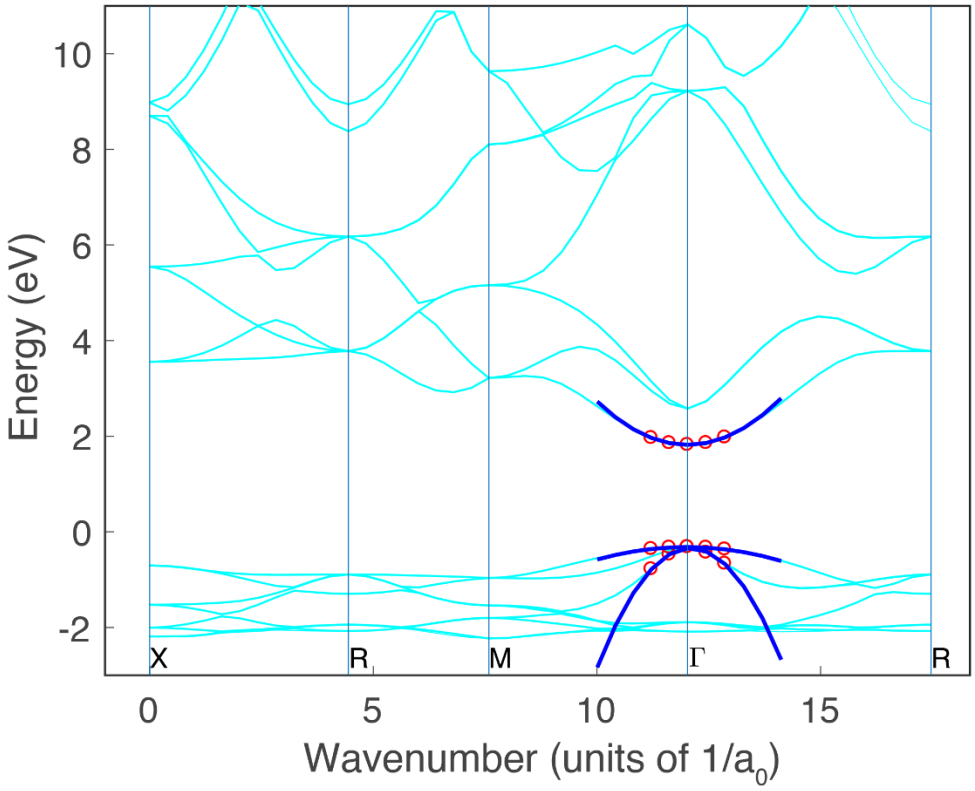

Figure 2.9: Electronic bands calculated by CASTEP modelling code.[33]

2.2.3 Phonon

Six atoms in the unit cell means 6×3 =18 phonon modes. We expect fifteen optical phonon branches and three acoustic branches. These 18 phonon modes, in the zone–centre, have the symmetries $2_{\Gamma_{12}^-} \oplus 3 3_{\Gamma_{15}^-} \oplus 3_{\Gamma_{25}^-} \oplus 3_{\Gamma_{25}^+} \; 1_{\Gamma_2^-}$

Of the three sets of triply degenerate Γ_{15}^- phonons, one set corresponds to the acoustic phonons while the other two are the infrared–active optical modes. The Γ_{15}^- mode is Raman-active. Optical phonons which are neither infrared-active nor Raman-active are said to be silent. TheΓ_2^-, $\Gamma_{12}^-$and Γ_{25}^- modes in Cu_2O are silent modes. Since the crystal has the inversion symmetry, the infrared-allowed modes are Raman forbidden and vice versa.

The vibrational mode description is shown in Figure 2.10. For a review of the techniques used to identify the phonons, usually photoluminescence phonon replica and infrared spectroscopy, see [34]–[36]In [34] a study of phonon dispersion relations by neutron scattering is also reported.

Considerable attention has been paid to the phonon spectrum in Cu_2O. After numerous infrared and Raman studies the phonon spectrum of cuprous oxide is now well understood. One of the main problems was that the observed number of bands

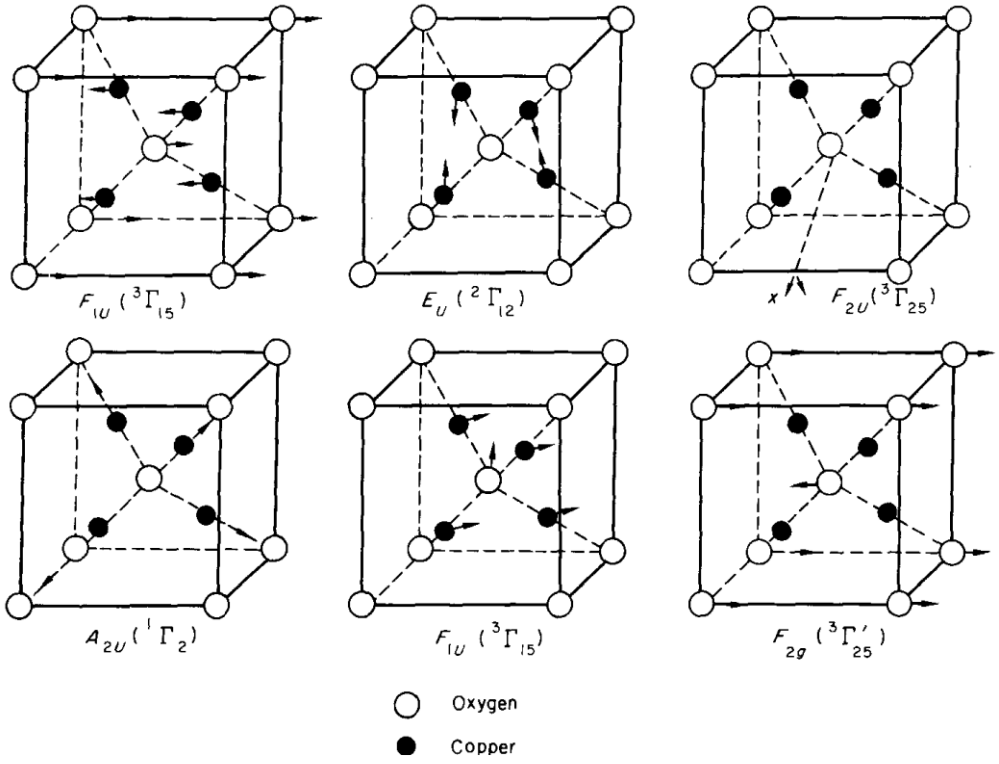

Figure 2.10: Pictorial representation of the vibrational modes of Cu_2O .

is much larger than that deduced from the group theory. This fact is now explained interpreting the spectra in terms of bi-phonons or multi-phonons processes in light absorption. An example are the absorption band at 0.14 eV and 0.10 eV [37], [38].

2.3 Growth of Synthetic Cu_2O

2.3.1 The Challenge: Phase diagram

Cu_2O (cuprous, $\mathcal{K}$) and CuO (tenorite, $\mathcal{T}$) are only two chemical compounds formed by oxygen and copper, which can be found in nature[1]. The phase diagram of binary system Cu-O in terms of temperature and oxygen partial pressure PO_2 is reported in Figure 2.11 [39]. Preparing Cu_2O presents several challenges, as it is stable only at oxygen pressures below a few hundred torr and within a narrow temperature range. As the oxygen pressure decreases, the stable region for Cu_2O shifts to lower temperatures, remaining below 1000°C. This is significant for growth processes where temperatures exceeding 1000°C are undesirable due to the dissolution of Cu.

Consequently, a practical temperature window for Cu_2O synthesis is between 700°C to 900°C, corresponding to an oxygen pressure range of 10^{-4} to 10^{-1} Torr. Additionally, unless special precautions are taken during the cooling of Cu_2O from the high temperatures at which it is prepared, certain reactions may occur. One such reaction is the surface oxidation of Cu_2O to CuO, described by the equation:

$$Cu_2O + \frac{1}{2}O_2 \xrightarrow{yields} 2CuO \qquad 2\text{-}1)$$

it's important to note that Cu_2O is unstable at room temperature. However, the kinetics of its transformation into CuO are so slow at this temperature that Cu_2O can be considered stable for most practical applications [40].

[1] There are also two other unstable compounds: Cu_3O_2 and Cu_3O_4 (paramelaconite). In these compounds, copper exhibits both oxidation states. Cu_3O_2 is the more prevalent of the two and can often be found as a surface defect in Cu_2O.

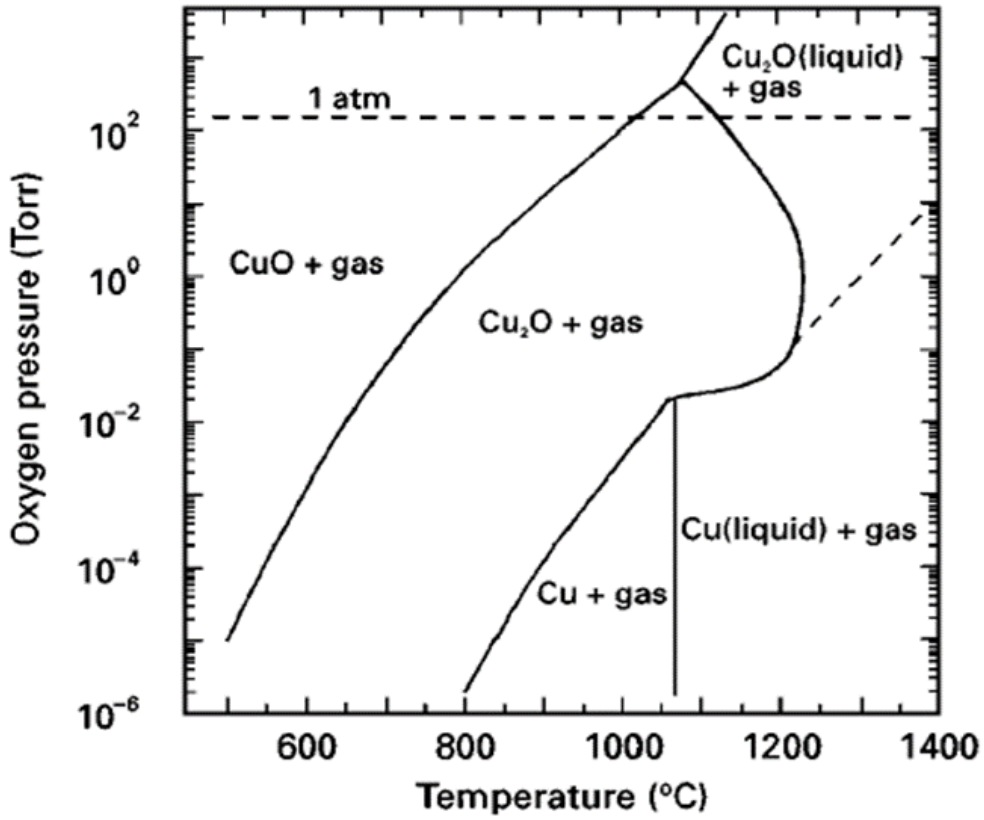

Figure 2.11: Phase diagram of the copper-oxygen system for pressure versus temperature [40].

2.3.2 Overview of Growth Techniques in Literature

The pursuit of high-quality single crystals has led to the development of various crystal growth techniques. Traditional methods, such as the Czochralski approach, have historically served as the cornerstone of crystal production. These methods have proven effective, yet they are not without their limitations, often relying on crucibles to facilitate crystal growth. Study by Zucker found that molten Cu_2O is highly reactive with most crucible materials[41]. MgO was found to be suitable crucible material for the Czochralski crystal growth of Cu_2O although some reactivity between MgO and molten Cu_2O was still observed over extended periods of time [41]. Therefore, a noteworthy alternative has emerged in the form of the crucible-free floating zone method. What sets this method apart is its absence of a crucible,

which imparts several key advantages. By eliminating the need for a crucible, the floating zone method not only ensures enhanced chemical purity but also opens the door to scalable crystal growth. These attributes make it an appealing choice for Cu_2O crystal growth [42].

2.3.3 Optical Float Zone Growth

Nonetheless, there are lingering challenges concerning growth conditions and the nature of microstructure defects. To successfully utilize the floating zone method for Cu_2O crystal growth, precise control over purity of starting material, temperature, and oxygen partial pressure within the Cu_2O stability region is essential, see Figure 2.11.

It is worth to mention how this method works, it starts by total oxidation of a high purity copper rod of technical (99.999% Cu) in air at 1045^{o}C for 3 days. At elevated temperature, Cu_2O will react with normally inert materials, including platinum [40]. To minimize contamination, V-shaped supports made from copper foil were placed along the entire length of an inverted alumina boat. Copper rods were then placed on top of the foil supports. Using this method, copper foil is the only material in contact with the copper rods and contamination is minimized. After cooling to ambient temperature in air, the surface layer of CuO is removed by either polishing or etching. Now the polycrystalline is ready to subject the floating zone method. The feed rod (Cu_2O polycrystalline rod) is suspended from holder, then the bottom edge is locally heated until it melts and connected to a seed rod, forming a molten zone. As both rods are gradually moved out of the molten area, a single crystal forms atop the seed rod. The rods are usually counterrotated for uniform mixing of the melt. Growth occurs inside a transparent quartz tube, allowing control over the gas environment and pressure, which is crucial for different material properties (Figure 2.12). Growth can now be achieved even under extremely high vacuum [43], high pressure [44], and very low oxygen partial pressure [45] depending on the desired obtained crystal.

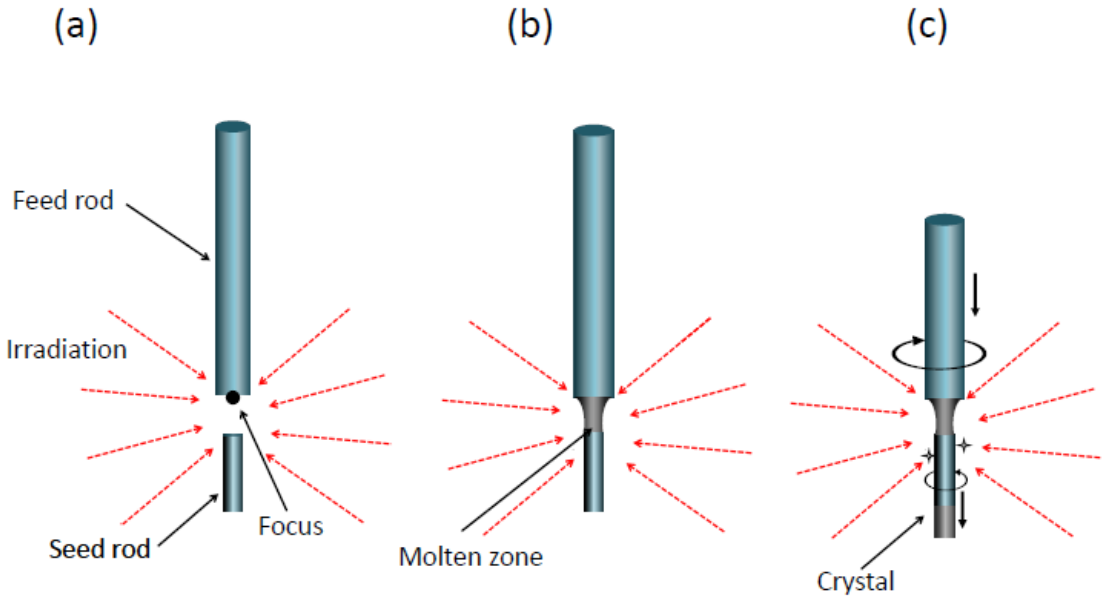

*Figure 2.12: illustration of the floating-zone processes. Here, the red arrows represent the light conversion to the focal point. (**a**) Local heating to the feed rod for melting. (b)forming the molten zone (c) growth the single crystal by pulling both the feed and seed rods (reproduced from* [46]*).*

.

A key challenge is maintaining the stability of the molten zone, which is held in place only by surface tension between the rods. The viscosity of the molten material and the power applied must be carefully controlled to prevent down-spilling or instability, both of which can disrupt crystal growth. Achieving a stable molten zone requires a sharp temperature gradient along the growth direction and a homogeneous liquid across the rod's diameter. Modern furnace technologies are critical for maintaining these conditions.

The local heating toward the focus is essential for stable zone. The heating has been generated by radio-frequency [47] electron beam [48] and arc heating [49]. In addition, optical heating has been adapted these days in most cases. The Cu_2O single crystal used in this work has been growth by using optical heating.

A floating-zone furnace with optical lamps, which uses horizontally configured optical lamps is shown in Figure 2.13 whilst the top view schematics of a typical furnace is shown in Figure 2.14a and b with four and two mirrors, respectively [50]. In the two-mirror furnace (Figure 2.14b), a halogen lamp is positioned at one focal point of an elliptical mirror, directing

radiation to converge at the other focal point, where the molten zone forms. The temperature in this zone can exceed 2000°C, allowing for the successful growth of various materials. However, a challenge arises with the light intensity profile in the molten zone, as shown in the lower panels of Figure 2.14b) and Figure 2.14. The intensity can oscillate with the azimuthal rotation angle (θ), leading to temperature fluctuations and potential nonuniformity in the liquid zone. While the four-mirror configuration (Figure 2.14a)[2] offers a more stable temperature profile than the two-mirror setup, these oscillations may still cause inhomogeneities in the liquid, affecting crystal quality. Counterrotating the feed and seed rods can help mitigate these nonuniformities.

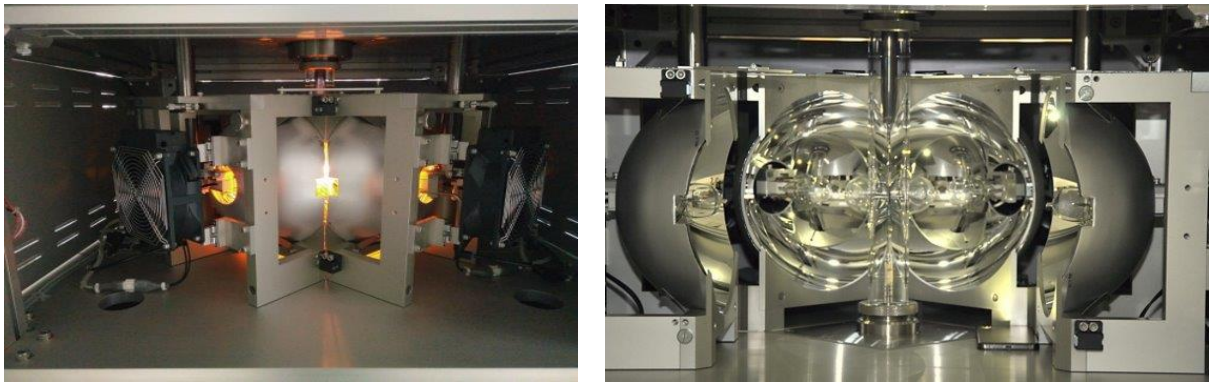

Figure 2.13: (a) The optical floating-zone furnace used for crystal growth, showcasing the setup with horizontally configured optical lamps that precisely control the heating zone to facilitate the floating-zone method. (b) Close-up of the mirrors and quartz tube within the optical furnace, illustrating how the mirrors focus light to create a localized high-temperature zone, essential for melting the material and promoting uniform crystal growth.

[2] To achieve uniformity in the molten zone, this work used the four-mirror configuration (Figure 2.9a), which provides a more stable temperature profile compared to the two-mirror setup (Figure 3b).

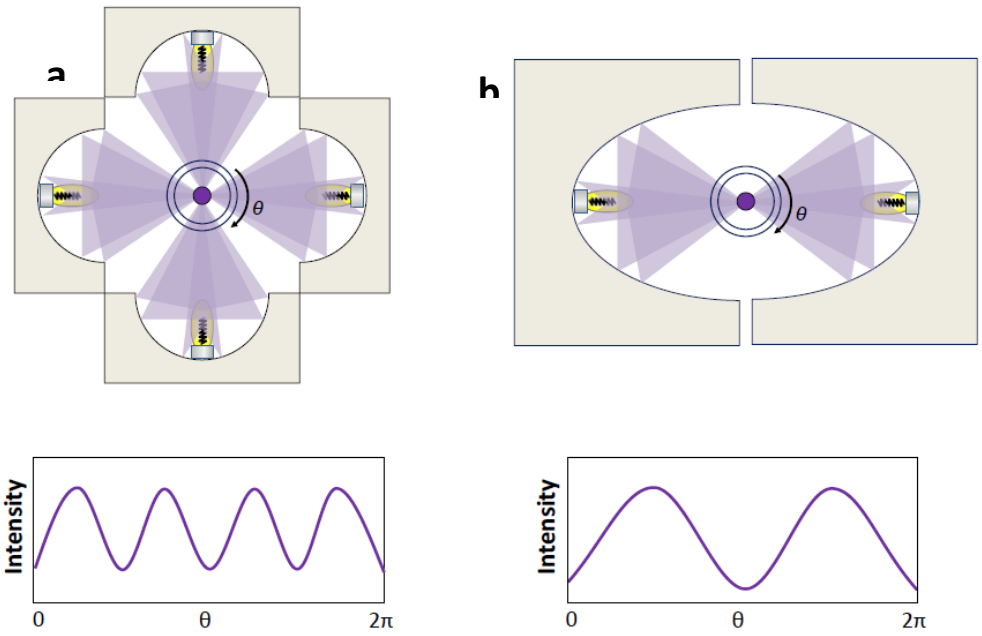

*Figure 2.14: Schematic drawings from the top view of the optical-lamp type floating-zone furnaces. (**a**) Four-mirror horizontal geometry with four lamps. (**b**) Two-mirror horizontal geometry with two lamps. Below each schematic graph represents the optical power intensity profile at the growth position along rotation within the transverse plane reproduce from*[46].

To prove that the floating zone is the favourable way to growth single crystal Cu_2O with a minimum concentration of microstructure defects and determine the optimum condition for growing Cu_2O single crystal Ito and his group compared the physical and chemical properties [12]. This study involved the fabrication of numerous Cu_2O crystals via diverse methodologies including melting growth furnace annealing FA[3], floating-zone method FZ, Czochralski Method and also natural crystal were examined by a variety of techniques. These crystals were subjected to photoluminescence spectroscopy to investigate defect concentrations, and this was carried out at T= 4.2K. The differences between their luminescence is shown in Figure 2.15. As seen significant differences are observed in the luminescence spectra of the samples. For the FZ specimen a set of luminescence spectra is shown, including the V_{cu} band at approximately 910 nm and Vo_2^+ band at about 720 nm, the intensity of V_o^{2+} is only one-eighth of V_{cu} band while for FA, only V_{cu} band is observed, this

[3] Polycrystalline Cu_2O can be obtained easily by heating copper metal at high temperatures between 1020 and 1120 ^oC in air.

band's intensity is approximately 18 times larger than in specimen FZ. For specimen GZ both the V_{cu} band and Vo band are prominently observed. The intensity of V_o^{2+} band in GZ sample is about 300 times larger and the intensity of the V_{cu} band are about 40 times larger than those in specimen FZ. Additionally, the Vo+ band at 820 nm is also observed in GZ sample. in contrast, when examining the natural specimen some intensity differences were observed. The luminescence intensity of V_{cu} band is lower than the FZ, however the V_o^{2+} band is prominently visible in the natural specimen and its intensity around 38 times larger than of FZ. This could be as the natural crystal is formed in an environment characterized by reduced oxygen concentrations deep within the Earth's interior. Notably, by considering the defects concentration the successful production of such single crystals was achieved using the FZ melting method. These crystals show the best value of photocarrier mobility and scattering times, measured at 4.2K. The following characteristics for photocarrier mobility and scattering times were displayed; i) $\mu_h \approx 1.8 \times 10^5 cm^2\, V^{-1} s^{-1}$ and $\tau_h \approx 60\, ps$ for hole ii) $\mu_{\bullet} \approx 1.3 \times 10^5 cm^2\, V^{-1} s^{-1}$ and $\tau_{\bullet} \approx 70\, ps$ for electron. These findings collectively indicate that the capture of photocarriers by impurities is notably ineffective at temperatures below 100 K in Cu_2O [12].

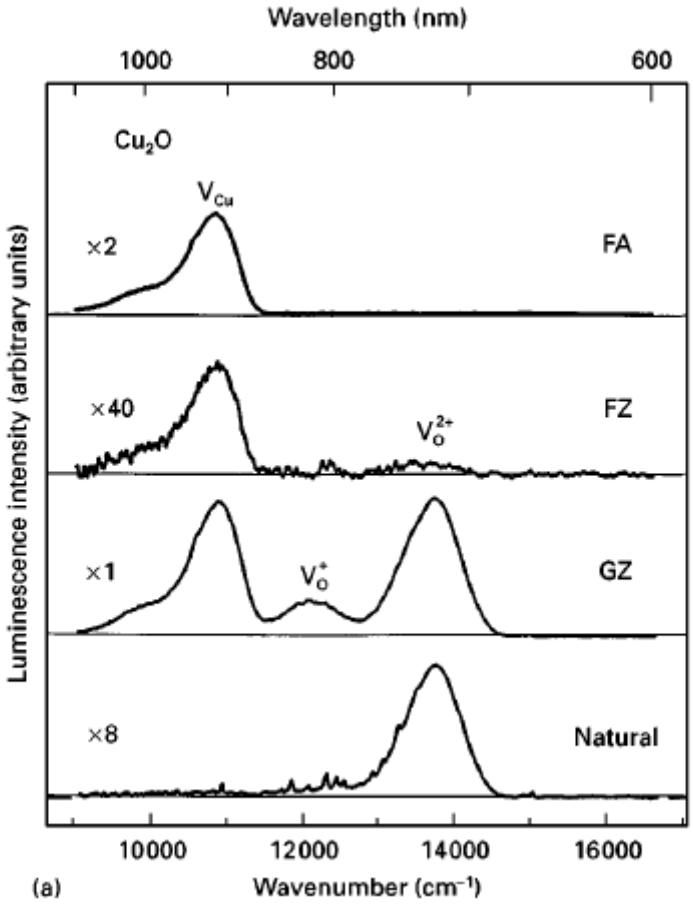

Figure 2.15: Photoluminescence spectra in near-infrared region of Cu_2O photoexcited by an Ar-ion laser (λ_{ex}=514.5 nm) at T= 4.2 K. Broad V_{Cu}- and V_O+ bands indicate that they are due to lattice defect centres such as copper and oxygen vacancy, respectively[12]

2.3.4 Defects and Impurities

2.3.4.1 CuO precipitate

Understanding the nature of defects in Cu_2O is crucial because they can significantly influence its physical properties, such as dislocations, grain boundaries, solute atoms, precipitates, or deviations from stoichiometry. Therefore, it is essential to evaluate data on basic electrical, magnetic, optical, and mechanical properties from single crystals of controlled quality. Early investigations of Cu_2O primarily used polycrystalline materials. Various methods have been applied to grow single crystals, including grain-growth of polycrystalline sheets [51], oxidation of single crystal copper [52], hydrothermal growth

[53], and more recently, melt growth with [41] and without a crucible [54], [55]. Among these methods, crucible-free growth from the melt offers significant advantages, particularly in meeting the requirements for chemical purity[4].

However, looking at the phase diagram there is several difficulties encountered in preparation Cu_2O: has high temperature. also, the ambient temperature and ambient atmosphere is a stable phase of CuO. So special care should be taken in the cooling process avoiding reaction in Reaction (1-1). Despite of that solid state phase transformations occurring within the bulk crystal, leading to internal precipitation of CuO, cannot be excluded either.

Various experiments are conducted to improve crystal growth with the most significant factor being atmospheric condition were studying extensively. Schmidy-Whitley employed a crucible-free technique to grow a Cu_2O single crystal in reduction condition. The resulting crystal exhibited various inclusions of CuO throughout the crystal. The CuO inclusion exhibited various microstructure in two different shapes: First one near the surface small polyhedral CuO [5] precipitates formed, while large tentacle -like[6] structures, initially thought to be pores, were identified as a combination of CuO precipitates and cavities through selective etching and microprobe analysis. The distribution of polyhedral CuO near the surface and tentacle-like precipitates near the axis continued throughout the crystals see *Figure* 2.16 and *Figure* 2.17 which show these two different types of precipitate. It was found that the extreme growth conditions the overlap between CuO/Cu_2O phases have significant role in defects formation [40].

[4] This is the technique that used to growth the single crystal for this project.

[5] Polyhedral CuO precipitates are solid, three-dimensional structures formed within a crystal lattice. They exhibit a regular, many-sided geometric shape resembling a polyhedron, which can have various faces, such as triangles, squares, or hexagons. These precipitates consist of copper (II) oxide (CuO) and are typically found within crystalline materials. The term "polyhedral" emphasizes the well-defined, multi-sided structure of these CuO precipitates, reflecting their ordered arrangement within the crystal.

[6] Tentacle-like CuO structures: Irregular, elongated formations resembling tentacles, found within a crystal lattice, often initially mistaken for pores. Comprised of cupric oxide (CuO) precipitates and cavities, typically located deeper within the crystal. Identified through selective etching and microprobe analysis.

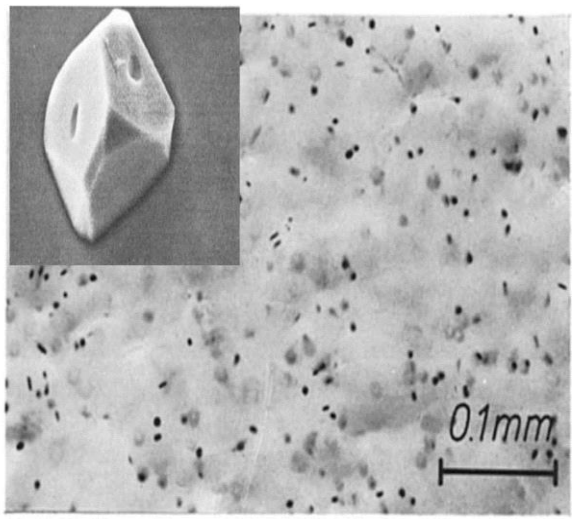

Figure 2.16: Optical transmission image of polyhedral cupric oxide precipitates within a melt-grown cuprous oxide single crystal (transversal section, near the surface). The inset shows a scanning micrograph after selective etching of the matrix [40].

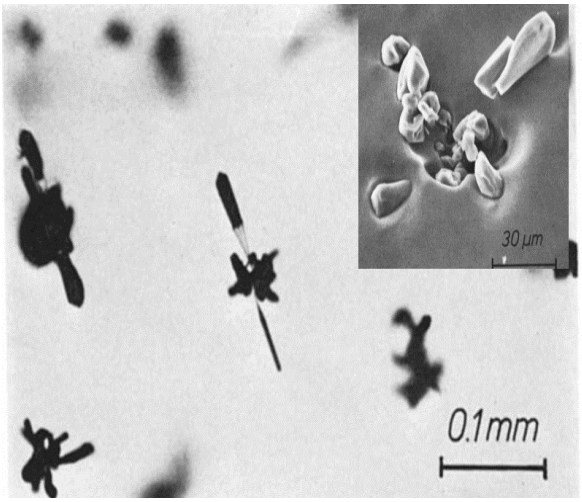

Figure 2.17: optical transmission of tentacled precipitates in a cuprous oxide single crystal grown from the melt (transversal section, near the core), the inset shows scanning micrograph after a selective etch of the matrix, revealing a complex of cupric oxide precipitation and porosity [40].

2.3.4.2 Vacancies point defects.

Another type of the defect is vacancies, it is known that a metal oxide will naturally be cation-deficient if its cation is oxidable or if it has a large positive oxidation number, according to standard structural inorganic chemistry, which is the case with $Cu^{(I)}O$ and $Cu^{(II)}O$ in Cu_2O. Before going ahead explanation of the notation used in describing crystal vacancies is required. The primary symbol denotes the type of point defect, where "V" represents a vacancy. The subscript indicates the location of the atom or vacancy, with "i" signifying an interstitial position, while the superscript denotes the electric charge relative to the ideal crystal, with "O" indicating neutrality. For instance, in Cu_2O, V_{cu}^{0} denotes a copper (Cu subscript) vacancy (V) with no charge (zero superscript); O_{cu}^{0} signifies an oxygen atom (O) occupying a copper site (Cu) with no charge; and V_{O}^{+} represents an oxygen (O subscript) vacancy (V) with a +1 charge.

Possible intrinsic point defects in Cu_2O include vacancies V_{Cu} and V_O, interstitials Cu_i and O_i, and the split vacancy V_{Cu}^{split}, which has been predicted by theoretical studies. According to Wright and Nelson [56], there are two types of copper vacancies. The regular vacancy represents a straightforward vacant copper site with the rest of the crystal structure remaining unchanged. In contrast, the split vacancy involves another Cu atom shifting from its original position to partially occupy the simple copper vacancy, as illustrated in Figure 2.18. This configuration leads to the formation of four bonds between the displaced copper and the nearest oxygen atoms, introducing disorder into the lattice, while the simple vacancy maintains the oxygen dangling bonds. Defects in Cu_2O come into two types the first one is Frenkel defect (V_{Cu}-Cu_i) and (V_O-O_i), the second form of defect is Schottky defect ($2V_{Cu}$-V_O), antistites Cu_O and O_{Cu}. Frenkel defect and Schottky are stoichiometric defects. in other words, their presence does not change the stoichiometry.

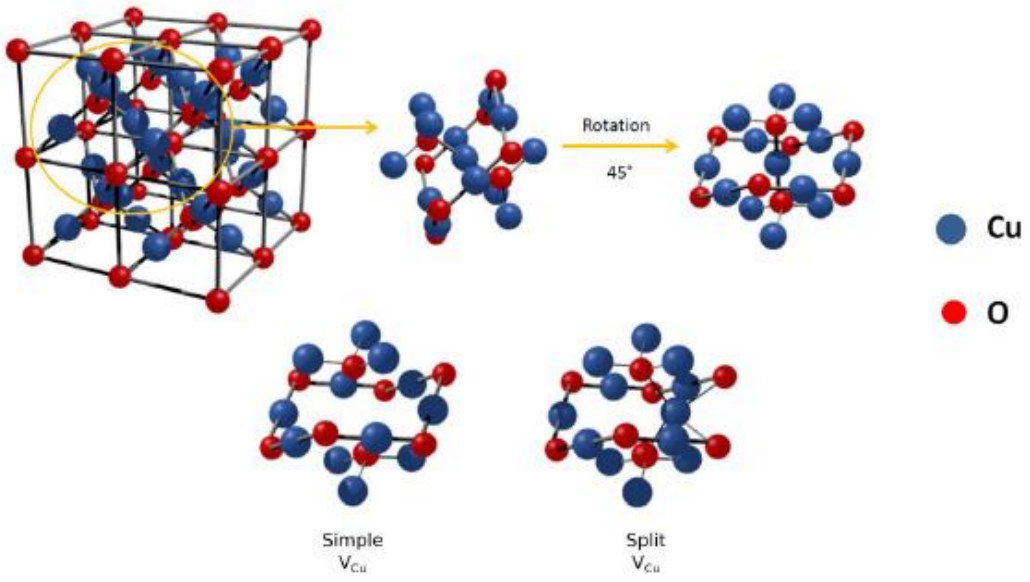

Figure 2.18: Configuration of a single copper vacancy in Cu_2O. Shown are the complete structure, a simple vacancy, and a split vacancy, with copper atoms represented by blue circles and oxygen atoms by red circles.

The formation energy is a useful concept need to be introduced here as it can determine the possibility of the vacancy formation and then which type of the pervious vacancies more likely to be in the crystal at different growth conditions. Formation energy is defined as the energy change associated with breaking the bonds of an atom with its ligands and forming new bonds with ligands in a reference system. This metric is used to evaluate the likelihood

of vacancy formation, its concentration, and to study the bonding environment within materials.

In their research on Cu_2O, Nolan and Elliot analyzed both simple and split copper vacancies [57]. They charted the defect formation energies against the Fermi level. Their findings indicate that the formation energy of a simple copper vacancy is 60 meV lower than that of a split vacancy, making the former the more stable configuration in Cu_2O. This observation is corroborated by theoretical studies conducted by Raebiger, Lany, and Zunger, who also reported that the formation energy of a split vacancy (1.0 eV) is higher compared to a simple vacancy (0.7 eV), with their results also depicted in Figure 2.19 [58].

Additionally, oxygen interstitials represent another potential source of defects in Cu_2O, contributing to the material's p-type conductivity. These interstitials can occupy two different positions within the unit cell: O_i^{oct} and O_i^{tet}. However, they are generally considered to have high formation energies and deep transition levels, making them less favorable compared to copper vacancies [59].

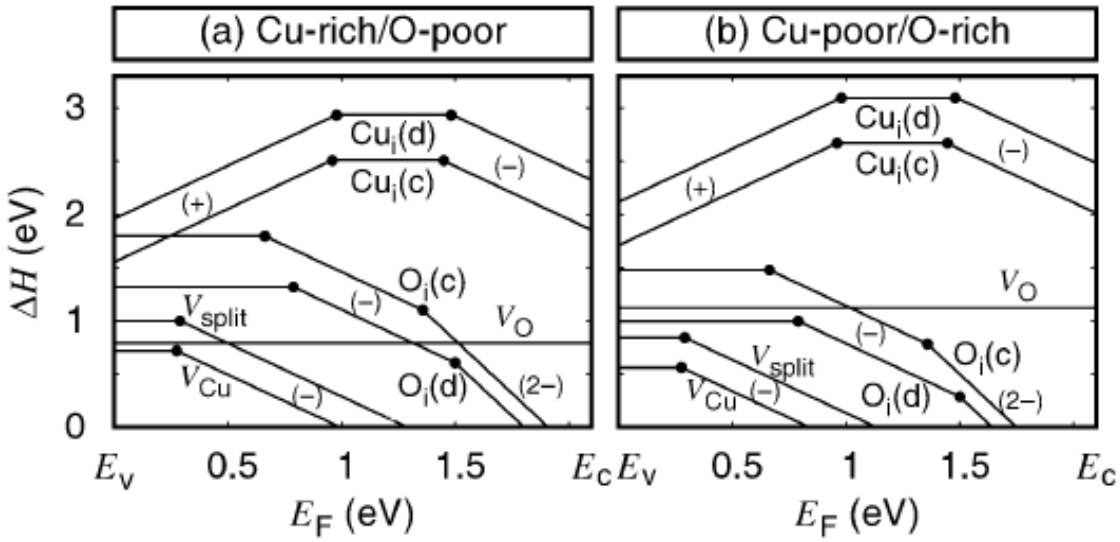

Figure 2.19: Calculated formation enthalpies of defects in Cu_2O as a function of the Fermi level. The labels "c" and "d" denote different interstitial sites within the unit cell. Each defect may exist in two or more charge states, as indicated by the + and – signs [58].

To optimize the Cu_2O material properties, post-growth annealing becomes a crucial phase in the crystal production process. Post-growth annealing is a controlled heat treatment process that serves to refine the crystal structure, eliminate defects, and improve the overall quality of the grown crystals. It involves subjecting the freshly grown crystal to specific thermal and environmental conditions to facilitate the rearrangement of atoms or ions within the crystal lattice. The useful attempt has been made by Chang et al [60]. They annealed a sliced sample that has been grown by floating zone method (< 1mm) as a consequence of the inverse of Reaction (2-2) to remove the CuO inclusions, when annealing the crystal within the crystal phase conditions (shown in Figure 2.11) the number of copper vacancies should increase as CuO inclusions are reduced to Cu_2O.

$$Cu_{Cu}^{Cu_2O} + V_{Cu}^{cu_2O} + O_O^{Cu_2O} \rightarrow Cu_{Cu}^{CuO} + O_O^{CuO} \qquad 2\text{-}2$$

The concentration of V_{cu} can be controlled by the amount of CuO formed in the bulk of crystal as it cools. The experiment was conducted in two different cooling conditions to monitor the amount of vacancies produce as following, annealed at 1050^{o}C for varying durations, ranging from 1 day to 5 days. Subsequently, certain samples were rapidly quenched to room temperature, while others underwent a slow cooling process at a rate of 5°C per minute. The copper vacancies concentration was then examined by obtaining the corresponding PL peak which was measured for each condition (see Figure *2.20*) the horizontal black line represents the average luminescence intensity of the as-growth samples. All quenched samples exhibit higher copper vacancy concentrations, while all 5^{o}C/min cooled samples contain lower copper vacancy concentrations. When compared to as-grown crystals the difference in the luminescence intensity between the quenched and slow cooling sample is an order of magnitude. They found that the slow cooling of annealed samples at a rate of 5°C/min is effective in reducing CuO to Cu_2O within a single day. However, samples subjected to slow cooling for durations of 3 and 5 days displayed anomalous behaviours, such as increased vacancy concentrations and a broader range of luminescence intensities compared to other samples cooled at the same rate. These disparities could likely be due to differences in the polishing depth, or the particular sections of the crystal used for the slices. In contrast, the wide variance in luminescence intensities

observed in the quenched samples was not linked to annealing variations but rather to inhomogeneities introduced by the rapid cooling process [60].

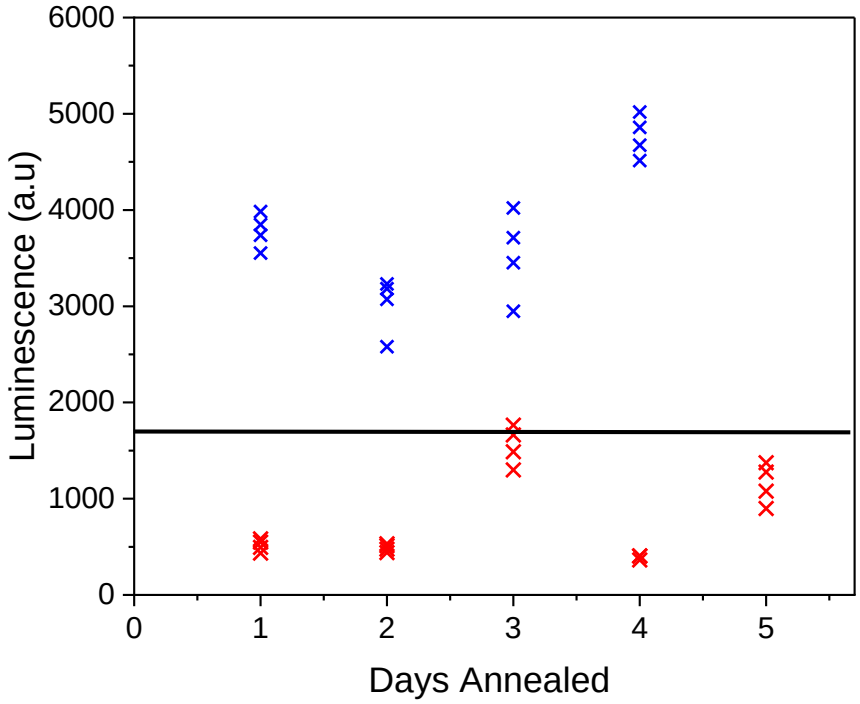

Figure 2.20: Copper vacancy luminescence in Cu_2O crystals annealed at 1045 °C for varying durations. Blue points correspond to samples quenched to room temperature, while red and green points represent samples cooled at a rate of 5 °C/min to room temperature. The lines show the average luminescence of samples that were not annealed, as reproduced from [60].

2.4 Assessing Material Quality

2.4.1 X-ray Diffraction

X-ray diffraction (XRD) is a powerful tool used to investigate the crystallographic properties of materials, including phase identification, crystallographic orientation, and film crystallinity. Intense diffraction peaks, known as Bragg peaks, are observed when strong constructive interference occurs. The resulting diffraction pattern is analyzed to confirm whether a Cu_2O sample is a single crystal. The XRD data can reveal several characteristics

indicating a well-ordered, continuous crystalline lattice with minimal grain boundaries or defects.

In the case of a single crystal, the XRD pattern typically exhibits only a few strong peaks, or even a single sharp peak, corresponding to a specific orientation of the crystal lattice relative to the incident X-ray beam. This suggests that the entire sample has a uniform crystallographic orientation.

For a Cu_2O single crystal, common peaks observed in the XRD pattern include: **(111) Plane**: usually the strongest peak for Cu_2O, appearing at a diffraction angle 2θ of approximately 36.4°, **(200) Plane**: this peak occurs at $2\theta \approx 42.3°$ but is less intense compared to the (111) peak and **(220) Plane**: another important peak, appearing at $2\theta \approx 61.4°$, though it is typically less intense than the (111) peak. These characteristic peaks help to identify the crystal orientation and confirm the single-crystal nature of the Cu_2O sample.

Laue diffraction is another powerful method for verifying single crystallinity. It uses a continuous spectrum of X-rays rather than monochromatic X-rays. When a single crystal is exposed to Laue diffraction, the resulting pattern consists of sharp spots, which represent specific crystallographic planes. In contrast, polycrystalline or defective crystals produce blurred or diffuse patterns [61]. Figure 2.21 presents a comparison of Laue patterns for synthetic and gemstone Cu_2O single crystals used in this work. These Laue patterns clearly highlight the cubic symmetry and single-crystal nature of both Cu_2O samples.

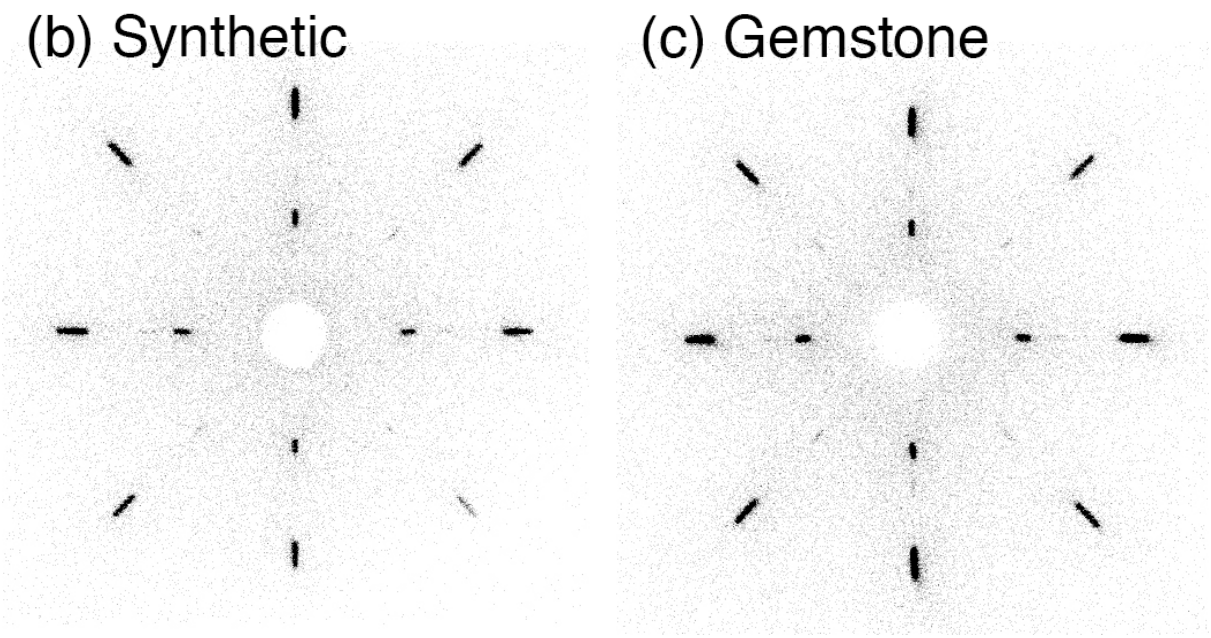

Figure 2.21: Laue spot patterns of (b) synthetic and (c) natural Cu_2O crystals for comparison. Both crystals were aligned with the incident X-ray beam perpendicular to the (100) crystallographic plane. The patterns clearly demonstrate the cubic symmetry and single-crystal structure of both Cu_2O samples. [14]

2.4.2 Conductivity

Studying electrical properties of Cu_2O samples as a function of temperature is important way to characterise the point defects of this material.

Chosen varieties of temperature low and intermediate temperatures, we are considering a temperature range where it takes a considerable amount of time for a material to reach thermodynamic equilibrium, a state where its properties no longer evolve over time. This extended equilibration period is much longer than the duration of the subjected measurement. Consequently, we can assume that the concentrations of defects within the material remain constant and unchanging during these measurements.

In this section first we will briefly discuss the important behaviour of dark conductivity and the persistent photo conductivity and how this used to discover this material is a composited material.

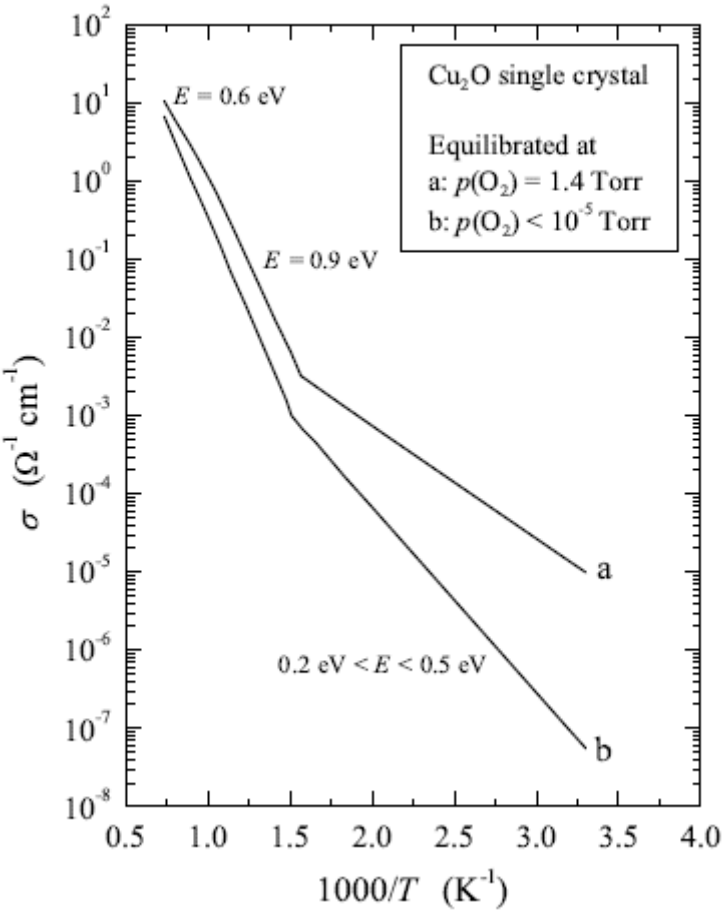

Figure 2.22: Conductivity of a Cu_2O crystal as a function of temperature. The measurements were performed equilibrating the crystal at 1000°C with an oxygen partial pressure of 1.4Torr and < 10^{-5} Torr. Three activated regions are clearly visible[62].

Studying the conductivity as function of temperature with the absence of incident light to find out the defect states by studying the activation energy. The pioneering study in this material was done on monocrystal by O'Keeffe as seen this dependency in Figure *2.22* [62]. Even if a great dependency of the activation energies the preparation condition exists, we can distinguish three temperature ranges, described by three different activation energies.

- At high temperatures, the activation energy remains relatively stable at 0.6 eV.
- At low temperatures, the activation energy varies within a range of 0.2 eV to 0.5 eV.
- At intermediate temperatures, the activation energy is highest, with a value of approximately 0.9 eV.

The activation energy at high temperatures is typically considered to be half of the formation enthalpy of charged copper vacancies. This formation enthalpy is obtained by summing the formation enthalpy of neutral copper vacancies with their ionization energy. At low temperatures, defect formation is essentially frozen, leaving the activation energy approximated as half of the ionization energy. This may be an oversimplification, as the material is often compensated. In a compensated material, the activation energy generally equals the acceptor ionization energy. At intermediate temperatures, the situation becomes more intricate. The effective pressure within cuprous oxide differs from the external pressure because cupric oxide is the stable phase at these temperatures. Thus, the effective pressure, which varies with temperature and is related to the dissociation pressure of CuO, results in increased activation energy for conductivity, as noted by O'Keeffe. His explanation considers the dynamics of defect complex formation and dissociation as influenced by temperature, and how these processes impact the activation energy for conductivity in the material. The natural of these defects in this stage was not clear.

One of the millstones in the analysis of the conductivity is the work of Brattain in 1951, his work was including the analysis of conductivity, it was discovered that Cu_2O is a compensated material, containing both acceptors and donors [63]. To understand how this conclusion was reached, consider the hole concentration as a function of temperature. At low temperatures, this shows an exponential trend with an activation energy of around 0.3 eV, reaching a saturation value at approximately 400K, in the range of 10^{14} - 10^{15} cm^{-3} (see Figure 2.23).

To explain this behaviour, Brattain initially considered a model with only an acceptor level and later a model with an acceptor level and one or more deep donor levels. When using the first model to fit the exponential portion of the data, it yields an acceptor concentration of approximately 10^{19} cm^{-3}. This value should ideally match the saturation value, but it doesn't. In reality, the saturation value is four orders of magnitude lower than this estimate. However, the second model, which assumes the material is compensated, provides a better description of the experimental data. With the exponential fit, it reveals a compensation ratio (NA/ND) of approximately unity, and by considering the saturation value, we arrive at similar concentrations of around 10^{14} - 10^{15} cm^{-3} for both acceptors and donors.

As per the earlier discussion, Cu_2O can be characterized as a compensated material. It features an acceptor level positioned at approximately 0.3 eV above the valence band and a deep donor level. The concentration of this deep donor level is just slightly lower than that of the acceptors. You can refer to the visual representation of these characteristics. (See Figure 2.24)

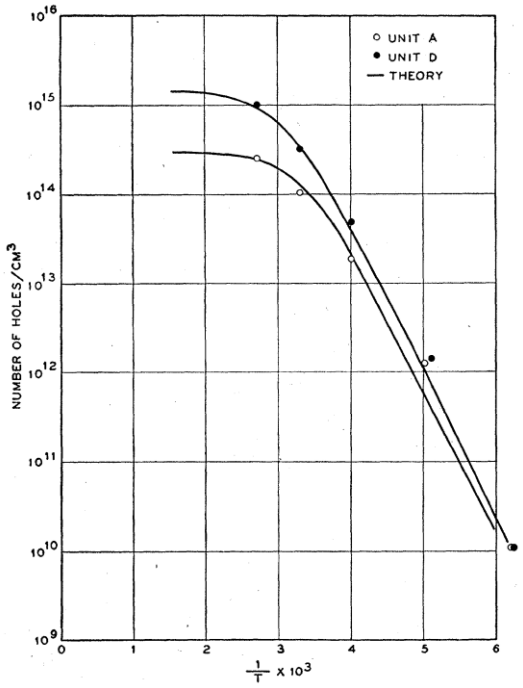

Figure 2.23: Hole carrier concentration plotted against the reciprocal of absolute temperature for two Cu_2O samples. This graph is sourced from Brattain's original publication [63].

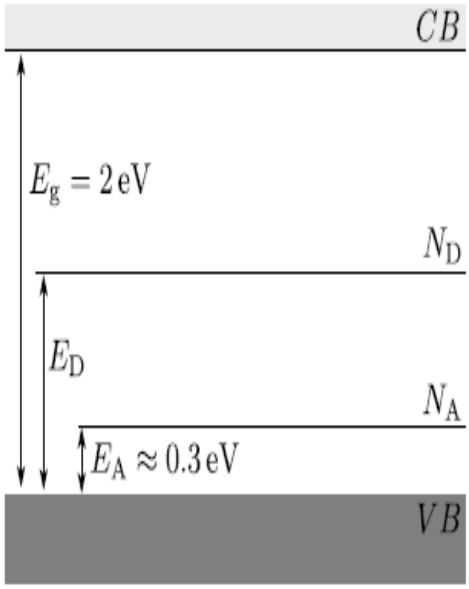

Figure 2.24: Basic band diagram for Cu_2O based on Brattain's research. It highlights the presence of both acceptor and donor levels, with acceptor levels located approximately 0.3 eV above the valence band, and donor levels positioned sufficiently deep so that all donors are ionized.

The last electrical investigation in seeking to explain the electric structure of Cu_2O accurately is passed on the persistent Photo conductivity (PPC) as the Cu_2O exhibit such phenomenon. This can be defined as increasing of the conductivity which persist for several days at room

temperature, even if the sample is kept in the dark. This metastable state is generated by illuminating the sample for some minutes. The PPC discharge can be easily speed up by the increase of the temperature, for example at 120^{o}C the decay time of PPC is few seconds [64]. In summary, during the illumination, the minority carriers are captured by deep defects (actually complexes) which in turn go in a new relaxed state. After the light is switched off the electron re-emission or hole capture from these defects is very slow because they are prohibited by a high energy barrier formed after the defect relaxation.

The outstanding work done in this field by the Strasbourg group, after gathering all available information, put forward a comprehensive electronic model [65], [66] to explain PPC and other properties of Cu_2O. Their model features four donor levels, including two shallow and two deep levels, along with a band of acceptors that stretches from 0.2 eV from the valence band to the middle of the band gap (as shown in Figure *2.25*). Additionally, this model incorporates a band of recombination centres, located between 0.45 eV and 0.65 eV from the valence band. This recombination centre band was introduced to account for the PPC spectrum and to explain both the magnitude and the time constant of photo-conductivity saturation. It's important to note that the authors did not provide a detailed explanation of the specific characteristics of these levels.

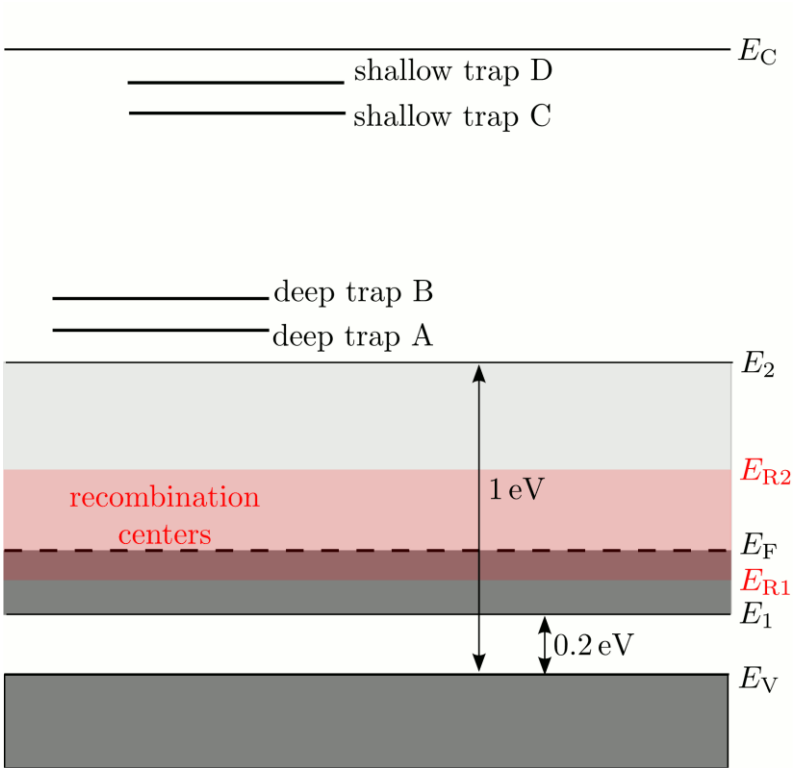

Figure 2.25: Electronic model proposed by the Strasbourg group. Four traps are present, two deep and two shallows. The acceptor levels are distributed in a band into which lies another smaller band of recombination centres[67].

2.4.3 Mobility

The hole mobility of free carrier is one of the most important parameters that need to be studied as it describes the electrical properties of material. Several experiments have been done on Hall mobility of positive holes in single crystal and how it becomes influenced by lattice defect and lattice scattering. The outstanding systematic studies in literature that have been done by Shimada and Masumi [68], Tazenkov and Gruzdev [69], and Zouaghi et. al [70]. All these studies were performed on Cu_2O growth by similar way.

Figure *2.26* shows the mobility vs temperature curves which been obtained by all mentioned studies. Tazenkov and Gruzdev and Zouaghi et. al. obtained work on polycrystals at slightly high temperature above 100K while Shimada and Masumi obtained on

monocrystal of Cu_2O at low temperature below 77K with a specific technique; they studied the Hall mobility by the material photoexcited, Shimada also applied a theoretical studied on basis of carrier-lattice interaction in polyatomic crystal to clarify the intrinsic scattering mechanism for a wide range of temperatures extending from 4.2K up to 400K. As clearly observed the highest value of hole mobility at low temperature (130,000 $cm^2 V^{-1}s^{-1}$).

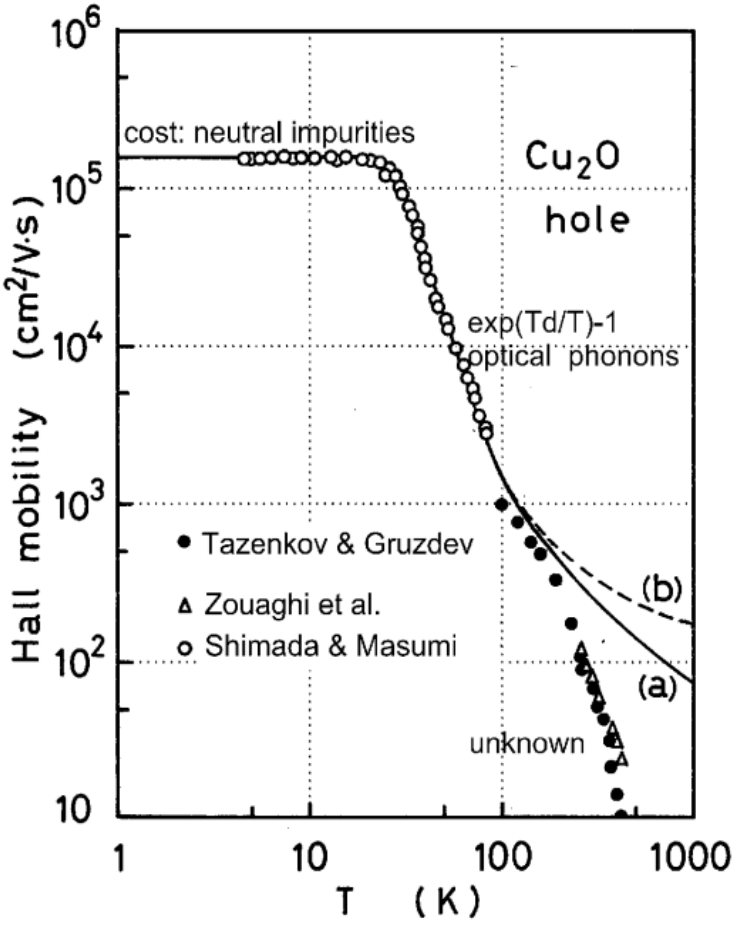

Figure 2.26: Hole mobility in Cu_2O. The curves are two theoretical predictions: a) considers both high and low energy LO phonons while b) considers only low energy LO phonons in the carrier–phonon scattering mechanism[68].

Splitting up the curves based on its behaviour over the temperature range, (i) below 20K the observed mobility is almost independent of temperature, this indicated the main scattering process is due to neutral impurities.

Between 40K-100K, the hole mobility as a function of temperature exhibits a clearly exponential decay on mobility as temperature increasing. In this temperature range the mobility could be affected by low-frequency longitudinal phonon (LO) scattering ($153cm^{-1}$), while above 100K the affect of the high-frequency LO phonon ($w=660cm^{-1}$) becomes remarkable. This could be proved by the numerical fits that have been done by Shimada and Masumi (the solid line (a)), it was obtained by considering a combination of scattering due to neutral impurity acoustical phonon and both low and high frequency LO phonon while excluded the effect of high frequency (the broken line (b)) which is emphasis the role of such frequency in this region is notable.

Above 200K, a substantial discrepancy arises between the theoretical curve and the experimental results in the study of Hall mobilities of slow electrons in AgCl. This deviation is not trivial and highlights significant differences in underlying mechanisms. In previous studies of AgCl, discrepancies in experimental results were minor and attributed to the spread of LO-phonon frequencies near the zone center, possibly due to anharmonicity[71]. However, in the present case, the discrepancy is much more pronounced and cannot be explained by a slight distribution of LO-phonon energies, as was the case in AgCl. Given that all experimental results for high-quality samples converge in this temperature range, there must be a fundamental mechanism at play.

Various hypotheses have been proposed to explain this discrepancy, but none have proven entirely satisfactory.

1. **Scattering from Ionized Impurities:** One explanation considered the scattering from ionized impurities. However, this theory predicts a mobility trend that increases with temperature, contrary to experimental observations, and requires an unrealistically high impurity concentration exceeding 10^{18} cm^{-3}[72].
2. **Auto-Trapping in Metastable States:** Another hypothesis, based on the Toyozawa-Sumi model, has been suggested for AgBr [73], [74]and TlBr [75]as well. This model attributes the decrease in mobility with temperature to the auto-trapping of charge carriers in metastable states, which only form above 200K. While this approach aligns

with some observations, it fails to provide a comprehensive explanation of the mobility trend across all conditions.

3. **Surface Effects on Hall Measurements:** The impact of surface conductivity on Hall mobility measurements has also been investigated. Dobrovol'skii and Gritsenko studied this phenomenon using both planar and transverse setups. They found that in planar setups, surface effects significantly influence measurements when resistivity exceeds 104 Ω·cm, leading to discrepancies as large as an order of magnitude. In contrast, transverse setups avoid surface effects and provide a more accurate measure of bulk mobility[76].

Despite these efforts, the lack of experimental mobility data above 500K remains a critical limitation. Such data would provide crucial insights for determining defect formation entropies and enthalpies through high-temperature conductivity measurements. Addressing this gap is essential for resolving the underlying mechanisms responsible for the observed discrepancies in Hall mobility trends.

The Hall mobility of Cu_2O at room temperature is consistently reported in the literature to be less than 10^2 $cm^2/V.s$ This low mobility is influenced by intrinsic scattering mechanisms. According to the theory of carrier-lattice interaction in polyatomic crystals, Shimada and Masumi [68]calculated the theoretical limit of free carrier (hole) mobility in Cu_2O caused by longitudinal optical (LO) phonon scattering (see LO phonon data in Figure 2.27). Similarly, Lee et al. [77]calculated the theoretical mobility limit due to ionized impurity scattering (see Figure 2.27).

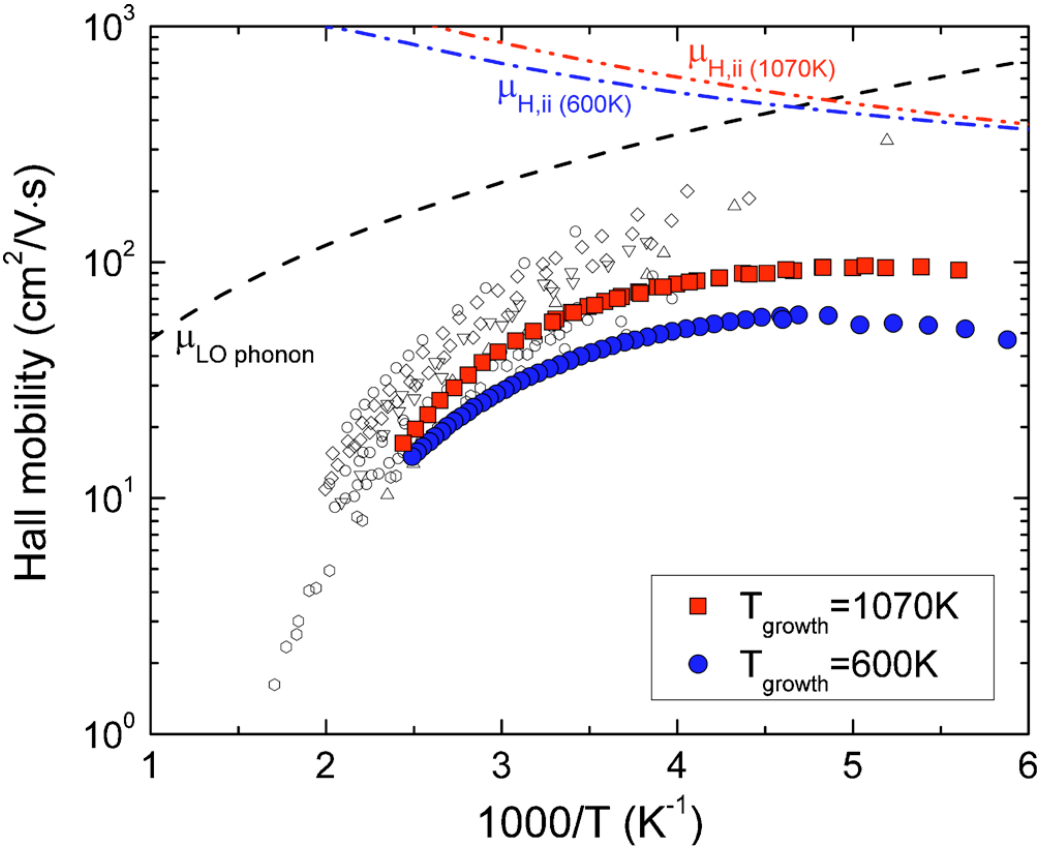

Figure 2.27: Theoretical limits of the free carrier mobility in Cu2O. Lines show its limits by LO phonon scattering and ionised impurity scattering. Open symbols represent temperature-dependent Hall mobilities of monocrystalline Cu_2O from various references (see reference [77]*), and close symbols represent Hall mobilities of Cu_2O sputtered at temperatures (600 and 1070 K).*

These studies indicate that the dominant intrinsic scattering mechanisms in Cu_2O vary with temperature: At high temperatures, phonon scattering dominates, while at low temperatures (below 200 K), ionized impurity scattering becomes the primary mechanism.

Comparing the free charge carrier mobility of Cu_2O with the common semiconductor material i.e., GaAs. The mobility of GaAs shows in the Figure 2.28 has three GaAs samples all of purportedly "high-purity" p-type the graph shows the Hall mobility of GaAs as a function of temperature. The curve exhibits the general trend of the semiconductor: at low temperatures (~10–100 K): The mobility increases with temperature, reaching a peak of approximately 10,000 cm²/V·s near 100 K, likely due to reduced impurity scattering. At intermediate temperatures (100–200 K): The mobility decreases slowly as phonon scattering begins to dominate. At higher temperatures (~200–300K and beyond): Mobility drops steeply due to increased phonon scattering.

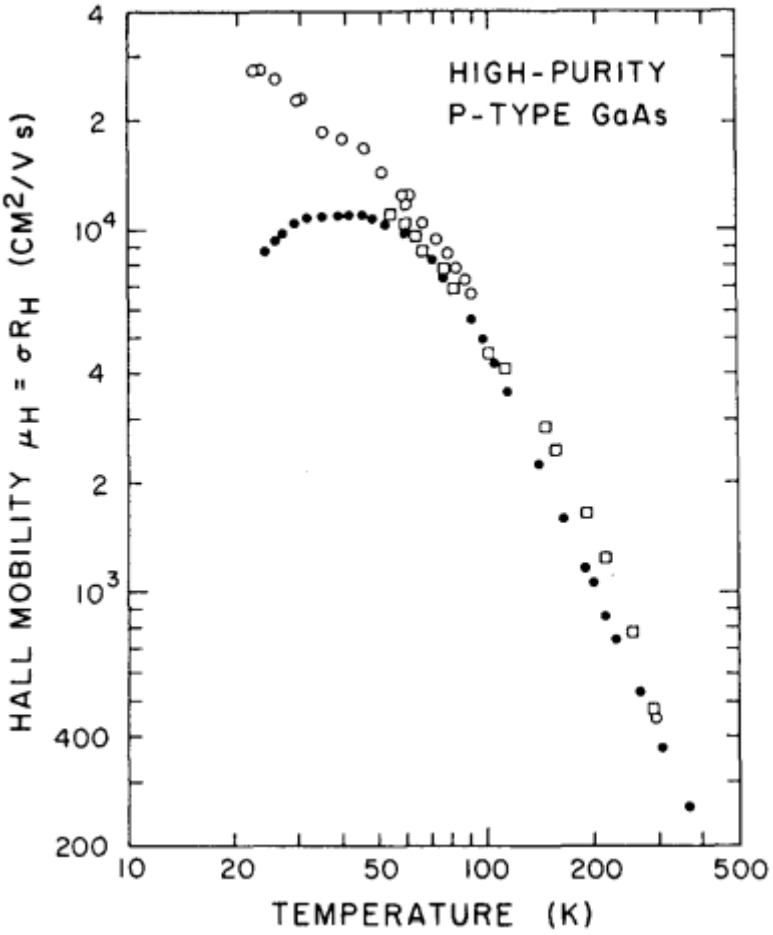

Figure 2.28: Temperature dependence of Hall mobility for three high-purity P-type GaAs VPE samples, after Wiley. m These samples represent the work of • Hill [78]□*Mears and Stradling*[79] *and* ○ *Zschauer*[80]*, In increasing order of low temperature mobility.*

The scattering mechanism that effected the carrier in this material was studied in the literature by many groups: Wiley's review goes into some details on scattering mechanisms for holes[81]. He pointed out the caustic phonon and nonpolar optical mode scattering are of comparable importance for T>100k with polar mode scattering probably less important. Ionized impurity scattering almost inevitably dominates for low temperatures, as seen to a small extent in the roll off of mobility below 40k for Hill's samples in Figure 2.28. ionized impurity scattering takes much greater toll of μ_p for strongly doped material, especially if heavily compensated. These scattering mechanisms can assume control of μ_p at room temperature which the doping is strongly enough as exemplified by the curve and data points of Figure 2.29

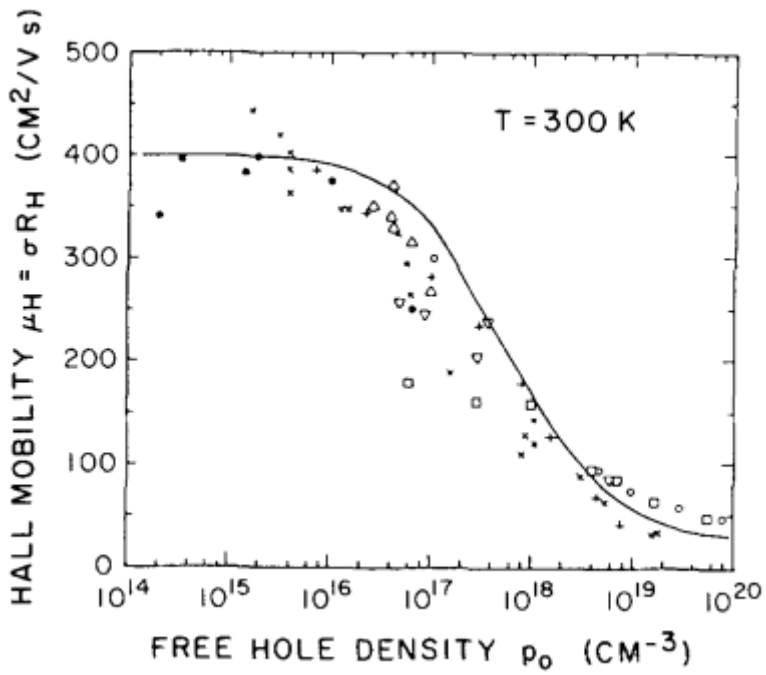

Figure 2.29: Variation of 300 K Hall mobility with hole concentration, after Wiley[81]*. The data points represent the work of Δ Rosi et al.*[82]*, □ Hill*[78]*, • Vilms and Garrett*[83]*, + Rosztoczy et al.*[84]*, ○ Emel'yanenko et al.*[85]*, and ▽Gasanli et al.*

The mobility of Cu_2O at room temperature is considered poor when compared to material like GaAs which are widely used in high performance electronics and optoelectronics due to its superior mobility. However, for applications where high mobility is not critical (e.g., in photovoltaic or certain sensor technologies) Cu_2O still be acceptable. More importantly the unique electronic structure of Cu_2O particularly its ability to host excitons with relatively high binding energy is a defining feature. This property makes Cu_2O especially significant in fundamental physics where the high exciton binding energy in Cu_2O makes it a model material for studying excitonic physics at room temperature and above which outweighing the limitation in mobility.

2.4.4 Photoluminescence

Photoluminescence is a widely utilized method for identifying defects in semiconductors. However, in the case of Cu_2O, it has primarily been applied to investigate exciton spectra.

Aside from exciton-related peaks, three distinct peaks have been identified in the emission spectra at wavelengths of 720 nm, 820 nm, and 910 nm, corresponding to energy levels of 1.72 eV, 1.51 eV, and 1.36 eV, respectively (see Figure 2.30). These bands exhibit asymmetry, especially at lower temperatures, with a full width at half maximum between 0.10 and 0.15 eV. The 910 nm band is consistently observed and has been attributed to the copper vacancy level. Additionally, a weaker band is noticeable around 1010 nm near the 910 nm peak. The situation is more complex for the other two bands. Bloem [86], [87] noted these peaks in samples annealed under low oxygen partial pressure and suggested they were caused by luminescence from two different charge states of oxygen vacancies ($V_O^+$and V_O^{++}). This interpretation is further supported by the observation that the intensity ratio of these two peaks appears consistent across all samples.

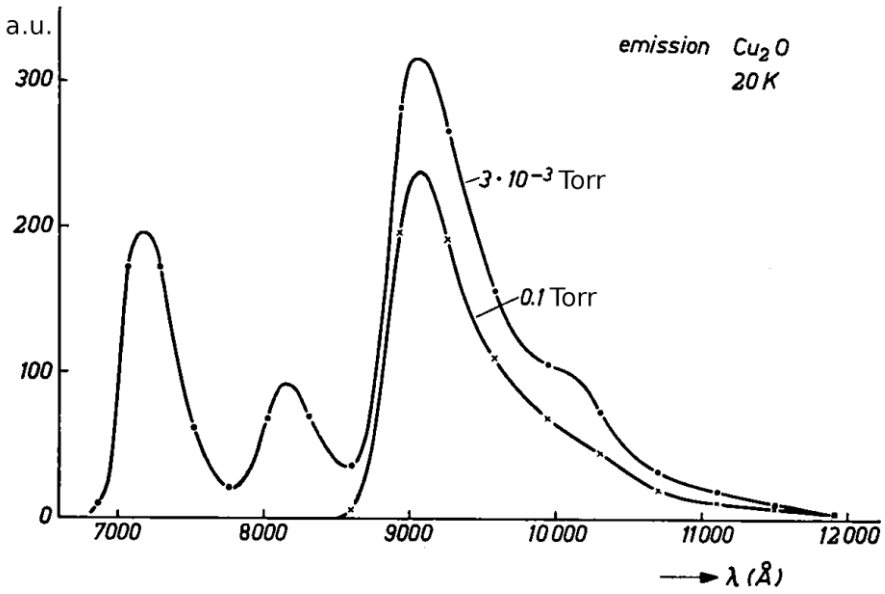

Figure 2.30: Photoluminescence emission spectra for two Cu2O samples [86].

More recent studies, however, have demonstrated that the relative intensities of these bands do not follow the correlation proposed by Bloem. Instead, a different dependence on illumination intensity was observed [88]: at low illumination intensity, the 820 nm peak is more prominent, while at higher intensities, the 720 nm peak becomes dominant. Additionally, the intensity ratio between these two bands varies depending on the sample preparation [19].

2.5 Excitons in Semiconductors

2.5.1 Optical absorption of exciton

Cu_2O exhibits a remarkable optical spectrum where various classes of transition predicted by exciton spectra theory are observed across different energy regions. Its investigation has also led to significant research on the Bose-Einstein condensation of excitons and the polariton properties and applications. At room temperature, the absorption coefficient suggests the presence of a direct forbidden band gap. This is due to a forbidden dipole transition between the upper valence bands and the lower conduction band, which can be clearly observed in Figure 2.31. The spectrum shows that Cu_2O begins to significantly absorb light at energies above approximately 2.4 eV. This energy corresponds to the dipole-allowed transition between the upper valence band and the second lower conduction band. In semiconductors of this type, when the exciton effect is ignored, the absorption coefficient α near the absorption edge depends on the photon energy $\hbar$w as [18], [89], [90]:

$$\alpha(w) \propto \begin{cases} (\hbar w)^{-1} (\hbar w - E_g)^{\frac{3}{2}} \; for \; \hbar w > E_g \\ 0 \qquad\qquad\qquad\qquad for \; \hbar w < E_g \end{cases} \qquad (2.5)$$

When comparing direct absorption edges, which yield an absorption coefficient proportional to$(\hbar w)^{-1} (\hbar w - E_g)^{\frac{1}{2}}$ with forbidden edges, it becomes evident that the latter's increase in absorption is slower as the energy approaches the band gap. Consequently, identifying forbidden absorption edges can be challenging unless there are significant exciton effects, such as in the case of Cu_2O.

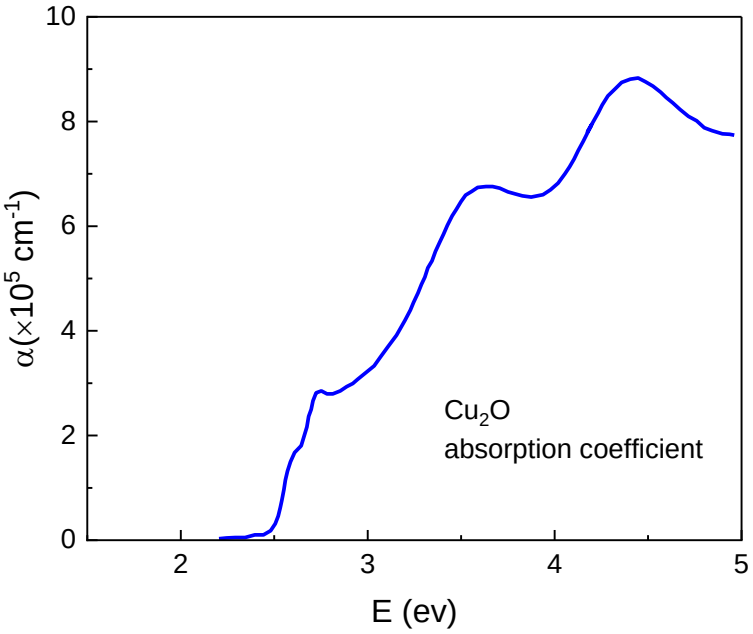

Figure 2.31: Room temperature absorption coefficient of Cu_2O depicted on a linear scale reproduced from[18], [91].

In 1957, Elliott [92] studied the absorption coefficient considering hole-electron interactions, specifically excitons. The absorption spectrum for a direct band gap semiconductor near the band gap consists of several contributions. Below the band gap, narrow peaks form due to exciton creation, which merge into a continuum as they approach the band gap. Excitons also lead to continuum absorptions from simultaneous phonon interactions. Above the band gap, the presence of excitons increases the continuum absorption compared to the case without interactions.

2.5.2 Hydrogenic Picture

The absorption characteristics of Cu_2O, particularly concerning excitons, lead us to explore the fundamental concept of excitons in semiconductor physics. Before delving into the behaviour of excitons within this material, it is crucial to establish a comprehensive understanding of excitons and their pivotal role in the optical properties of semiconductors. In a semiconductor, when an incident photon excites an electron from the valence band to the conduction band, a positively charged hole is left behind in the valence band. The resulting electron-hole pair can be bound by Coulomb attraction, forming a neutral

quasiparticle known as an exciton, which possesses an integer spin. This system can be modelled similarly to a hydrogen atom, where the electron and hole mimic the proton-electron interaction in hydrogen. The exciton's properties, such as its (i) radius and (ii) binding energy, are analogous to those of a hydrogen atom, but with significant differences due to the reduced effective mass of the electron and hole, as well as the dielectric environment of the semiconductor [93], [94]:

(i) exciton radius described by,

$$r_n = \frac{m_o}{\mu} \varepsilon_r \, n^2 \, a_H = \, n^2 \, a_x \qquad (2.6)$$

Where a_H is the Bohr radius of the hydrogen atom (0.53 A^o), $a_x = \left(\frac{m_o \varepsilon_r}{\mu}\right) a_H$ is the exciton Bohr radius for an exciton system with elementary charges e in a medium with dielectric constant ε_r, reduced mass μ and n the principal quantum number.

Excitons can be classified into two types based on the relationship between the excitonic Bohr radius a_x, and the lattice constant *a*: Frenkel excitons and Wannier-Mott excitons. Frenkel excitons have a radius that is equal to or smaller than *a*, resulting in a strongly bound state that is typically localized to a single site, with the electron and hole remaining closely associated. In contrast, Wannier-Mott excitons have radius significantly larger than the lattice constant, leading to a lower binding energy and a delocalization across multiple lattice sites. The presence of atoms inside the exciton orbit causes screening of the Coulomb interaction between the electron and hole. This screening reduces the strength of the electrostatic attraction, resulting in a smaller binding energy for Wannier-Mott excitons.

(ii) Exciton binding energy

In the excitonic system the coulomb interaction binding the electron and the hole decreases the energy of the pair compare to the non-interacting pair. The electron and hole can be

treated as two interacted particles with masses m_e^*, m_h^* respectively. The corresponding binding energy of exciton [93], [94]

$$E_x = -\frac{\mu}{m_0}\frac{1}{\varepsilon_r^2}\frac{R_y}{n^2} = \frac{R_x}{n^2} \qquad (2.7)$$

Where R_x excitonic Rydberg and given by:

$$R_x = \frac{\mu}{m_0}\frac{1}{\varepsilon_r^2}R_y \qquad (2.8)$$

Where R_y is the Rydberg energy of the Hydrogen atom (≈13.6ev), μ is the reduced mass for electron and hole and m_0 the rest mass of electron. Equation (2.2) and (2.3) show that the behaviour of excitons in semiconductor materials is linked to their principal quantum number (n). In a semiconductor the energy of the exciton created in a direct transition at *k* = 0 is equal to the energy required to create the electron-hole pair, namely E_g, less the binding energy of exciton, which is given by$E_x = -\frac{\mu}{m_0}\frac{1}{\varepsilon_r^2}\frac{R_y}{n^2} = R_x$ n2 (*2.7*.

Energies at which these lines are observed are given by:

$$E_n = E_g - \frac{R_x}{n^2} \qquad 2.9)$$

2.5.3 Ortho- and Para- Excitons

The band structure of Cu_2O includes a total of 10 valence bands and 4 conduction bands. Figure 2.32 illustrates the two lowest conduction bands and the two highest valence bands at the zone centre [95]. The direct energy gap between the highest valence band and the lowest conduction band is 2.17 eV at a temperature of 10K [96]. The lowest conduction

band, Γ_6^+, is primarily composed of Cu4s orbitals, while the highest valence band, Γ_7^+, arises from Cu3d orbitals.

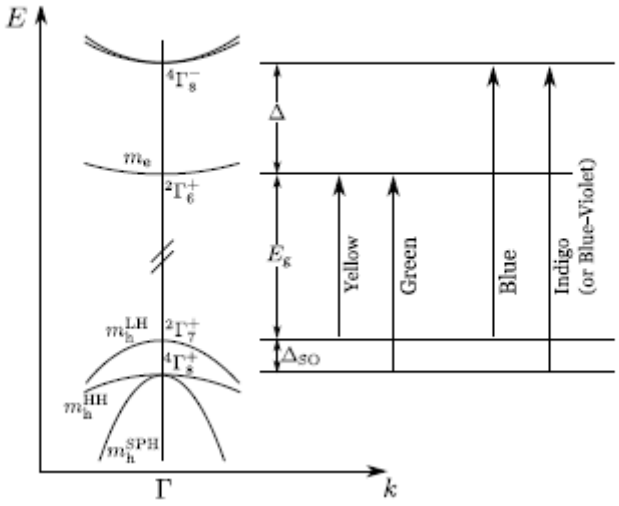

Figure 2.32: The band structure of Cu2O around the centre of the Brillouin zone (Γ point) is presented. Each band is associated with its corresponding irreducible representation. On the right, the transitions responsible for the four exciton series (yellow, green, blue, and indigo) are depicted

The yellow series are derived from the highest valence band and the lowest conduction band between $\Gamma_7^+$and Γ_6^+, the green series across $\Gamma_8^+$and Γ_6^+ , the blue series across $\Gamma_7^+$and $\Gamma_8^-$and finally the indigo series is generated by the electron–hole pairs across the Γ_8^+ and Γ_8^- (Figure 2.32) [20].

The yellow series is direct, but dipole forbidden. To see if a transition can be made, we should calculate the absorption coefficient:

$$\alpha \propto \sum_i \Gamma_f^\pi / D_i / \Gamma_i^\pi \qquad 2.10)$$

where Γ_f and Γ_i correspond to the final and the initial states, respectively, with parity π, and D_i proportional to p_i for the dipole operator and to p_i^2 for the quadrupole operator [97]. For the Cu_2O the lowest conduction band and the highest valence band have the same positive parity. The dipole operator has a negative parity. When we integrate over the space, the absorption coefficient will therefore always be zero. The quadrupole operator

has a positive parity. This means that the matrix element can be non-zero, which is the case for the *yellow* transition.

For excitonic levels the total parity is determined by the product of the parities of the valence band, the conduction band and the exciton envelope wave function. Since both valence and conduction bands have a positive parity, the total parity is determined by the parity of the exciton level. For an excitonic *s*-state, the parity is positive, and the transition to the ground state is dipole forbidden, but quadrupole allowed. For a *p*-state, the parity is negative, and the transition to the ground state is dipole allowed.

Due to spin-orbit interaction, every excitonic level is split into a triplet ortho level (J=1) and a singlet para level (J=0). The corresponding wave functions of the ortho and para levels can be written as follows:

Ortho **Para**

$$|O_{-1}\rangle = |\downarrow_e\downarrow_h\rangle \qquad |p\rangle = (|\uparrow_e\downarrow_h\rangle - |\downarrow_e\uparrow_h\rangle)/\sqrt{2}$$

$$|O_0\rangle = (|\uparrow_e\downarrow_h\rangle + |\downarrow_e\uparrow_h\rangle)/\sqrt{2}$$

$$|O_1\rangle = |\uparrow_e\uparrow_h\rangle$$

For the 1s exciton state the ortho-paraexciton energy splitting is 12 meV. Because only transitions between levels can be made when ΔJ=±1, decay from any paraexciton state to the ground state is forbidden for all orders of perturbation. This suggests that theoretically paraexcitons can live very long. Practically, the lifetime is limited by the defects and impurities. For 1s orthoexcitons decay to the ground state is quadrupole allowed. However, the lifetime of 1s orthoexcitons is mainly limited by transition to the lower lying paraexciton state and reveal a value around 1.2 ns [98].

Almost 60 years ago Hayashi [99] observed a series of hydrogen-like lines in the absorption spectrum of solid cuprous oxide which was cooled below the room temperature. During the

same time investigators from Leningrad (St-Petersburg)[100] and Strasbourg [101] made more accurate measurements of the wavelengths of these lines over a wide range of temperatures. The absorption spectrum of the Cu_2O oxide crystal as shown in Figure 2.33. Several absorption lines corresponding to transitions to the ortho exciton *p*-states are clearly observed. All lines are superimposed on a background due to the tail of the phonon assisted absorption to the conduction band continuum.

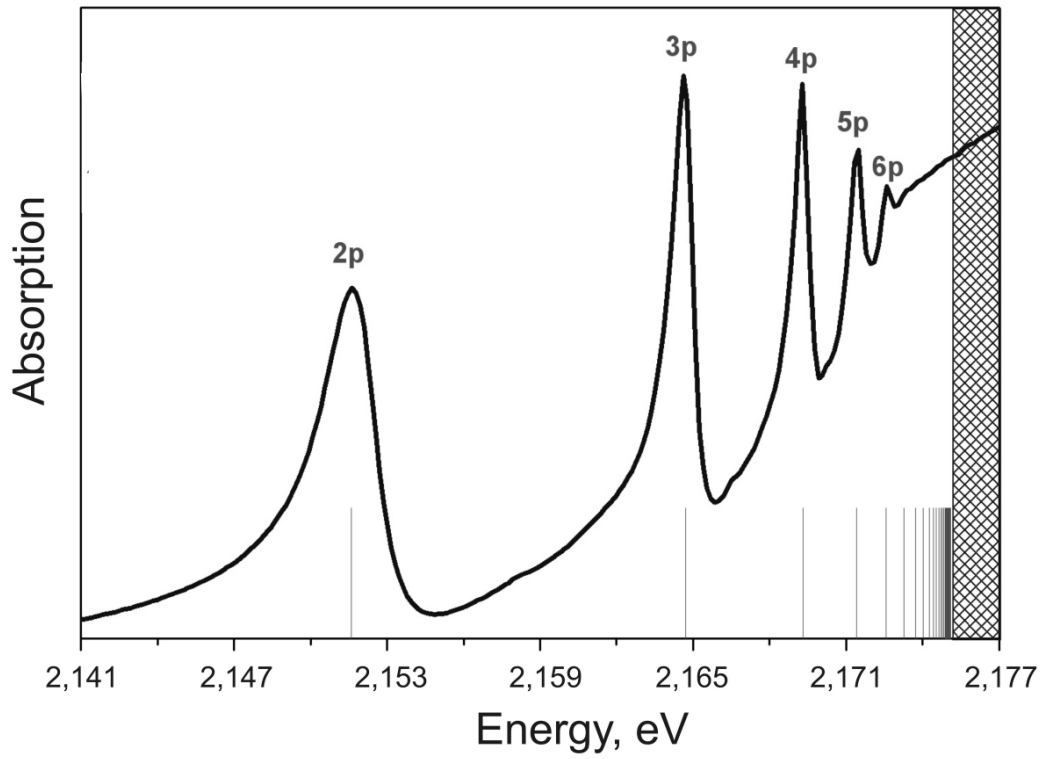

Figure 2.33: Optical absorption versus photon energy in cuprous oxide at 1.2K, showing a series of exciton lines for Cu_2O [102].

As mentioned above, the n=1 level cannot be observed in absorption spectrum, since the transition to this state is only quadrupole allowed. However, one can observe n=1 orthoexciton luminescence (Figure 2.34). The n=1 level energy position deviates from the hydrogen model. The n=1 exciton Bohr radius (7Å) is comparable with the lattice constant (4Å): the screening of the interaction is different than for the higher states giving the binding energy of 150 meV.

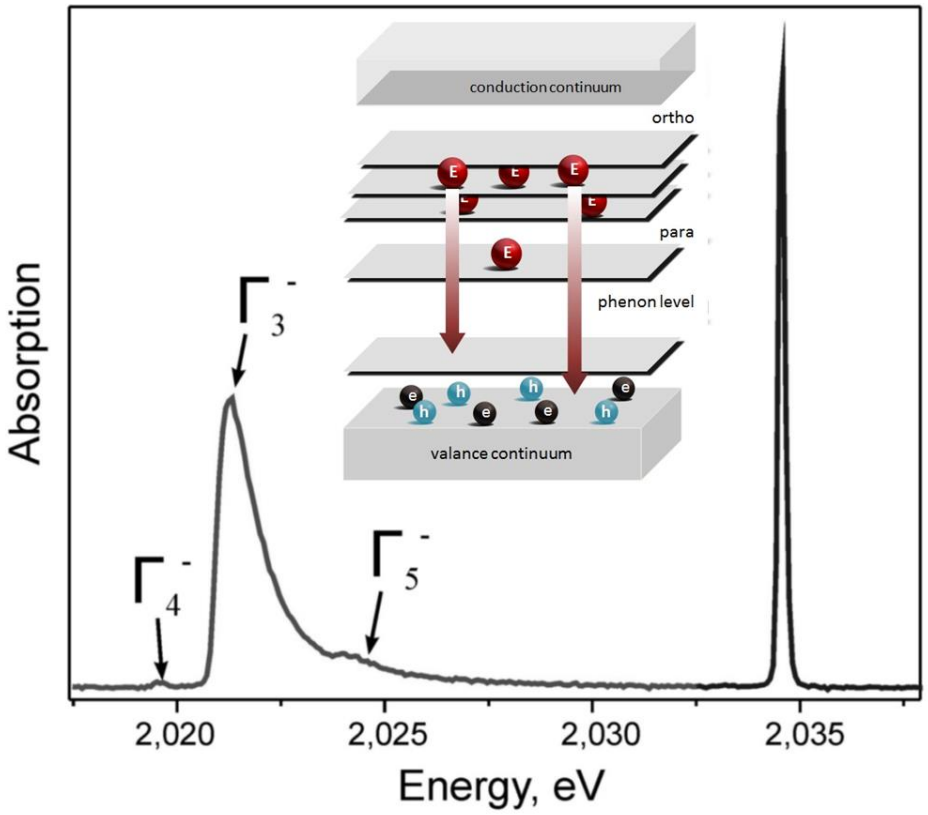

Figure 2.34: Luminescence spectra of excitons in Cu2O[102]

The luminescence spectrum of Cu_2O at T=1.2 K is presented in Figure 26, the sharp band observed at 2.035 eV is due to the direct recombination of the orthoexciton. The broad spectral lines are phonon-assisted orthoexciton lines. Since there are several optical phonons with the appropriate symmetry to participate in the recombination process, each having a different energy, there are several phonon replicas observed in the luminescence spectrum. There are clear lines from phonon-assisted orthoexciton (Γ_5^+) transitions with the simultaneous excitation of Γ_5^- (2.024 eV), Γ_3^- (2.026 eV), and Γ_4^-(2.020 eV) phonons [103].

2.5.4 Rydberg Atom

The spectral lines of hydrogen were first identified by Anders Jonas Ångström in 1862 [104]and later characterized using an empirical formula by Johann Jacob Balmer in 1884 [105]. A more comprehensive theoretical framework was introduced by Johannes Robert Rydberg in 1890, extending to spectral lines emitted by any atom with a single valence electron [106]. In 1913, Niels Bohr formulated his quantum model of the atom[107], aligning with Rydberg's formula $E_n = \frac{-R_H}{n^2}$. With E_n representing the energy of the quantum state, R_H denoting the Rydberg constant for hydrogen, and n being the principal quantum number, Rydberg's formula fundamentally applies to any system where an atom's valence electron is distant from the positively charged nucleus. In such cases, the atom is said to be in a Rydberg state, resulting in a distinct and systematically ordered energy level series.

Rydberg states are observable in high-energy environments, such as interstellar media in space [108]. The development of advanced laser technologies, particularly the tunable dye laser in the 1970 [109], enabled the controlled excitation of specific Rydberg states in laboratory settings[110]. This progress was further enhanced by the introduction of laser cooling and trapping techniques in 1998[111], which significantly improved precision in experimental studies.

The fundamental properties of Rydberg atoms have been extensively reviewed in various studies [112]and will be briefly summarized here. Rydberg atoms are highly excited atoms in which the valence electron is, on average, far from the nucleus. Their behavior closely follows the physics of highly excited hydrogen atoms, with energy levels governed by the Rydberg formula.

These atoms exist in weakly bound states, characterized by large polarizabilities and significant spatial extensions. They can be created at high energy levels, approaching the ionization threshold, making them highly sensitive to external influences. As a result, they strongly interact with their surroundings, including macroscopic external electric fields and fields induced by nearby Rydberg atoms or molecules.

Rydberg atoms have long lifetimes, often reaching hundreds of microseconds, leading to narrow spectral lines for transitions between these states and enabling prolonged interaction times. Their unique scaling properties are summarized in Table 2-3. Due to their exaggerated characteristics, Rydberg atoms provide a high degree of control over both individual atoms and single photons, making them valuable for numerous practical applications.

Table 2-3: Scaling properties of Rydberg atoms [110]. n is the principal quantum number.

Property	Scaling
Binding Energy	n^{-2}
Orbital radius	n^2
Dipole moment	n^2
Polarizability	n^7
Radiative lifetime	n^3

Rydberg atoms are highly effective for sensing electromagnetic fields in the microwave and terahertz frequency ranges[113]. Their fundamental properties remain constant over time and space, making them ideal as precise measurement devices. These atoms enable real-time detection and can sense individual photons without absorbing them [114]. The ability to detect microwave and terahertz radiation is crucial for numerous applications, including WiFi, Bluetooth, mobile networks, aerospace communications, self-driving vehicles, and security scanners at airports. Additionally, Rydberg atoms can serve as gas sensors [115] or function as an ion microscope [116].

A key feature in many applications of Rydberg atoms is the **Rydberg blockade** [63–65]. When a single photon excites an atom to a Rydberg state, it strongly interacts with nearby atoms, shifting their energy levels and preventing multiple simultaneous excitations. This effect suppresses the transmission of additional incoming photons within a defined **blockade volume**. Since its first experimental demonstration in 2004[117], [118], the Rydberg

blockade has been leveraged for generating non-classical photonic states. This capability enables the creation of a medium that exhibits nonlinearity at the level of just two photons, paving the way for advancements in Rydberg-based quantum optics [119].

Additionally, Rydberg atoms play a crucial role in quantum state engineering [120] and serve as a powerful platform for quantum simulations [121]. They naturally realize a two-level system, which is essential for quantum metrology and quantum information processing [122]. By positioning ground-state atoms at optically resolvable distances and manipulating them using tightly focused optical fields, large amounts of data can be stored, and complex algorithms necessary for quantum simulators can be executed efficiently.

Replacing ground-state atoms with Rydberg atoms introduces new possibilities, such as strong interatomic interactions over distances of several micrometers and novel dynamical effects, including the Rydberg blockade. These characteristics make Rydberg atoms a versatile tool for advancing quantum technologies.

2.5.5 Rydberg Excitons

Rydberg excitons have a sizeable principal quantum number (represented as ‘n’). The qualities of Rydberg excitons are markedly different to those of their ground-state excitons but what makes them distinct is that they are found in a semiconductor, thereby making then the only Rydberg system to exist in a solid material. With regards to Cu_2O, there is only a loose binding of the electron-hole pair that forms the exciton, and it is spread over a region extending to approximately 10 billion crystal unit cells. Therefore, the radii of Rydberg excitons are sizeable, with a modified Bohr radius of 1.4µm, resulting in them being subject to the influence of external perturbations. Rydberg excitons are quasiparticles in a crystal environment (ε Cu_2O) with an effective mass (m*) and complicated band structures and features interaction with phonons. Consequently, there are differences in terms of how they react to external fields as well as the scaling of size and binding energy.

Much like Rydberg atoms, Rydberg excitons also have a Rydberg blockade. When an exciton is injected, this prevents other excitons being created within a radius of 10 μm. Unlike Rydberg atoms, it is possible for excitons that have μm-sized extensions, and which are highly excited to be precisely positioned within a crystal using macroscopic energy potential landscapes. Furthermore, they have the ability to sense elementary excitations in the vicinity as a quantum level. Consequently, there is considerable interest amongst researchers in Rydberg excitons in Cu_2O owing to the fact that they facilitate macroscopic, well-controlled quantum systems[123]. They have presented researchers with considerable opportunities to explore, resulting in a wide range of practical applications being found. However, whilst Rydberg excitons in hydrogen-like excited states in semiconductors and Rydberg atoms have similar physical qualities, there are issues which need to be overcome because the exciton states have limited lifetimes and small energy gaps.

The Rydberg blockade effect continues to attract considerable attention from researchers seeking to produce applications for creating single-photon sources. Single-photon sources are fundamental for quantum technologies and are used in various applications such as communication security [124]; the use of quantum repeaters to extend the possibilities of transmitting quantum information [125]; realising advances in photonic quantum computing [126]; enabling single-photon states to be amplified in a controlled manner to facilitate the processing of quantum signals [127], [128]; improving the quality of entangled quantum states in entanglement purification [129]; and facilitating greater entanglement in quantum systems [130]. Importantly, Rydberg atoms offer an effective platform to enable such single-photon sources to be realised, drawing upon their unique qualities to enable progress to be made in quantum technology.

Khazali et al. utilised the Rydberg blockade effect for excitons in Cu_2O to produce a single-photon source [10]. More specifically, they selected a Cu_2O crystal that was smaller than the volume of the Rydberg blockade. As can be seen in Figure 2.35a, a monochromatic continuous wave laser was used to excite the crystal, resulting in the production of yellow nP Rydberg excitons. The Rydberg excitons interacted strongly with each other, resulting in a significant shift which meant that only one exciton could be created. Consequently, a two-level quantum system resulted which could serve as a single-photon source. Khazali et al.

were able to separate the single photons emitted from the pump laser, thereby improving the single-photon source's utility. This entailed either the Cu_2O crystal being embedded in a waveguide or a cavity being exploited to improve emissions utilising the Purcell effect in a direction transverse to the laser beam [131].

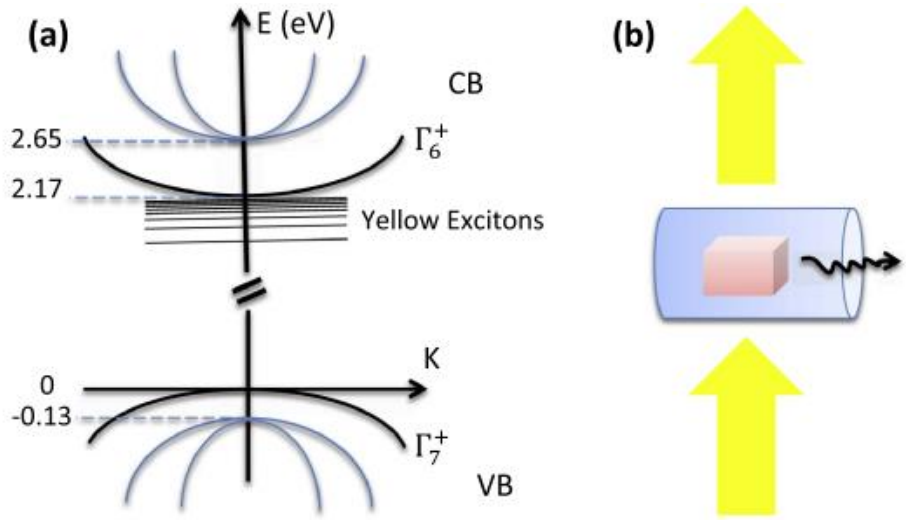

Figure 2.35: (a) Yellow Rydberg exciton level scheme. A combination of the Γ_4^- envelope, Γ_6^+ conduction and Γ_7^+ valence bands are used to produce the nP yellow Rydberg excitons, yielding an ortho-exciton symmetric wavefunction. A single-photon dipole transition is used to excite the excitons. (b) A Rydberg exciton is produced in a crystal smaller than the volume of the blockade for the single-photon source proposal. Rydberg excitons interact strongly, resulting in a level shift which means that only a single exciton can be created. The result is a two-level system capable of serving as a single-photon source. A crystal is embedded in a cavity or waveguide to spatially separate the single exciton from the pump laser to select or improve the emission transverse to the pump [10].

Whilst Rydberg excitons in Cu_2O offers a wide variety of applications, researchers have sought to produce and manipulate in numerous alternative solid-state materials. However, efforts to make use of excitonic systems in alternative settings have demonstrated that the resulting excited states are constrained. For example, the direct bandgap semiconductor GaAs has a limited Rydberg energy (Ry = 4.2meV) and a maximum principal quantum number (n_{max}) of 3 [8]. Increasing n causes a blending of the exciton states into the electron-hole continuum transitions, thereby hampering efforts to observe certain states when conducting experiments. Meanwhile, experiments have realised a n_{max} of 5 when investigating transition metal dichalcogenides[132], despite the fact that their binding energies can be twice those achieved by GaAs. There are numerous factors which may explain these materials' limitations, including the fact that higher n values are associated

with a loss of oscillator strength, thereby making it more challenging for higher exciton states to be detected. Moreover, phonon relaxation constrains the lifetime of excitons, thereby causing strong broadening [133].

Consequently, the unique qualities of Cu_2O mean that it is an exceptional material. Bulk Cu_2O offers excitonic behaviour that can be reproduced and that is well understood, thereby offering a consistent benchmark. Numerous studies have explored the production of Rydberg excitons and the first of these featured P-type envelope function excitons which were tracked up to a value of n=9 [100]. However, subsequent research has demonstrated that the series have achieved n=25 [8]. The linewidths of Cu_2O are relatively small, while its Rydberg energy is relatively large (in the region of 90 meV), thereby making it possible for these highly excited states to be observed [134]. These features of Cu_2O result from the band-to-band transitions' limited oscillator strength which are prohibited in the electric dipole approximation [134].

2.5.6 Effect of Defects on Exciton Wavefunction

2.5.6.1 External influence

Cu_2O offers excellent qualities when researching or producing highly excited Rydberg excitons and the most recent research achieved findings of n=28 [135]. Be that as it may, Cu_2O has known limitations which effectively make further research and the attaining of higher excitonic states more challenging. Among these challenges are external magnetic and electric fields. Researchers have devoted considerable efforts to establishing the influence exerted by magnetic and electric fields in a bid to theoretically and experimentally unpick the detail of how excitonic levels are structured [136], [137]. In addition, the high field regime whereby the fields' interaction energy exceeds the electron-hole coulomb interaction in highly excited states where there is low binding energy has been shown to be associated with significant deviations from the Landau or Stark level patterns. Such variance could be suggestive of a shift to quantum chaotic behaviour [138]. States that are highly

excited, have a sizeable n and have a significant density are particularly associated with such complexity. (Need more details see this reference[138])

The thermal effect is another notable external factor that needs to be considered. If these variables can be successfully addressed, it creates the possibility of achieving higher quantum numbers for the series of P excitons by reducing the temperature. Aßmann et al. set out to examine excitons that have high quantum numbers in an attempt to better understand the challenges that make this difficult. More specifically, Aßmann et al. sought to reduce the temperature to 1.3K in a ^{4}He cryostat, equating to a thermal energy K_BT of 0.116mev. At n=25, the binding energy is $R_{yd}/n^2 \approx 0.140$mev. Subsequently, the ^{4}He cryostat was replaced by a ^{3}He-^{4}He dilution refrigerator that had optical access, thereby enabling the temperature to fall below 1 k, ultimately reaching 50 mK. By doing so, they managed to achieve a n_{max} of 28 and they observed that reducing the temperature below 720 mK had no effect on n_{max} Figure 2.36 illustrates that absorption rates were not improved for states up to n=27 by lowering to temperature to sub 800 mK, albeit that modest increases in absorption were recorded for n=28). This suggests that there are other limiting factors in addition to thermal dissociatation, with residual charged impurities possibly determining the limit to what can be observed in terms of highly excited excitons in in Cu_2O.

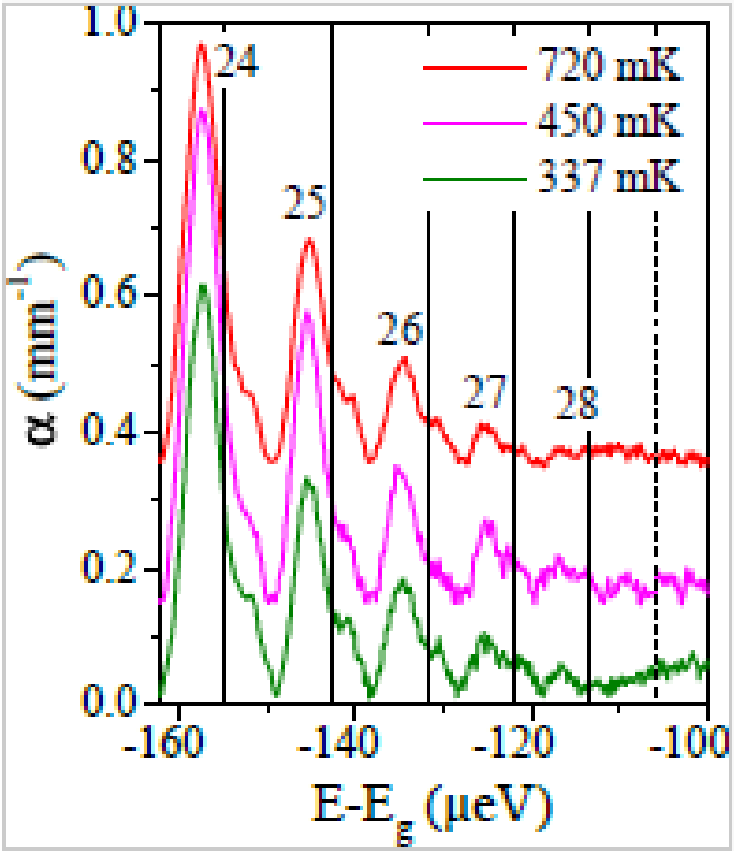

Figure 2.36: Temperature range from 720 mK to 337 mK with a low excitation power of 200 nW. Reducing the temperature below 800 mK does not increase absorption for states up to n=27, but a slight absorption begins to appear for n=28[135].

2.5.6.2 Internal effect

Based on the observations, it was believed that the positioning of the various samples and their quality ultimately limits Cu_2O's highly excited exciton state. If the crystal has impurities at a density as low as 10^9 cm^{-3}, this can cause the excitons to experience an electric field, resulting in them being ionised if the field's interaction energy equates to the state's binding energy. In such a scenario, there is a significant reduction in the strength of the oscillator at that stage, with the loss of the exciton line in the ionisation continuum (valance/conduction band). The reduction in the strength of the oscillator is of a far greater magnitude than would be anticipated based on the n^{-3} dependence of oscillator strength and the hydrogen model[27].

In addition, they were able to confirm that n_{max} lacks consistency. Indeed, it can alter from one sample to another, and it can also vary depending on where it is positioned in a sample.

As such, it appears that there is no limit on n_{max} and nor is it standard across the various experimental conditions. Using a sample of good quality, they examined the recordings of exciton spectra at various locations (see Figure 28). The measurements were recorded at a temperature of T = 0.8 K and the highest number of exciton lines was found to be n=26. The value of n_{max} at other locations was lower (n=22 in some cases) but every position recorded a value of n=20. They sought to establish electron-hole transitions' band gap positions. This entails efforts to identify the exact energy point that there is a loss of exciton resonances, resulting in a levelling-off of the absorption spectrum. In **Error! Reference source not found.**, arrows represent the band gap edge positions. The results indicated that reductions in the effective band gap are associated with changes in n_{max}.

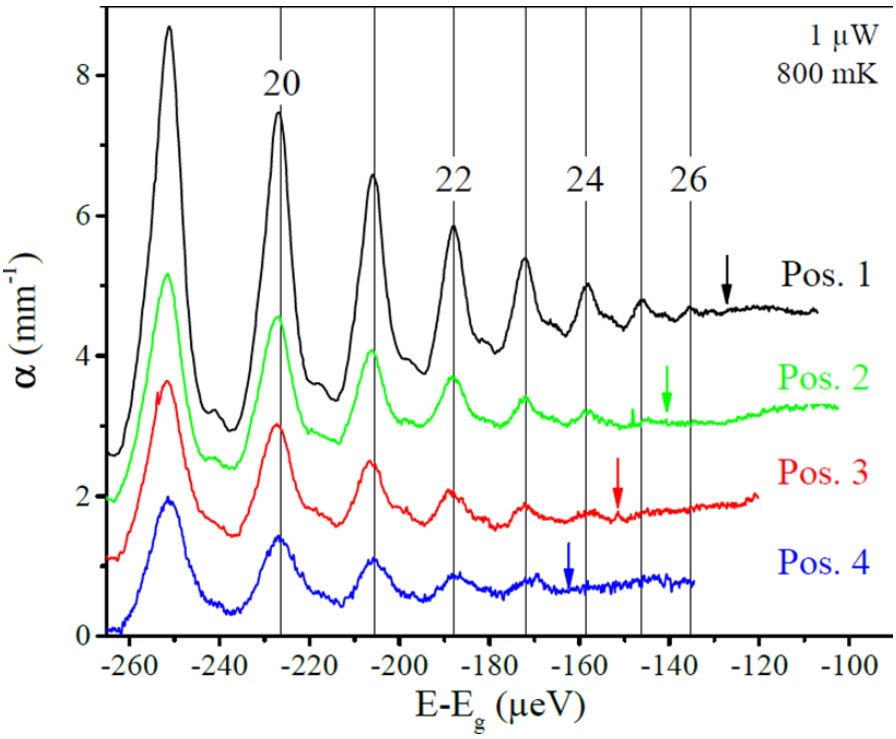

Figure 2.37: Comparisons of absorption spectra achieved in standardised conditions (including an excitation power of 1 μW and a temperature of 800 mK) but with the samples in different locations indicate differences in the observable resonance peaks and the quantity of P excitons observed. The arrows show that a reduction in nmax for a given location brings about a change in the effective band gap to lower energies[135].

.

The difference between the anticipated bandgap and that which was observed was attributed to the impurities (especially material with a density of $<10^{10}cm^{-3}$). More specifically, it was claimed that there was an electric field as a result of these impurities

which influenced the excitons. The presence of the electric field results in the coulomb potential tilting between the hole and electron as a result of the Stark effect. Consequently, the exciton close to the bandgap experiences tunnelling and ionises. For this reason, the observable exciton series has a capped n_{max} that differs within and between samples as a result of differences in the density of impurities. A reduction in temperature causes the impurities to become less mobile, thereby reducing the effect of the electric field on the excitons. It is possible to extend the exciton series by significantly lowering the temperature. Impurities have a more pronounced effect on excitons that are highly excited. In addition, excitons that are highly excited are more responsive to the presence of electric fields.

Krüger et al. conducted research to establish how the density of impurities (ρ_{ci}) affects the bandgap (Figure 2.38). It is also possible to establish the highest principal quantum number that can be observed. Krüger et al. found evidence to indicate that the bandgap shift depends on the charged impurities' density (ρ_{ci}). It approximately adheres to a power law:

$$\Delta E_g(\rho_{ci}) = -(0.71 \pm 0.17)\mu ev(\rho_{ci}/cm^{-3})^{0.254\pm0.01}\alpha\rho_{ci}^{1/4} \qquad 2.11)$$

Free electrons initiate a change in the band gap that is induced by plasma[19,20]. When energy is pumped to exceed a threshold, an electron-hole plasma results and this causes Rydberg excitons to experience the Mott transition phenomenon. This process brings about a reduction in the bandgap, but it is only when the band gap reaches the locations of the excitonic resonances that they are influenced. More specifically, this results in the loss of the resonances, resulting in a merger with the ionisation continuum. This may be due to Cu_2O featuring impurities which act as a source from which holes and free electrons can be released.

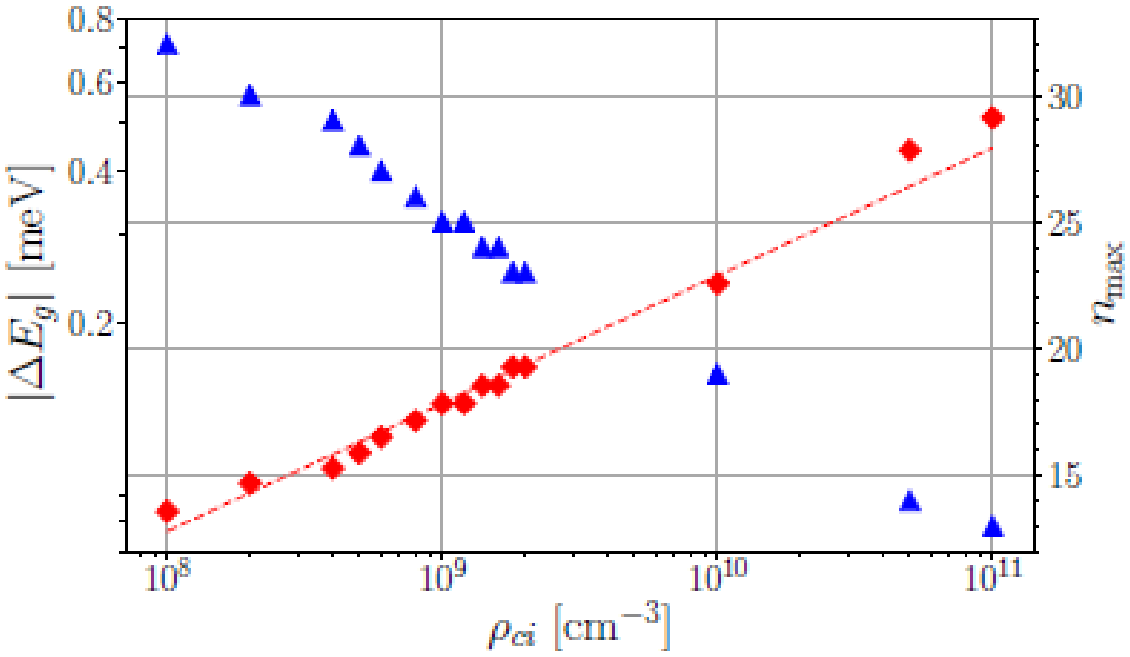

Figure 2.38: A shift in the band-gap E_g (ρ_{ci}) (depicted by red diamonds) with the red line representing a power-law fit, whilst the blue triangles indicate the highest principal quantum number that can be observed n_{max} (ρ_{ci})[139].

2.6 Conclusion

This chapter provided a fundamental background on Cu_2O's crystal structure and electronic band structure to enhance the understanding of its optical and electrical behaviour. The challenges involved in the growth of synthetic Cu_2O were discussed, particularly the complexities presented by the Cu-O phase diagram and the different types of defects. These factors highlight the need for a controlled environment to grow high-quality single crystals. Various growth techniques were reviewed, with the float zone technique identified as the most effective. Additionally, post-growth treatments, such as controlled heat treatment, were explained as methods to refine the crystal structure, eliminate defects, and improve the overall quality of the Cu_2O single crystal.

The chapter then focused on the assessment of single crystal quality through tools like electrical conductivity measurements and hole mobility analysis, concluding with photoluminescence studies to better understand the material's behaviour.

Lastly, the chapter explored the optical absorption characteristics of Cu_2O, including the formation of ortho and para excitons, and the study of Rydberg excitons. The impact of defects on the behaviour and visibility of Rydberg excitons was discussed, emphasizing their importance in understanding the optical properties of Cu_2O.

Chapter 3 : Methodology

3.1 Introduction

This chapter provides a comprehensive overview of the sample preparation and experimental procedures conducted in this thesis. This focuses on exploring the electrical properties of Cu_2O, along with spectrally resolved photoconductivity measurement in NIR region and absorption spectra in the MIR, and THz regions, with the primary objective of identifying defect states within the bandgap.

The Cu_2O single crystal used in this study was grown using the optical floating zone (OFZ) technique. The preparation process, including precise cutting and planarization of the samples, will be described in detail. Additionally, the chapter outlines the photolithography process, which was employed to fabricate three distinct device configurations, each designed for different experimental purposes: (i) a Circular Transmission Line Model (CTLM) for measuring specific contact resistance (ρ_c) and evaluating the quality of Au-Cu_2O contacts, (ii) a Van der Pauw (VdP) configuration for Hall effect measurements to determine carrier concentration, mobility, and the effect of defects on transport properties, and (iii) a photoconductivity device for investigating the spectral photoresponse of Cu_2O.

The chapter will also detail the photoconductivity measurement setup, which utilizes a nanosecond-pulsed laser as the illumination source to resolve the photoconductive spectrum in the NIR region. Special procedures to optimize the obtained photoresponse spectrum preventing any interference from the environment or used optics will be discussed. Lastly, the experimental setup for investigating defect-related spectral features in the MIR and THz regions using FTIR spectroscopy will be introduced.

3.2 Cu_2O Single Crystal Processing; from Sample Preparation to Device Fabrication

This section outlines the process of preparing synthetic Cu_2O for various electrical and optical studies. It begins with a brief overview of sample cutting and the Planarizing to prepare the samples, making them ready for being examined. Following this, the section details the fabrication process of different devices designed for the electrical studies involved in this project.

The starting material using in this work was a 5mm-diameter copper cuprite rod, the Cu_2O feed was prepared by thermal oxidation of the copper metal rod at 1100^oC for approximately 40 hours in air at atmospheric pressure. The oxidation rods were then used to grow the single-crystal material in a Crystal System Corporation optical furnace (model FZ-T-10000-H-VII-VPM_MII_PC). Localized heating was achieved by bringing the light from four lamps to a joint focus on the sample using four semi ellipsoidal mirrors. (See section 2.3.3)

3.2.1 Sample preparation

The cuprite single crystal needs to be properly prepared to perform characterisation, and later experiments. Electrical experiments require planarized samples which are optically flat on at least one side. This requirement is necessary to perform optical lithography. Optical experiments have further constraints. The sample needs to be planarized on both sides to facilitate transmission, and different sample thicknesses are required depending on the spectral range of interest. In the optical range, where the material is highly-absorbing above bandgap, samples need to be thinned below 100 μm to ensure >1% transparency. For infrared and THz experiments, the samples need to be considerably thicker, typically >1mm, because the absorption cross sections of atomic-scale defects are small. Some experiments additionally require that there is a small wedge angle between both optical faces to prevent Fabry-Perot fringing in transmission geometry. Figure 3.1(a) shows the starting point of both the natural gemstones samples and the synthetic material. The natural samples started out

as large single crystals that have been extracted from cuprite mineral. They have been shaped and polished into gemstones before we acquired them. The synthetic material also shown in this figure started as cylindrical rods, typically a few centimetres long and with diameters of between 5-6 mm.

The sample preparation process is divided into two stages which must be executed correctly to ensure a satisfactory result. The first stage involves rough cutting to the correct geometry, typically slices (or wafers) of 1mm thickness. Thicknesses of 1mm facilitates easy handling for the subsequent preparation steps. Because cuprite single crystal material is relatively soft, it needs to be embedded in a protective resin matrix to prevent the crystal shattering, shown in Figure 3.1(b). At this point the crystal can also be orientated along a particular crystal axis should this be necessary for further experiments. This stage is followed by the planarization process which smooths the crystal surface.

However, before starting sample cutting and planarization, it should be mounted in resin so that it can be held in the correct orientation. The crystal is embedded in a thick block of resin to facilitate its handling and improve the preparation result. There are two techniques to mount the sample; hot compression mounting and cold mounting, each of them has specific tasks and resins. In the former the sample is processed under heat and high pressure. The latter has been using in this study, where the Cu_2O is placed in a mould, the correct amounts of ViaFix powder and ViaFix Liquid which are measured carefully (by either volume or weight) are then mixed thoroughly and poured around the sample.

(i) Cutting:

The crystals were sliced into 1mm thickness perpendicular to the crystal axis. This was done by abrasive wet cutting which is preferred for its ability to minimize damage. The cutting is achieved using an abrasive cut-off wheel which has diamond grit embedded in a binder. A Struers Secotom-50 cutter machine was used in this work. A lubricating liquid (water, in this case) was used to protect the sample from heat generated by friction and to clear away debris from the cutting area, as shown in Figure 3.1(c).

Figure 3.1: (a) Cu2O material initially in bar form. (b) The sample securely embedded in resin for processing. (c) Abrasive wet cutting process using a precision diamond saw to achieve smooth, undistorted surfaces essential for further preparation.

(ii) **Planarization**

Planarization is the most common method for smoothing surfaces through mechanical force. This process uses a slurry (typically nano-sized abrasive particles dispersed in an acidic or basic solution) in conjunction with a polishing pad and rotating ring. Abrasive particles are applied in progressively finer steps to remove material from the surface until the desired smoothness is achieved. This process can stop when the surface meets the requirements for specific examinations or proceed to a near perfect finish.

In this study, the front and back surfaces of Cu_2O was prepared using a Struers LaboPol5 lapping machine. This preparation is divided into two operations: lapping and polishing.

1. Lapping

Lapping is the initial step where a hard disk is used to achieve material removal through mechanical abrasion. This is typically done either with a disk embedded with large abrasive particles (similar to sandpaper) or with a hard disk combined with a lapping fluid that contains the abrasive particles (like a slurry). For this study, lapping was performed using hard disks, such as MD-Priano, with SiC abrasive particles for Plane Grinding (PG) to level the Cu_2O surface.

- Plane Grinding (PG): This step is designed to remove larger surface deformations and ensure a uniform, flat surface across all specimens. The use of relatively coarse, fixed

abrasive particles helps expedite the material removal. In this case, SiC was utilized with the MD-Priano disk, effectively flattening the sample as see in Figure 3.2(a).

- Fine Grinding (FG): Following plane grinding, fine grinding uses a softer disk, such as MD-Largo, with smaller abrasive particles (DiaPro Largo 9 µm diamond lubricant) for more precise material removal. The diamond particles become embedded in the disc surface, ensuring accurate flatness. The result from this step is shown in Figure 3.2(b).

2. Polishing

Polishing is distinctly different from lapping. While lapping employs hard disks with larger abrasives, polishing involves using soft cloths and much finer abrasive particles, typically on the nanoscale. This process aims to remove the surface damage introduced during lapping and to refine the surface finish.

- Rough Polishing: The first polishing step was done using a Struers DP-DAC woven acetate cloth disk with Diapro DAC 3 µm diamond lubricant. This rough polish removes deeper scratches and imperfections leave the surface with minimal scratch mark preparing the surface for finer polishing as see in Figure 3.2(C),
- Final Polishing: The final stage of polishing was done using a DP-NAP cloth with DiaPro NAP 1 µm diamond lubricant. The high viscosity of this suspension allows for a smoother, clearer finish, revealing a transparent dark red appearance characteristic of the Cu_2O material. The polished crystal was optically clear near the outer edges, while black inclusions were observed toward the centre seen in Figure 3.2.

Throughout both the lapping and polishing phases, the sample is examined after each step under a microscope to monitor the preparation quality. Minimizing preparation time is crucial to avoid waste and potential damage to the sample.

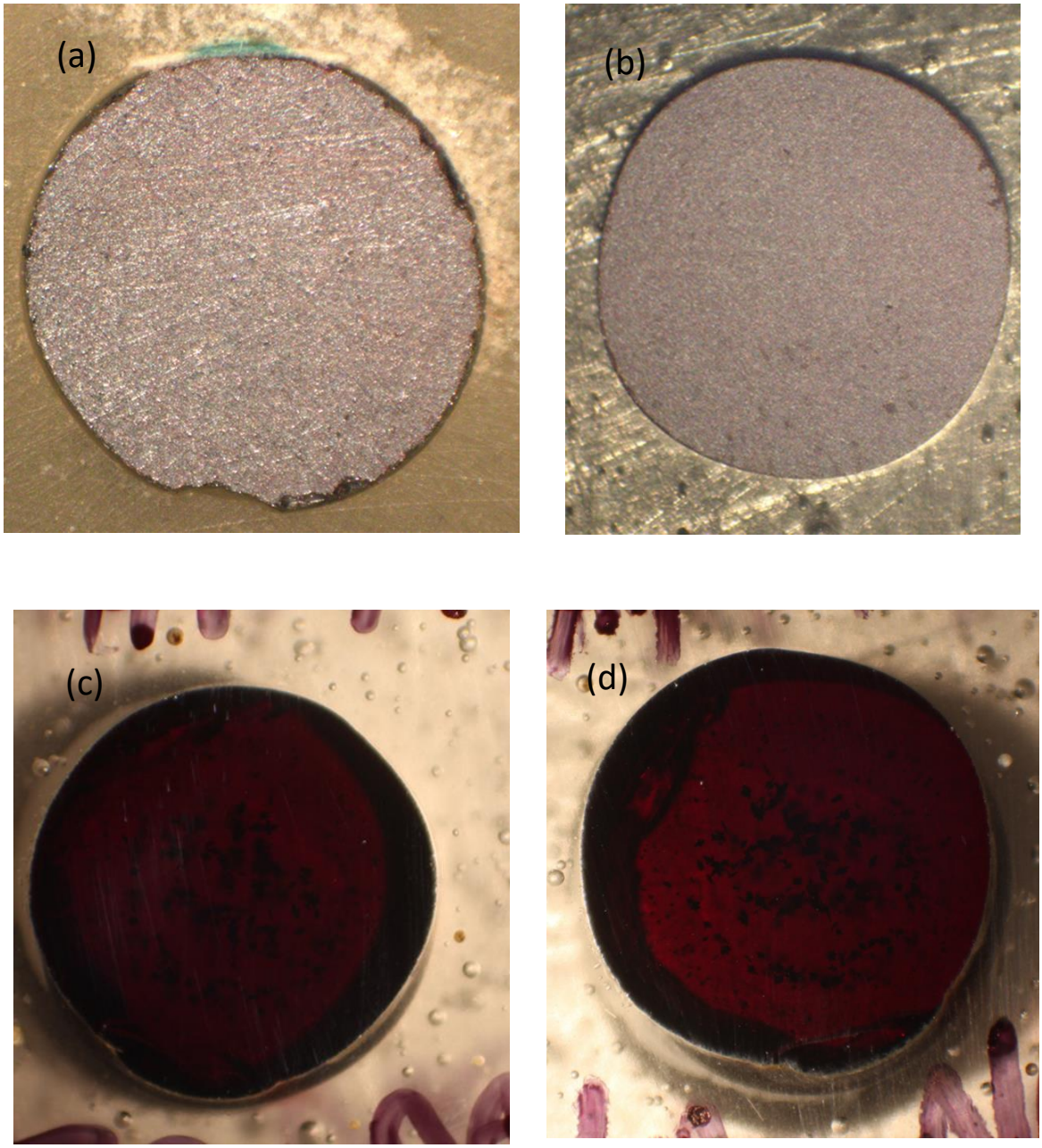

Figure 3.2: sample preparation stages (a) surface of Cu_2O crystal after PG showing a levelled surface with visible scratches (b) surface after using FG resulting in a smoother more uniform surface (c) after the first rough polishing step with DP-DAC cloth showing a significant reduction in surface damage (d) final polished Cu_2O surface using DP-NAP cloth revealing a dark red transparent finish with clear optical clarity and visible black inclusion near the centre of the crystal.

The common problems that have been faced in sample preparation is scratches and pull-out. Scratches as Figure 3.3 shows are grooves in surface of samples, produced by the point of abrasive particles or pulled-out material (Cu_2O or mounting resin). This issue could be

solved by having regard to the following: i) making sure that after the PG the surface is uniform over the whole surface. ii) cleaning the sample and holder after every step is essential avoiding the contamination of the grinding/polishing surface through large abrasive particles from a previous step. iii) If there are still scratches left over from the previous step after finishing the current step, increasing the preparation time by 25 to 50% could be help. Pull-out is another common problem that could be met during the polishing process. Figure 3.4 depicts the pull-out as cavities left after grains or particles that are torn out of the sample surface during abrasion. They are found in hard and brittle materials, and in materials with inclusions, and this is the reasons that occurs frequently in Cu_2O single crystals. Hard or brittle materials cannot be deformed plastically, so small parts of the surface material shatter and may fall out or be pulled out by the polishing cloth. The other possible explanation for this is related to inclusions which may be brittle or have other thermal expansion values than other parts of the crystal. In this case, the relatively loose or broken inclusions can be pulled out by a long-napped polishing cloth. To eliminate this issue i) a napless polishing is recommended as it does not tend to “pluck” particles out of the sample. Furthermore, most of the napless cloths have a lower resilience, thus providing higher removal rates. ii) making sure every step removes the damage from the previous one and has to introduce as little damage as possible of its own. iii) Check the samples after every step, to find out when pull-outs do occur. It is also critical to ensure sufficient lubrication to minimise pull-out, especially at the later stages of polishing.

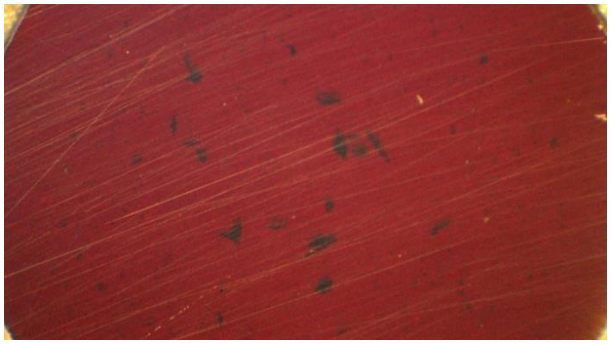

Figure 3.3: microscopic image of Cu_2O single crystal during polishing with scratches

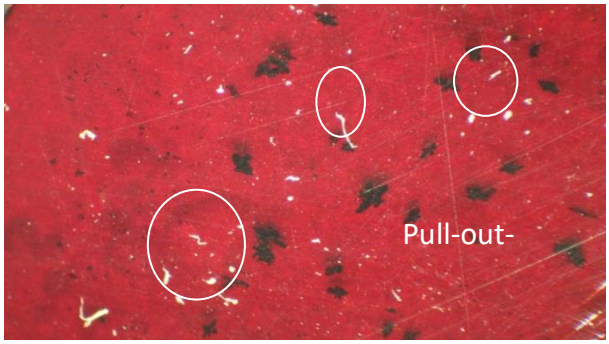

Figure 3.4: A microscopic image showing a pull-out mark.

3.2.2 Device Fabrication:

All the devices were fabricated and initially tested using a class 1000 and class 100 clean room (Institute for Compound Semiconductors) environment within the School of Physics and Astronomy at Cardiff University.

Contact photolithography is used during the fabrication process to pattern three different configurations: (i) the Circular Transmission Line Model (CTLM), which is detailed in section 3.3.1 the Van der Pauw (VdP) method, described in Section 3.3.2, and (iii) the photoconductivity device, which is covered in Chapter 3.4. This process normally starts with the initial preparation and cleaning of the sample using N-Methyl-2-pyrrolidone (NMP), Acetone, and Isopropyl Alcohol (IPA) sequentially for 5 min each, ensuring thorough cleaning. The sample was then effectively dried using a Nitrogen gun. Subsequently, the dehydration step followed, with the sample placed in direct contact with a hot plate at 120°C for 2 min, eliminating any residual moisture from the sample surface and creating optimal conditions for subsequent lithography processes.

The fundamental role of such process is transferring the desired pattern from a photomask (usually a clear glass tile, with a metallic opaque pattern) onto a polymer film, known as a photoresist. The photoresist is deposited onto the semiconductor substrate, initially in liquid form, and distributed into an even layer across the surface using a mechanical spin coater,

Figure 3.5b. This step involved applying a thin film of the negative tone photoresist; two steps were taken for the resist application - TI prime resist adhesion promotor at 4500 rpm for 45 sec, soft baked at 120°C for 2 min, followed by AZ nLof 2020 photoresist at 4500 rpm for 45 sec, soft baked at 110°C for 1.5 min. Depositing a TI prime layer before applying AZ 2020 photoresist enhances adhesion between the resist and the substrate, ensuring better pattern transfer during lithography [140]. This step is crucial for lift-off processes, as it facilitates the subsequent removal of unwanted materials after deposition.

Once the photoresist has been applied, the mask is brought into very close proximity to the Cu_2O, and the mask and substrate combination is exposed to ultraviolet (UV) radiation. The areas of opaque metal on the mask block the UV radiation from reaching the photoresist underneath on the surface of the substrate. The exposure of the resist to UV radiation alters its chemical make-up, such that when immersed in a developer solution the unexposed photoresist (for negative tone resist) or exposed (for positive tone resist) is removed. The alignment of the mask to the substrate, and exposure to UV radiation was performed by using a *Karl Suss Contact Mask Aligner*. The photoresist AZ nlOF 20xx is only i-line sensitive (365nm) the exposure dose for this was 65mJ/cm^3 so the exposure time was 5.5s as illustrated in Figure 3.5c. The post-exposure bake (PEB) on a hot plate at 110°C for approximately 1 min is an essential step was performed to cross-link the exposed resist. The final step in the photolithography process involved developing the unexposed resist by immersing it in AZ 726 MIF for 1.5 min, effectively removing the unexposed regions. The sample was then rinsed with de-ionized water for more than 30s, as shown in Figure 3.5d. To ensure the precision of the development process, continuous inspection under an optical microscope was conducted. Following pattern transfer, the ashing process took place, wherein the substrate underwent an oxygen plasma treatment in a specialized chamber. The plasma chemically reacts with the remaining photoresist, breaking down the organic material into volatile gases, resulting in a clean surface. These precise and systematic photolithography steps ensured accurate and reliable patterning of the sample.

The metallization process involved depositing a 300nm thick layer of Au without an adhesion layer. The deposition was carried out using the common thermal evaporation method. In this technique, the source metal (Au) was placed in a resistive heated crucible or

filament, and its temperature was raised through Ohmic heating by passing a high current through the filament. This caused the source metal to melt and vaporize providing a beam of metal which is deposited into the target area, as well as the surface of the bell jar or deposition chamber [4]. To ensure an ultra-clean and contamination-free deposition, the evaporation was conducted under a high vacuum condition, reaching below 1×10^{-6} mbar. To monitor the film thickness during the process, a quartz crystal was used. The metallization process in this work was performed using the *Edwards E306 thermal evaporation vacuum system*. For the ohmic contact metallization process, the substrate was heated up to 100°C both before and during the evaporation process. This step helped improve the adhesion of the metal film to the substrate Figure 3.5e. Once the metal film was successfully deposited onto the sample, the next step was to remove the photoresist layer and any unwanted metal on top of the photoresist. This was achieved by immersing the sample in 1165 for 1h at 80°C or at room temperature overnight, followed by immersion in acetone for 10 min, and then in IPA for 5 min, as depicted in Figure 3.5f.

By following these systematic and carefully executed metallization processes, a well-adhered and high-quality metal film was achieved, paving the way for successful device fabrication and further electrical characterizations.

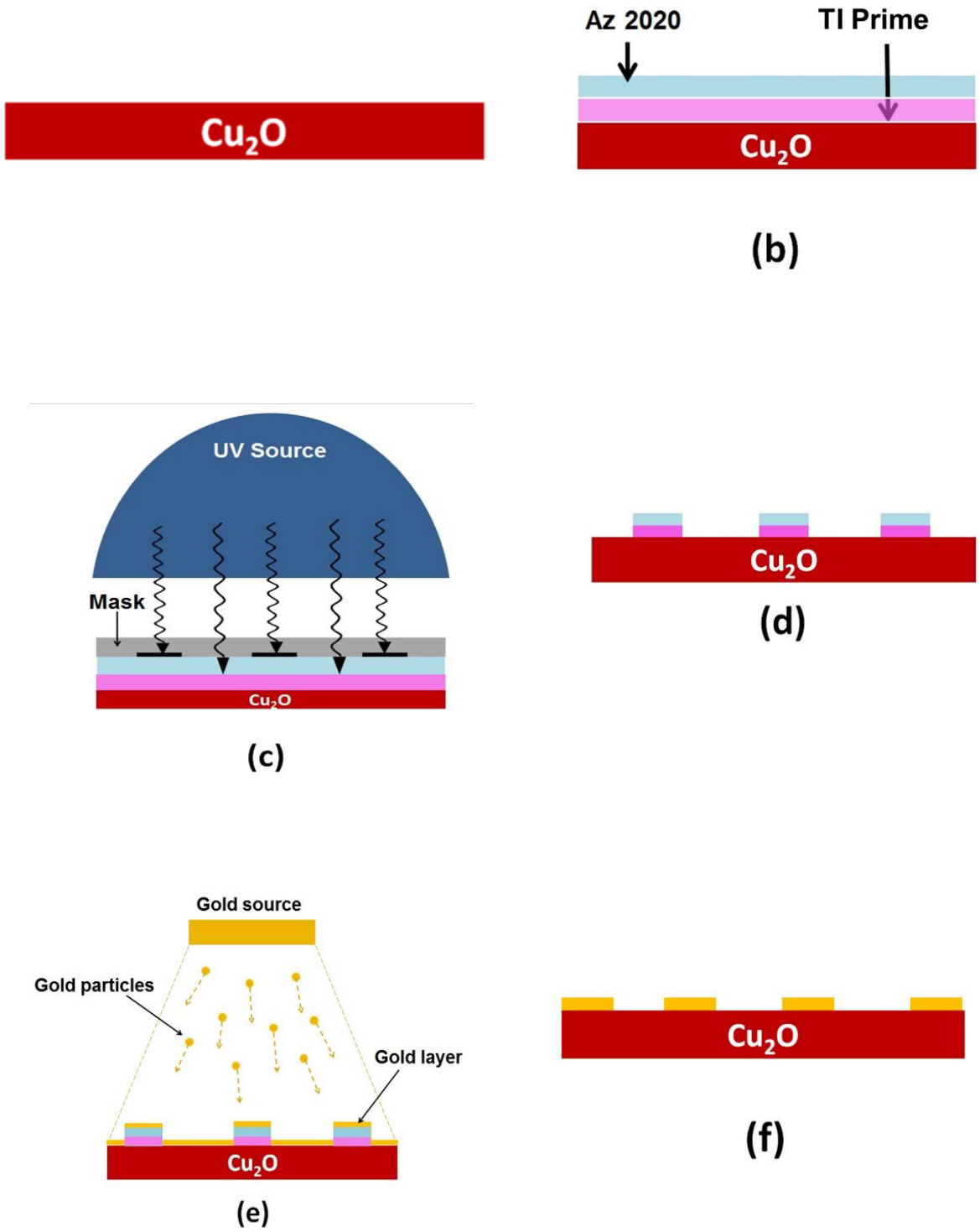

Figure 3.5:schematic of the main processing step in depositing a contact metal (Au) (a) the polished Cu_2O sample ready for cleaning and processing (b) application of TI prime and AZ 2020 photoresist to Cu_2O (C) exposure of the photoresist using (i-line) UV radiation and a glass mask pattern with opaque metal (d) the resultant resist profile after development of exposed resist (e) thermal evaporation from gold source where a film is deposited onto the Cu2O and resist surface (f) the remaining gold contact after removal of unwanted resist and metal.

To conduct electrical measurement the fabricated devices underwent a mounting process into 20-way ceramic packages. These packages feature an inner recess measuring 3.6mm by 3.6mm for sample placement, as illustrated in Figure 3.6. Initially, the fabricated samples were cut into smaller sections, each with dimensions smaller than 3.6mm by 3.6mm, using a diamond saw. These smaller sections were then affixed into the 20-way ceramic packages using Low Temperature GE Varnish, renowned for its robust bonding capabilities and efficient thermal conductivity even at low temperatures.

To establish electrical connections between the ceramic package pin contacts, highlighted in Figure 3.5 , and the specific contact pad on the semiconductor device, a modified West Bond 7400A wedge-wedge wire bonder was utilized. This device had been adapted for the use of fine gold wire with a diameter of 12.5 µm. The wire bonding process, achieved through wedge bonding, involved the application of both force and heat onto the wire and contact pad to create a secure bond.

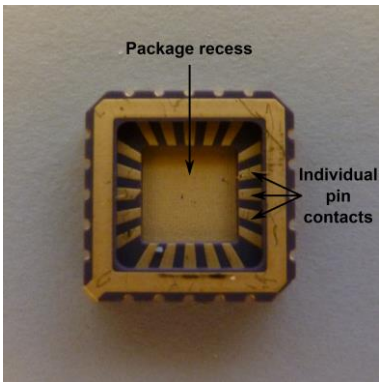

Figure 3.6:Visual depiction of a standard 20-way ceramic package employed for sample mounting. The diced sample chip finds placement within the package recess through the application of low-temperature GE varnish. The establishment of electrical connections occurs between the contacts on the semiconductor substrate and the individual pin contacts on the package, achieved by a gold wire using the wedge bonding technique.

3.3 Electric properties

In this section, we employ several experimental techniques to investigate the electrical properties of Cu_2O and its interface, with a focus on the fabrication and measurement of Au-Cu_2O contacts. The methods used are as follows: (i) Circular Transmission Line Model (CTLM): A CTLM configuration was designed and fabricated to measure and analyse the quality of the Au-Cu_2O contact by determining the specific contact resistance (ρ_c) using the 2-wire technique. (ii) Measuring the Cu_2O conductivity (σ) alongside with (iii) Hall Measurements: Hall effect measurements were conducted to characterize the electrical properties of Cu_2O, providing key parameters such as carrier concentration and Hall mobility, and the type of dominant charge carrier in Cu_2O.

3.3.1 Ohmic Contact; Circular Transmission Linear Model (CTLM)

The first device that was fabricated is Circular Transmission Line Model (CTLM). This was chosen in this study to evaluate the quality of the contact resistance by assessing the specific contact resistance (ρ_c). The typical CTLM layout we designed is shown in Figure 3.7. This structure was proposed by Marlow and Das[1]. It consists of circular contact is separated the surrounded contact by a ring-shaped gap. The CTLM structures that have been using in this work comprise six different gaps spacings on the mask (8, 16, 24, 32, 40 and 48 um). These devices are distributed radially throughout the crystal. Each gap spacing is strategically positioned to enable multiple measurements of same gap and facilitate averaging of the resistance to enhance the accuracy of ρ_c. Then implying 6 averaging separate measurements have been carried out, yielding 6 different resistance values. The measured resistance changes with changing gap spacing. There are two reasons to use CTLM method instead of the conventional TLM method: the absence of mesa etching to control current spreading between contacts and to avoid current crowding effects that have been found in linear TLMs.

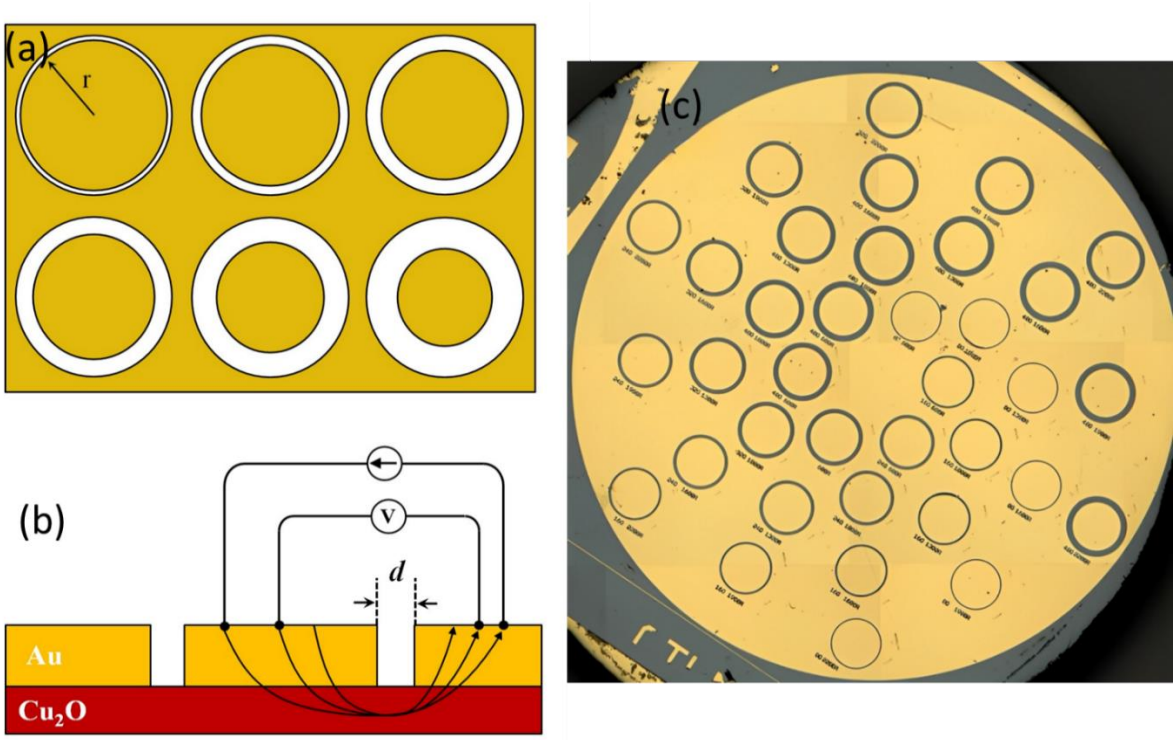

Figure 3.7: (a) typical planar view of CTLM structure that proposed by Marlow and Das, (b) across section of the CTLM structure d is gap spacing which is a variable (C) the CTLM fabricated devices shown the radially distributed of the devices throughout the crystal.

In this structure, shown in Figure 3.7, the current flows isotropically between the inner (of radius r) and outer electrodes. Therefore, as the gap spacing varies, there is a corresponding change in the measured resistance, when this resistance is graphed against the gap spacing, it produces characteristic curve as depicted in Figure 3.8 (indicated by squares). This non-linear relationship can be converted into a linear one by applying correction factors to the measured data (this correction factor is described by $c = \frac{R_1}{s} ln \frac{(R_1+s)}{R_1}$) [141] where R_1 is the radius of the inner contact and s is the gap spacing . This linear fitting is also (represented by circles) illustrated in Figure 3.8. Using this fitting to find the following parameter i) contact resistance R_c; (intercept with the Y-axis = $2R_c$), ii) transfer length L_T; which measures the quality of ohmic contact (intercept with x-axis= $2L_T$) and iii) from the slope the sheet resistance R_{sh} of the semiconductor can be calculated where R_{sh} being the sheet resistance of the semiconducting layer underneath the metal contact. Hence, the specific contact resistance can be calculated as following:

$$\rho_c = R_{sh} L_T [\Omega cm^2] \qquad (3.1)$$

The resistance R between the contacts for the circular configuration [142] follows the equation:

$$R = \frac{R_{sh}}{2\pi}\left[ln\frac{R_2}{R_2 - s} + L_T\left(\frac{1}{R_2 - s} + \frac{1}{R_2}\right)\right] \qquad (3.2)$$

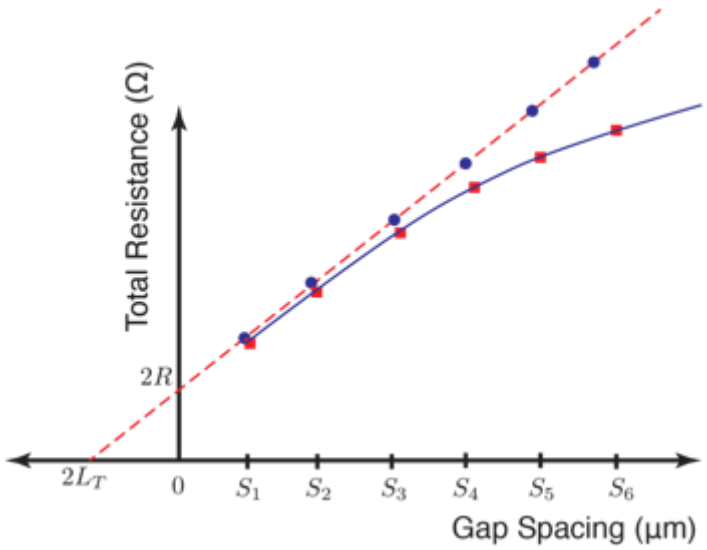

Figure 3.8: Total resistance versus gap spacing before (circles) and after (squares) applying correction factors.

This measurement was carried out by using 2-wire technique. A probe station in the clean room at Cardiff University's Institute for Compound Semiconductors was used to characterize the device at room temperature once fabricated. The Keithley 2401 Source-Measure Unit (SMU) is used as a source meter, and the probe station and source meter were interfaced with a computer allowing automation of the (I-V) measurement via software written in Python. Figure 3.9 shows the basic principle of 2-wire measurement. The voltmeter in green has a very high resistance, allowing only an insignificant current to pass through it. As a result, the current measured by the ammeter in red can be seen as virtually identical to the current passing through the device in blue. This arrangement ensures that the current reading captured by the ammeter accurately represents the current flowing through the device.

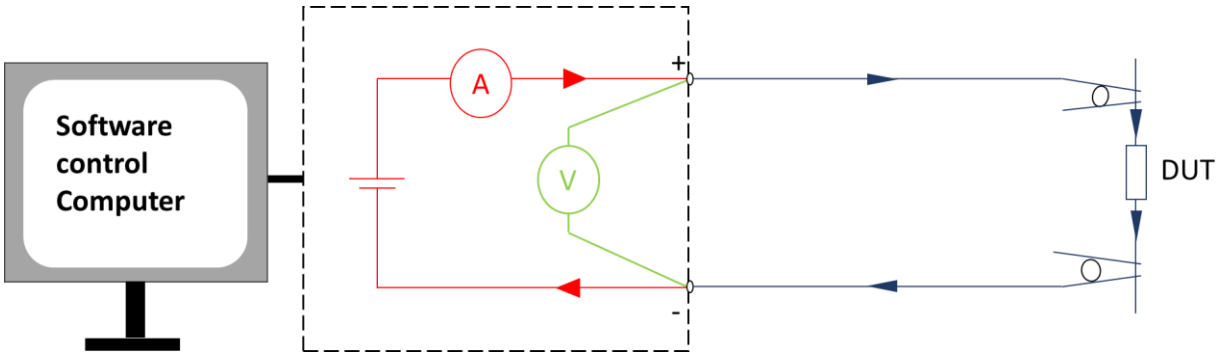

Figure 3.9: Schematic Illustration of the Current-Voltage (I-V) Measurement Circuit. This diagram depicts the configuration of the measurement hardware and the implementation of the two-wire technique for evaluating the Device Under Test (DUT). Detailed explanations of the components and methodology are provided in the main body of the text.

3.3.2 Hall measurement; Van der Pauw (VdP)

Hall effect measurements determine carrier density and Hall mobility when performed alongside resistivity measurements in semiconductor materials. The Hall effect occurs when moving charge carriers are subjected to a magnetic field, resulting in a force due to the Lorentz effect. Figure 3.10 shows schematic diagram illustrating the Hall effect concept, where a magnetic field is applied perpendicular to the direction of the charge carriers' motion, causing them to accumulate on one side of the material. This accumulation generates an opposing electric field E_y. When equilibrium is reached, this field can be described by the following relationship:

$$E_y = v_x B_z \qquad (3.3)$$

Where v_x is the carrier carrier drift velocity and B_z is the applied magnetic field.

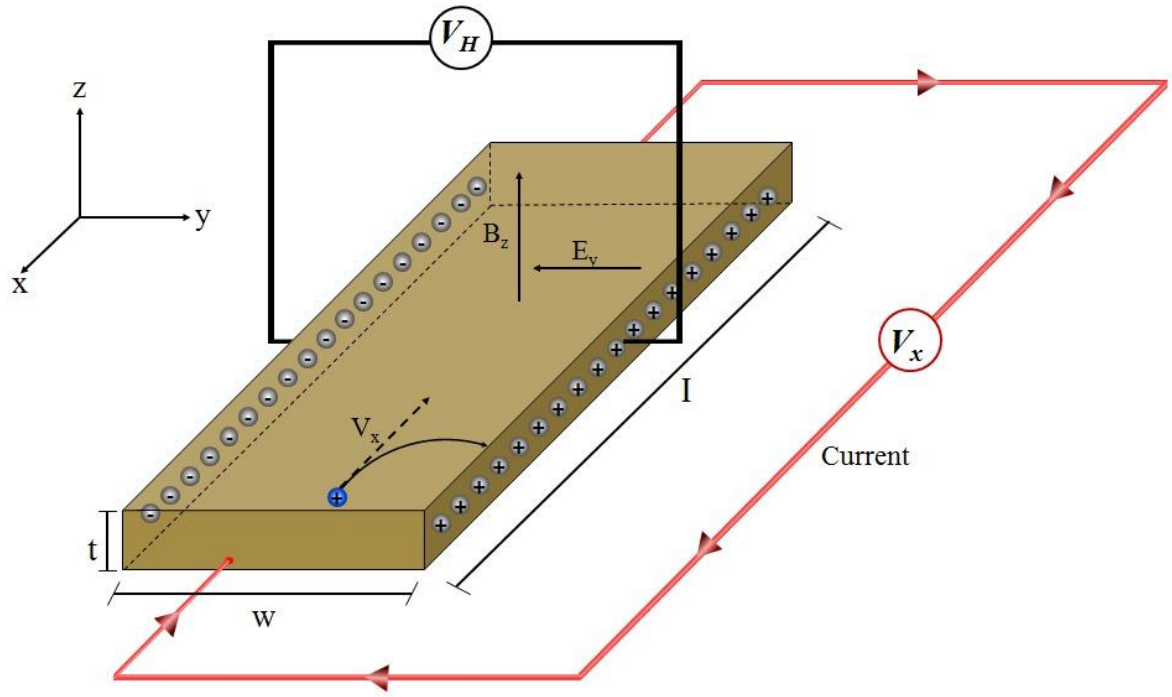

Figure 3.10: Schematic of the Hall effect, showing charge carriers deflected by a magnetic field (B_z), creating an electric field (E_y) perpendicular to both the current (I)) and the field.

The Van der Pauw configuration is a widely used method for applying the Hall effect in semiconductors. It offers an elegant method to measure the resistivity and conductivity of samples using four contacts. This technique is versatile, allowing measurement on samples of almost any shape. By passing a known electrical current through the sample and analysing the resistance at different points along its perimeter, this method determines the sample's electrical properties [143].

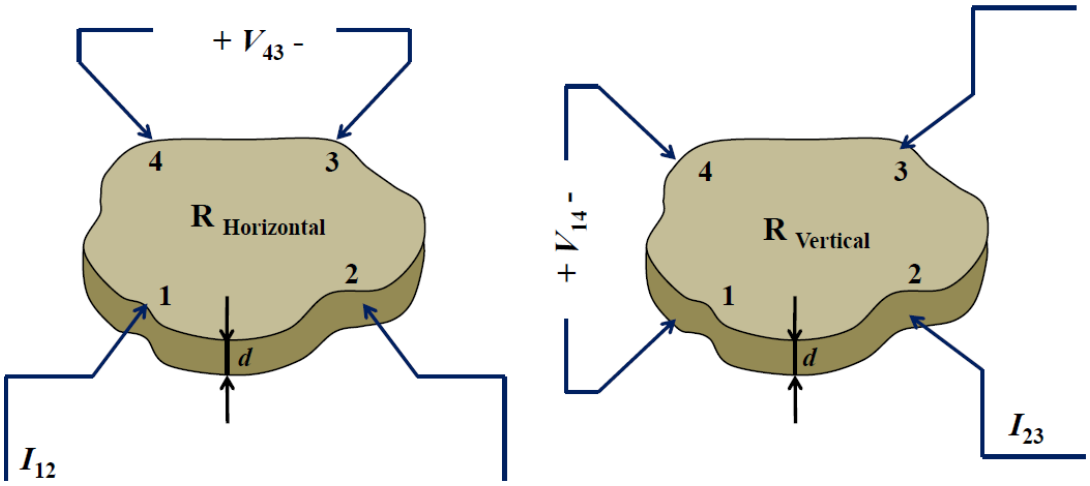

Figure 3.11: Horizontal direction resistance Rhorizontal and vertical direction resistance Rvertical of a flat sample with arbitrary shape.

The method for obtaining the zero-magnetic-field resistivity is as following (refer to Figure 3.11 for the contact labels).

(i) **Vertical resistance** / A current I_{23} is driven from contact 2 to contact 3; the resulting voltage V_{14} is measured between contact 1 and 4. The resistance $R_{23,14} = |V_{14}|/I_{23}$ is computed.

(ii) **Horizontal resistance** / A current I_{12} is driven from contact 1 to contact 2; the resulting voltage V_{43} is measured between contact 4 and 3. The resistance $R_{43,12} = |V_{43}|/I_{12}$ is computed.

(iii) The resistivity ρ is calculated using:

$$\rho = \frac{\pi}{ln2} d \frac{R_{23,14}+R_{43,12}}{2} f \qquad (3.4)$$

Where the function *f* dependents on the ratio $R_{23,14}/R_{43,12}$ and d is the sample thickness. It is recommended that one tries making a new contact if $R_{23,14}/R_{43,12}$ is bigger than ~3 [144].

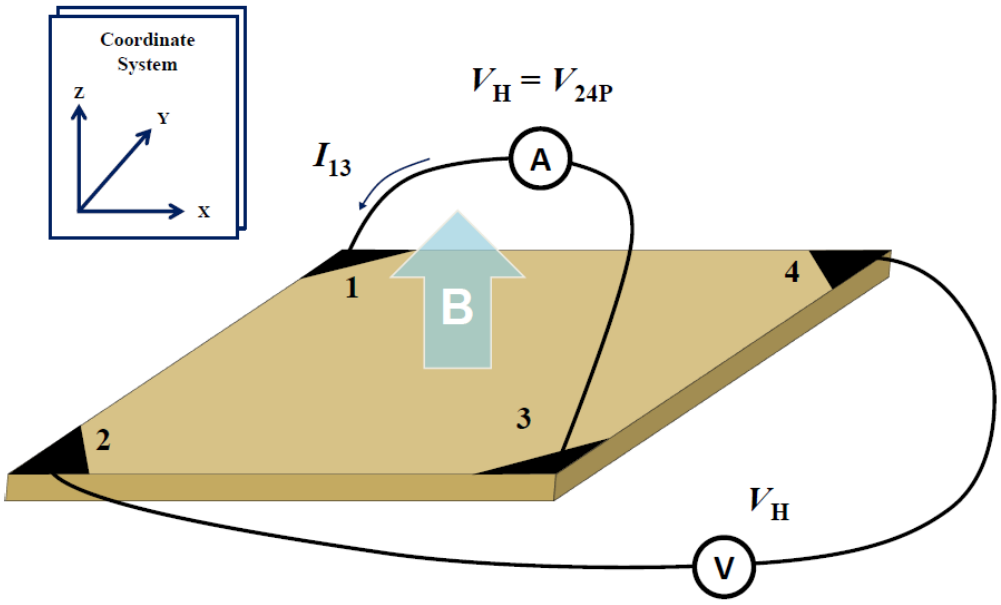

Figure 3.12: Hall voltage measurement using the four-probe van der Pauw configuration. Image reproduced from [145].

A Hall measurement is another sort of measurement can be done by using VdP configuration which is very useful for semiconductor material characterisation since electrical properties (i.e., the majority carrier type, density, and mobility) can be obtained from the induced Hall voltage. The Hall voltage (V_H) can be measured using the same Van der Pauw sample with an applied magnetic field (B) as seen in Figure 3.12 . This can be summarised as following:

(i) A current I_{13} is driven from 1 to 3 and the voltage between 2 and 4 ($V_{24}(B)$ is measured in finite field B and at B=0 to give

$$R_{H1} = \frac{(V_{24}(B) - V_{24}(B=0))d}{I_{13}B} \qquad (3.5)$$

(ii) A current I_{24} is driven from 2 to 4 and the voltage between 1 and 3 ($V_{13}(B)$ is measured in finite field B and at B=0 to give

$$R_{H2} = \frac{(V_{13}(B) - V_{13}(B=0))d}{I_{24}B} \qquad (3.6)$$

(iii) The Hall coefficient is the average of these values;

$$R_H = \frac{1}{2}(R_{H1} + R_{H2}) \qquad (3.7)$$

By knowing the R_H,

$$R_H = \frac{1}{qp} \qquad p \gg n \qquad (3.8)$$

where q and ρ are the elementary charge and carrier (i.e., hole) density for a p-type sample, respectively. The carrier density is determined from the calculated R_H and Equation (3.6). Finally, using the Hall coefficient and $\rho^{-1} \approx \rho q \mu_{Hall}$ (i.e., when p>>n) [146], the Hall mobility (μ_{Hall}) is given as:

$$\mu_{Hall} = qp\mu_{Hall}\left(\frac{1}{qp}\right) = \frac{R_H}{\rho} \qquad (3.9)$$

Thus, μ_{Hall} is obtained by a simple calculation using the calculated $R_H$and ρ .

To determine the electrical characteristics (such as electrical resistivity, carrier density, and mobility) of the Cu_2O crystal, van der Pauw samples were created (refer to Figure 3.13). This involved the fabrication of Au electrodes at the crystal's four corners, with the crystal measuring 3.6 x 3.6 mm in size and the contact being 0.6 mm or 1/6 of the sample edge. The electrodes were formed using the fabrication process mentioned previously in section 3.2.2. Subsequent resistivity and Hall measurements were conducted at different temperatures.

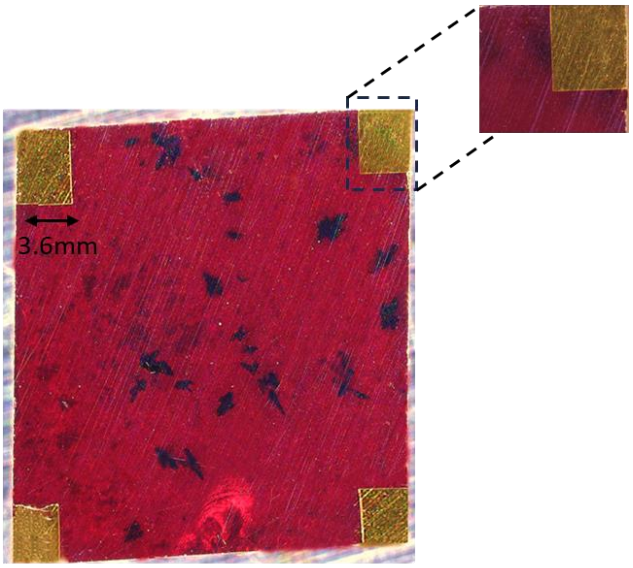

Figure 3.13: Optical microscope image of the Van der Pauw geometry employed for Hall measurements in Cu_2O, featuring a square-shaped contact with a length-to-sample edge ratio of 1/6. Inset zooms in on the details of the contact.

The experimental setup for the VdP measurement, started with the sample being mounted in a pulse tube cryostat. The 20-way ceramic packages were fitted into a holder attached to the cold finger of an *Oxford Instruments Optistat AC-V12* setup. This setup includes several components: a *PT403 cold head* and *a CP830 helium gas compressor*, both from *Cryomech, Inc*. The compressor is water-cooled, and the entire system is regulated by an *Oxford Instruments Mercury iTC temperature controller*. A notable feature of this system is its ability to cool samples down to 2.8 K without using liquid cryogens, which greatly reduces operational costs and simplifies handling. The PT403 cold head maintains a vacuum in the sample space, achieved using an *Oerlikon Leybold Vacuum* Turbolab 8*0* basic turbomolecular pump system paired with a dry compressing backing pump.

Pulse tube cryorefrigerators utilize a compressor to create oscillating gas flow, leading to cooling through helium gas expansion in two pulse tubes. The first tube cools between 40K and 75K, attached to the first stage cold plate, while the second reaches down to 2.8K, connected to the second stage cold plate. A regenerator balances the temperature of the incoming and outgoing gas. Samples are mounted on a copper cold finger linked to the

second cold plate, which is equipped with a resistive heater and a Rhodium-Iron thermometer for precise temperature control.

For I-V measurements we used an *Agilent Technologies E5270B* precision current-voltage analyzer and an *Agilent Technologies E5281B Medium Power Source Monitor Unit (MPSMU)*. Both the temperature controller and the I-V analyzer were connected to a computer. This setup allowed for fully automated I-V-T (current-voltage-temperature) measurements, controlled by custom software written in Python. The software facilitated an automated temperature sweep across the entire range. At each temperature setting, it performed a voltage sweep for the device being tested and recorded the current in that range. To ensure thermal stability, we typically waited 10 minutes at each temperature before conducting the I-V measurements.

For the Hall measurement, the same equipment was utilized with a key addition: a magnet to generate a magnetic field. The sample was carefully positioned between the poles of this magnet, integrated within the existing cryostat setup. To facilitate the exploration of the Hall effect in the Cu_2O sample, both the software and the wiring connections were adapted. This modification enabled the study of the Hall effect under varying temperatures and magnetic field strengths.

3.4 Photoconductivity measurement

The third device was specifically fabricated to study the photoconductivity effect in Cu_2O. We implemented the Spectral Photoconductivity characterization technique in our laboratory due to its capability to identify spectral features within the material's band gap. This method uses a nanosecond-pulsed tunable laser, allowing precise control of the emitting wavelength to illuminate Cu_2O's active area. Combined with a time-resolved tool, this setup enhances the detection of spectral features in the sub-bandgap region, maximizing the sensitivity and accuracy of the measurement.

3.4.1 Experimental Component

I. Light source:

The Ekspla NT242E combines a nano-second optical pump at 1064nm which generates a train of 10ns optical pulses at 10Hz. The wavelength tuning is provided by mixing the harmonics in an Optical Parametric Oscillator to give signal (410-709)nm idler and (710-2300)nm idler beams. The active semiconductor area of the device was illuminated perpendicular to the plane of the sample with this pulsed ns laser beam.

II. Optical configuration:

Detecting such signals demands meticulous parameter selection. Understanding variations in sample resistance due to incident radiation, the circuit's impedance, the capabilities and constraints of the photodetector, and the magnitude of noise sources is crucial. This collective comprehension aids in choosing the appropriate instruments for effective analysis.

Fundamental to the success of the photoconductivity measurement experiment are two distinct yet interdependent facets: the optical and electrical measurements, each meticulously structured with purposefully chosen components and setups to ensure precise characterization of the material's response to incident radiation.

The optical setup for the photoconductivity measurements involved using a nanosecond tunable laser and a carefully partitioned experimental setup. The work area was divided into high and low-power regions to safeguard the integrity of the photodiode and prevent sample ablation. The high-power region, enclosed within a protective box featuring an 8 mm aperture, directed the laser light through a series of precise steps. The tunable laser pulse train was directed towards a CaF_2 window positioned at a 45-degree angle. Approximately 2% of the laser power was reflected, and this reflected beam was redirected by the Au mirrors through an Iris into the designated low-power region. Within the low-power area, the laser beam passed through another CaF_2 window, illuminating the sample under investigation after redirection by another Au mirror. Concurrently, a portion of reflected light from the window underwent expansion through a BK7 f=-50mm plano-convex lens, ensuring illumination of InGaAs photodiodes (Thorlabs DET10D2) while

avoiding saturation at the Gaussian beam centre. The spectral response of the InGaAs reference detector meant that wavelength tuning was restricted to longer than 800 nm in this experiment. Data collection was triggered optically using a Si photo- diode (Thorlabs PDA100A) to collect 532 nm light used internally in the ns laser as part of the process to generate tunable output. This intricate arrangement ensured controlled light transmission, redirection, and expansion, facilitating safe and precise photoconductivity measurements throughout the experimental procedure.

Thorough consideration guided the selection of CaF_2 windows and an Au mirror in the optical measurement setup. Their effectiveness in transmitting IR radiation and maintaining spectral integrity without altering the output spectrum was pivotal. CaF_2 and BK7 demonstrated linear transparency to Vis/IR radiation, ensuring the transmission of the desired spectrum without introducing any spectral features. Additionally, the reflective attributes of the Au mirror preserved spectral fidelity, corroborated by Figure 3.14's demonstration of the optics' flatness in this region. This underscores their critical role in facilitating an unaltered, accurate representation of the IR spectrum essential for precise photoconductivity measurements the whole optical setting can be seen in Figure 3.15.

(a)

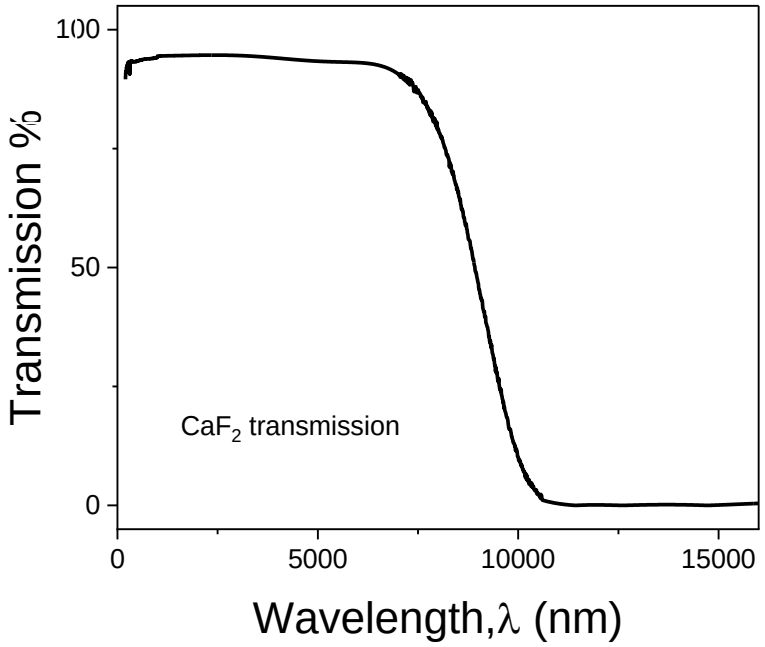
100
50
0
Transmission %
CaF2 transmission
0
5000
10000
15000
Wavelength,λ (nm)

(b)

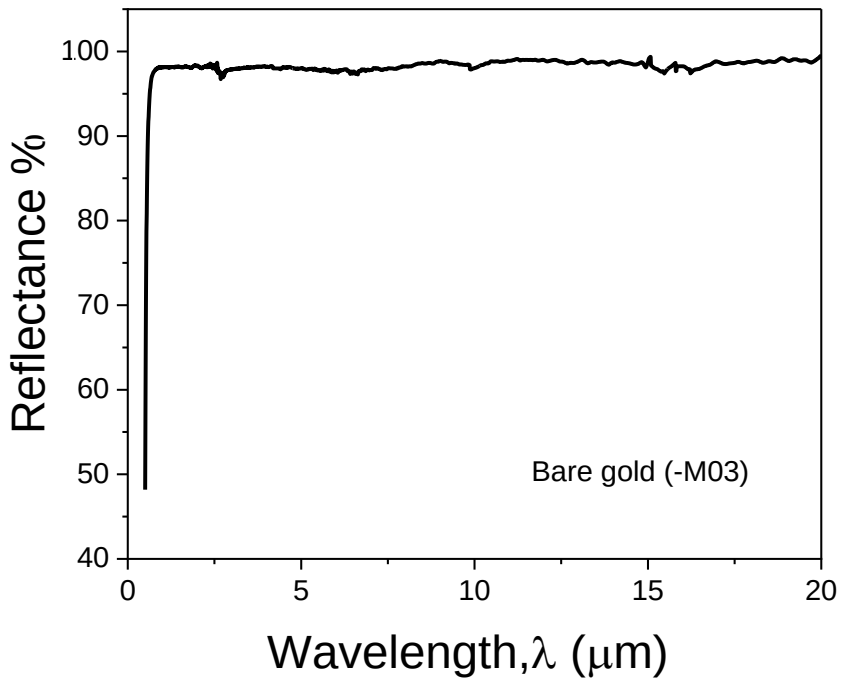
100
90
80
70
60
50
40
Reflectance %
Bare gold (-M03)
0
5
10
15
20
Wavelength,λ (μm)

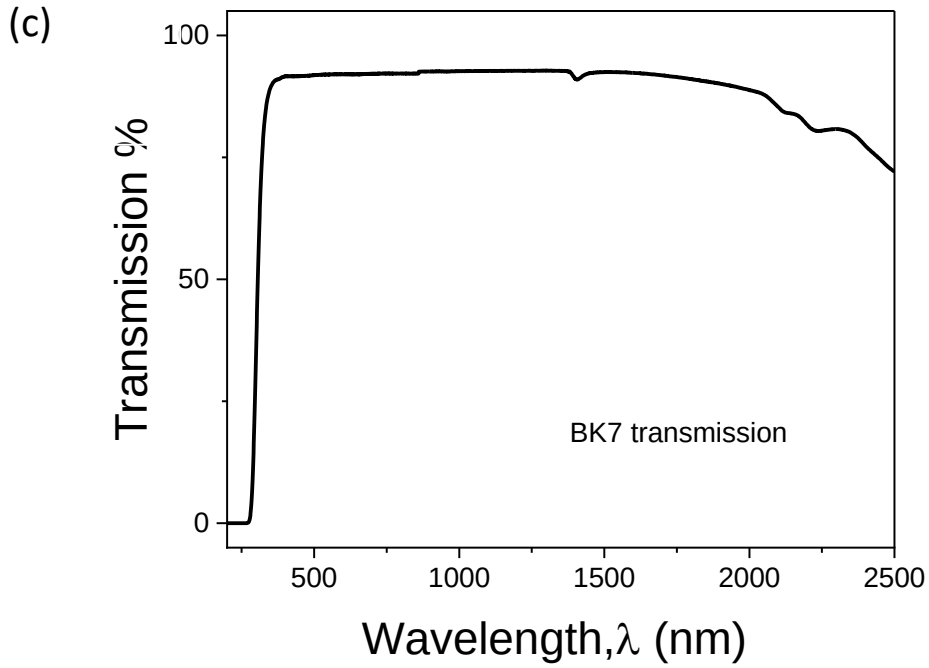

Figure 3.14: Spectral response for (a) CaF_2 window, (b) Au mirror, and (c) BK7 window. These optics demonstrate their consistent and smooth response across the region of interest, ensuring that no additional spectral features are introduced[147].

III. Electrical configuration:

Electrical connections for the time resolved photoconductivity measurement were made by contacting the two Au contact pads with a constant current source to bias of the sample, while the voltage transient subsequent to laser excitation was captured using a Tektronix DPO 3034 digital oscilloscope. This instrument is essential in this work to achieve the time resolved measurement. Enhancing the stability of the constant current source within the circuit, a high-frequency bias tee was integrated, serving to aid in stabilization measures during the measurements (acting like a low pass filter).

A Python program was used to automate the measurement and data acquisition. This was done by controlling the laser wavelength, selecting range from 710-1500 nm in 10 nm steps. Once the light with specific wavelength excites the sample the oscilloscope records the electrical transient in response to this as well as the diode reference response. In addition,

both the oscilloscope and the Python program performed averaging over multiple acquisitions by collecting multiple measurement for each wavelength. Once the measurements were done the program saved the data for further analysis. These measurements were made at an ambient temperature of 23 °C.

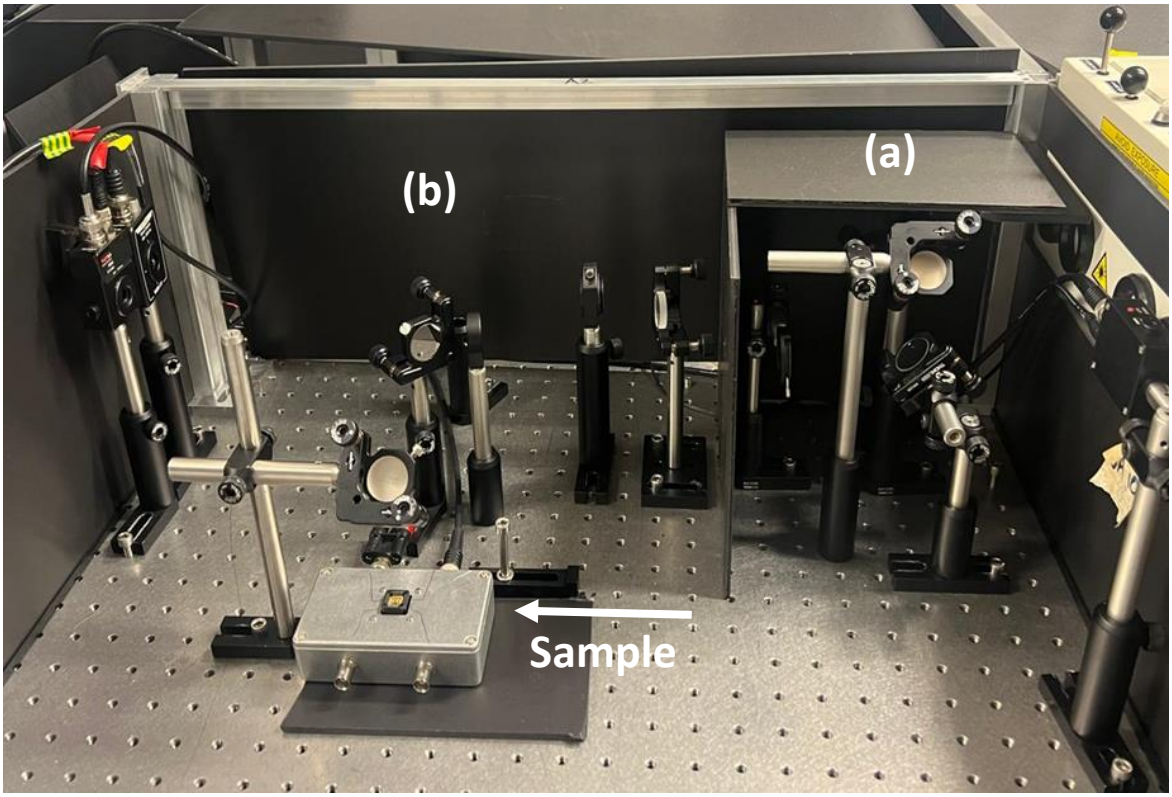

Figure 3.15: the optical experimental set-up showing (a) high power region and (b) low power region.

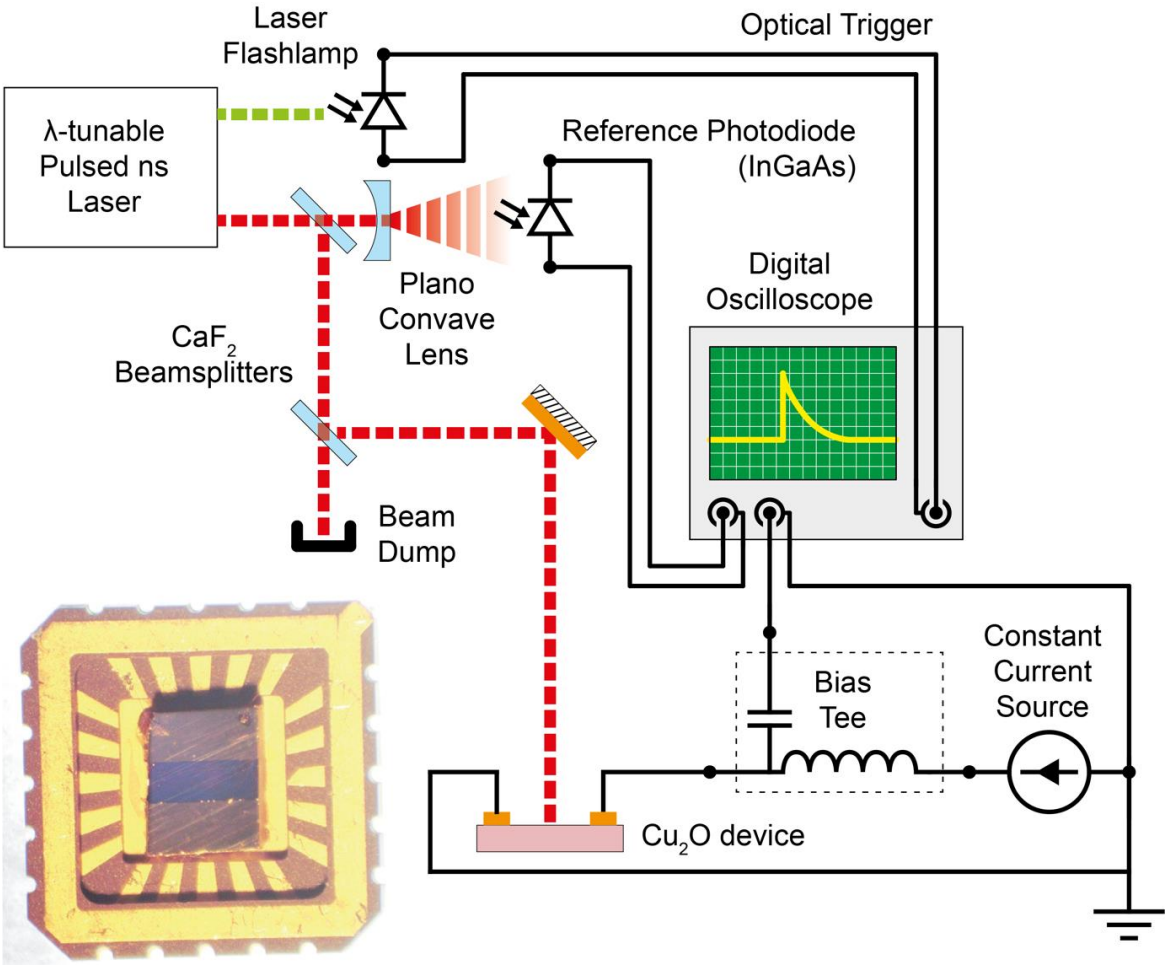

Figure 3.16: Experimental Diagram. The laser output passes through two CaF_2 windows which act as beam splitters to reduce the pulse energy. CaF2 is used because it has a flat spectral response in this wavelength range. The main beam is incident on the Cu2O photoconductive device, while the less intense beam is directed onto the reference photodiode. A CaF2 plano- concave lens is used to expand the beam to reduce the intensity on the reference photodiode. A second silicon photodiode close to the laser generates an optical trigger from the laser flash-lamp. The Cu_2O photoconductive device is biased by a constant current source. A bias tee is used to reject electrical noise as well as to DC-couple the current source and RF-couple the measured transient into the oscilloscope.

An initial problem arose in the form of electronic ripples, seen on the oscilloscope. These unwanted fluctuations, overlaying the device response reading after laser activation made it not easy to accurately capture essential data for the photoconductivity signal.

Despite careful checks and adjustments such as utilization of a high-frequency bias tee for stability in the current source, these measures did not entirely mitigate the ripples, suggesting a more complex and subtle origin.

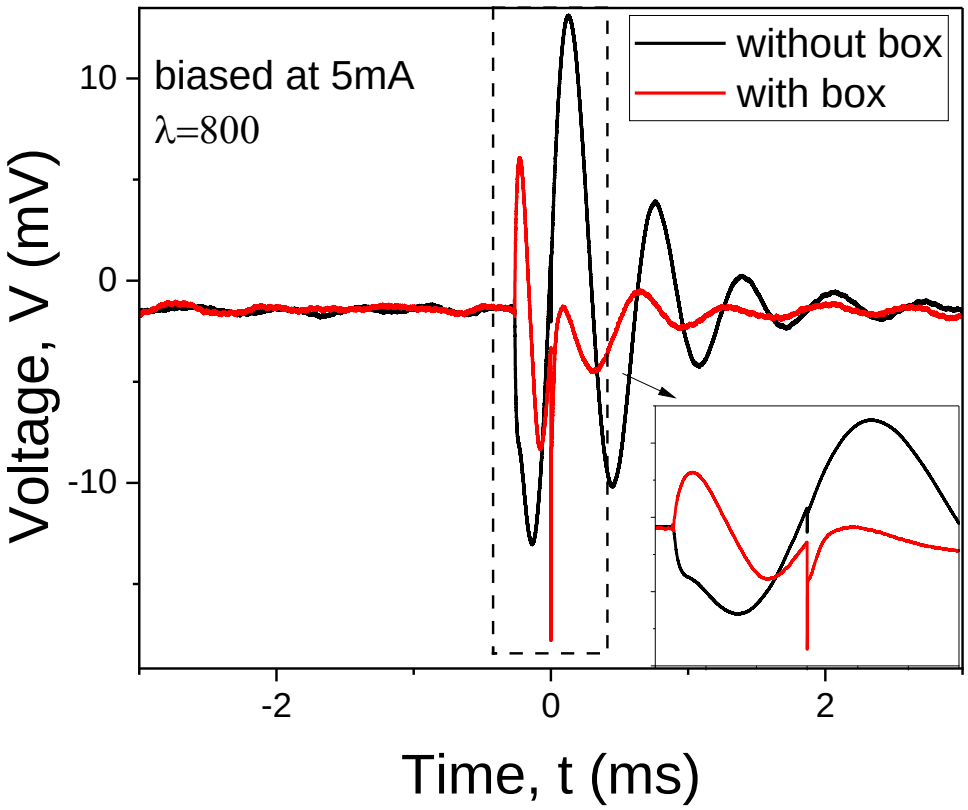

Figure 3.17: Oscilloscope time traces for the Cu_2O single crystal. The black trace shows the voltage over time without any shielding, where significant ripples are observed. The red trace represents the voltage over time with the problem fixed by enclosing the setup in a die-cast box, significantly reducing the source ripples. The inset highlights the improved device response when the die-cast box is added.

Further investigation revealed potential influences from transient responses within the component's impedance mismatch, the coupling of parasitic elements within the circuit, the device may act like capacitor, the electrical pick up from the surrounding environment and the electrical pulse introduced to the circuit when the laser flash lamp is fired. In response to this challenge, the introduction of a grounded die-cast aluminium box provided a notable reduction in observed ringing and enhancing the device response as seen in Figure 3.17.

The shielding effect of the box mitigated external electromagnetic influences effectively reducing the amplitude of the unwanted oscillation on the oscilloscope. The inset shows the

effect of such adding to the experiment on the device response itself where the signal-to-noise improves helping to more reveal the device response, raising and the decay time, peak value and over all shape of waveform. While this solution significantly improved the measurement setup's performance, the persistence of the ringing indicates that the problem is not fully resolved by enclosing the sample in a box. This is because the flash lamp in the laser introduces unavoidable electrical background. That is synchronised to the excitation, because of this it could not be eliminated completely.

3.4.2 Absorption measurement

To measure the absorption coefficient in Cu_2O at the IR region by means of crystal optical transmission, therefore a system was assembled to perform transmission in Cu_2O. The transmission measurement system contained a tunable laser as a light source, set of optics (serving to protect the photodiode and sample), integrating sphere attached with InGaAs photodiode. The transmission rate was determined by a sample in/out procedure described as following:

The tunable laser was setup in the IR range (800-1500 nm) which was delivered to the integrating sphere through a set of optics. Then the photo-generated current signal $I_{source}(\lambda)$ resulting from the incident radiation was read with in the absence of the sample. Then the Cu_2O was placed on the integrating sphere, so the–detector received the radiation transmitted through the sample and generated a small current signal $I_{transmit}$ (λ). These measurements were averaged for readings 30 times and then the transmission rate was calculated as

$$T(\lambda) = \frac{I_{transmit}(\lambda)}{I_{source}(\lambda)} \quad 3.10)$$

$$A(\lambda) = -log_{10}(T) \quad (3.11)$$

The measured transmission rate was used to calculate the Cu_2O absorption coefficient using

$$\alpha(\lambda) = -\frac{1}{t}\left\{\frac{1}{2R(\lambda)^2}\left(\sqrt{\frac{\left(1-R(\lambda)\right)^4}{T(\lambda)^2}+4R(\lambda)^2}-\frac{\left(1-R(\lambda)\right)^2}{T(\lambda)}\right)\right\} \quad 3.12)$$

where R is the reflectivity, T the transmission and t is the crystal thickness.

It is worth to mention that the integrating sphere was used at the first place by using it in an initial arrangement where the light pulse train was collected from the attached power meter interface. When the data was processed, both source and transmission current, seemed to have a high variance at shorter wavelengths (from 800 to 900 nm), which translates into a high standard deviation in that region. Beyond 900 nm, the spectra converged, suggesting more consistent behaviour and a lower standard deviation. This variance affected the obtained absorption spectrum where at this region we could observe a dip and notably sharp peak. Evidence of this is shown in the results shown in Chapter 5.10.

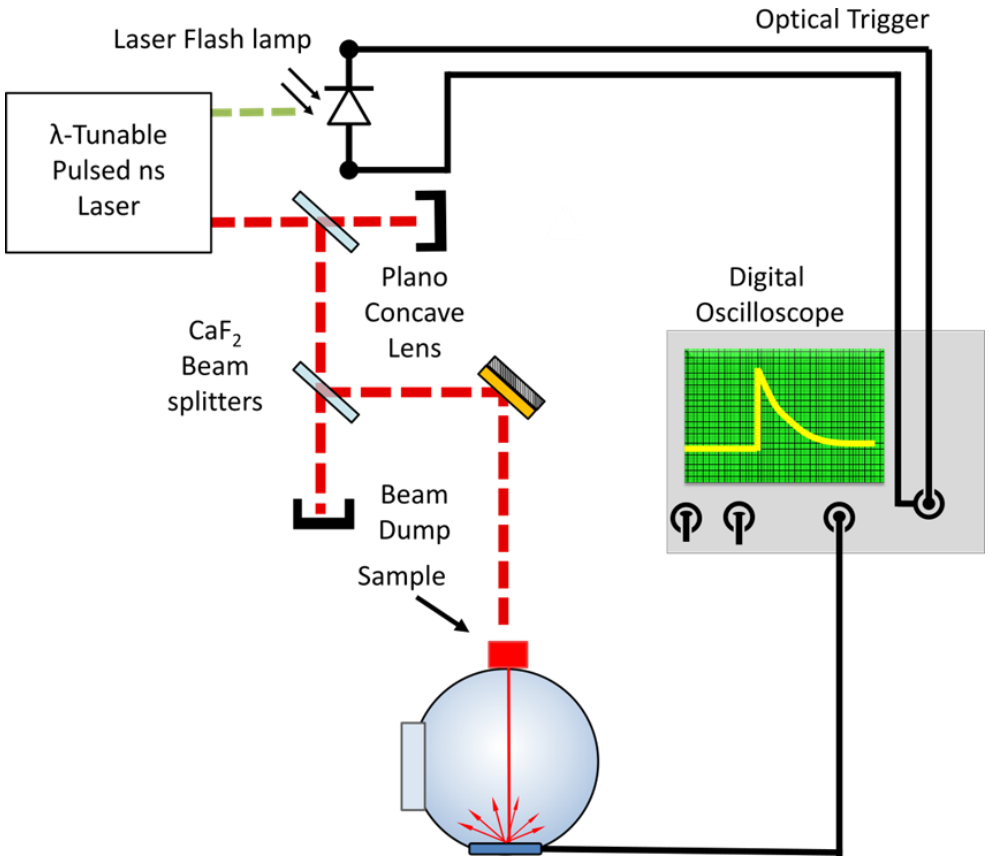

Figure 3.18: The modification in the experimental set-up to measure the absorption spectrum by added the integrated sphere and attached this with the oscilloscope.

The replacement of the power meter interface with an oscilloscope significantly enhanced the consistency of spectral measurements. Unlike the power meter, which averages light intensity over time, the oscilloscope provided advanced signal processing capabilities that improved the quality and reliability of the data.

The oscilloscope was selected for its ability to perform time-resolved signal analysis, capturing rapid fluctuations in the photodiode signal with high temporal resolution. This feature proved invaluable for studying light transmission properties that vary over time or dynamically respond to pulsed light sources. Additionally, its wide bandwidth allowed detection of high-frequency signal components that were otherwise smoothed out by the power meter's averaging nature.

To further enhance measurement accuracy, the oscilloscope incorporated real-time noise filtering techniques. Specifically, low-pass filtering was utilized to isolate desired signal frequencies while suppressing unwanted noise. An averaging function was applied, averaging signals over 256 acquisitions to produce a smoother and more defined representation of the signal. The oscilloscope was optically triggered to ensure precise and consistent signal capture, isolating relevant waveform portions based on predefined criteria such as edge or pulse triggers. This feature effectively minimized variability in measurements, a significant limitation of the power meter interface.

A Python program was used to automate the measurement and data acquisition processes. It controlled the laser wavelength across a range of 800-1500 nm in 10 nm steps. For each wavelength, the oscilloscope recorded light transmission both through the sample and without the sample. The program also performed averaging across multiple acquisitions for each wavelength, thereby enhancing the reliability and accuracy of the measurements. After completing the measurements, the program saved the data for further analysis. All measurements were carried out at an ambient temperature of 23 °C.

3.5 MIR and THz measurement

To obtain the MIR and THz absorption spectra of Cu_2O we used Fourier Transform Infrared Spectroscopy (FTIR). In contrast to conventional (dispersive) spectroscopy, in FTIR spectroscopy the light shines into a certain configuration of mirrors, forming a Michelson interferometer. One of the mirrors is moved to vary the path length in the interferometer. As this mirror moves, each wavelength of light in the beam is periodically blocked, transmitted, blocked, transmitted, by the interferometer, due to wave interference. Different wavelengths are modulated at different rates, so that at each moment or mirror position the beam coming out of the interferometer has a different spectrum[148]. The prime aim of conducting such measurements was to examine impurity states, phonon modes, and other key electronic properties across a range of temperatures for revealing any spectral distinguishing feature between natural and the synthetic Cu_2O. The experimental setup for this measurement is shown in Figure 3.19 for MIR measurements using the MTC

detector, and in Figure 3.20 for THz measurements where a bolometer was used as the detector.

3.5.1 Experiment Components

The rapid scan measurement outlined above was performed with several specific settings, described one by one here:

I. Light source

A Globar is used as a thermal light source for infrared spectroscopy. The preferred material for making Globar is silicon carbide that is shaped as rods. When inserted into a circuit that provides it with electric current, it emits radiation from ~ 2 to 50µm wavelength via the Joule heating phenomenon.

II. Cryostat and Cooling

The cryostat was evacuated to a pressure of approximately 10^{-5} mbar, as measured by an Edwards vacuum AIM-X-NW25 gauge. The low pressure was necessary to allow cooling of the samples, as without a vacuum inside the cryostat the ambient heat would leak in and prevent useful cooling. The vacuum was achieved by a turbo pump.

Both absorbance and emission experiments require temperatures in the 20-300k range. Each sample is held at the end of a cold finger inside a custom flow cryostat based on an Oxford instruments Microstat HE and ColdEdge Stinger. An Oxford Instruments Mercury iTc temperature controller and associated sensor are used measure the temperature, while a resistor-based heating element again controlled by the Mercury iTc was used to heat the sample.

III. Spectrometer setting

The resolution related to the data point density in the FT the being that the resolution is ½ the data point density. The nominal spectral resolution of our measurements was 4 cm^{-1} the instrument will compute the spectral data point every two wavenumbers as the quality of the spectrum depended on the wavenumber. The higher the resolution required, the more data points that must be measured i.e. the interferogram must be longer which means the

mirror should move further. The resolution used in this work gives a mirror movement distance of 0.8cm as the distance scanned by the moving mirror equals $^{1}/_{resolution}$. However, the interferogram was measured as fully double sided, thus the mirror was moved between plus and minus 0.8 cm with respect to the zero-path difference position. This means that the true mirror movement distance was 1.6cm. In addition, it should be noted that a much higher resolution is possible with the Vertex 80v system, which has a maximum of $0.075cm^{-1}$ for a total possible mirror movement of 13.33cm. However, as the experiment must be repeated 100 times at each mirror position, higher resolutions would cause a prohibitively long measurement time.

IV. Detector and Amplifier

For the MIR regime a Kolmar MCP0393 photovoltaic HgCdTe element with a $1mm^2$ active element was used, its active element requires cooling to liquid nitrogen temperatures to function. The detector is reverse biased by 50mV to increase the response speed, this gives an approximate signal rise time of 20ns and an exponential fall lifetime of 40ns. The MCT photoconductive detector is coupled to an internal amplifier, with BNC output. The side looking LN_2 pour filled Dewar has a 12-hour hold time. Detector to amplifier connections is inside the Dewar, minimizing electrical pick up and simplifying system integration. While for the THz regime the bolometer detector was used here. The detector used in our experiments is cooled to liquid helium temperatures via an inner dewar of liquid helium surrounded by an outer jacket of liquid nitrogen. The millimetre-waves are converted to a voltage signal, which passes through a low-noise preamplifier before being processed by a lock-in amplifier.

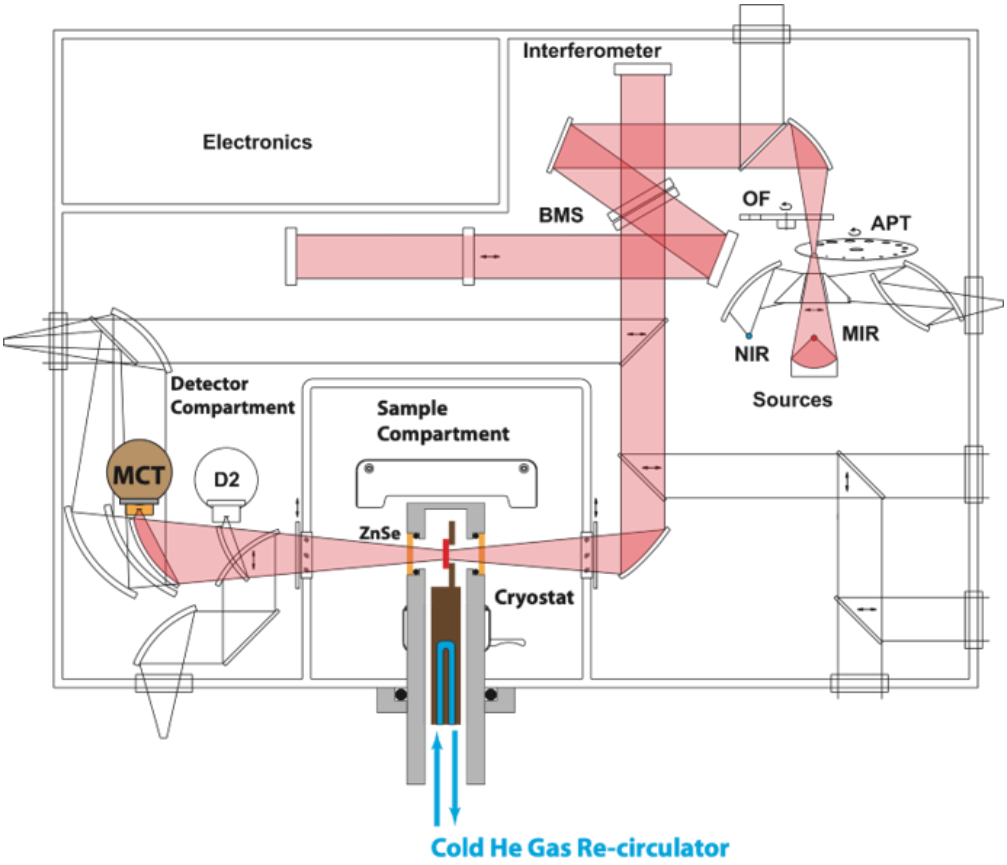

Figure 3.19: Absorbance Experiment set-up using a Bruker Vertex 80V Fourier Transform spectrometer. Beam path is highlighted in partially transparent red. NIR is a near-infrared lamp. MIR is a mid-infrared globar lamp. BMS is a beamsplitter, selected for the wavenumber range of what is being measured. APT is an optical aperture selector, to control lamp intensity and beam size. OF is an optical filter wheel.

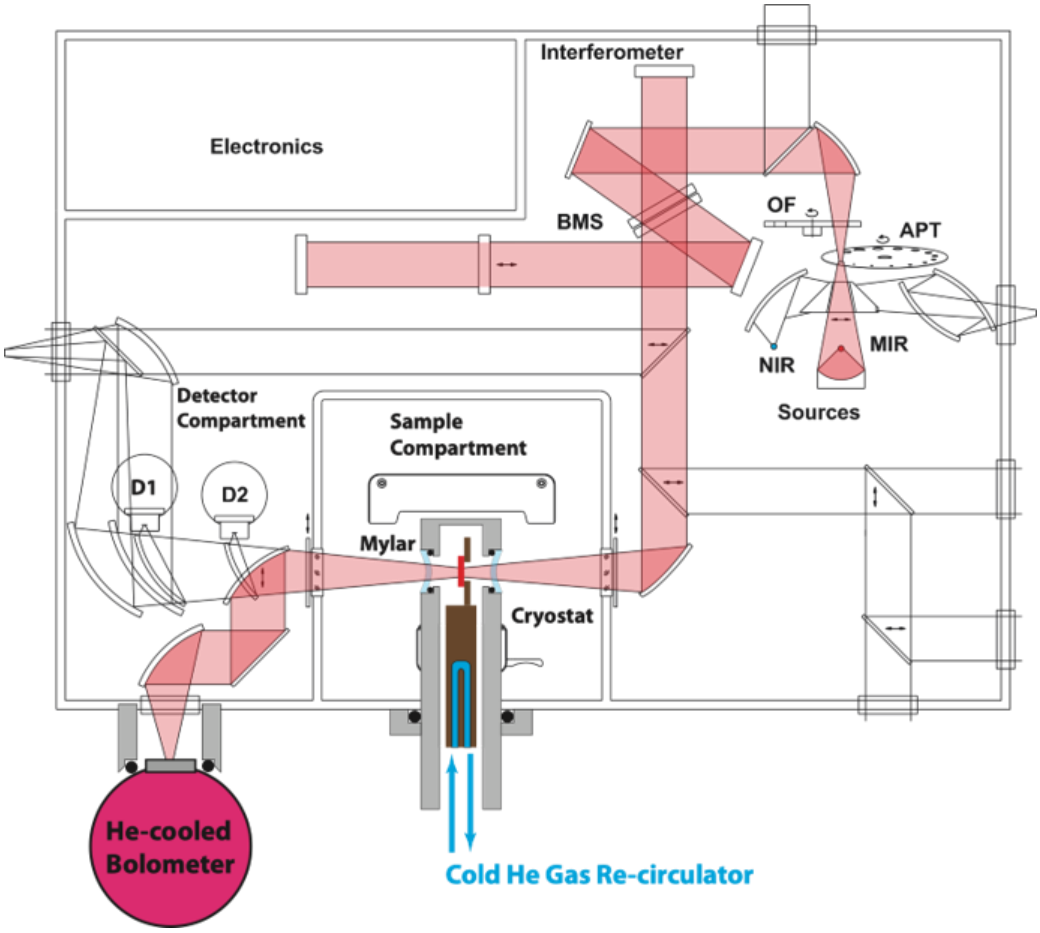

Figure 3.20: Absorbance Experiment set-up using a Bruker Vertex 80V Fourier Transform spectrometer for THz measurement Beam path is highlighted in partially transparent red which is detected by bolometer.

3.5.2 MIR & THz Absorption spectroscopy

To conduct absorbance spectrum by using the FTIR spectrometer in Figure 3.19, the samples were placed by using a copper holder as shown in Figure 3.21b this has a custom design featuring four strategically placed holes of identical diameter. Three of these holes contain samples secured with low temperature GE varnish, while the fourth hole was intentionally left open to allow for background spectrum measurements. This setup was used to align a beam with each sample and a detector, facilitating the collection of spectral data for each sample. This method ensures precise spectral analysis by isolating the influence of the samples from the background. Sample alignment was controlled by a homemade arm that

enables precise manual alignment of the samples monitoring this process by installing a webcam in the sample compartment. This setup allows for careful movement and positioning of each sample relative to a detector.

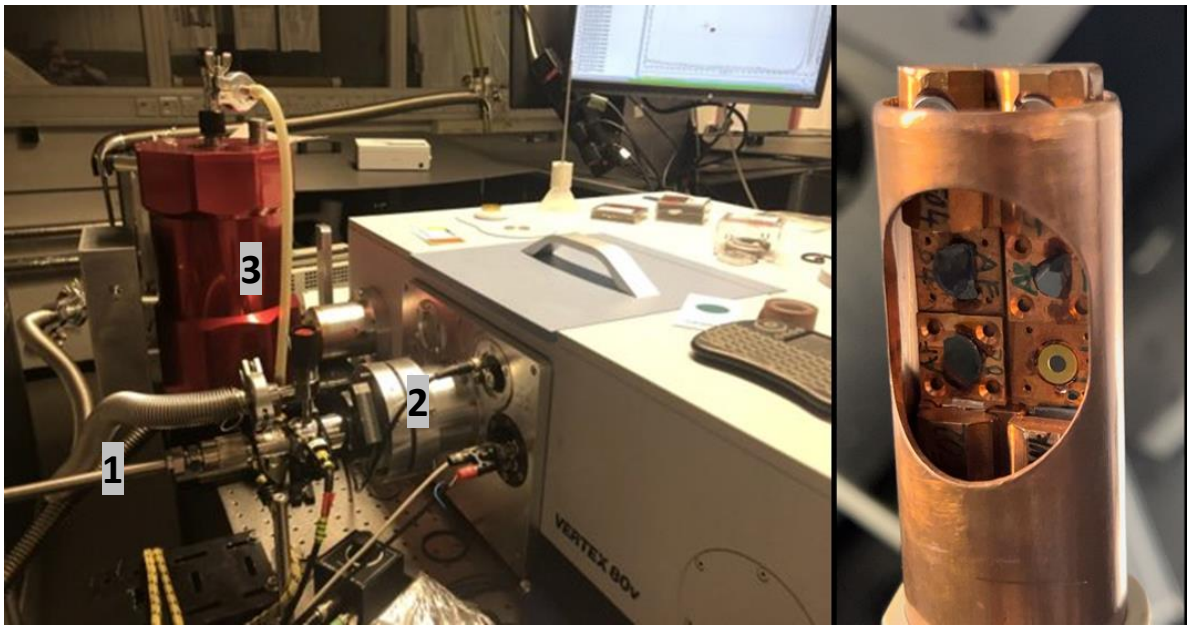

Figure 3.21: (a) The FTIR used in this work (1) the cold finger and (2) homemade sample alignment kit (3) the detector (b) Close-up view of the sample holder, which contains four holes. The samples are secured in these holes using GE varnish. The empty hole is used for taking the background spectrum to ensure accurate measurements.

Now that the measurement of a spectrum has been outlined, the measurement of an absorbance spectrum can be described. Firstly, a background spectrum is measured using the experiment set-up of Figure 3.21 for a background spectrum there is no sample (through the hole), only the lamp light spectrum is measured. Secondly, the sample was placed in the sample position, and the spectrum of light that can pass through the sample unabsorbed was measured. The sample temperature was controlled by a closed-cycle ColdEdge™ “Stinger” recirculating helium cryostat.

The OPUS software was used to run the experiment by collecting the sample's spectral data and the background. It processes the information in real time, generating the absorption spectrum, which is ready for analysis once the scan is complete.

3.6 Summary

This chapter described various experiments conducted in this thesis, starting with the sample preparation for different electrical and optical measurements. This included cutting, planarization, and selecting the appropriate thickness for each type of measurement. The fabrication process and the resulting devices were presented in different configurations, each serving specific electrical studies, such as CTLM, VdP, and the photoconductivity device. The spectrally resolved photoconductivity experiment was thoroughly explained, including the optical and electrical setup designed to prevent interference and to obtain the Cu_2O photoresponse spectrum, aimed at identifying any defect states in the NIR region. This was followed by obtaining the absorption spectrum for both natural and synthetic Cu_2O to investigate defect-related states in the THz and MIR regions.

Chapter 4 Optimizing Ohmic Contact Formation and Electrical Transport Properties in bulk Synthetic Cuprous Oxide Cu_2O

4.1 Introduction

The primary objective of this chapter is to first explore the formation of an efficient Ohmic contact for Cu_2O, material based on specific criteria, for example, achieving low specific contact resistance [149]. Recognizing the pivotal role of metallization enhancing the Ohmic contact and then device performance. There are many reports in literature extensively examining the Ohmic junction between Cu_2O and various metals **(such as Ti, Ag, Au, Pd and Cu)** [150]–[152], exploring how the metal work function influences the junction type and subsequent contact at the interface, based on the Schottky contact model: which can predict Ohmic or Schottky contacts based on the work function differences between the metal and semiconductor. However, our research specifically targeted the evaluation of gold (Au) as a contact material for metallization of bulk Cu_2O that have been prepared by optical FZ technique. Au is superior not only for achieving low resistivity but significantly improving the stability of these devices [153]. The specific contact resistance of the Au contacts being developed will be obtained by examining the circular transmission line measurement (CTLM) configuration.

Au was selected as the material for the ohmic contacts due to its unique and superior properties that are critical for ensuring reliable and accurate measurements. Gold exhibits exceptionally low specific contact resistivity, primarily due to its high work function, which is crucial for achieving a good ohmic contact. This property facilitates efficient charge carrier injection and extraction, which is essential for achieving true ohmic behavior.

The low contact resistance provided by Au is particularly important in this study to accurately measure the intrinsic electrical properties of Cu_2O. High contact resistance could

otherwise influence the measurements and lead to inaccurate interpretations of Cu_2O's electrical characteristics.

Additionally, Au's chemical inertness and resistance to oxidation are vital for maintaining the stability of the interface over time. This ensures consistent performance even under varying conditions such as high or low temperatures and exposure to environmental factors like moisture and air. These attributes collectively make Au an ideal choice for the ohmic contacts in this work.

Secondly, this chapter also aims to characterise the Hall properties of the Cu_2O crystal, by examining the material impurity levels, and mobility of charge carriers. We utilize the Van der Pauw sample configuration and subject the sample to a wide range of temperatures ranging from 300K to 95K in 5K increments and externally applied magnetic fields ranging from -0.5T to 0.5T. This range of temperatures was chosen aiming to provide a comprehensive analysis of the electrical conductivity and majority carrier concentration as a function of temperature to therefore identify the activation energy values which may offer insights into how defects within the Cu_2O single crystal behave, their potential origins and their influence on these critical electrical parameters.

4.2 Metal-Semiconductor contact

A metal-semiconductor interface is described as Ohmic when the applied voltage and resulting current flow have a linear relation. However, good Ohmic contacts generally need several additional properties to ensure functionality and practicality in devices. First of all, they need to have a low specific contact resistivity. Secondly, the Ohmic contact must be thermally stable, reproducible, have smooth surface morphology with good edge definition, be low cost, non-corrosive, and finally, the Ohmic contact must be scalable to keep up with the ever-decreasing size of devices [97]. In reality, there will always be trade-offs between the different criteria. For example, a gold-based Ohmic contact scheme (like those used in this work) has advantages over other metallization schemes in terms of its resistivity,

stability, and resistance to corrosion. Despite these advantages, the use of gold in diodes also comes with challenges, such as increased cost and poor morphology [98].

These properties can be categorized into physical characteristics that define an Ohmic contact and practical considerations that ensure its viability for manufacturing and real-world applications as following: these are the physical and intrinsic properties required to ensure that a contact behaves as an Ohmic contact:

Specific Contact Resistance (ρ_c): Specific contact resistance is a parameter that indicates the resistance encountered when current flows across the interface, normalized to the area of contact. This parameter, extracted as ($\Omega \cdot cm^2$), serves as a benchmark for the quality of an Ohmic contact. A small specific contact resistance is essential to allow for large current flow at low supply voltage.

Linear Current-Voltage (I-V) Relationship: An Ohmic contact is defined by its linear I-V behaviour, which indicates that current flows freely across the metal-semiconductor interface without significant rectification.

Good Electrical Conductivity: The metal used for the Ohmic contact must have high electrical conductivity to ensure minimal resistive losses during current flow.

Energy Band Alignment: To achieve Ohmic behaviour, the energy bands of the metal and semiconductor must align in a way that minimizes or eliminates the Schottky barrier. This can often be achieved through heavy doping or work function engineering.

Thermal Conductivity: High thermal conductivity is important to dissipate heat generated during operation, preventing device degradation. While the desirable properties that ensure the Ohmic contact is suitable for manufacturing and long-term use are:

Thermal Stability: The Ohmic contact must maintain its properties under operating and processing temperatures to ensure reliability.

Reproducibility: The process to create the Ohmic contact must be consistent across batches to ensure uniform performance across devices.

Surface Smoothness and Edge Definition: A smooth surface morphology is essential for easy interconnect wiring, while good edge definition prevents unwanted short circuits and enhances device yield. These are particularly important for high-yield device requirements but less critical in self-aligned structures.

Corrosion Resistance: Oxidation or corrosion during processing can deteriorate contact properties and hamper long-term reliability. While metals such as gold and platinum are inert and resist corrosion, other metals might require a protective layer despite being more cost-effective.

Scalability: The Ohmic contact scheme must support miniaturization to accommodate the ever-decreasing size of devices.

Cost-Effectiveness: While materials like gold have excellent resistivity and corrosion resistance, their high cost can be a limiting factor. A balance must be achieved between material properties and economic viability.

4.2.1 Metallization Scheme

The Ohmic junction between Cu_2O and various types of metals has been intensively investigated in literature; for example, Singh group investigated the influence of the work function and the resulting junction type at the interface on the type of contact. They used different metal (Ti, Ag, Cu, Au, Pd) [150]. Cu_2O exhibited linear and symmetric I-V behaviour for all the used electrodes and this was explained using Schottky contact model. This model determines the characteristic of the metal-semiconductor junction based on the difference between the work function of metal (Φ_m) and semiconductor (Φ_s). According to this model an Ohmic contact is formed when the metal's work function is higher than the p-type

semiconductor ($\Phi_m > \Phi_s$). Conversely a Schottky barrier is created in such material when the metal's work function is lower than the semiconductor one ($\Phi_m < \Phi_s$). [7]

The theoretical barrier height was evaluated using the Schottky model [154], according to the relation:

$$\emptyset_{bp} = V_{od} + E_F - E_v \quad or \; V_{od} + \Delta E_v \tag{4.1}$$

$$V_{od} = \emptyset_s - \emptyset_m \tag{4.2}$$

where $\emptyset_{bp}$ denotes the barrier height for holes in a p-type semiconductor, V_{od} is built in potential and ΔE_v is the valence band offset. The value of ΔE_v is 0.3 eV for Cu_2O [155]. The calculated barrier heights of the various metal contacts with Cu_2O layers are given in Table *4-1* on the basis of the Schottky model.

Table 4-1: Metal work functions and theoretical barrier heights of the metal-oxide contacts calculated from Schottky model. Work function value for Cu_2O is 4.84 eV.

Metal	Work function (eV)	Theoretical barrier hight $\emptyset_{bp}$ (eV)	I-V characteristics
Ti	4.33	0.82	Linear
Ag	4.74	0.40	Linear
Au	5.20	Ohmic	Linear
pd	5.30	Ohmic	Linear

[7] In contrast, according to the same model for a metal and an n-type semiconductor material a Schottky contact is formed when ($\Phi_m > \Phi_s$) and an ohmic contact is formed when ($\Phi_m < \Phi_s$).

Both Au and Pd are predicted to form Ohmic contacts with Cu_2O as their work function higher than the Cu_2O's (4.84 eV). However, it has been found that Ti and Ag also exhibit a linear, Ohmic I-V relationship despite having 4.33 eV and 4.74 eV as a value of their work functions respectively, and not Schottky contacts as the model suggests. This may be because these metals alter the surface of the semiconductor reducing a small region of the Cu_2O to form a region of metallic Cu at the interface. This is possible as both Ti and Ag metals are readily oxidised (thus reducing Cu_2O to Cu at the interface), forming stable oxides. The resulting oxygen deficient region at the interface is believed to form another type of barrier having properties somewhat similar to Cu–Cu_2O Ohmic contact [156].

This theory was supported by the study of Yang et al. In which they evaluated the junction using metal with work function lower than Cu_2O, mainly (Pt, TiN, TaN, Cu, Al, Ru and Ti) such materials should form Schottky barriers according to simple Schottky contact model. They analysed the barrier properties between Cu_2O and electrode experimentally from C-V measurement under the reverse bias condition extracting the built-in potential (V_{bi}) and then calculate the barrier height. The experimental values did not agree with those predicted by the simple Schottky model and were similar to Ohmic contacts [151].

They attributed this behaviour to the low work function metal reducing Cu_2O to form a region of metallic copper at interface, where these metals are easily oxidised in presence of oxygen and form a stable oxide. Figure *4.1* shows the measurement reported by Young et al. where a metallic Cu peak was found around the interface region of a Cu_2O/Ru contact. This is identified as a shoulder on the main Cu_2O peak.

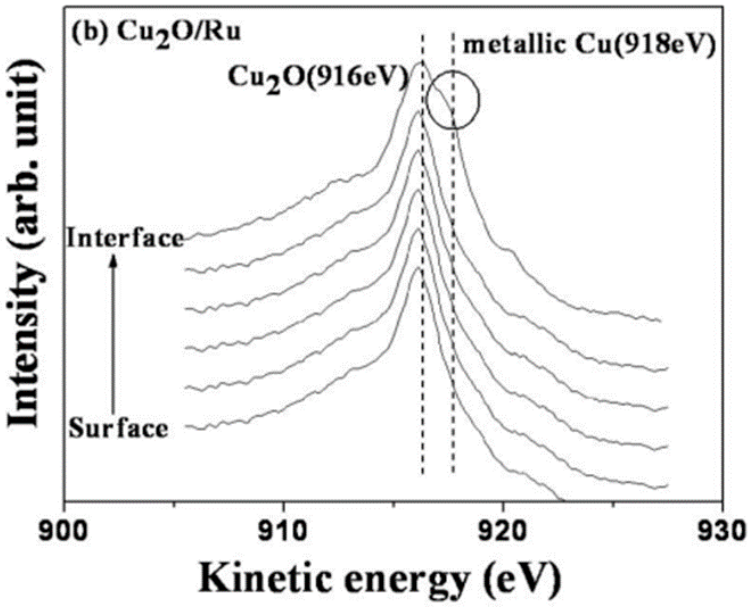

Figure 4.1: Auger depth profile of LMM transition line of Cu_2O in Cu_2O/Ru produced by Young group [151].

4.2.2 V-I Characterization of Au-Cu2O Contacts Using CTLM

The voltage-current (V-I) characteristics of Au and Cu_2O metal-semiconductor contacts were investigated using the circular transmission line method (CTLM). About 300nm Au was deposited on top of Cu_2O crystal and then annealed at 100°C to alloy the contact. The geometry for single unit of this structure is show in Figure 4.2, is a circular contact with radius r_1, that is separated from the surrounding electrode by a ring-shaped gap, s, varied gap spacings: 8 µm, 16 µm, 24 µm, 32 µm, 40 µm, and 48 µm are used and $r_2=r_1+s$. Details of the CTLM devices have been explained in the methodology section 3.3.1. The V-I measurements were conducted in the voltage range from -1.0 V to +1.0 V.

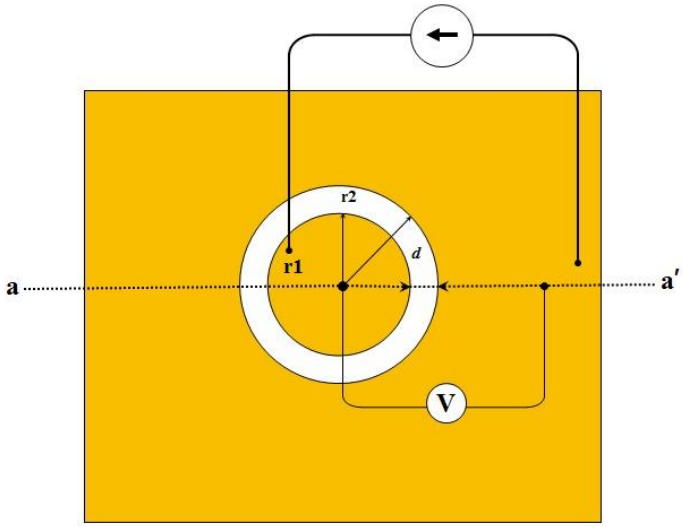

*Figure 4.2: Top view of the CTLM structure. r_1, and $\mathbf{r_2}$ are the radii of the inner and outer disc contact, respectively, and **s** is the gap spacing, which is a variable.*

The results are shown in Figure *4.3*, where linear V-I characteristics for all the gap spacings indicate Ohmic behaviour of the Au-Cu_2O contacts. This linearity is consistent across the entire voltage range tested, with no significant deviation from Ohmic performance observed. The line with steepest gradient, and thus lowest resistance, is obtained from the smallest, 8um, gap spacing, and the subsequent lines correspond to device with increasing gap spacing up to 48 µm. It is noteworthy that the linearity of the V-I characteristics and the subsequent analysis of resistance versus gap spacing provide critical insights into the electrical behaviour of the Au-Cu_2O contacts. The consistent linearity across varied spacings reinforces the reliability of the contacts, which is crucial for the intended study/investigation of this materials.

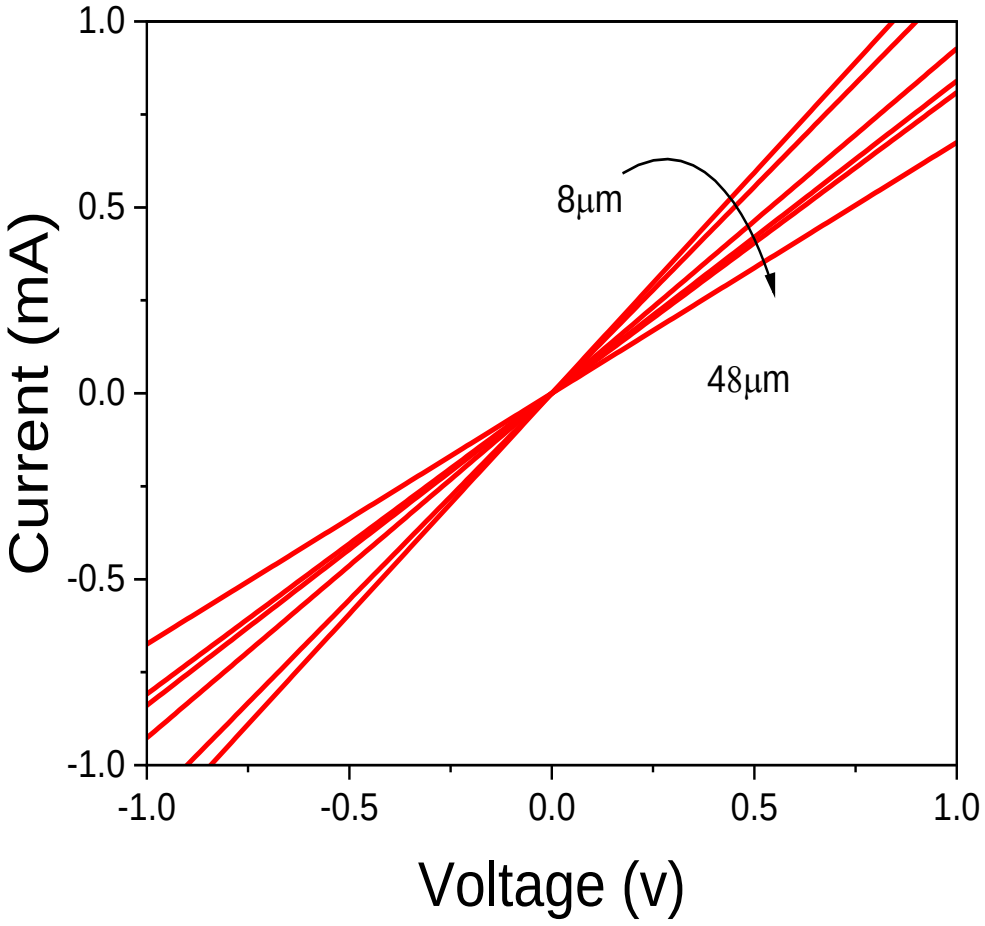

Figure 4.3: Current-Voltage characteristics as a function of gap size. Inset: Fabricated CLTM patterns. The central circular contact pad has a constant diameter of 400 μm, while the gap to the common contact is varied between 8-48 μm.

To determine the specific contact resistance (ρ_c), we first calculated resistance values from the slopes of the V-I characteristic for each gap spacing which was subsequently plotted as a function of the gap spacing in Figure 4.4 marked as open circles, showing a non-linear behaviour. The non-linearity in this plot is expected for the CTLM method and requires the use of correction factors to adjust the data for proper analysis. The correction factors are based on theoretical expectations where uniform current distribution is assumed, and it corrects for any discrepancies caused by edge effects or non-uniform current spread in the circular transmission line method [141]. The corrected resistance value is obtained by

dividing the measured resistance value by the correction factor, c. the correction factor for different gap spacing is shown in

Table 4-2, where c is given by:

$$c = \frac{r_1}{s} \ln \frac{(r_1 + s)}{r_1} \tag{4.3}$$

Table 4-2: Correction factor values for different gap spacing the inner radius r_1=200µm.

Gap spacing µm	**Correction Factor C**
8	0.98052
16	0.96201
24	0.94441
32	0.92763
40	0.91161
48	0.8963

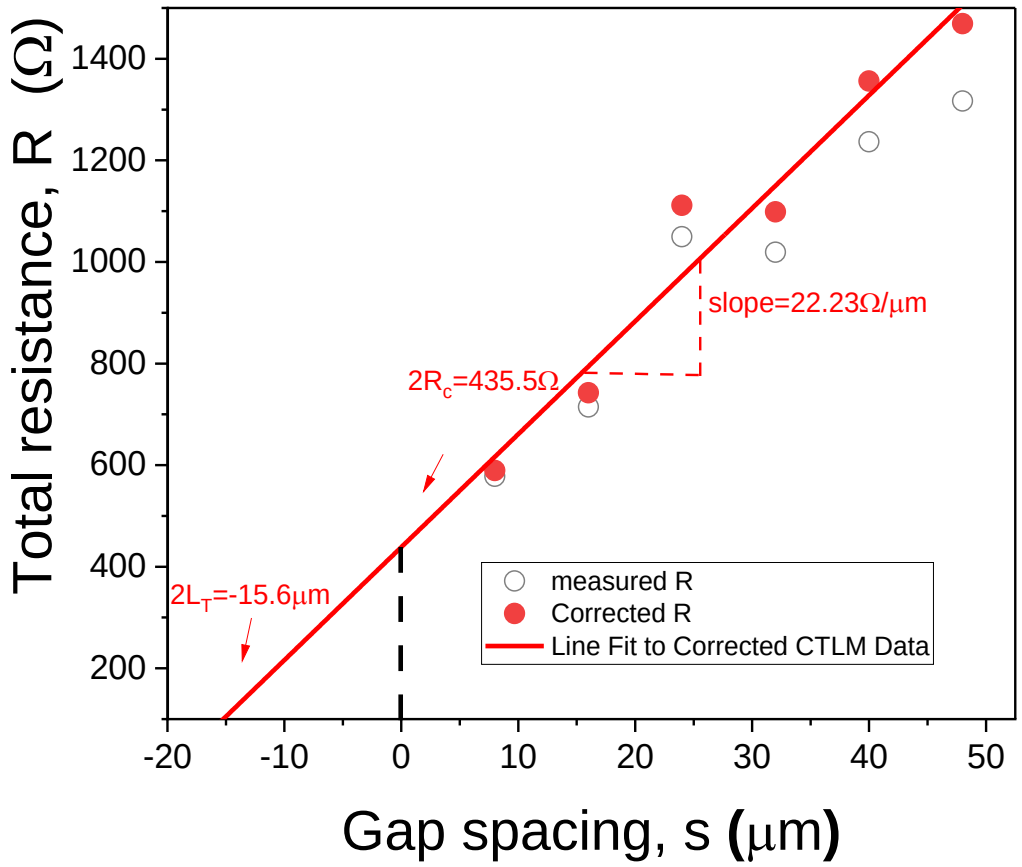

Figure 4.4: Corrected resistance as a function of gap spacing. The black opened circles represent the measured resistance values, and the red closed squares are the corrected resistances. The red line is linear least squares fit to the red squares.

The linear fit to the corrected resistance yields the following parameters: (i) the y-intercept $=2R_c$ where R_C is the total contact resistance, then $R_C=217.7\Omega$ and (ii) x-intercept yields $L_x=2L_T$ then, L_T is found to be $7.8\ \mu m$, this transfer length is measured for Ohmic quality of metal contact. Typically, a shorter L_T means a better Ohmic contact. (iii) From the slope of the linear fitting the sheet resistance R_{sh} of the Cu_2O layer could be obtained where $\frac{\Delta R_c}{\Delta s} = \frac{R_{sh}}{2\pi r_1}$ the sheet resistance, R_{sh} is found to be

$$R_{sh} = \frac{\Delta R_c}{\Delta s}.(2\pi r_1) = (\ 22.23\ \Omega.\mu m^{-1}).(2\pi\ .200\ \mu m) = \ 2.792 \times 10^4 \Omega/\square$$

Using the unit convention ohms per square (Ω/□) to avoid confusion with volume resistance. Finally, (v) using the expression for the contact resistance ρ_c in terms of the sheet resistance R_{sh} and the transfer length L_T in Marlow's paper[157] to give:

$$\rho_c = R_{sh}.L_T^2 = (2.792 \times 10^4\ \Omega/\square).(7.8 \times 10^{-4} cm)^2 = 1.698 \times 10^{-2} \Omega.cm^2$$

This value of specific contact resistance is comparable with values in the range 10^{-2} to 10^{-4} Ω·cm^2 reported in the literature [152]. Details of additional methods explored to achieve Ohmic contacts are given in the Appendix A.

4.3 Electrical properties at low and intermediate temperatures:

With a fabrication process developed for the formation of reliable Ohmic contacts, in this section we aim to examine the electrical properties of Cu_2O at low and intermediate temperatures in an attempt to characterize the defects within the material. By 'low and intermediate temperatures' we refer to a temperature range where achieving thermodynamic equilibrium takes significantly shorter than the duration of the measurement, allowing us to assume that the defect concentration remains constant. Previously, we have mentioned that Cu_2O is inherently a p-type semiconductor. This will be consistently demonstrated through experiments involving the Hall effect for our crystals. Measurement techniques using the Hall effect may be used to understand the electrical properties and behaviours of Cu_2O and extract quantifiable parameters such as the majority carrier density, mobility, and the type of charge carriers (p-type or n-type). Additionally, sometimes it is also possible to gain further insight about the defects present in the material because the defects influence the electrical transport properties of the material, with this effect being observable in their electrical conductivity behaviour. In the following section we present the finding from Van der Pauw- Hall measurements over range of temperatures (between 300K and 95K) and using subsequent analysis these results will be directly connected to the electrical properties of Cu_2O and the material impurities.

4.3.1 Electrical Conductivity

The electrical conductivity of Cu_2O was measured using the Van der Pauw -Hall measurement in the absence of externally applied magnetic fields. This technique involves using four contacts where their dimensions and locations are related to the sample edge length, explained in detailed in section 3.3.2. The measurements were carried out in a cryogenic environment to maintain a stable and controlled temperature for the sample. Figure 4.5 shows a semi-log plot of the calculated electrical conductivity (σ) of a Cu_2O sample at zero externally applied magnetic field as a function of temperature between 300K and 95K. Below 95K the Ohmic contact has frozen out, becoming highly resistive and thus resulting in no current flow below this temperature for the appliable voltage range of the test instrumentation.

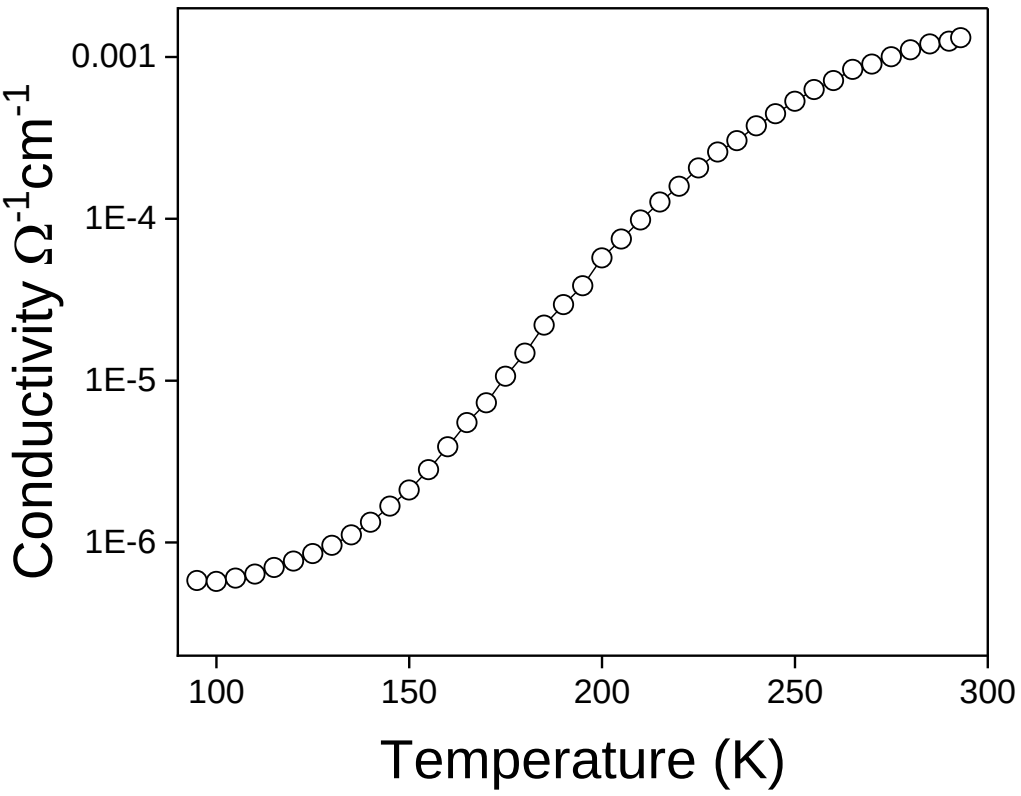

Figure 4.5: Measurement of conductivity in Cu_2O as a function of temperature.

Figure 4.5 shows that at low temperature the electrical conductivity is low, and increases with the rise of temperature, i.e., the temperature coefficient of resistance is negative and this is a characteristic of a bulk semiconductor [158],[159]. With the expectation that the relationship adheres to an Arrhenius-type response commonly associated with thermally activation process which relates to the conductivity and temperature as shown in Equation 4.4)) [158]

$$\sigma = \sigma_0 \exp \frac{-E_a}{K\,T} \qquad \Omega^{-1}\,cm^{-1} \tag{4.4}$$

where E_a is activation energy (eV), k=Boltzmann constant = 8.618×10^{-5} (eV/K) =1.38066×10^{-23} (J/K) and T= absolute temperature (K).

Replotting the electrical conductivity data from Figure 4.5 against $\frac{1000}{T}$ and fitting the curve carefully it is possible to identify two different temperature ranges associated with two different activation energies, as shown in Figure 4.6.

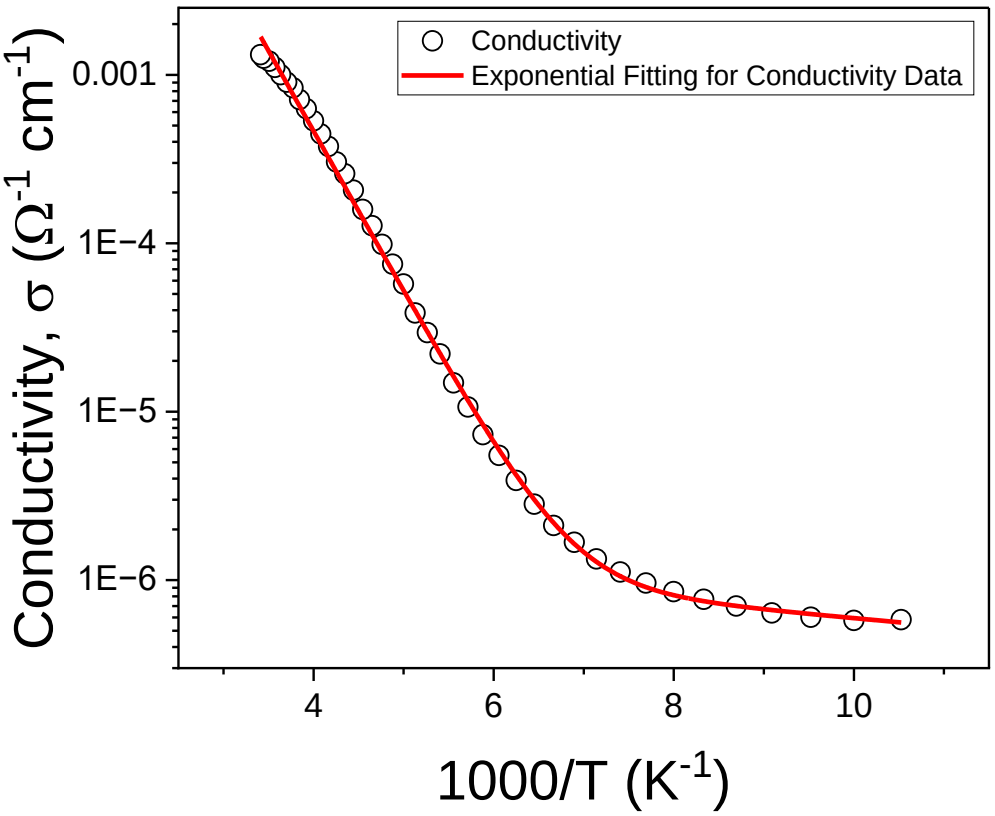

Figure 4.6: Arrhenius plot of Cu_2O single crystal conductivity with a two-region composite model fit. The distinct slopes correspond to different activation energies, implying varying conduction mechanisms.

Typically, where there is more than temperature range where a single activation energy clearly dominates, the activation energy can be extracted by fitting the Arrhenius equation (Equation 4.4)) over a selected temperature range only (where a semilog plot of σ against $\frac{1000}{T}$ is linear). However, whilst the temperature range to fit over for the higher temperatures is more obvious (approximately 4 to 6 on the 1000/T K^{-1} scale), it is less so for the low temperature regime. Therefore, to provide a robust, bias free, fit to the data a composite a dual-exponential composite model was created, Equation(

(*4.5*).

$$\sigma(T) = A\exp\left(\frac{-E_{a1}}{KT}\right) + B\exp(\frac{-E_{a2}}{KT}) \quad \Omega^{-1}\,cm^{-1} \tag{4.5}$$

To obtain the fit shown in Figure 4.6 first each linear region (the initial estimation for the first region was from 140K to 95K and the second region was between 300K to 140K) were approximately fitted separately to determine the initial fitting values for the composite fit (for the pre-exponential factor A,B and activation energies (E_{a1} and E_{a2})), then using these initial estimates Equation (

(*4.5*) was fit across the entire temperature range. During this fit optimization stage, the program employs the Levenberg-Marquardt algorithm to optimize the parameters in our chosen nonlinear fitting model (exponential fitting) by minimizing the sum of squared residuals. Once this optimization is complete, these parameters are used to fit the data points. The goodness of fit is then evaluated using the R-squared value, which is approximately 0.98, indicating an excellent model-data correlation. By plugging the obtained values in to Equation

(*4.6*), we can have the activation energies in this temperature range;

$$\sigma(T) = 3.030\exp\left(\frac{-0.18}{KT}\right) + 1.82\exp(\frac{-0.09}{KT}) \;\; \Omega^{-1}\,cm^{-1} \tag{4.6}$$

The first activation energy, E_{a1}, dominates in the temperature range from 293K to 140K, as determined by fitting the composite model Equation

(*4.5*) to the Arrhenius plot shown in Figure 4.6. The calculated value of 0.2 eV corresponds to an acceptor state in Cu_2O that lies above the valence band by this energy. This state plays a significant role in the material's conductivity, as carriers must overcome this energy to participate in charge transport within this temperature range [63]. Additionally, the second

activation energy E_{a2} derived from the same composite equation found to be 0.09 to 0.1 eV in the temperature range of 95K to 140K. This suggests the presence of another acceptor state lying just above the valence band contributing to the conductivity [160].

These two distinct activation energy values indicate the presence of two different conduction mechanisms, as evidenced by the observed two-stage temperature dependence of conductance (σ). This finding significantly contributes to a deeper understanding of acceptor states, specifically sub-band states within the bandgap.

4.3.2 Hall Effect measurements:

Using the same Cu_2O sample measured to extract the electrical conductivity in section 4.3.1 but applying an external magnetic field, the sample can be measured in a Van der Pauw Hall Effect configuration (described in section 3.3.2). The Hall voltage (V_H) as a function of magnetic field (B) and thus temperature (T) can therefore be measured (methodology described in section 3.3.2).

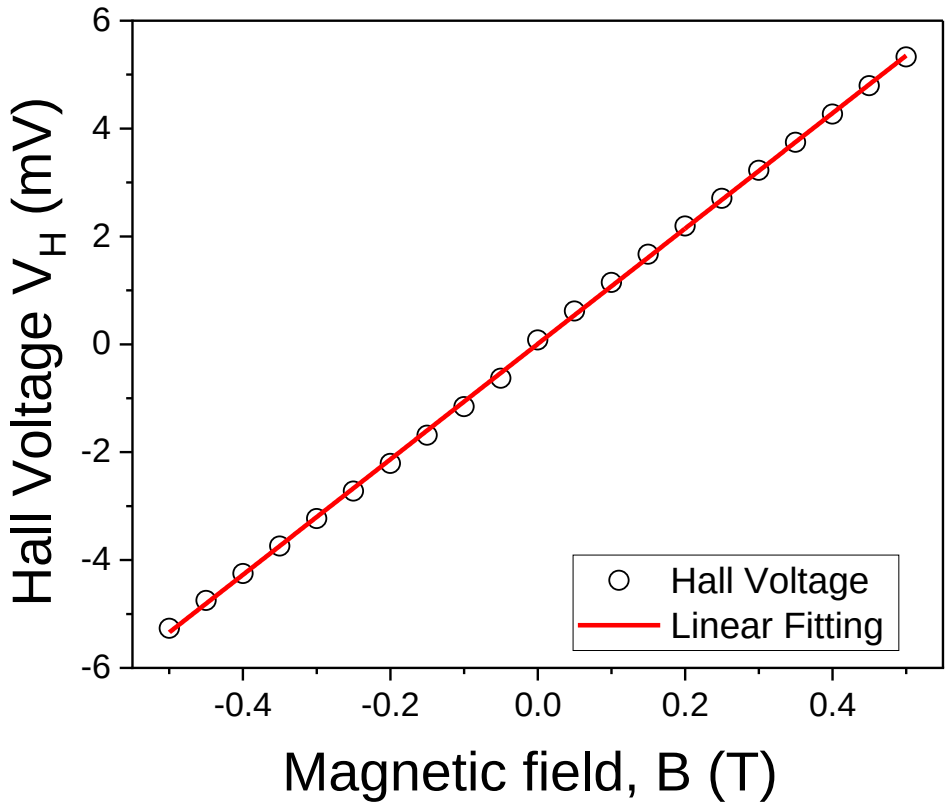

Figure 4.7: Hall voltage (V) versus magnetic field (B). The linearity indicates a single majority carrier with uniform mobility, suitable for basic Hall effect analysis. A positive Hall coefficient confirms holes as the majority carriers.

In Figure 4.7, the Hall voltage (V_H) is plotted as a function of the magnetic field (B). The data points show a clear linear relationship, with the voltage increasing as the magnetic field increases. This linearity indicates the presence of a single majority carrier (i.e., holes or electrons) with uniform mobility, which is typical in bulk semiconductor materials. The positive slope of this linear fit indicates a positive Hall coefficient, which confirms that the majority charge carriers in the material are holes. This result is consistent with the expectation for p-type semiconductors, where holes dominate the charge transport [161].

Hall measurements are an important tool to characterize the electrical properties of the material, especially in semiconductors where the measured majority carrier concentration (p) and mobility which can vary with temperature. Figure 4.8 show the measured hole

carrier concentration and calculated mobility between 300K and 95K. As shown in this figure, mobility steadily decreases as temperature increases, while hole carrier concentration gradually rises. This inverse relationship is typical of semiconductors: increasing temperature causes thermal excitation of electrons, leading to higher carrier concentration, whilst mobility decreases due to enhanced scattering mechanisms. This mobility trend is consistent with the pioneering work of Shimada and Masumi, who observed similar behaviour in their studies of monocrystalline Cu_2O[68].

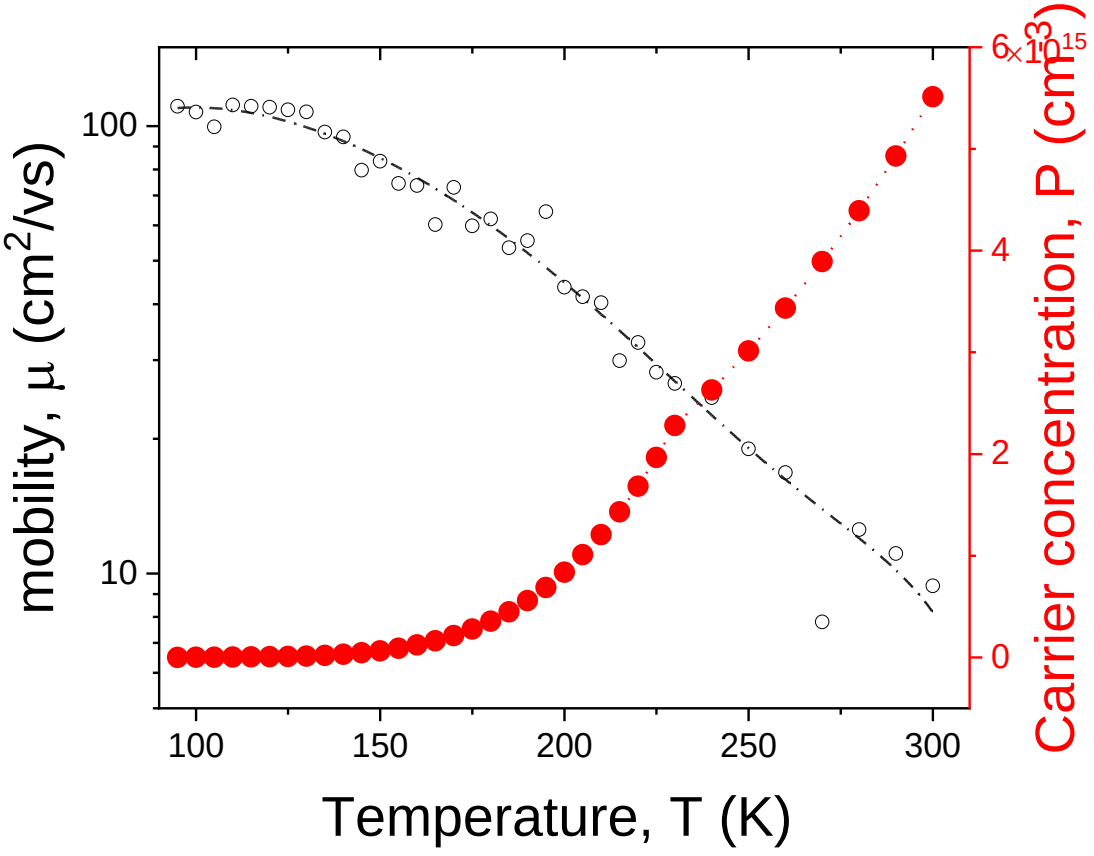

Figure 4.8: Temperature Dependence of Mobility and Carrier Concentration in Cu2O: as the temperature increases, mobility (μ) shows a decreasing trend, while carrier concentration (P) increases, indicating a typical semiconductor behaviour.

The temperature dependence of the hole concentration (P) can be fitted with an analytical expression considering two states with two activation energies, based on the information from the conductivity measurement. [63], [162]

$$P = \frac{N_{A1}}{1 + \frac{\mathcal{G}_A P}{N_v\, e^{\frac{-E_{A1}}{KT}}}} + \frac{N_{A2}}{1 + \frac{\mathcal{G}_A P}{N_v\, e^{\frac{-E_{A2}}{KT}}}} \qquad cm^{-3} \qquad 4.7)$$

Where $N_v = 2(\frac{2\pi m^* KT}{h})^{\frac{3}{2}}$ is the effective density of valence band states, N_{A1} and N_{A2} are the concentrations of two acceptors, m* is the hole effective mass of equal to $0.58m_0$[20], h is the Planck's constant= 6.63×10^{-34} Js , $\mathcal{G}_A$ is the degeneracy factor (here assumed to be 1), and E_{A1} and E_{A2} are the activation energies of the two acceptor states.

To fit the measured data to Equation 4.7), the initial parameters used were the E_{A1} and E_{A2} that were found from the conductivity measurements (0.2 and 0.1 eV respectively). Iterated the values of N_{A1} and E_{A1} to fit the intermediate temperature region of the measured P_{Hall} vs 1000/T curve then iterated the values of N_{A2} and E_{A2} to fit the lower temperature region. The raw hole concentration data, final fit, and fit parameters to Equation (4.7) are shown in Figure 4.9. The extracted activation energies show two distinct carrier levels with activation energies E_{A1} and E_{A2} equal to 0.2 eV and 0.1 eV for our Cu_2O crystal. These activation energies are in the range of previously reported experimental values, between 0.16 eV and 0.42 eV[160], [163]–[165]. We also estimated the acceptors densities for both states from the same fit to be 1.463×10^{18} cm^{-3} and 4.160×10^{17} cm^{-3} respectively.

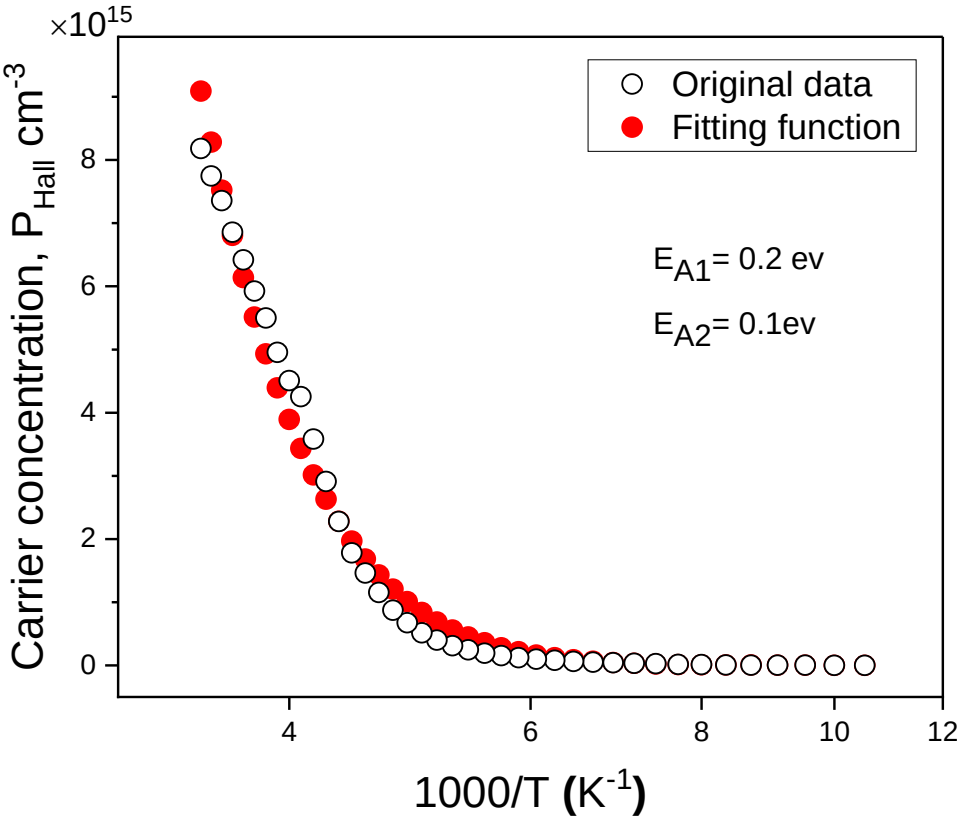

Figure 4.9: Temperature dependent carrier concentration (P vs 1000/T) of Cu_2O the red circle indicates the fit to Equation 4.7) using the parameter given.

As shown previously the measured Hall mobility, increases as the temperature decreases (see Figure 4.8). To further understand this behaviour, we have modelled theoretical mobility values from five different carrier scattering mechanisms using analytical equations; (1) ionized impurity scattering (μ_{ii}), (2) natural impurity scattering (μ_n), (3) acoustical phonon scattering (μ_{AP}) and (4,5) optical low and high photon scattering ($\mu_{OP,low}$, $\mu_{OP,high}$). For ionized impurity scattering the following model was used[166]:

$$\mu_{ii} = \frac{\left(\frac{8}{\pi}\right)\left(\sqrt{\frac{2}{\pi}}\right)\left(\frac{\varepsilon_0^2 \varepsilon_{Cu2O}^3 (KT)^{3/2}}{q^3\sqrt{m^*}}\right)}{N_i \ln\left[1+\left(\frac{3\varepsilon_0 \varepsilon_{Cu2O} KT}{q^2 N_i^{1/3}}\right)^2\right]} \quad cm^2/Vs \tag{4.8}$$

Where ε_0= permittivity of free space = 8.85418×10^{-12} (F/m), ε_{Cu2O}= relative dielectric constant of Cu_2O =7.11 [167], T= absolute temperature (K), N_i= ionized impurity concentration (cm^{-3})(=P), q=1.60218×10^{-19} (C). The dependence of ionized impurity scattering on temperature can be intuitively understood by considering that elevating the temperature increases the carrier thermal velocity. This reduces the time a carrier spends in the vicinity of the ionized impurity and hence its deflection when it passes the ion, which increases the mobility. The neutral impurity scattering was estimated using Ergionsoy's model: [168]

$$\mu_n = \frac{\pi^2 m^* q^3}{10\,\varepsilon_0 \varepsilon_{Cu2O} n_N h^3} \quad cm^2/Vs \tag{4.9}$$

Where n_N is the density of the neutral impurity. Since the acceptor ionization rate (p/N_A) is <10% for the Cu_2O based on the extracting value using Equation4.7) we assumed $n_N=N_A$. Note that the neutral impurity is temperature independent. Then we consider the longitudinal optical (LO) phonon scattering which was modelled by Shimada and Masumi. The Hall mobility of Cu_2O is limited such scattering as following: Longitudinal optical high-frequency phonon scattering [68]

$$\mu_{LO,high} = 268\left(e^{220/T} - 1\right) \quad cm^2/Vs \tag{4.10}$$

And Longitudinal optical (LO) low-frequency phonon scattering as [68]

$$\mu_{LO,high} = 102\left(e^{951/T} - 1\right) \quad cm^2/Vs \tag{4.11}$$

Finally, we considered the acoustical phonon scattering by using the following formula: [68]

$$\mu_{AP} = 1.6 \times 10^8 T^{-3/2} E_I^{-2} \quad cm^2/Vs \tag{4.12}$$

Where E_I is the deformation potential of the valence band = 2 eV.[169]

Each of the scattering models were calculated as a function of temperature and combined using Matthiessen's rule:

$$\frac{1}{\mu_{models}} = \frac{1}{\mu_{ii}} + \frac{1}{\mu_n} + \frac{1}{\mu_{OP}} + \frac{1}{\mu_{AP}} \tag{4.13}$$

A comparison of the theoretically calculated values and the experimentally obtained Hall measurement data are shown in Figure 4.10 for the Cu_2O single crystal. The comparison of the calculated and experimental data shows good agreement across the temperature range examined. We find that the dominate scattering mechanism is the optical phonon scattering and we also observe that since the acceptor concentration is relatively high (Figure 4.9) the

impact of ionized impurity scattering and neutral impurity scattering (from nonionized acceptor) on μ_{Hall} is not negligible, but have a small effect on carrier transport in these samples.

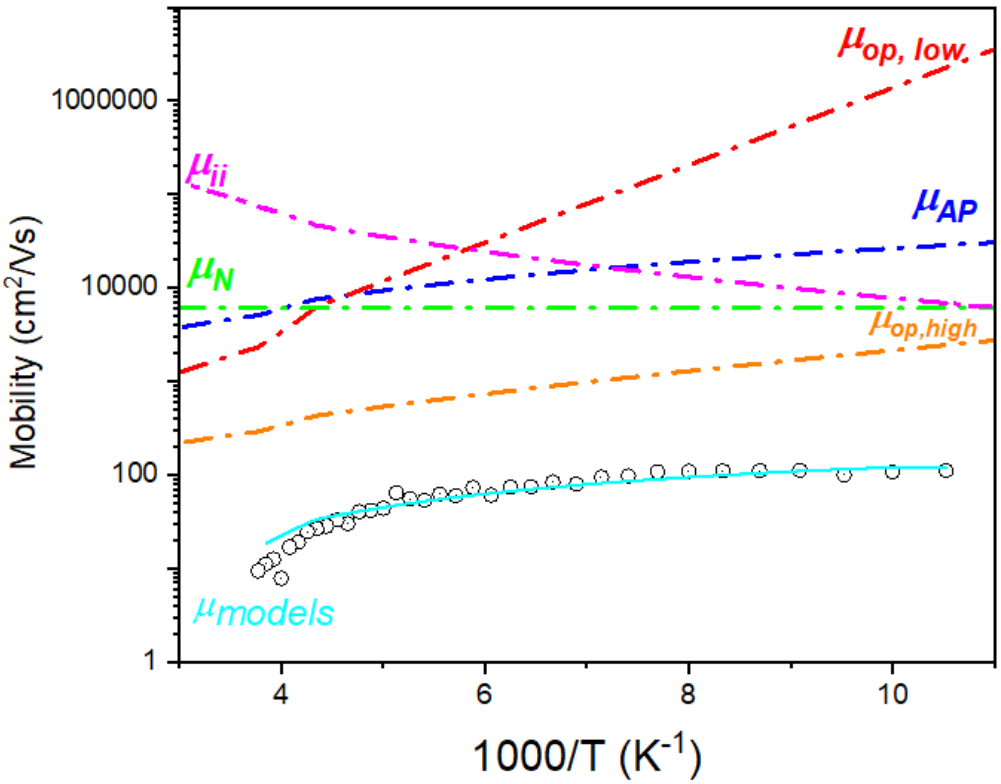

Figure 4.10: Temperature-dependent Hall mobility (μ_{Hall} vs 1000/T) for single-crystalline Cu_2O bulk substrate. Symbols indicate the experimental data, while lines represent the predicted mobility values due to ionized impurity scattering (ii), neutral impurity scattering (N), and optical phonon (OP) and acoustical phonon (AP) scattering as well as the total predicted mobility (models), as labelled.

4.4 Conclusion:

In this chapter, we successfully established and characterized an Ohmic contact between Cu_2O and Au using the CTLM configuration. This method stands out for its simplicity and efficiency in the fast and accurate determination of contact resistance, requiring only a single process step for implementation. The specific contact resistance derived from the

CTLM measurements was found to be $\rho_c = 1.698 \times 10^{-2}\ \Omega\ cm^2$, demonstrating the technique's effectiveness. More importantly this demonstrated that the Ohmic contact can be made to Cu_2O - which is important for make use of this material different applications. It has also allowed you to then be able to do the low temperature electrical properties measurements.

Furthermore, we experimentally investigated the hole transport and scattering mechanisms in Cu_2O single crystal using temperature-dependent Hall measurements in the Van der Pauw configuration. This study involved analysing conductivity, carrier concentrations, and Hall mobility of the carriers within Cu_2O over a temperature range from 95K to 293K. This temperature-dependent analysis was crucial in determining the activation energies, revealing two shallow acceptor levels: one at 0.2 eV and another at 0.1 eV, up to room temperature. We also showed that the Hall mobility was mainly limited by photon scattering and neutral impurity scattering.

Chapter 5 Enhancing Defect Spectral Signatures in Cuprous Oxide (Cu_2O) Single Crystal Bulk Material Using Photoconductive Laser Spectroscopy

5.1 Introduction

Recent theoretical studies have shown how defects in single crystal Cu_2O detrimentally affect some of the desirable optical properties, such as the ability to host high principal quantum number excitons [139]. The primary focus in this chapter is to explore how photoconductivity measurements can be harnessed to extract information about these defects. Atomic-scale defects in the perfect crystal lattice, from the inclusion of extrinsic impurities, or from vacancies (missing atoms at lattice sites) lead to localised states with sharp well-defined energy levels. If these levels lie within the bandgap, then they can leave optical signatures. Resonant absorption of a photon with energy matching the gap between the localised state and the conduction or valence band will change the charge-carrier population in one of the bands, which in turn will change the electrical conductivity. Thus, sweeping the wavelength of the light illuminating a sample should result in a measurable photocurrent signature when the light is resonant with the energy of the defect level.

Traditional photoconductive spectroscopy usually employs diffraction from a grating in a monochromator to achieve spectral filtering of a broadband light source. However, this wavelength filtering results in a weak photon flux at the desired wavelength, which limits the sensitivity of the measurement. We have improved on the traditional photoconductivity technique by using a pulsed wavelength-tunable nanosecond laser available in our laboratory as the light source. The laser increases the photon flux at the desired wavelength by several orders of magnitude, which in turn enhances the sensitivity of the photoconductivity measurement because the defect is now much more likely to interact with a photon.

The measurements presented in this chapter show the photo-response of a simple two-contact Cu2O device particularly in the wavelength range corresponding to below bandgap illumination, where the device would not normally be very sensitive to light. The main result is that we detected several sharp peaks at wavelengths longer than 800 nm, indicating sub-band gap energy levels (i.e. below 1.55 eV). These peaks suggest several defect states (some of which have not been previously observed).

The chapter is structured as follows: Section 5.1 describes the specific details of our improved laser photoconductive experiment. Section 5.2 describes the signal processing techniques used to deconvolve the photo response from the background. Section 5.3 describes the analysis of the extracted photoconductivity transient. In section 5.4 we explore the dependence on pulse energy, while in section 5.5 we explore the dependence on dependence on device bias. Sections 5.5 and 5.6 justify the assumptions used to normalise the photoconductivity response with respect to variations in laser intensity across the spectrum. In section 5.7 we describe attempts to improve the signal to noise ratio by employing improved electromagnetic shielding to reduce electrical pickup from the laser flash lamp discharge. In section 5.8 we discuss the deconvolved photoconductivity results. In section 5.9 we discuss the validity of our photoconductivity results in light of some additional XPS data recorded in Cardiff School of Chemistry. Section 5.10 concludes the chapter.

5.2 Laser Photoconductivity Experiment Details

As mentioned in the introduction, we aimed to improve on the traditional photoconductivity technique by employing a wavelength-tunable laser instead of the conventional spectrally filtered of a broadband light source, with the aim of increasing the photon flux and thereby enhancing the sensitivity. A schematic of the experimental setup used to investigate the photoconductive response of the two-contact Cu2O device to sub-bandgap laser excitation is shown in Figure 5.1.

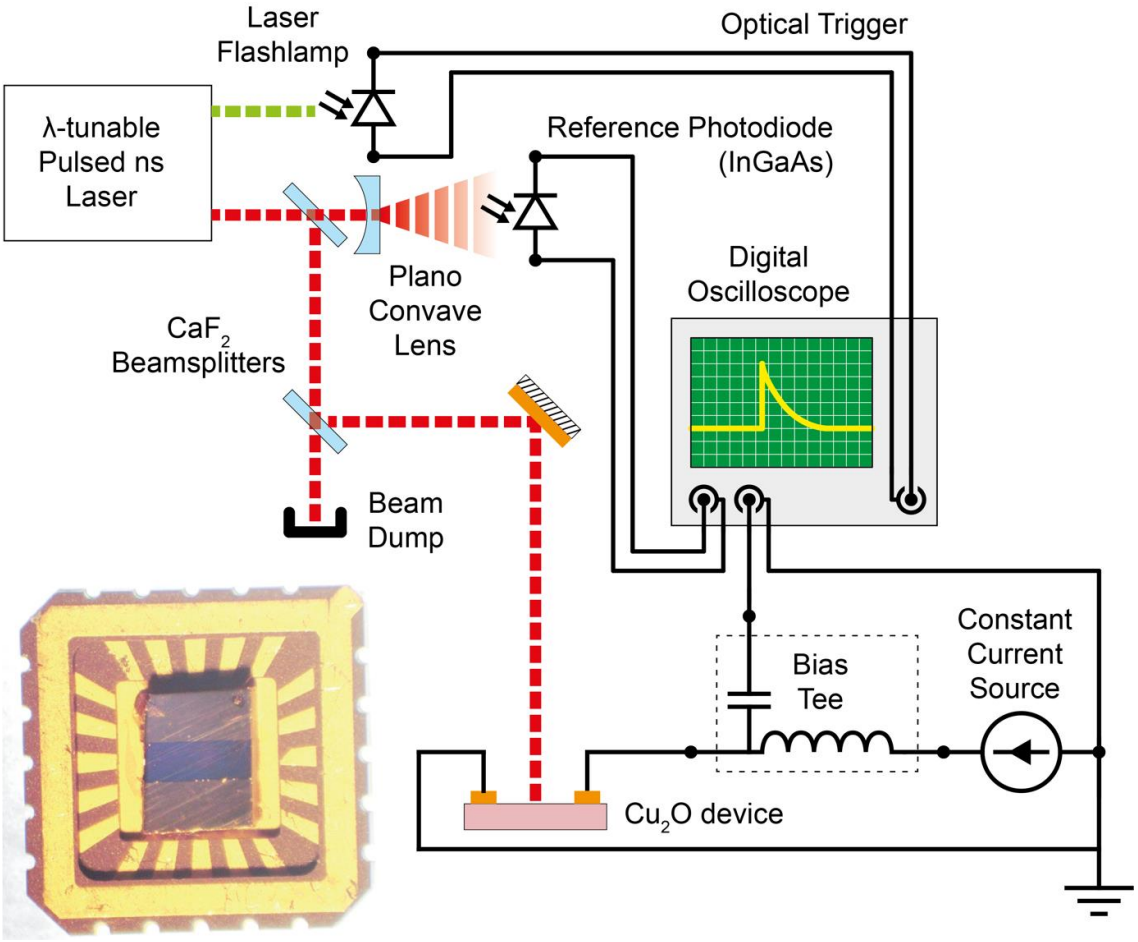

Figure 5.1: The laser output passes through two CaF_2 windows which act as beamsplitters to reduce the pulse energy. CaF_2 is used because it has a flat spectral response in this wavelength range. The main beam is incident on the Cu2O photoconductive device, while the less intense beam is directed onto the reference photodiode. A CaF_2 plano-concave lens is used to expand the beam to reduce the intensity on the reference photodiode. A second silicon photodiode close to the laser generates an optical trigger from the laser flash-lamp. The Cu_2O photoconductive device is biased by a constant current source. A bias tee is used to help stabilise the constant current source. The transient is coupled through the bias tee capacitor onto the oscilloscope. Inset: Photo of the Cu_2O photoconductive device.

The optical/infrared excitation is provided by a bespoke EKSPLA NT242B laser, which emits ns pulses with energies in the mJ range, at a repetition rate of 10 Hz, wavelength-tunable between 410-2600 nm. Beamsplitters were used to reduce the pulse energy and to direct light onto a reference InGaAs photodiode (Thorlabs DET10D2). A plano-convex lens placed before the reference photodiode was used to expand the beam to avoid saturation. The spectral response of the InGaAs reference detector meant that wavelength tuning was restricted to longer than 800 nm in this experiment. A silicon photodiode (Thorlabs

PDA100A) was used to generate an optical trigger from the flash-lamp. We took great care not to introduce additional spectral features by using CaF_2 for transmission optics and uncoated gold mirrors for reflection optics, which have flat spectral response in this region. Biasing of the sample was provided by a constant current source, and the voltage transient following laser excitation was recorded on a Tektronix DPO 3034 digital oscilloscope. We found that adding a bias tee to the circuit helped with the internal stabilisation of the constant current source.

To enhance the stability of the constant current source within the circuit, a high-frequency bias tee was integrated. A bias tee is a three-port network device designed to separate or combine DC and high-frequency signals in electronic circuits. It typically consists of an inductor and a capacitor: the inductor allows DC signals to pass while blocking high-frequency signals, and the capacitor allows high-frequency signals to pass while blocking DC signals. This dual-function design enables a bias tee to superimpose a DC bias onto a high-frequency RF signal or extract the two components for independent analysis.

In the context of this work, the bias tee was critical for separating the constant DC bias applied to the sample from the high-frequency transient signals generated after laser excitation. This separation ensures that the high-frequency signals, which carry the photoconductivity response, are transmitted to the oscilloscope without distortion or interference from the DC bias. Additionally, the bias tee acted as a low-pass filter to enhance the stability of the constant current source, minimizing noise and improving the accuracy of the measurements.

5.3 Signal Processing: Extracting the Photoconductivity

The oscilloscope trace showing the raw recorded signal is shown in Figure 5.2

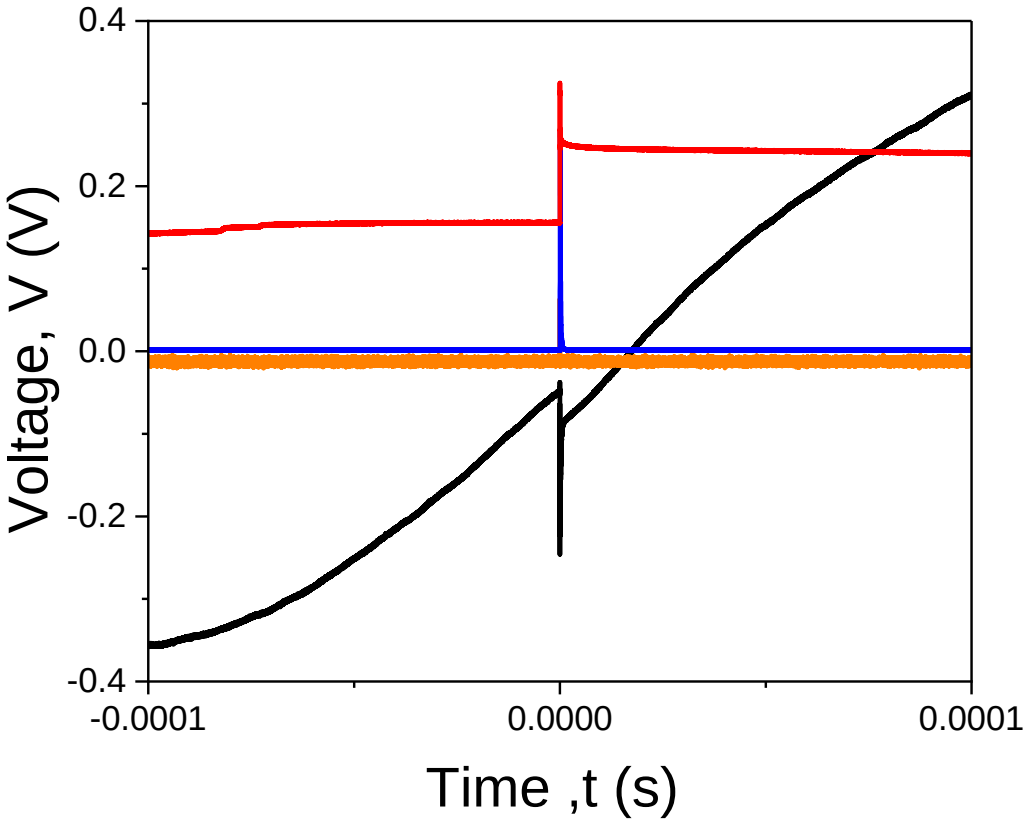

Figure 5.2: Digital oscilloscope display showing device transient photoresponse in red biased at 5mA. The reference photodiode photoresponse is in blue for InGaAs and in orange for Si (both look like delta functions on this timescale). Shown in black is the trigger photodiode response (which records the 2nd harmonic 532 nm green light generated from the 1064 nm YAG fundamental (sharp decay) superimposed on top of the flash lamp).

This raw signal appears to have a significant amount of background noise and electrical pick up, making it challenging to analyse and interpret accurately. This background can come from a variety of sources including the flash lamp which is used to pump the laser as it is optically pumped, electronic interference, thermal fluctuations, and other environment factors which interfere with the true signal. To address this problem, we optimized the oscilloscope (Tektroknix^{TM} DPO 3034) settings and deconvolved the electrical pick up numerically. The averaging function of the oscilloscope was applied where the signal from 256 acquisitions was averaged on the oscilloscope. The signal therefore represents a more accurate depiction of the signal as demonstrated by a smooth and more defined

appearance. In addition to this the oscilloscope is equipped with additional noise reduction techniques in form of digital filter. This type of filter is designed to alter the spectral characteristic of a signal, by attenuating certain frequency components allowing frequencies to pass through. In this case a low pass filter attenuate frequencies above a certain cut off, allowing only lower frequency components to pass through. In this experiment the input bandwidth limit act as an analogue low-pass filter, having several bandwidths to choose from. It is noticed that at 20 MHz the noise is substantially reduced.

Dealing with the device response as recorded shown in Figure 5.3a. This shows a typical "electrical ringdown" recorded at 1400 nm and a bias of 5 mA, which appears like a sinusoid with a decaying envelope. However, the device transient photoresponse signal (shown in the box) is not clearly distinguishable due to larger time scale displayed. Once the time scale is expanded its response becomes more visible.

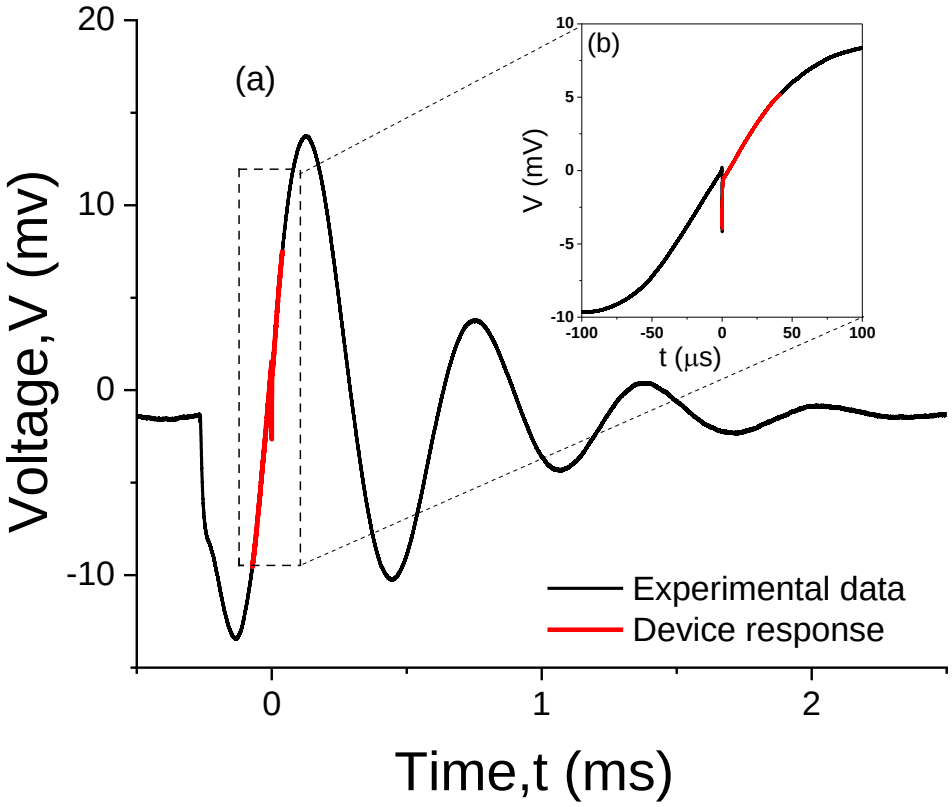

Figure 5.3: Photoresponse time trace at 1400 nm biased at 5mA (a) as recorded, and (b) with an expanded scale showcasing the device's transient photoresponse, differentiating responses sharp and relaxing.

Figure 5.3b displays the dynamics of the transient photoconductive signal of the Cu_2O after exposed to the ns pulsed laser. Initially, the device exhibits a sharp and immediate decay in voltage, followed by a relaxation phase (in red), leading to a slower photoresponse. Also, there is an offset noted in the graph where the oscilloscope trace starts to below the zero line. Correction of the baseline offset is essential for understanding the dynamic optical process within the Cu_2O.

We planned to deconvolve the device response from this consistent background (the electrical pick up) by subtraction of the response of the system when there is no light (the dark response) by its response after illumination. Unfortunately, because this is an active device, the excitation light generates charge carriers which changes the device impedance. The change in impedance results in a small amplitude change and phase shift, as shown Figure 5.4.

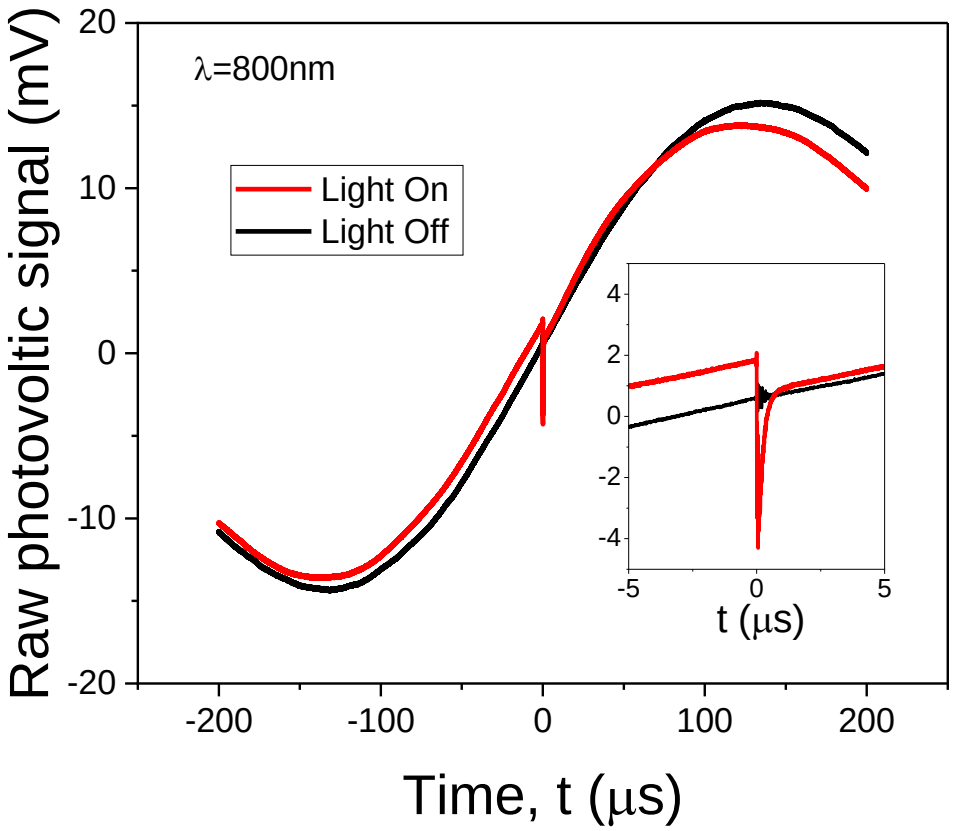

Figure 5.4: Comparing the electrical pickup with, and without, the excitation light blocked. Note the electrical "ringdown" in the main figure. The inset zooms in on the photoconductivity transient. The ringdown was present both with and without the light blocked. However, the inset demonstrates that a simple subtraction would not remove the ringdown because the frequency has change and the phase has shifted.

This forced us to implement a numerical method to simulate the background. Normally, software such as Origin Lab is used to estimate background levels based on a subset of points defined by the user. However, this approach is not very effective because it is both inaccurate and selecting the right points can be challenging, time-consuming and more importantly it could introduce error and human bias. This becomes especially problematic when dealing with large numbers of transient traces. Therefore, we had to numerically estimate this background noise from the data in post-processing. Then subtracting the estimation of background from raw spectrum led to a more interpretable signal, allowing determine peak wavelength and measure the amplitude of peaks more accurately.

As seen Figure 5.4, the shape of the electrical pickup trace suggested the simplest fitting function would be a cubic curve. A cubic polynomial model was then fitted using the least squares method, and the accuracy was confirmed through residual analysis. By doing so we could identify and characterize the meaningful spectral features of the device response. It was observed that while the majority of electrical pickup signals were smooth, occasionally (< 5% of measurements) triggering problems caused a phase jump which manifested as a wobble on the curve when the oscilloscope calculated the average. An example of this and how to treat statistically are shown in the Appendix C.

Our method seeks to align a cubic fit closely with the baseline of the device trace to remove any distortion accurately. This involves modelling the curvature of the background around the area of interest as follows:

$$V_i = \beta_0 + \beta_1 t_i + \beta_2 t_i^2 + \beta_3 t_i^3, \tag{5.1}$$

Where V_i is the measured voltage, t_i represents time, and $\beta_0, \beta_1, \beta_2 \; and \; \beta_3$ are the coefficients to be estimated. To find these coefficients we used initial estimation values to solve this equation. Subsequently, we apply a cubic fit around the area of interest, indicated by the magenta colour (see Figure 5.5). Subtracting this fit from the raw data effectively removes the baseline. The resulting timescale trace is then clean, facilitating easy identification and analysis, as shown in Figure 5.6**.**

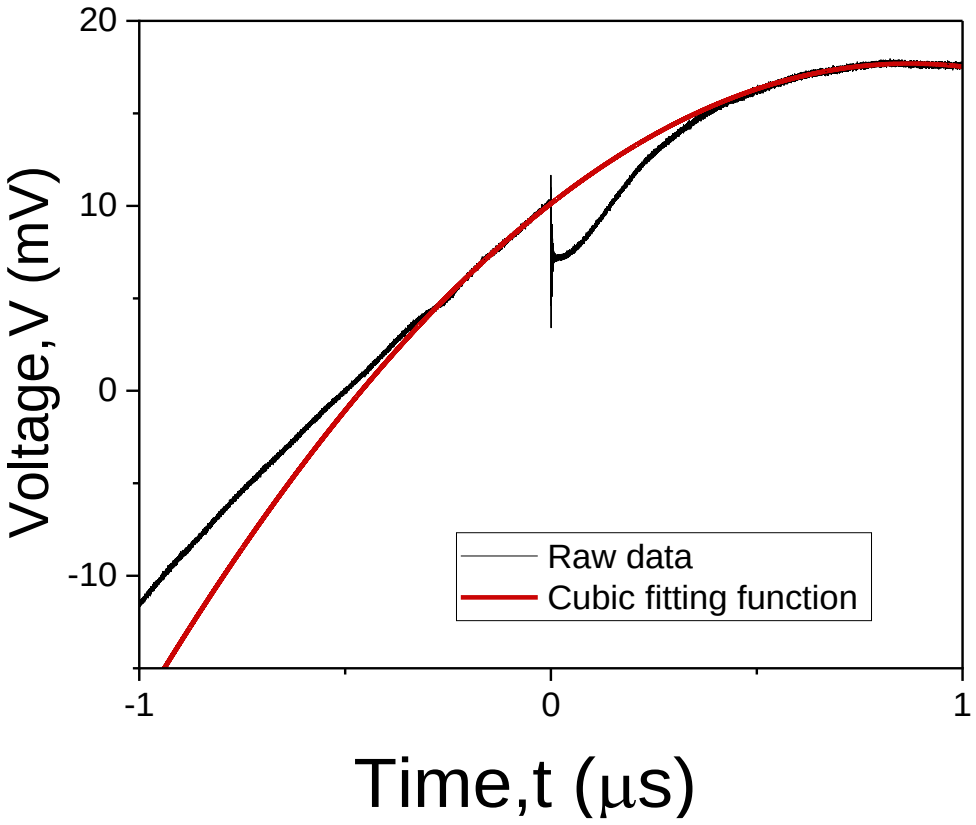

Figure 5.5: Background correction of time trace using cubic polynomial Fitting. This graph shows the raw data trace (black), The overlaid cubic function (red) demonstrates the fitting process, aimed at closely matching and removing the baseline offset to deconvolve the underlying signal.

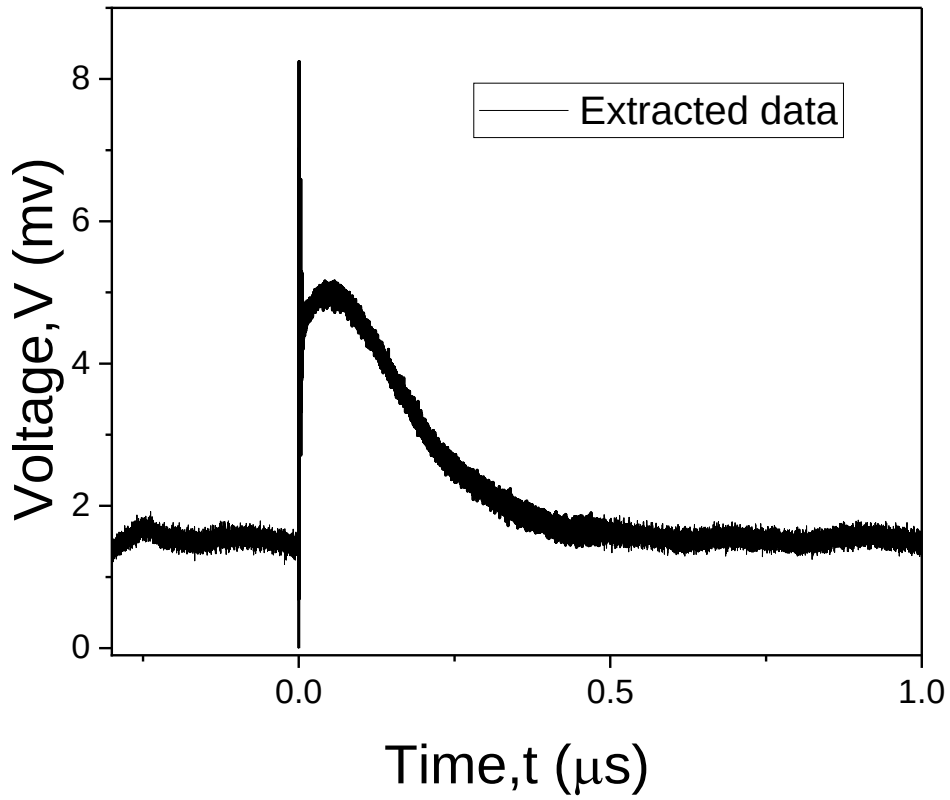

Figure 5.6: Deconvolved photoconductivity signal with cubic background fit subtracted.

In computing the spectrum, we also need to take account of pulse-to-pulse intensity variations, which is accounted for by recording a simultaneous time trace with the monitor photodiode. First, we need to correct the reference photodiode responses DC offset, which is achieved by subtracting (or adding) the average DC background away from the centre (generating a one-point offset). This process is shown in Figure 5.7.

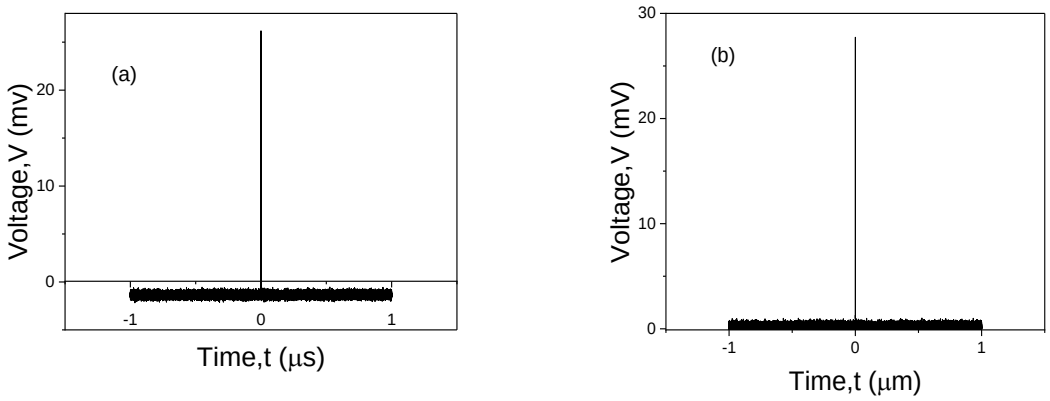

Figure 5.7: Photodiode transient photoresponse at 1400 nm: (a) the initial transient photoresponse with a baseline offset, (b) the transient photoresponse after applying a one-point baseline offset correction, resulting in a stabilized and normalized signal.

5.4 Analysis of the Photoconductivity Transients

The extracted photoconductivity transients for each laser wavelength were subsequently analysed. Each time trace had several things in common regardless of laser excitation wavelength. The photoconductive transient has two different decay mechanism with deferent time scales. Initially, there is a fast rise in the signal, limited by the instrumentation, that coincides with the laser excitation pulse. Following this, the photoconductive transient decays with two distinct components that occur at different timescales. The faster component exhibits high-frequency oscillations (ringing) superimposed on the decaying signal. Notably, this ringing persisted even when the light was blocked, as shown in the inset in Figure 5.4.

After several hundred nanoseconds, the fast decay levels off, as seen in the inset of Figure 5.8(b), before a further slow decay over tens of microseconds. We have applied simple exponential fits to these decays to estimate the lifetimes. However, we emphasize that these fits are not based on a specific physical model and are intended only to provide an approximate timescale for the decay process.

These two components exhibit significantly different spectral behaviours and, as such, should be analysed separately. To better understand the spectral behaviours of these components. we integrated the area under each transient response curve over time for one sweep. This integration was done as follow:

$$I_n = \Delta t \sum_{i=0}^{n} V_i \quad 5.2)$$

I = the integrated wave form Δt = time step $V =$ voltage $i =$ data point index. For the fast component the baseline was calculated by fitting the data with an exponential curve that included an offset, as shown in the inset of Figure 5.8(b). Essentially, this approach helps in separating the contribution of the fast component from that of the slow component for analysis or quantification purposes.

Then, extending this process to multiple wavelengths sweeps and averaging them out, the data was compiled and plotted as a function of wavelength. Each sweep captures the photoresponse across the given light wavelengths. To ensure accuracy and reduce the impact of noise or variations in individual sweeps, the results are averaged (see Appendix C for this). This approach allows for a clearer analysis of the distinct characteristics of the fast and slow decay phases within the photoconductive response.

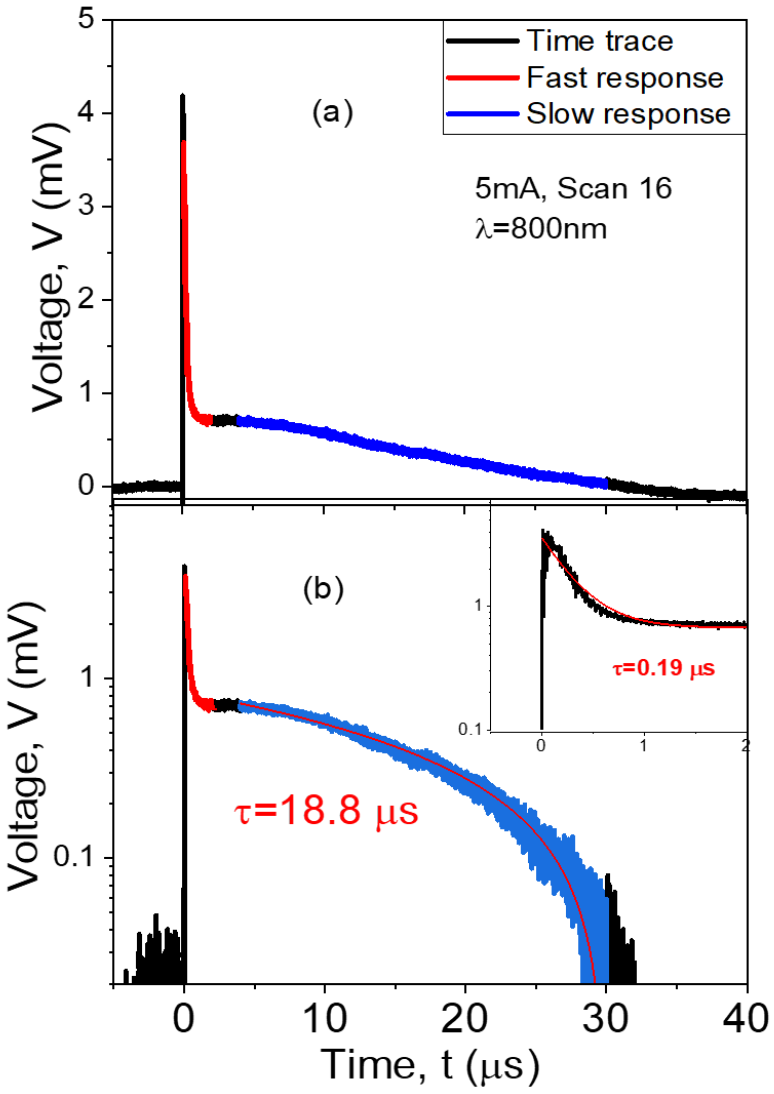

Figure 5.8: (a) Transient response of the Cu_2O photoconductive device to ns laser pulses with λ = 800 nm light after numerical deconvolution from the background electrical ring-down signal. (b) The same data on a semilogarithmic plot showing single exponential fits of the two decay components of the transient. The main plot highlights the slow component while the inset focuses on the fast component. Note that in both cases the polarity of the change in signal has been inverted to accommodate the logarithmic scale. The peak represents a relative increase in the photoconductive current (corresponding to a decrease in the two-terminal resistance) before re- turning to the nominal baseline value (zero).

Two averaged decay responses were then plotted across all wavelengths between 800nm and 1500nm to create the photoresponse spectra. The obtained fast and slow spectra are shown in Figure 5.9 these spectra unprocessed, display noticeable differences in their peak wavelengths, intensities, and overall shapes. Such variations underscore the necessity of

normalizing the spectra to facilitate fair and precise comparisons. Normalization is designed to adjust the spectra, accommodating the fluctuation in laser intensity, and distinguishing the device's response from environmental effects. This process ensures that observed discrepancies are not merely due to these variances, thereby enabling a more dependable analysis and interpretation of the data.

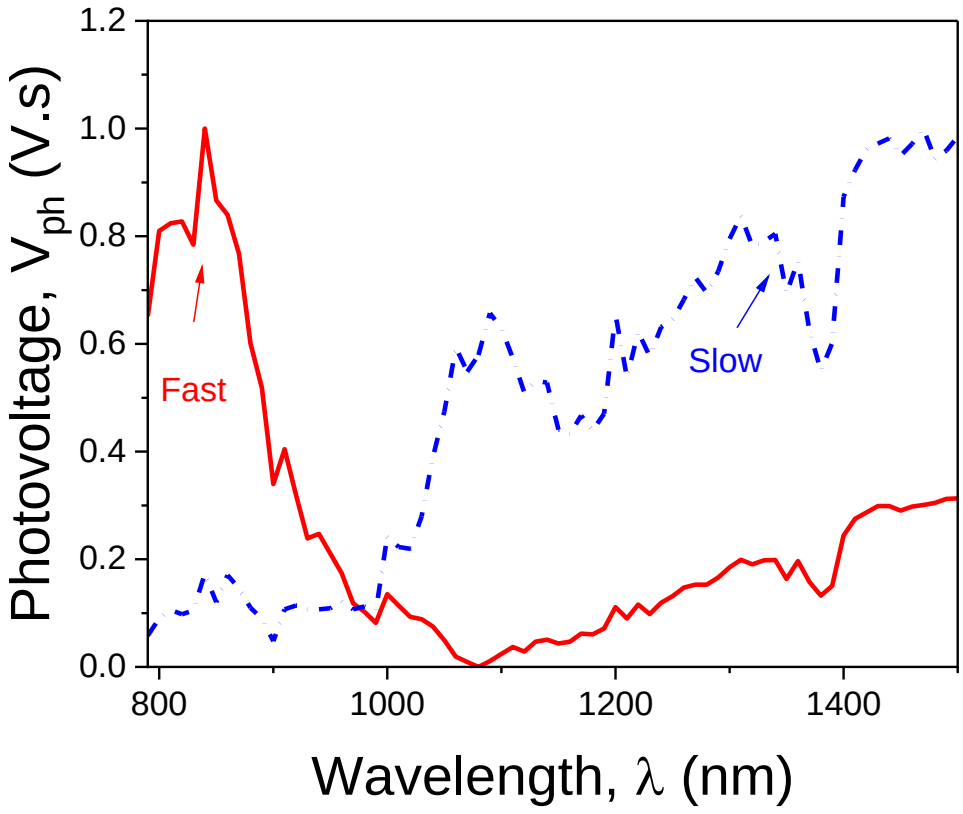

Figure 5.9: Normalized unprocessed spectra obtained by integrating the transient photoresponse for fast (red) and slow (blue dashed) responses across all wavelengths from 800nm to 1500nm.

5.5 Laser Pulse Energy Dependence

Some sanity checks needed to be performed prior doing the normalization step. Initially, a critical measurement of pulse energy dependence was conducted to establish a foundational understanding before proceeding with further analysis. The investigation focused on the photocurrent (I_{ph}) response under varying incident pulse energy (P) levels.

The magnitude of I_{ph} exhibits a dependence on the incident pulse energy P following a power-law relationship, expressed as:

$$I_{ph} \propto P^{\gamma} \quad (5.3)$$

Where γ represents the power-law exponent and P pulse energy of the laser. This relationship is crucial for understanding the behaviour of charge carriers—electron-hole pairs—generated upon absorption of photons with appropriate energy by the semiconductor material [170].

During this measurement, the Cu_2O device was subjected to light intensities adjusted through a set of neutral density filters with optical densities (OD) of 0.2, 1.0, 2.0, 3.0, and 4.0, corresponding to transmission percentages of 62%, 23.8%, 13.8%, 4.64%, and 1.84%, respectively, at a wavelength of 840 nm. The relationship between photocurrent and light intensity for both responses fast and slow photoresponse were thereby quantified, revealing a linear increase in photocurrent with enhanced light intensity[8], as depicted in Figure 5.10.

The observed linear relationship (i.e. γ = 1) between photocurrent and incident power suggests efficient electron-hole pair generation and separation within the Cu_2O device, aligning with the ideal scenario where (γ) approaches unity. The linear relationship helps in validating the device response as the photocurrent is solely determined by the photogeneration of electron-hole pairs. If this deviates from linearity it could suggest issues such as nonlinearity process, non-uniform illumination, or other mechanisms at play that could distort the analysis [171].

[8] We emphasize that the attenuation of these filters was checked and confirmed to be consistent across the wavelength range of interest (800 nm - 1500 nm). This relationship was examined at different wavelengths (840 nm, 930 nm, and 1500 nm).

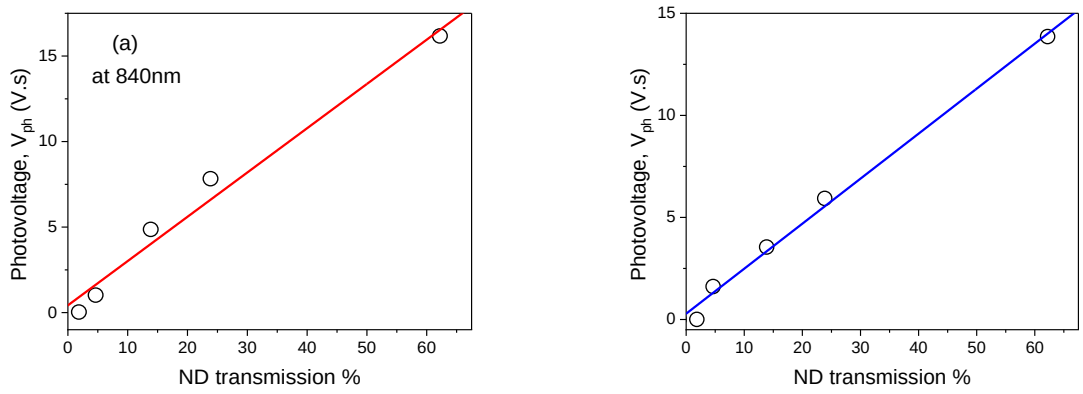

Figure 5.10: Linear correlation between light intensity and photocurrent in a Cu_2O device across optical densities. Utilizing different neutral density filters the device's photocurrent was assessed and 840nm wavelengths (a) fast response (b) slow response. The plot reveals a direct proportionality of the photocurrent to light power, consistent with an increased rate of photon absorption and carrier excitation within the semiconductor's band structure.

5.6 Bias Dependence of Photoresponse

The second dependency that needs to be checked is the relationship between the photoresponse and the applied biased voltage that was measured at 1500nm at the same laser pulse energy. The result is illustrated in Figure 5.11 for both the fast and slow photoresponse. Generally, at these biasing values from 0.5 to 7.0 mA the device follows the theoretical trend i.e., increasing the device bias leads to a linear increase in photoresponse. Hence the device could be biased safely up to 7 mA without becoming saturated. Knowing the saturated limit allows for accurate characterization of device's behaviour and avoiding the saturated regime where the thermal affect is pronounced which could lead to high power dissipation which in turn affects the reliability of the measurement [172].

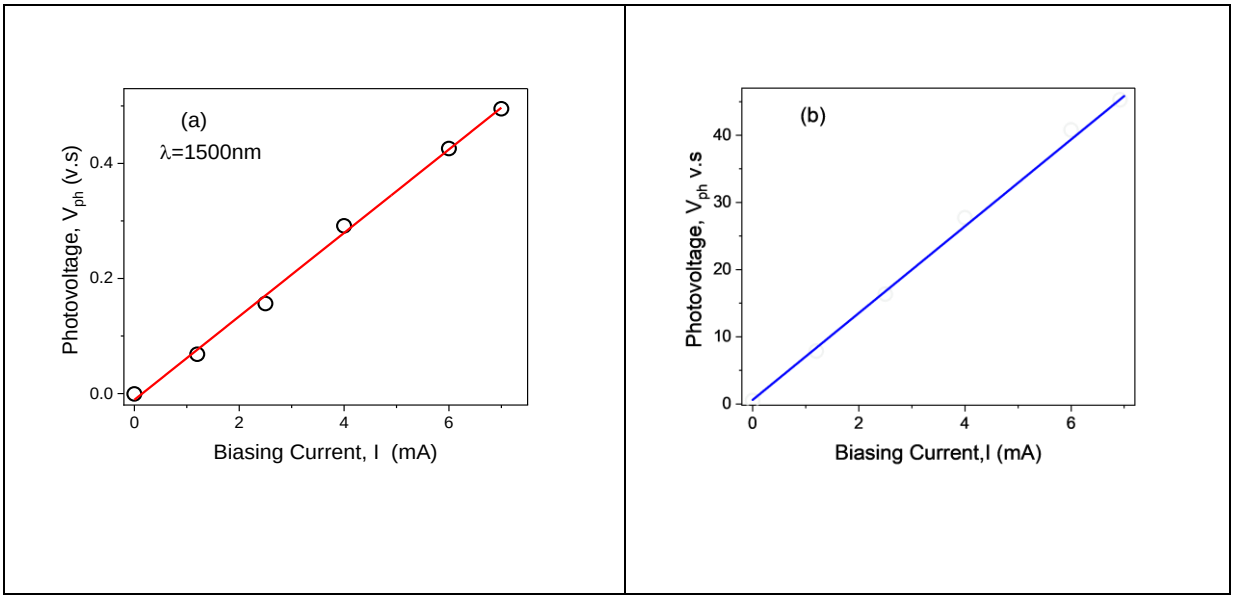

Figure 5.11: Photoresponse as a function of device biasing at a fixed light pulse energy: (a) fast response; (b) slow response. The sensitivity shows a strong linear dependence up to 7 mA.

5.7 Calibrated Spectral Photoconductivity Response

The previous section conclusively demonstrated that both pulse energy and applied current exhibit linear behaviour. Leveraging this discovery, we can now normalize the device's measured photoresponse by using an InGaAs photodiode as a reference diode incorporating into the experiment setup (see section 3.4). The initial step involved acquiring calibrated responsivity data for the DET10D2 InGaAs photodiode from the manufacturer (Thorlabs). After obtaining the calibration data, the reference photodiode's response was measured by integrating its photoresponse over the relevant area. The calibration factor was then calculated by dividing the integrated photodiode response by its corresponding responsivity values. Simultaneously, the photoresponse of the Cu_2O sample was recorded alongside the photodiode response. To derive the calibrated photoresponse of the Cu_2O sample, the measured sample response was divided by the calibration factor. The normalized fast and slow photoconductivity spectrum for the Cu_2O single crystal at the bias of (2.5, 5 and 7 mA) is shown in Figure 5.12.

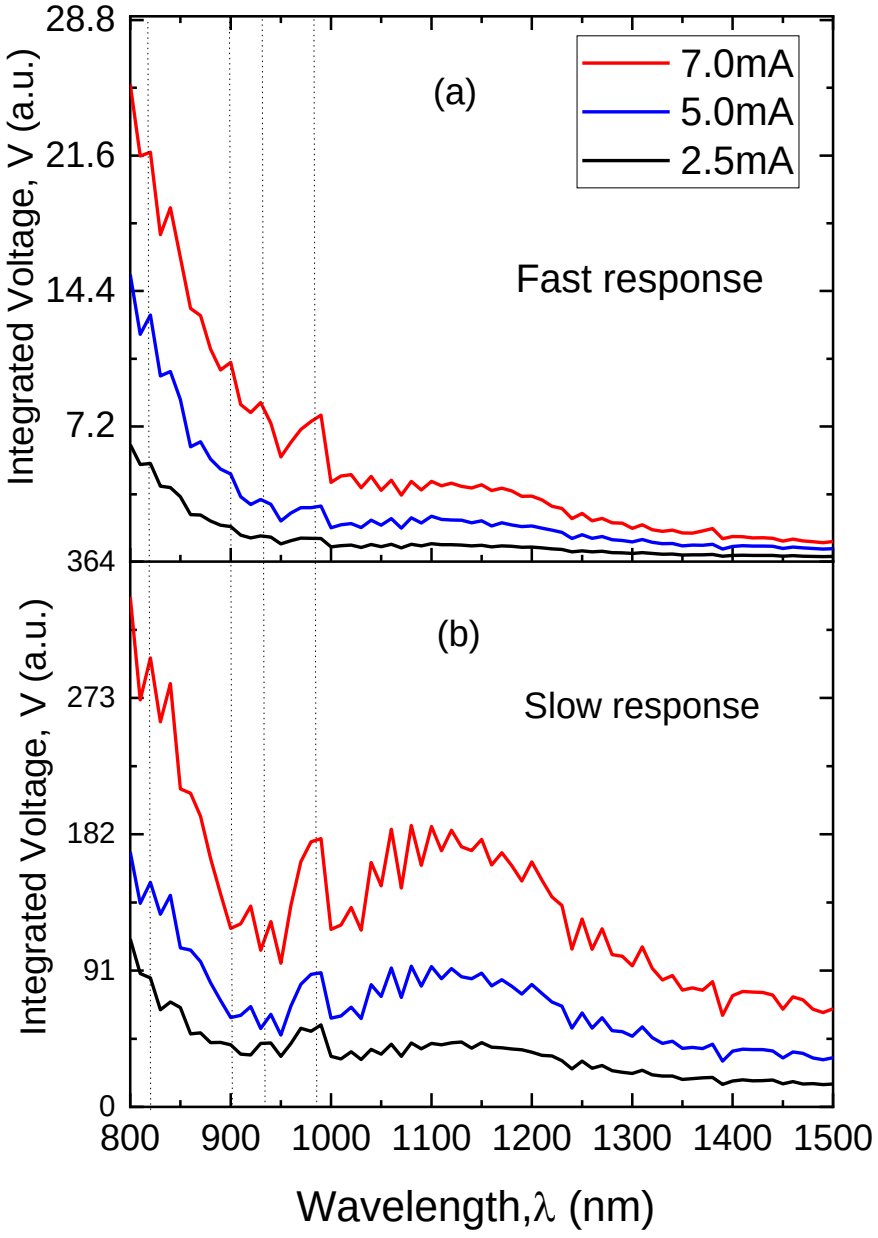

Figure 5.12: (a) Spectral behaviour of the fast photoconductive transient component for three different bias conditions (2.5,5.0, and 7.0 mA). Laser fluctuations at each wavelength were considered by dividing by the reference photodiode signal. The curves represent the average of around 20 wavelength scans in each case. (b) Spectral behaviour of the slow photoconductive transient component under the same conditions.

The data presented is the cumulative average of between 20-25 sweeps across wavelength between 800 and 1500nm (the number of sweeps was consistent for one bias but varied for

different biases). The whole set of data with their averaging as well as the result spectra of the visible region are presented in the Appendix B.

The fast response component is significantly more pronounced at shorter wavelengths and its intensity decays rapidly between 800-1000nm, diminishing before reaching 1500 nm. Conversely, the intensity of the slower-response component initially shows the same response as the fast response at short wavelength before gradually growing stronger again at longer excitation wavelengths.

Notably, in two responses their shape offers important information about presence of the defect states in the sub-band region. The photoresponse starts to build up somewhere below 1000 nm. The increase continues monotonically which moves toward the near band edge region (in the visible region). This tail response is absent in conventional spectral techniques. This type of photoresponse below the bandgap in semiconductor can be interpreted using the model for the defect/impurity density of states distribution in semiconductor bandgap suggested by Qiu et al [173].

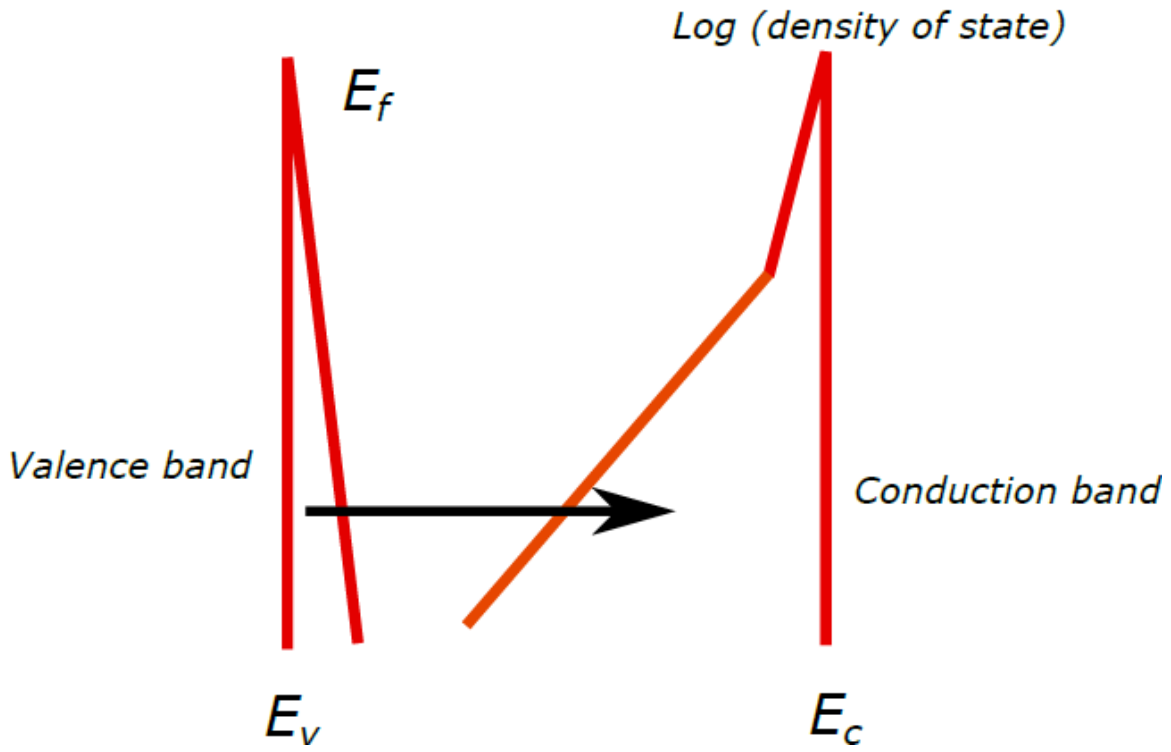

Figure 5.13: Schematic distribution of states available for optical transitions in P-type. The states between Ec and Ev are assumed to be localized states. The arrow represents schematically an optical transition for sub-band gap light absorption (from Qiu et al.) [173].

This model describes the presence of a deep gradual tail within the bandgap as follows, in P-type semiconductors the Fermi level in thermal equilibrium at room temperature is near the valence band edge, E_v. In these materials, the primary optical transition responsible for sub-bandgap optical absorption below the band gap occurs from the valence band to the conduction band tail. The observed photoconductivity tail can be attributed to the conduction band tail. (See Figure 5.13)

In addition to the spectrum shape there are hints of resonant peaks in the photoconductivity spectra Figure 5.12 that appear to correspond to the energies of known defects in this material, but the signal to noise ratio is not strong enough to be definitive.

5.8 Improvements from Enhanced Electromagnetic Shielding

One of the major issues with this measurement was the relative magnitude of the photoconductivity signal relative to the magnitude of the background electrical ringdown pickup. The laser is flashlamp pumped, and the electrical discharge from the capacitor bank created an electrical impulse that is easily picked up. A metal box (with external grounding) was designed and additional BNC cabling was introduced throughout to enhance the shielding in the hope of preventing this pickup. The metal box did significantly improve the signal, but we were unable to completely supress this electrical ringdown pickup.

The device transient response before and after shielding is shown in Figure 5.14. As shown prior to including the box (the black time trace), a high level of noise (electrical interference) and less clarity in the devices response's is pronounced. However, the red transient photoresponse shows enhancing in the device photoresponse as a result of reducing the electrical interference and noise which allows observing the true behaviour of the device.

We ran the same experiment as before; three curves were recorded at three different bias current (1.5, 3.0 and 5.0mA) and averaged over 20 wavelength sweeps. By applying the same analytical process as before to obtain the fast and slow photoresponse of the device,

and then normalizing this with the reference photodiode, we obtained the spectral behaviour of the fast and slow photoconductive responses, as shown in Figure 5.15

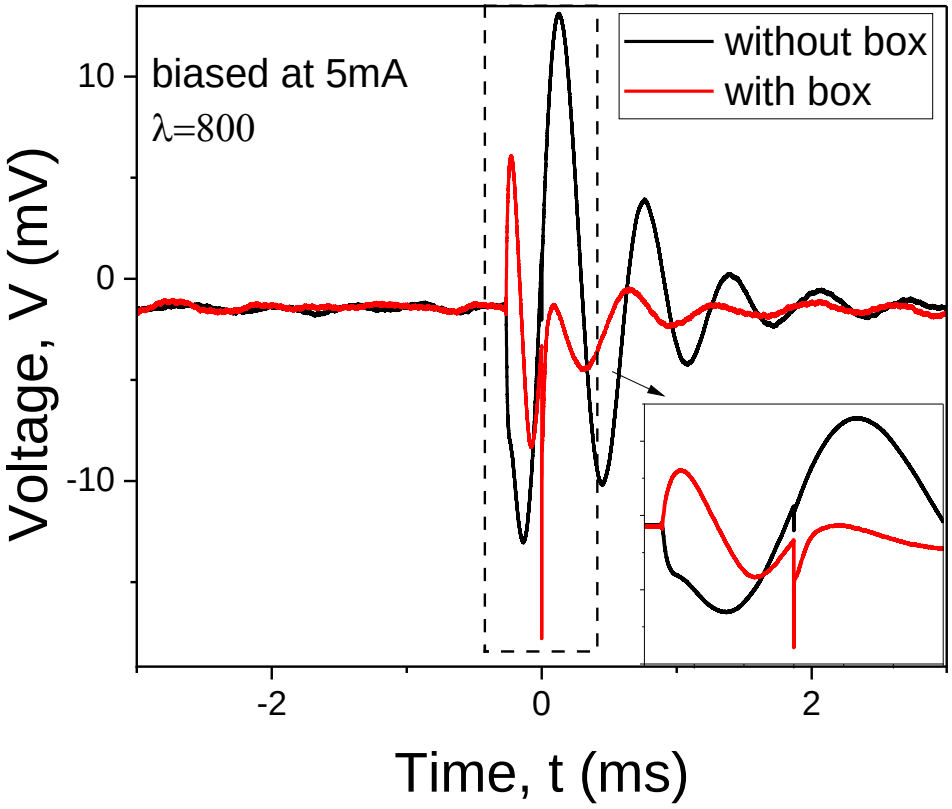

Figure 5.14: Oscilloscope time traces for the Cu_2O single crystal. The black trace shows the voltage over time without any shielding, where significant ripples are observed. The red trace represents the voltage over time with the problem reduced by enclosing the setup in a die-cast box, significantly reducing the source ripples. The inset highlights the clearer device response when the die-cast box is added.

It is notable that in the previous measurement without the grounded metal box, the slow component photoresponse showed a strong increase at longer excitation wavelengths, where (see Figure 5.12). When the device was placed in the grounded die-cast aluminium box, the overall background noise level (caused by electrical pickup) was significantly reduced for all bias currents. The tail beyond 1000 nm is significantly diminished. Both components now show resonance spectral features at same shorter excitation wavelengths (820 nm, 900nm nm, 930 nm, and 980 nm). These spectral features are consistent at all bias levels.

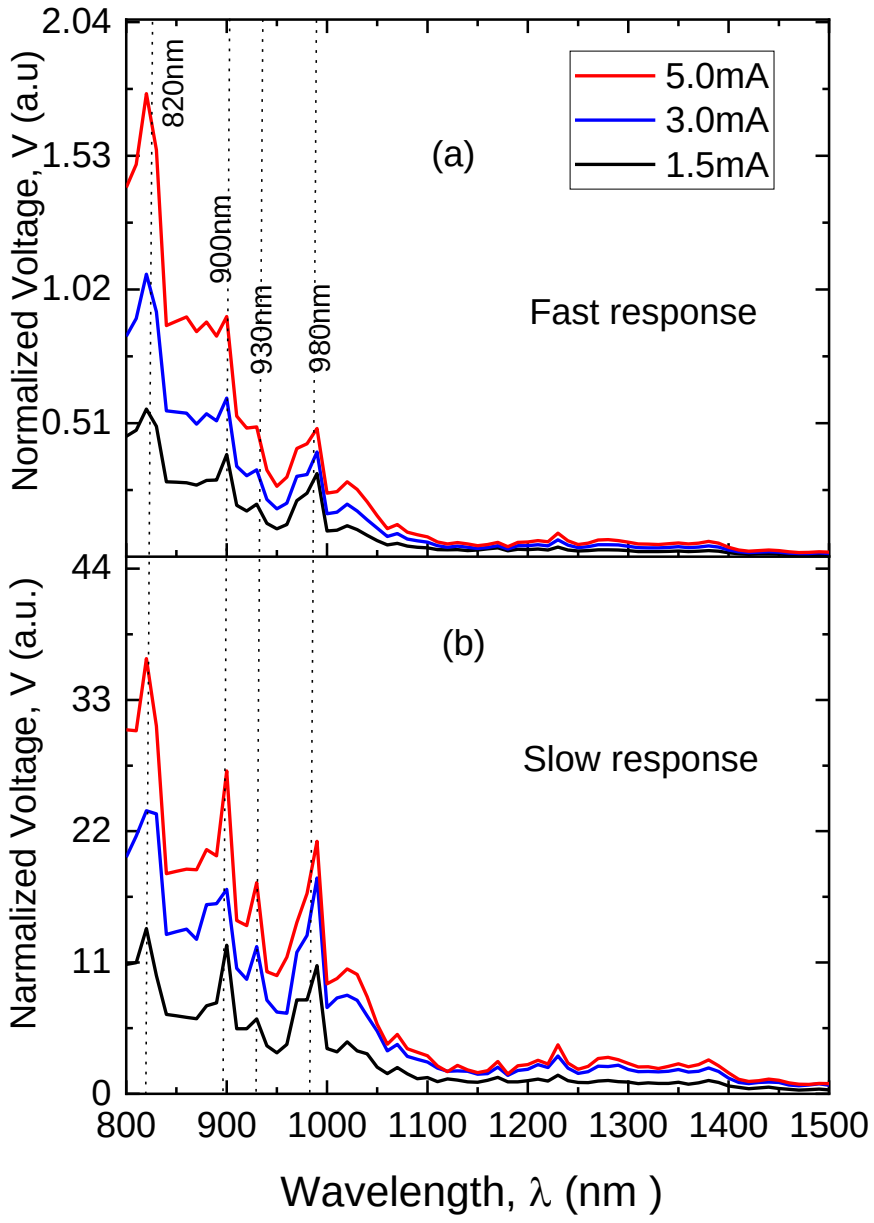

Figure 5.15: (a) Wavelength dependence of the fast photoconductive transient component for the shielded device under three different bias conditions (1.5, 3.0, and 5.0 mA). Power fluctuations at each wavelength were corrected by normalizing with the reference photodiode signal, accounting for the spectral response. This ensures the results reflect constant excitation fluence. Each curve represents the average of approximately 20 wavelength scans. (b) Wavelength dependence of the slow photoconductive transient component under the same conditions shows a reduction in background noise at longer wavelengths after shielding the device. The dashed lines indicate possible defect levels reported in the literature.

We believe that the fast component of the photoconductivity transient can be explained by electron-hole pair generation. These charge carriers contribute to enhanced conduction. At resonance wavelengths, the carriers rapidly decay into defect states, creating distinct features in the photoconductivity spectrum. We observe a similar fast transient when the device is exited with wavelengths that correspond above bandgap excitation.

On the other hand, the slower conductivity response shows the same resonance peaks. Defects in the semiconductor create trap states that capture either an electron or a hole, leaving the untrapped carrier free to move back to the valance band with long decay time. The trapped carrier is taking longer to escape and recombines with its counterpart leaving a signature in the spectrum [174]. Past photoluminescence (PL) measurements at room temperature on this same synthetic material identified a broad luminescence peak around 930 nm, which is linked to copper vacancies [14]. The broadness of this peak, with a full width at half maximum (FWHM) of about 100 nm, is characteristic of a bound-to-continuum transition. In the photoconductivity spectra, we can clearly identify three peaks, at 900 nm, 930 nm and 980nm., these peaks fall within the broad emission peak observed in PL, indicating that there might be more complexity within the room temperature PL emission, potentially obscured by the broad nature of the PL recombination. This peak attributed to copper vacancy [67].

Moreover, in our room temperature measurements, we have observed a distinct resonance peak at 820nm. This feature could be due to ionized oxygen vacancies. Such a signature is consistent with the PL findings of ionized oxygen vacancies (V^{+O}) reported at an energy of 1.51eV (820nm) by other researchers [87].

5.9 Transient Photoresponse at Selected Wavelengths

As seen previously illuminating Cu_2O at 980nm induces a significant peak in photoconductivity spectra This feature is attributed to activation of specific defect states within the Cu_2O. Conversely at for example 800nm this distinctive peak is absent (see Figure 5.15), suggesting different interaction mechanisms or lack of response with key defect

states at this wavelength. Studying the variance in decay time for transient photoresponse for slow component with changing the illumination wavelengths provide crucial insights into the energy-dependent dynamic of carrier trapping, recombination, and over all influences of defects on device performance [175]. The room-temperature transient response slow component for the two representative wavelengths (980nm and 800nm) are shown in Figure 5.16(a) and (b) respectively. The persistent photoconductivity at 980nm in the slow decay process suggests presence of trap state in the crystal samples at this specific wavelength and provides valuable information on carrier transport properties in semiconductors material [176], [177] .

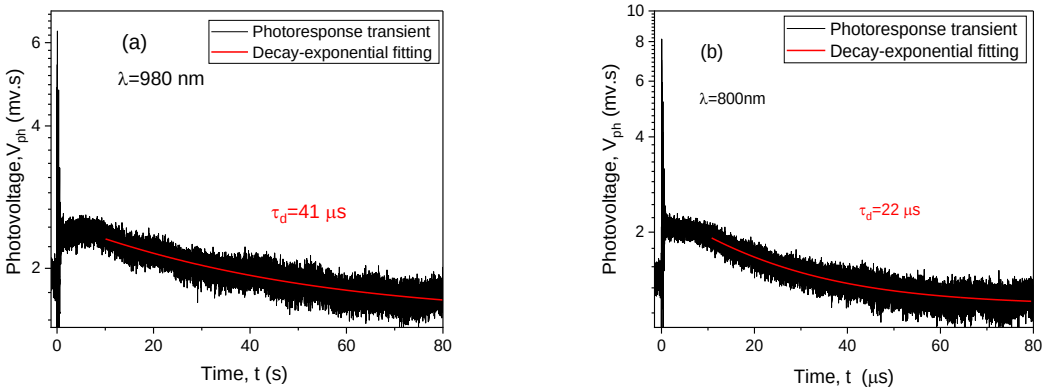

Figure 5.16: Transient photovoltage response of Cu_2O under (a) 980nm and (b) 800nm illumination. Faster decay ($\tau \approx 22$ μs) is observed at 800 nm, while slower decay ($\tau \approx 41$ μs) at 980 nm is linked to defect state. The varying decay times reveal differences in carrier dynamics and defect interactions.

5.10 Comparison with Absorbance Spectrum

To validate the effectiveness of the laser photoconductivity method for material analysis, we conducted an experiment studying the same crystal. by using the laser setup of the photoconductivity measurements but changing the way of measuring the radiation. We equipped a Thorlabs S145C integrating sphere with a PM100USB power and Energy Meter Interface to capture the absorption spectrum of the sample, as displayed in 3.4.23.4.2 This spectrum was derived from the transmission spectrum which in turn was calculated by

dividing the intensity of the transmitted light (I) by the intensity of the incident light (I_0), illustrated in Figure 5.16 (a) and (b) respectively. These spectra represent the power distribution of the pulsed light measured in NIR range (800-1500nm) for both the background and the sample. The observed discrepancies in line spread at shorter wavelengths seems inaccurate. The discrepancies effect could be seen in the absorbance spectrum Figure 5.16c causing a big dip at short wavelengths.

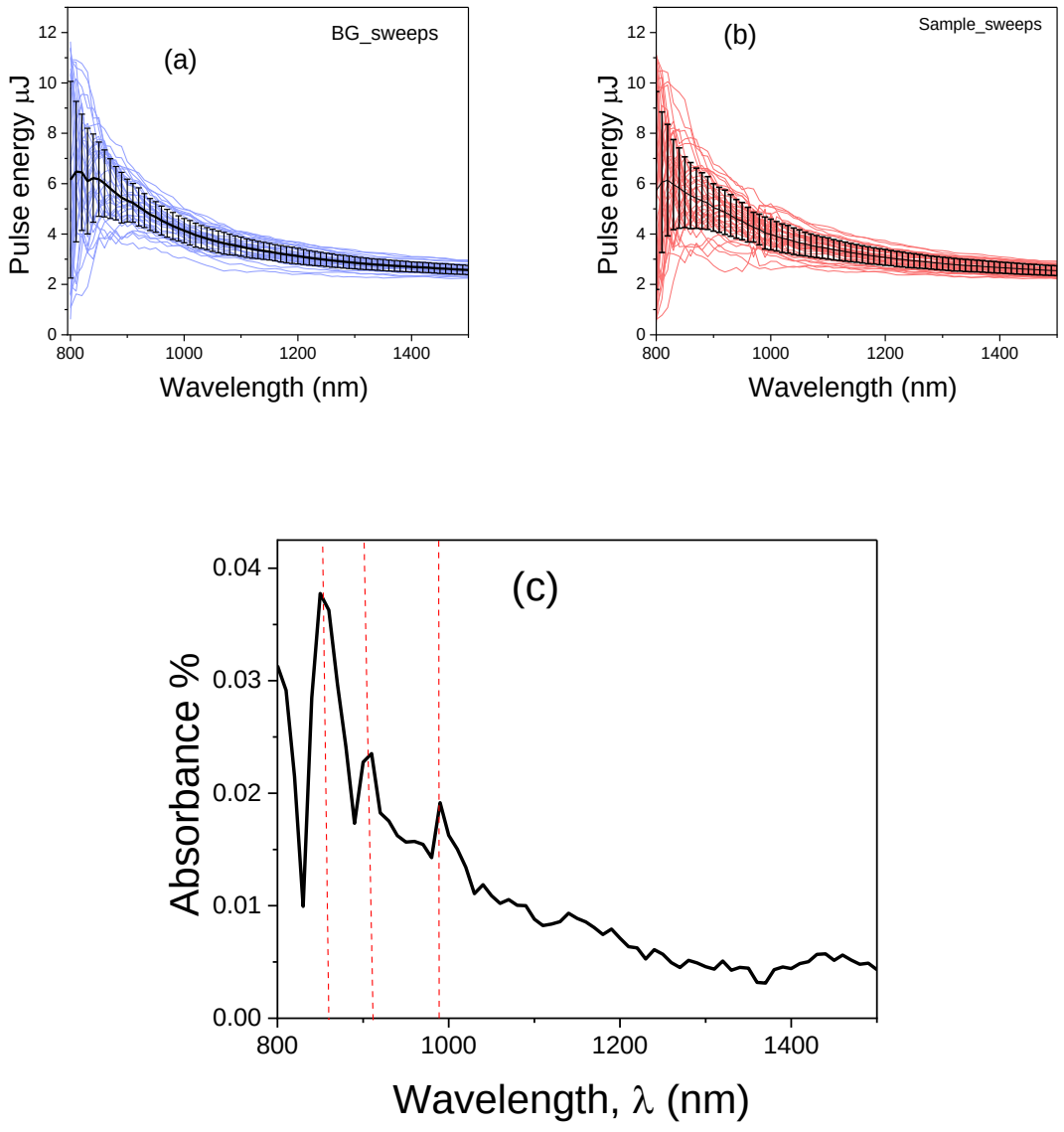

Figure 5.17: (a) and (b) show the power distribution spectra for background and sample measurements between 800nm and 1500nm with standard deviation bar. Discrepancies at shorter wavelengths are due to averaging by the power meter. (c) Absorbance spectrum shows peaks below the bandgap, consistent with previous photoconductivity data, with a noticeable dip at shorter wavelengths caused by measurement fluctuations.

This inconsistency in the spectrum was determined to be because the power meter interface works by taking measurements periodically (analogue bandwidth between DC-100KHz dependent on setting), which are not synchronised to the laser pulse. This results in a large number of measurements taken where the laser is off, reducing the signal to noise ratio of the averaged results. Short-term fluctuations in the laser output energy are also not captured by the power meter interface.

Following this attempt, we continued to use a Thorlabs S145C integrating sphere but replaced the power meter interface and directly connected the integrating sphere InGaAs photodiode and oscilloscope, triggered to the laser pulse. Analysis of the raw data from the oscilloscope was processed in the same way as previously described in 3.4.2. We measured the transmitted light through the sample and a background scan (laser emission with the sample removed) for multiple sweeps as shown in *Figure 5.17*(a) and (b), and the spectra are consistent along the entire wavelength range. The obtained absorbance spectrum reveals distinct peaks below the bandgap these findings were consistent with the spectrum found previously from photoconductivity.

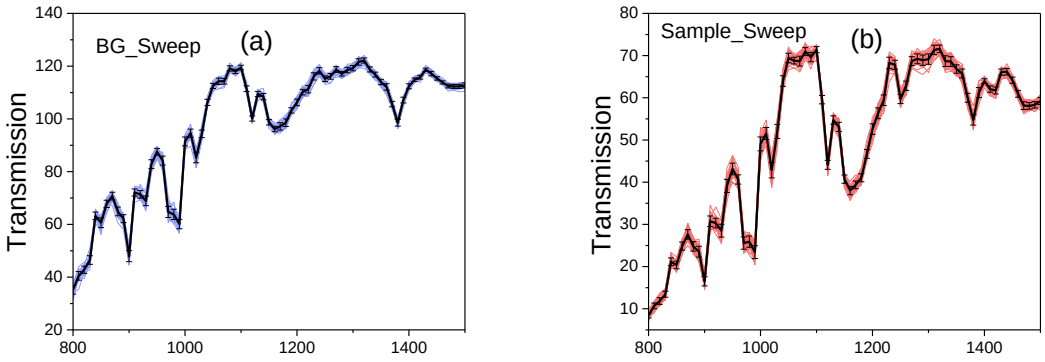

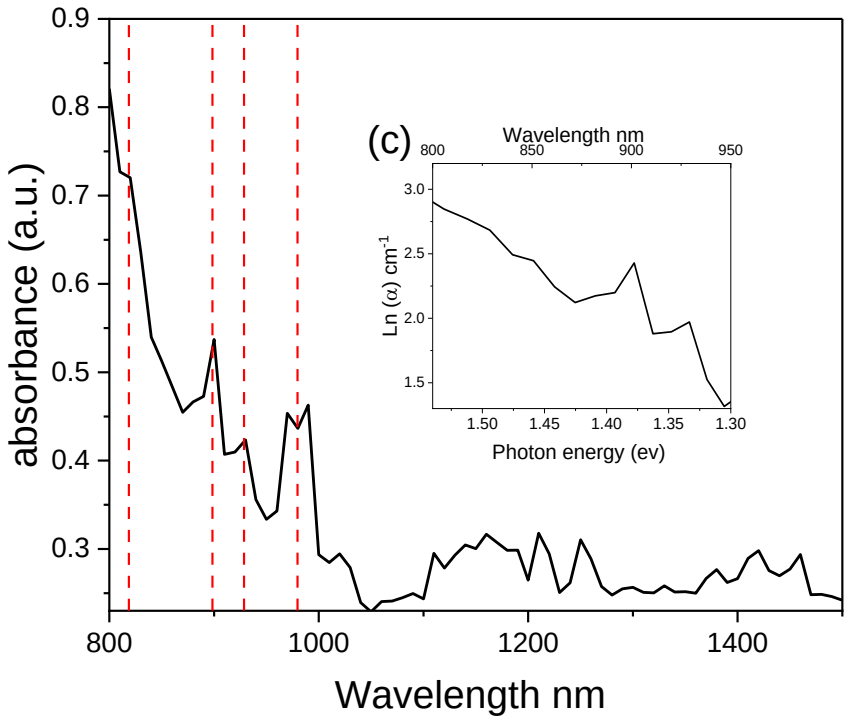

Figure 5.18: (a) 20 sweeps of transmitted light spectrum of Cu_2O single crystal using oscilloscope (b) 20 sweeps of the background scan (c) Laser absorption spectrum of the Cu_2O. The inset of (c) Extracted absorption coefficient α for Cu_2O plotted as a function of excitation photon energy E(eV).

The inset in *Figure 5.17*(c) represents the absorption coefficient α of Cu_2O single crystal plotted as a function of photon energy (eV). This was calculated from the following equation:

$$\alpha(\lambda) = -\frac{1}{t}\left\{\frac{1}{2R(\lambda)^2}\left(\sqrt{\frac{\left(1-R(\lambda)\right)^4}{T(\lambda)^2}+4R(\lambda)^2}-\frac{\left(1-R(\lambda)\right)^2}{T(\lambda)}\right)\right\} \quad (5.4)$$

Where R is the reflectance, T is the transmission and t is the sample thickness in cm^{-1} . the sample reflectance (0.25%) for Cu_2O single crystal across the wavelength (800nm – 1500nm)

[178]. For the photon energy below 1.54 eV the Urbach energy (E_u) was determined to be 0.150 eV, based on the trend observed in the inset of *Figure 5.17*(c), where $\alpha(E) \propto \exp(\frac{E}{E_u})$. The measured Urbach energy of our bulk Cu_2O is as shown appears relatively high. This elevated value can be attributed to the high sensitivity of the advanced time-resolved spectroscopy technique employed, utilizing a nanosecond pulsed laser. This technique is more sensitive to subtle variations and transient states in the absorption edge, capturing more intricate details that conventional UV-vis spectroscopy may not detect.

However, it is important to note that we could not obtain data just below the bandgap due to the limitations of the InGaAs photodiode, which has a spectral sensitivity range starting from 800 nm. This restriction prevented us from accurately capturing the exponential tail closer to the band edge, which is the typical region for Urbach energy extraction. Despite this, the consistent exponential behaviour observed further below the bandgap suggests that the extracted Urbach energy is still reflective of the material's overall optical characteristics.

5.11 Additional Information from XPS

We sent a small piece of the Cu_2O material to Cardiff University School of Chemistry where Dr David Morgan performed an XPS analysis [179]. The XPS was employed to gain insights into the accurate chemical composition of the Cu_2O crystal surface. Figure 5.20 shows the XPS spectrum of Cu_2O in a wide range, the survey XPS scans commonly showed Cu2p, O1s, C1s, Cu3s, Cu2s, and Cu3p. The position of these peaks was aligned with standard binding energy of C with approximately 284.5 eV. Figure 5.20 shows the measured BE values of the O1s signals for the Cu_2O compound were all found in the 520–540 eV XPS range. This peak was resolved into sub-peaks from metal oxygen band (M-O), oxygen-related defects bonds such as oxygen deficient sites (V_0) and contamination species (OH-). Generally, it is well-known that the M-O and oxygen-related defect peaks in metal oxygen are located at 350.6ev and 531.9 eV, respectively as well the peaks that found at 534ev related to the species and organic material [180]–[182].

Furthermore, a distinct feature was observed in the focusing on Cu2P spectrum specially Cu2P1/2 (see Figure 5.21). Characterized by main peak at 931 eV a shoulder around 933 eV and satellite peak in close proximately 962 eV. These supplementary peaks are linked to Cu+2 [183], [184]. This provides an insightful connection between spectral features and the chemical composition, enhancing our understanding of the sample's surface environment.

The multi-peak phenomenon initially observed in the spectrum can be attributed to the contamination introduced during the polishing process that in the first place used to facilitate the study, the sample underwent a polishing process using a water-based diamond abrasive. This introduced certain contamination to the sample surface, manifested in the XPS spectrum as a series of peaks, reflecting the various elements inadvertently added during the polishing process. In order to rectify this issue and obtain a reliable assessment of sample's true chemical composition a subsequent surface etching process was conducted using dilute acetic acid. This etching procedure successfully removed the introduced contamination effectively.

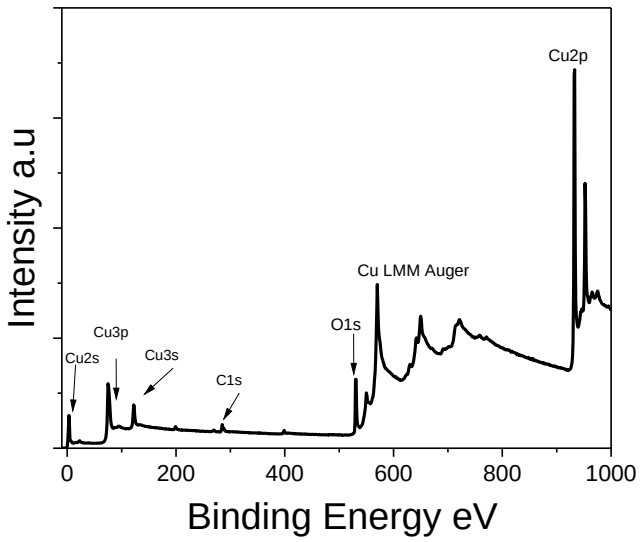

Figure 5.19: Complete X-ray photoelectron spectrum of Cu_2O

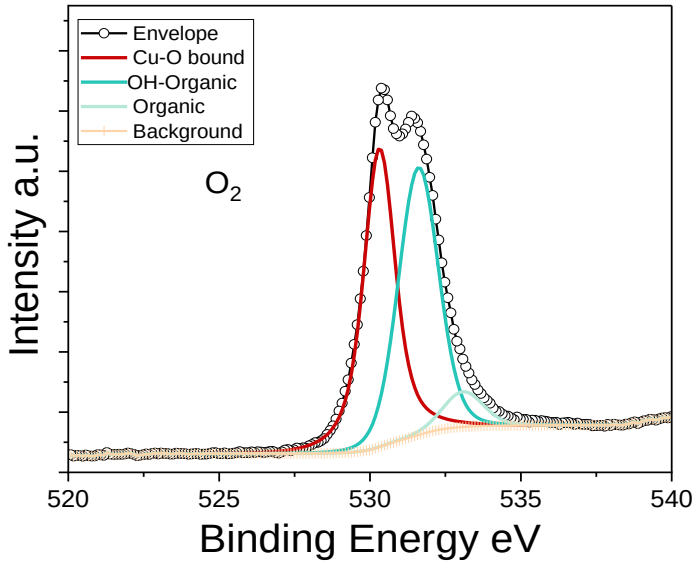

Figure 5.20: X-ray photoelectron spectroscopy binding energy spectrum for the O1s core level as received.

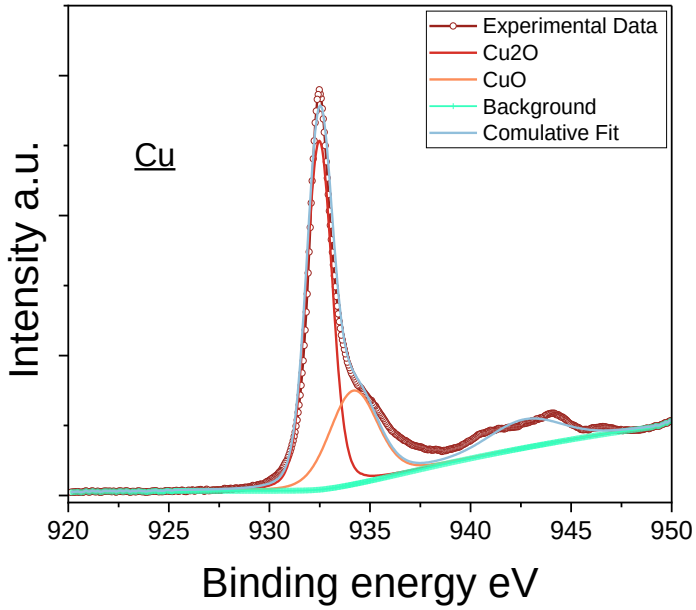

Figure 5.21: X-ray photoelectron spectroscopy binding energy spectrum for the 2p 3/2 core level as received.

After a gradual etching process and then averaging the measurements, the O1s spectrum retaken and depicted in Figure 5.22. the previously observable peaks corresponding to (OH) groups, and the organic components have vanished. This disappearance strongly implies the success of the etching procedure in eliminating the contamination. By employing a multi-Gaussian peak fitting technique, the distinct constituents (O^{2-} and O_v) within the board's asymmetric O1S spectrum have been discerned. Notably, the peak centred at 530 eV is indicative of oxygen ions bonded with metal ions, referred to as lattice oxygen O^{2-}. Conversely, the peak exhibiting a higher binding energy (O_v), centred at 531.4 eV, is linked to oxygen ions situated within oxygen-deficient regions within the crystal structure, also known as oxygen vacancy states.

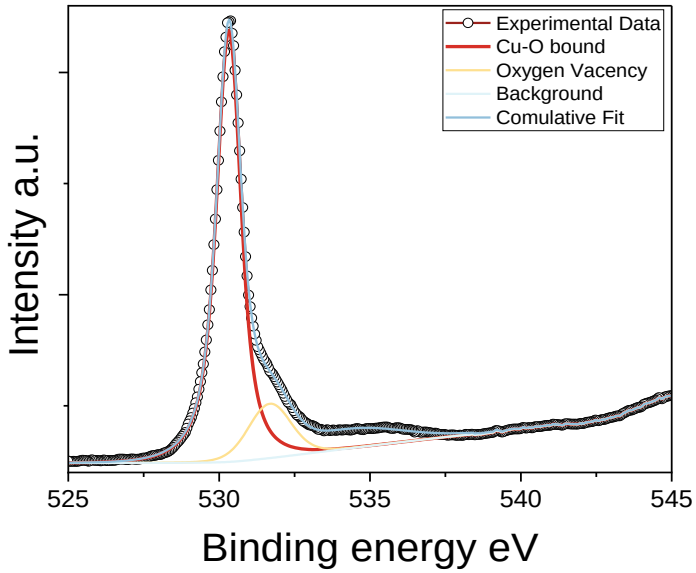

Figure 5.22: X-ray photoelectron spectroscopy binding energy spectrum for the O1s core level after etching.

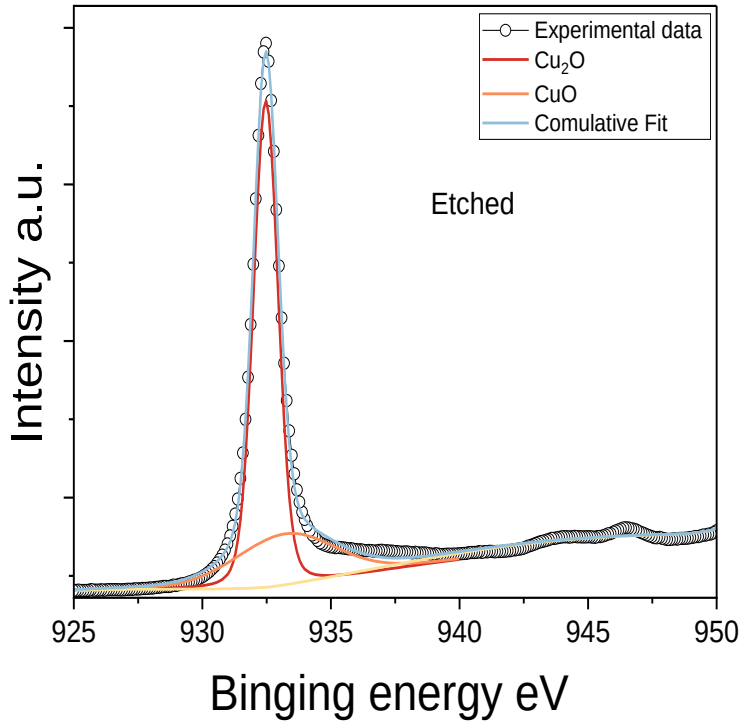

Figure 5.23: X-ray photoelectron spectroscopy binding energy spectrum for the 2p 3/2 core level after etching.

Similarly, the Cu2p was retaken after etching, the spectrum as shown in Figure 5.23 characterized by the main peak as previous Cu^{+} and the shoulder that refer to Cu^{2+} has notably reduction. This was identified by accurately applying multi-Gaussian fitting approach, the peak positions for both phases are observed at 931 eV and 933 eV, respectively. By assessing the integrated area of Cu^{+} and Cu^{2+} peaks, the relative content of Cu^{2+} is estimated to be 26%. The XPS analysis serves as corroborative evidence highlighting deviations in the crystal's stoichiometry.

5.12 Conclusion

In conclusion, we have investigated the room-temperature photoconductive response of Cu_2O to sub-bandgap excitation using pulsed laser light. The measured photoconductivity

spectra reveal two distinct recovery components: A fast component that coincides with the laser excitation, followed by a recovery phase on the order of hundreds of nanoseconds. A slower component that recovers over tens of microseconds. These two transient components exhibit markedly different excitation spectral dependencies. There are indications of resonances that align with known impurity features, such as the neutral copper vacancy (V_{Cu}) and the singly ionized oxygen vacancy (V^{O+}). Our measurements are consistent with previous room-temperature PL experiments on the same material. We believe that the characterization method presented here could be valuable in developing a faster feedback optimization loop to monitor changes following post-growth treatment of crystals. This could help unlock the significant potential of Cu_2O materials for quantum technology applications, such as single-photon sources.

Chapter 6 Detection of Impurity States in Cu_2O Single Crystals using MIR & THz Fourier Transform Spectroscopy

6.1 Introduction and Rationale

Our experiments thus far have exploited the wavelength tuning range of the pulsed laser excitation source. The longest wavelength that the laser can reach is 2.6 microns. However, even this is problematic because the laser uses a different nonlinear mechanism to generate longer wavelength light, and hence it uses a different optical channel. The impurity levels that are reachable with short wave infrared light are also relatively deep (i.e. they lie near the middle of the band gap). It is also possible that much shallower impurities could affect the visibility of high principal quantum number (Rydberg) excitons. The states associated with shallower impurities would lie much closer to the conduction or valence bands. In order to access such states, we would need photons of lower energies, corresponding to wavelengths in the mid-infrared or THz bands.

Little is known about the mid-infrared or THz spectroscopy of Cu_2O. The work described in this chapter was aimed at detecting their presence in Cu_2O using Fourier Transform infrared (FTIR) spectroscopy. FTIR has a number of significant advantages over diffractive spectroscopy at longer wavelengths (as discussed in the Methodology section). FTIR has previously been used to study shallow donor and acceptor states in silicon [185]. At low impurity concentrations, where the impurities or defects are sufficiently far apart that their wavefunctions don't overlap, the spectral lines associated with these states tend to be very narrow (particularly in pure elemental single crystals like diamond and silicon). This is because the large spatial extent of the impurity wavefunction serves as an effective sensor for assessing the local crystal environment around defect. Deviating away from the perfect

crystal (for example, by introducing additional germanium atoms into silicon) results in inhomogeneous broadening of the spectral lines [185]. Thus, the shape of the spectral lines of shallow impurities can also tell us something about the quality of the host material.

However, there is an additional complexity when investigating the spectroscopy of shallow donors. Because these states lie much closer to the valance or conduction bands, their binding energies tend to be of the order of 10s of meV. Since the product of the Boltzmann constant and room temperature (kT) is about 25 meV, then shallow impurity levels are usually already ionised. This is why phosphorus and boron in silicon make good n- and p-type dopants respectively. The unbound extra donor electron or acceptor hole is free to contribute to the conductivity of the material. In order to perform spectroscopy of the shallow impurity in its ground state, the temperature of the host must be cooled far below the binding energy of the impurity. Thus we needed to using a cryogenic system to perform the spectroscopy experiments. This was the closed-cycle ColdEdge™ “Stinger” helium re-circulator (as discussed in the 3.5.1).

The chapter is organised as follows. A brief description of the experiment follows in section 6.1. In section 6.2 we discuss the MIR spectroscopy work, and in the following section 6.3 we describe the THz spectroscopy. The chapter concludes with section 6.4, where we discuss our findings.

6.2 Fourier Transform Infrared (FTIR) Spectroscopy Experiment

FTIR spectrometers can in principle be used for any wavelength range from ultraviolet to microwaves. However, it becomes more advantageous to use FTIR with increasing wavelength. There are three key components of the FTIR spectrometer that must be carefully chosen to match for the wavelength range of interest: (1) The illuminating source, (2) the beamsplitter, and (3) the detector. For any absorption spectroscopy measurement (including grating spectrometers, the illuminating source must clearly cover the wavelength

range of interest. For visible spectroscopy a tungsten halogen lamp is often used. For longer wavelengths it is more common to use a globar source. A globar is an incandescent filament, basically a wire coated in silicon carbide. The globar behaves as a black body source, where the peak emission wavelength is dictated by the temperature. Globars can cover most of the infrared and the beginning of the far-infrared (THz) band. For lower frequency THz (and longer microwave) measurements different sources need to be used, such as mercury lamps. The beamsplitter is the critical optical component of the Michelson interferometer. Clearly the beamsplitter material must be transparent in the wavelength range of interest. At visible wavelengths materials like quartz or CaF2 are often used but these materials become opaque beyond a few microns. For the infrared band typically the beamsplitter will be made from potassium bromide (KBr), or Zinc selenide. KBr has the disadvantage that is hygroscopic, while zinc selenide has the disadvantage that it is toxic. Moving towards the THz requires another change. The most common beamsplitter material is Mylar^{TM}. Different thicknesses of Mylar are used for different bands to avoid issues such as Fabry-Perot fringing. The final choice is the detector, which needs to show responsivity at the wavelength range of interest. Silicon photodiodes are often a good option for the visible range. Liquid nitrogen cooled mercury cadmium telluride (MCT) detectors are typically used to cover most of the infrared band. Liquid helium cooled bolometers are used for the THz band.

For this work a Bruker VERTEX 80v spectrometer is used, allowing spectroscopy to be performed over a wide range of the electromagnetic spectrum. The VERTEX 80v is a high-end research grade FTIR spectrometer. It has the advantage that it can be completely evacuated, which is important for MIR and particularly THz measurements. This is because normal air contains both carbon dioxide and water vapour. These molecules are infrared actives and have many vibrational and rotational modes at MIR and THz frequencies. This can obscure the spectrum, and the best mitigation is simply to remove these molecules by evacuating the entire optical path.

6.3 MIR Spectroscopy Experiments

Figure 6.1 shows the VERTX 80v configuration used to perform the MIR spectroscopy experiments.

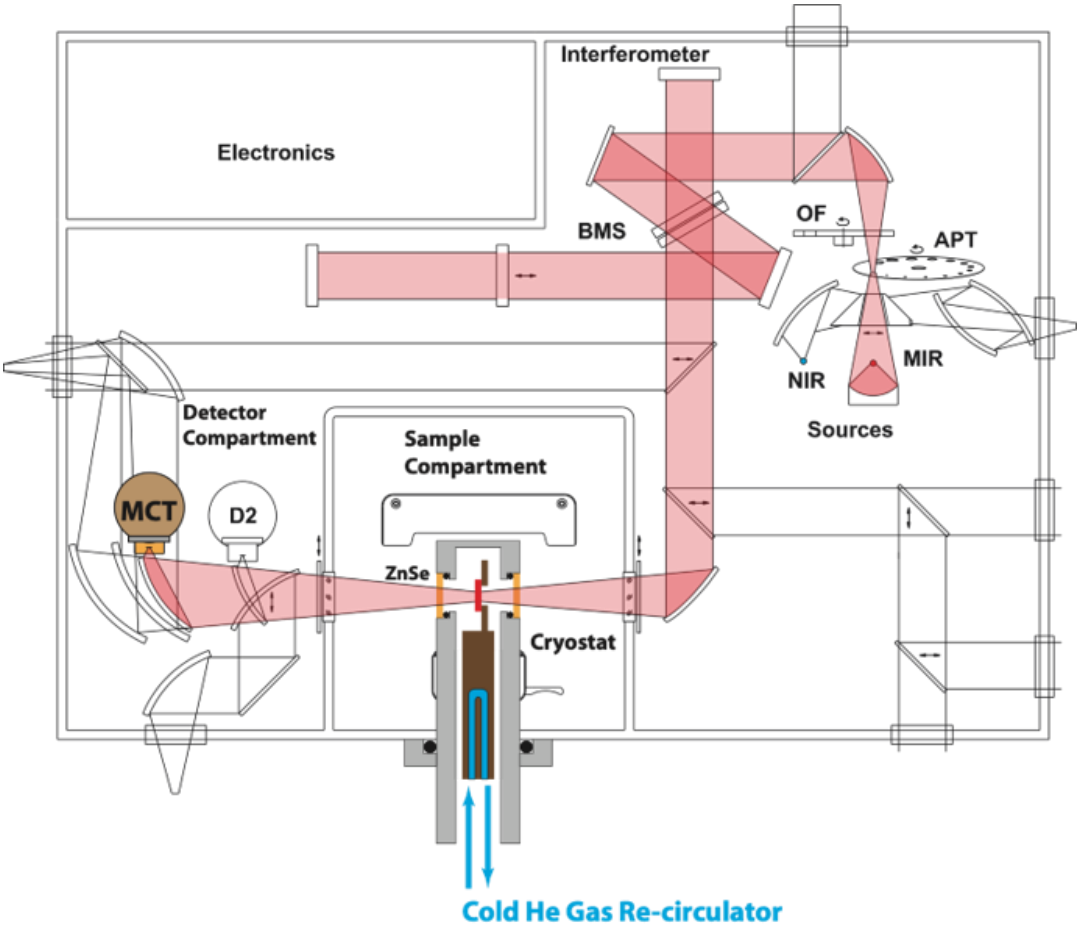

Figure 6.1: MIR absorbance Experiment set-up using a Bruker Vertex 80V Fourier Transform spectrometer. The beam path is highlighted in partially transparent red. NIR is a near-infrared lamp (not used here). MIR is a mid-infrared globar lamp. BMS is a beamsplitter, selected for the wavenumber range of what is being measured (in this case KBr). APT is an optical aperture selector, to control lamp intensity and beam size. OF is an optical filter wheel (not used here). The beam is focused through ZnSe cryostat windows onto the sample. The transmitted beam is collected and focussed down to a spot on the MCT detector. The entire beam path is in vacuum.

For MIR regime, the MCT photovoltaic detector (a Kolmar model MCP0393 with a 1mm HgCdTe element) was used. Its active element requires cooling to liquid nitrogen

temperatures to function. The detector is reverse biased by 50mV to increase the response speed, this gives an approximate signal rise time of 20ns and an exponential fall lifetime of 40ns. The MCT photoconductive detector is coupled to an internal amplifier, with BNC output. The side looking LN2 pour filled Dewar has a 12-hour hold time. Detector to amplifier connections is inside the Dewar, minimizing electrical pick up and simplifying system integration.

The natural samples used in this study were sourced from Namibia. For the optical experiments conducted, the samples underwent specific preparation steps to meet the experimental requirements. Both sides of the samples were planarized to facilitate light transmission. Depending on the spectral range of interest, the thickness of the samples was carefully adjusted.

For these specific regions infrared and terahertz experiments, thicker samples were necessary, typically > 1 mm, due to the smaller absorption cross sections of atomic-scale defects. To further optimize the experimental setup, a slight wedge angle was introduced between the optical faces to minimize Fabry-Perot fringing in transmission geometry. These preparation methods ensured that the samples were suitable for a variety of optical and spectroscopic analyses.

Figure 6.2 shows that the MIR region from 100meV to 743.8meV ($800cm^{-1}$-$6000cm^{-1}$) absorption spectra for (a) synthetic and (c) natural samples recorded for a range of temperatures 18K and 300K the spectra have a number of different peaks. The strongest features are due to the optical properties of Cu_2O. The peaks remain largely consistent with temperature, which suggests their origin is not from shallow impurities – we would expect shallow impurities to become ionised at higher temperatures. Some peaks might be resulting from contamination in the spectrometer itself rather than from the sample.

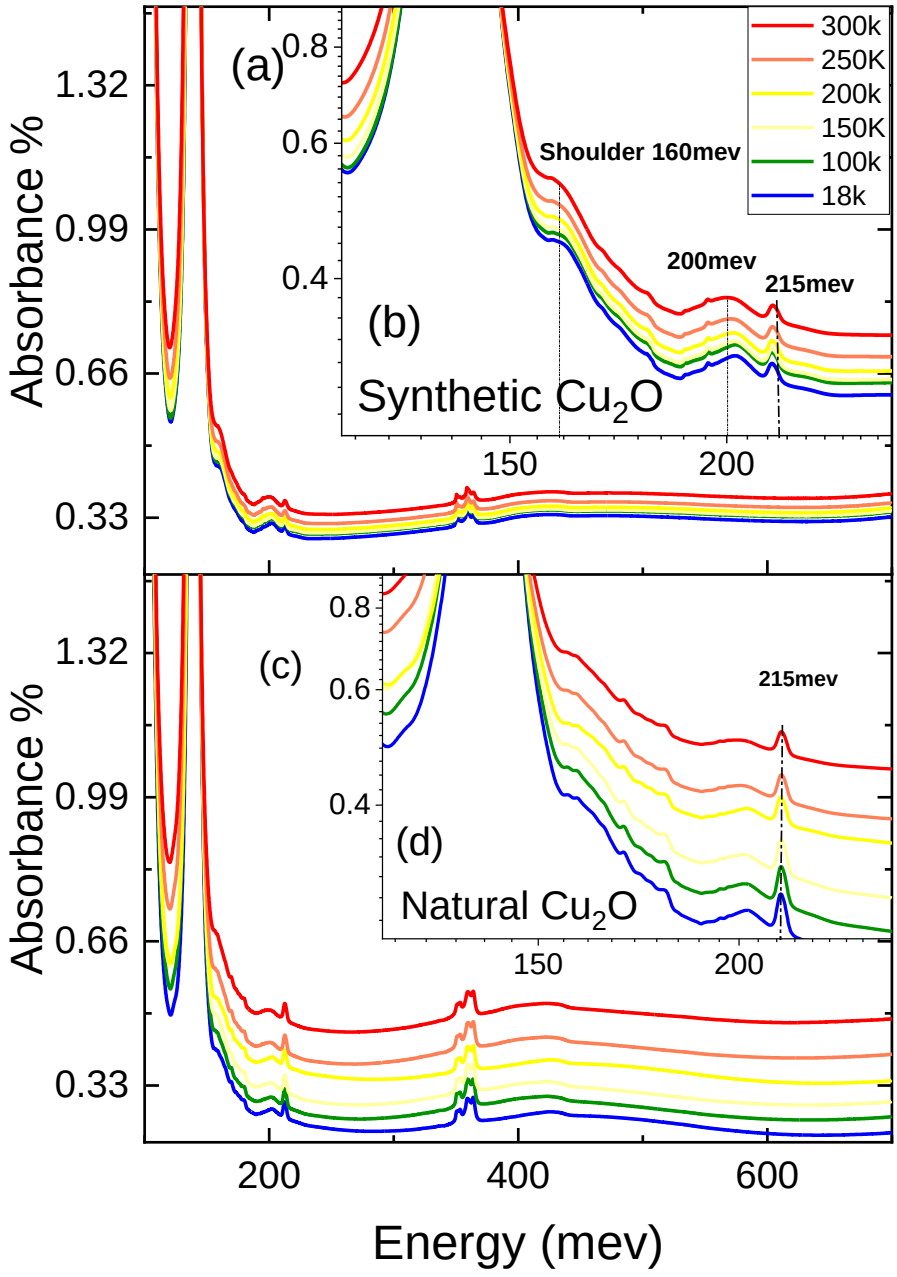

Figure 6.2: The mid-infrared (MIR) transmission spectra of a 1 mm thick synthetic Cu2O crystal were recorded at temperatures ranging from 18 K to 300 K. The inset (b) provides an expanded view of the long-wavelength region near the Reststrahlen band edge. The MIR transmission spectra of a 1.2 mm thick natural Cu2O gemstone, measured under similar conditions. The inset (d) also shows an expanded view of the region near the Reststrahlen band edge.

Water vapor and carbon dioxide are the primary atmospheric contaminants of concern in FTIR spectra. Water vapor has absorption bands in three main regions near 452.5 meV, 464.9 meV and 197.1 meV (3650 cm^{-1}, 3750 cm^{-1}, and 1590 cm^{-1}) [186], [187]. In our spectra, these bands are absent, indicating no detectable water vapor. Carbon dioxide has absorption bands around 74.3-92.9 meV, 278.9-291.3 meV and 446.3-464.9 meV (600-750 cm^{-1}, 2250-2350 cm^{-1}, and 3600-3750 cm^{-1}) [188]. The minor peak observed at 359.5meV (2900 cm^{-1}) in all temperature conditions can be attributed to carbon dioxide. Our synthetic and natural samples exhibit two prominent features observed in the range of 100-155meV (800 cm^{-1} -1250cm^{-1}). As we will see later, these can be attributed to Reststrahlen overtone bands, specifically between 100-115 meV and 135-155 meV, (800-927 cm^{-1} and 1088-1250cm^{-1}) which dominate the mid-infrared (MIR) spectra at all temperatures.

Additionally, there are several distinct features that can be seen when the x-axis is expanded: A shoulder around 160 meV, related to the second Reststrahlen overtone band is present in both samples. However, it becomes more pronounced in synthetic samples and sharpens to a discernible peak at lower temperatures, likely resulting from the highest energy longitudinal optical (LO) phonon. The peak at 215 meV is also shown in both samples exhibiting minimal temperature dependence. It becomes slightly sharpener at lower temperatures. This peak's presence in both samples suggests it is a consistent feature of CuO. Another peak appears at lower energy levels in the synthetic sample at around 200meV. The physical origin of these spectral features remains a topic of discussion.

For Cu_2O theoretical predictions indicate that the copper simple vacancy (V_{cu}) and split-off vacancy (V_{Cu}^{split}) are the dominate acceptor in Cu_2O with activation energies of 230 meV and 470 meV above the valance band maximum respectively [58], [63], [189]. The 470 meV band is not observed in either of our samples. We observe a 215 meV band in both samples and a 200 meV band in the synthetic sample, either of these could fit the copper vacancy states. Two traps have been hypothesised theoretically in Cu_2O: this model incorporates a band located from 450 meV to 650 meV and another acceptor state at 200 meV. Also, these have

been observed experimentally in deep level transient spectrum (DLTS), of this material at 450 meV and 250 meV above the valence band reference [190].

6.4 THz Spectroscopy Experiments

THz spectroscopy allows us to investigate even smaller energy scales, i.e. whether there are very shallow impurity states very close the conduction or valence bands. Figure 6.3 shows the VERTX 80v configuration used to perform the MIR spectroscopy experiments.

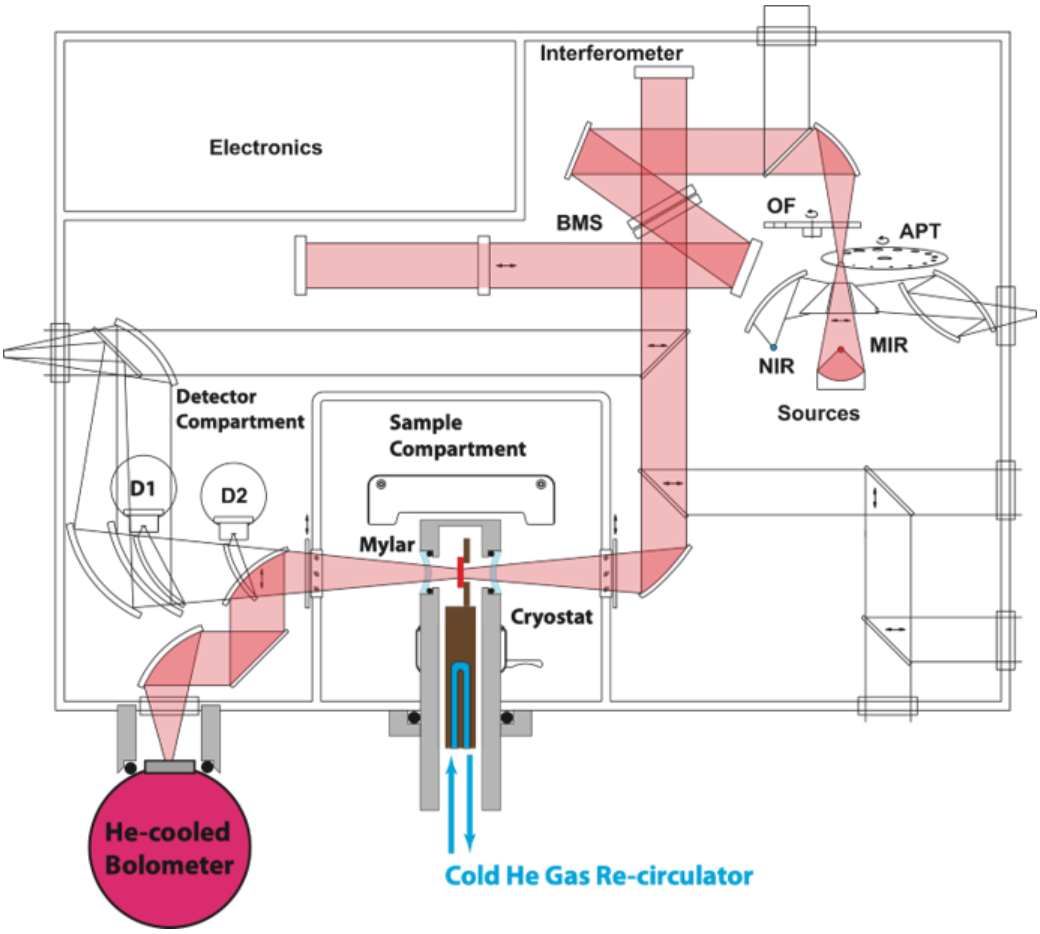

Figure 6.3: THz absorbance Experiment set-up using a Bruker Vertex 80V Fourier Transform spectrometer. The setup shares some commonality with the MIR setup but there are some important differences. The source a globar and the optical path to the sample is the same, but the beamsplitter BMS is Mylar. The cryostat windows are polypropylene. The detector is a liquid helium cooled bolometer. The entire beam path is in vacuum.

For the THz regime, we need a different source/beamsplitter/detector combination. The source is still a globar because the long wavelength emission tail extends sufficiently far into the far-infrared/THz range. However, the KBr beamsplitter is not transparent to THz light, so this has been exchanged for a Mylar beamsplitter. MCT detectors are not sensitive to light with wavelengths longer than about 20 microns, so we also need to use a different type of detector. The bolometer is a thermal detector, where the detector and low-noise pre-amplifier essentially transduces a change in temperature due to radiation falling on the sensor into a voltage. The sensor needs to be cooled to liquid helium temperatures via an inner dewar of liquid helium surrounded by an outer jacket of liquid nitrogen.

Figure 6.4 presents the THz absorption spectra for both synthetic (a) and natural (c) synthetic Cu_2O across a temperature range of 100K to 350K.

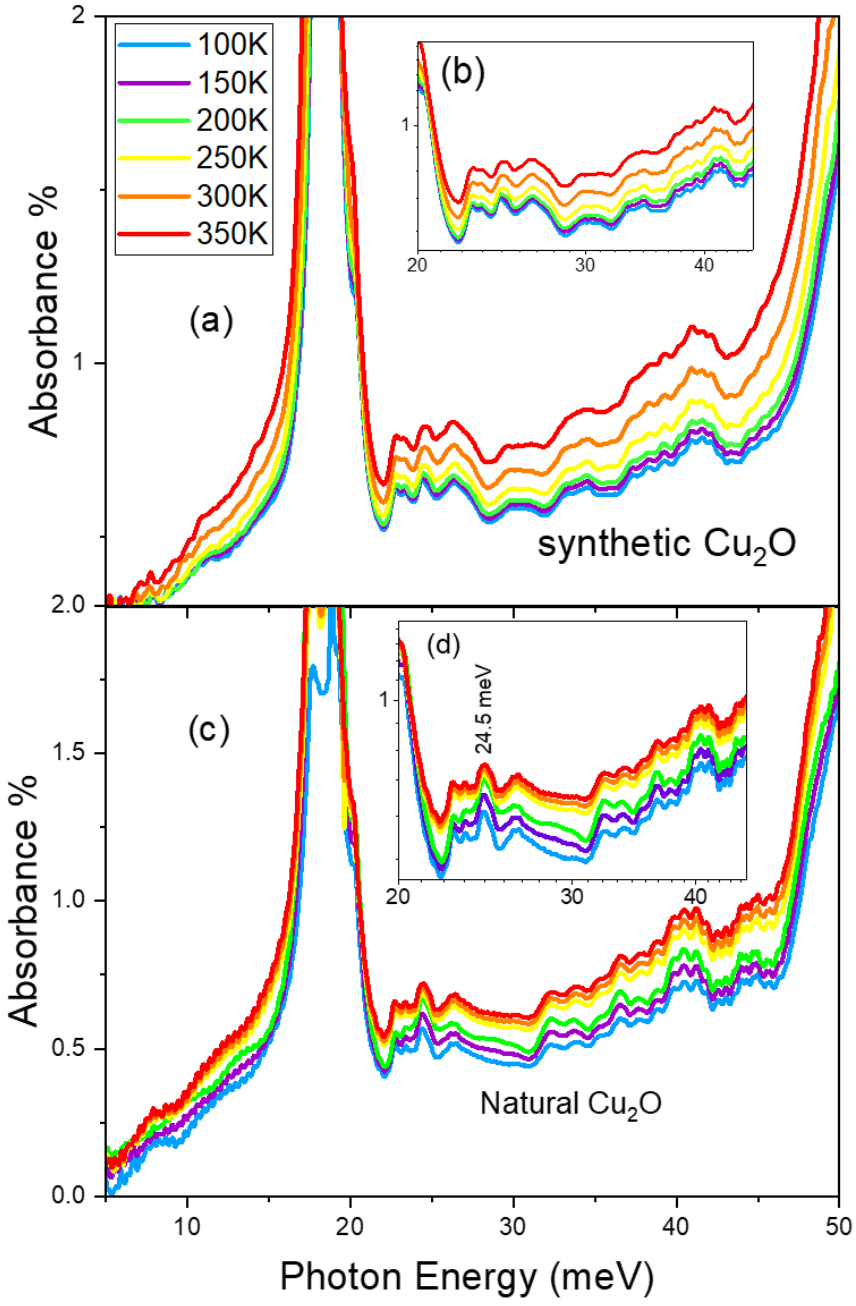

Figure 6.4: THz absorption spectra of synthetic (a) and natural (c) Cu_2O across temperatures from 100K to 350K. Both samples show a sharp peak in the lower energy range (10–20 meV), the inset (b) and (d) show expanding view of high photon energy between 20–30 meV range, multiple resonant features are visible in both materials. The natural Cu2O shows more distinct peaks, particularly around 24.5 meV, while the synthetic Cu_2O exhibits broader and smoother peaks.

Both samples exhibit a consistent sharp spectral feature between 10meV and 20meV, with the intensity increasing as the temperature decreases. Expanding the x-axis from 20 meV to 30 meV reveals multiple spectral features in both materials, which remain consistent throughout the measured spectra which suggests it is an inherent feature of the material. The natural sample displays more distinct peaks, particularly at 24.5 meV, while the synthetic Cu_2O shows similar features but with broader and smoother peaks. The temperature dependence of these features indicates some sharpening at lower temperatures suggesting some connection with phonon modes. Both samples show a significant rise in absorbance towards 50 meV.

6.5 Discussion

It is helpful to plot both the MIR and THz data on a single plot as shown in Figure 6.5. It is clear that there are four intense absorption bands.

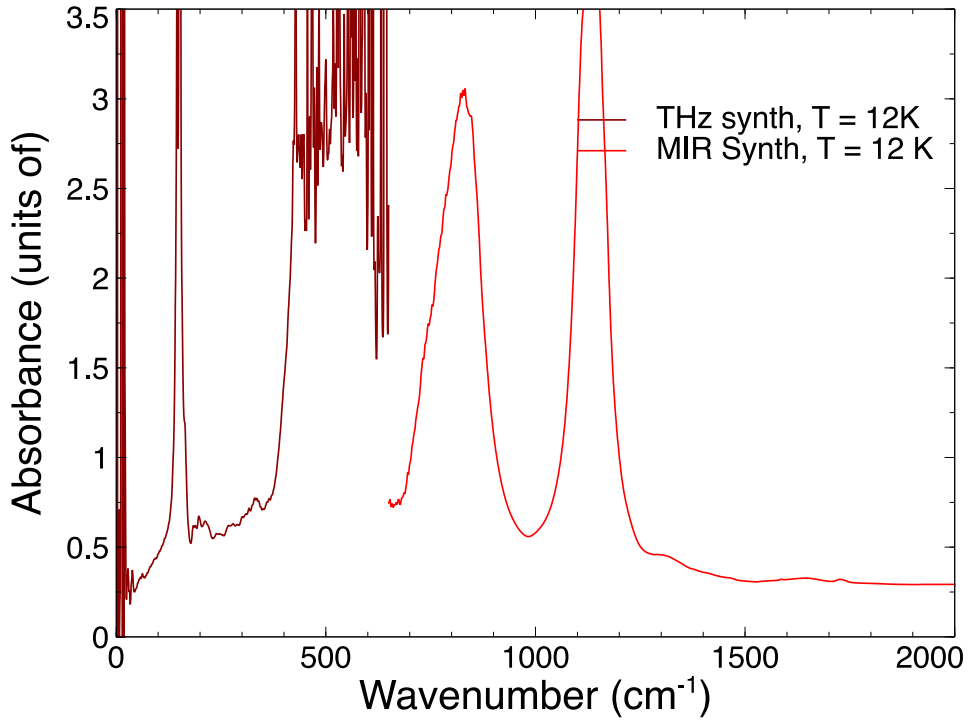

Figure 6.5: Combined MIR/THz absorption data for the synthetic sample at 12 K

So, can we explain the MIR/THz features in the absorption spectrum? Figure 6.6 shows the calculated phonon dispersion curves for Cu2O, with the phonon density of states. This data was calculated by our collaborators Alistair Brewin and Prof Stewert Clark at the University of Durham, using the CASTEP modelling code.

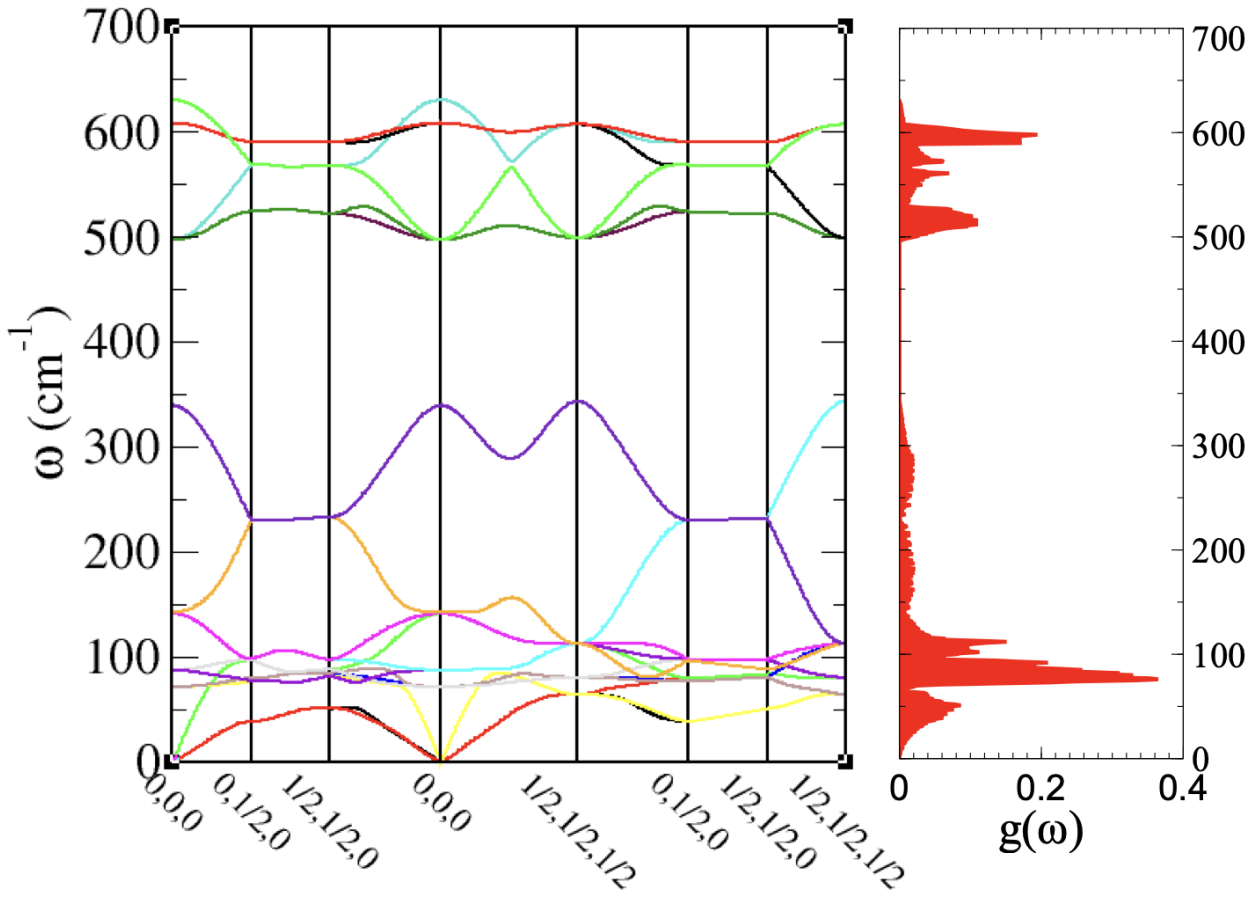

Figure 6.6: On the left, the phonon dispersion curves for Cu2O calculated using the CASTEP code. On the right, the phonon density of states associated with these dispersion curves.

One immediate observation is that it is clear from both plots in Figure 6.5 that the highest phonon mode in Cu_2O lies below 650 cm^{-1} and that there are no phonon modes above this. This initially poses a problem for explaining the two strong absorption bands in the MIR data. It is easier to understand what is going on if we overlay the phonon density of states from Figure 6.6 on the MIR/THz absorption data, as shown in Figure 6.7

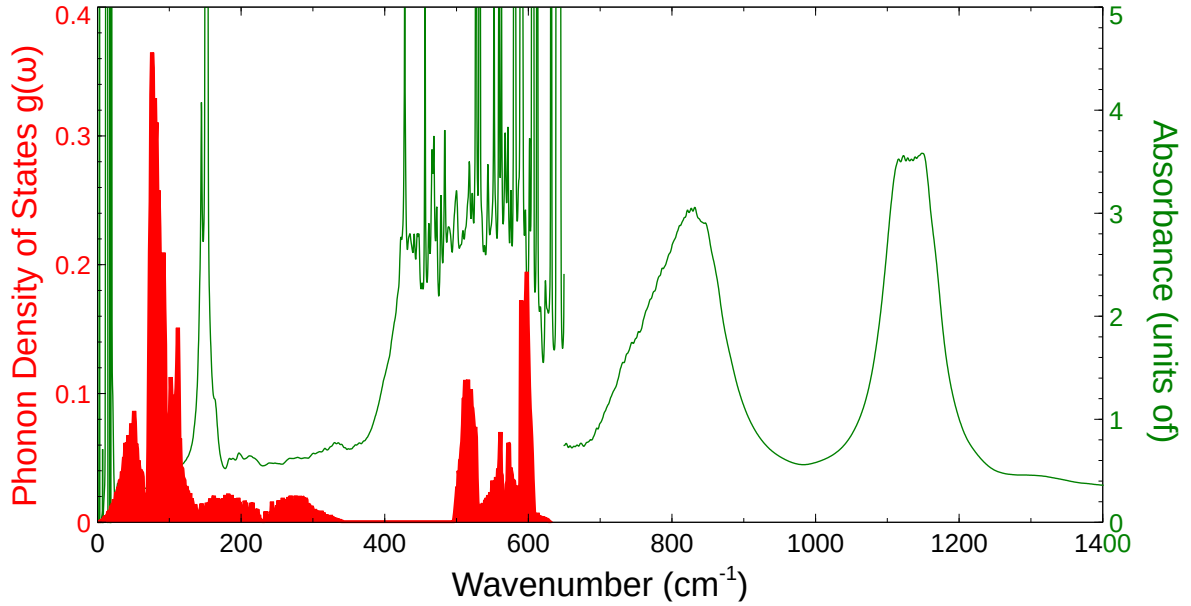

Figure 6.7: Combined MIR/THz absorption data for the synthetic sample at 12 K, with the calculated phonon density of states overlaid

Figure 6.7 indicates that the spectral absorption feature centred at 20 meV (160 cm^{-1}) corresponds to the peak at around 100 cm^{-1} in the phonon density of states. Note that we don't expect–the modelling presented in this study is not intended to provide precise quantitative predictions for the absorbance spectrum based on the phonon density of states (DoS). Instead, its primary objective is to reproduce the qualitative shape and relative positions of the peaks. While the spectral absorption feature centred at 20 meV (~160 cm^{-1}) does not perfectly overlap with the DoS peak around 100 cm^{-1}, this misalignment can be attributed to simplifications in the modelling process and experimental limitations. These discrepancies highlight the challenges inherent in correlating measured spectra with theoretical simulations in complex systems.

We hypothesize that the observed MIR spectral features are linked to multi-phonon absorption processes. This hypothesis is supported by the observation that the spectral

location of these features corresponds approximately to twice the energy of the dominant THz phonon band. This suggests that the MIR features may arise from higher-order phonon interactions, consistent with the energy scaling expected from multi-phonon processes.

The optical thickness of the sample plays a crucial role in the interpretation of the observed spectra. For optically thick samples, phonon bands are expected to manifest as regions of 0% transmission in the absorption spectrum. This phenomenon accounts for the noisy feature observed in the 400–600 cm^{-1} range of the THz absorption spectrum, as the bolometer detector used in this region has a lower dynamic range. Consequently, strong absorption results in noise rather than well-resolved spectral features.

The differences in detector sensitivity and dynamic range further explain the observed absorbance values. In the bolometer measurements, 0% transmission corresponds to an absorbance of ~3 due to the limited dynamic range. By contrast, the MCT detector, with its significantly higher dynamic range, would register 0% transmission as an absorbance of ~5. The maximum absorbance observed in the MIR spectrum is ~3.6, which indicates that a small amount of light (<0.1%) is still being transmitted. This observation supports the hypothesis that the MIR features correspond to higher-order replicas of the absorption bands associated with the dominant peaks in the phonon density of states.

The broad absorption band beginning above 50 meV (~400 cm^{-1}) aligns qualitatively with peaks in the phonon density of states. This suggests a direct relationship between the MIR spectral features and the underlying vibrational modes of the material. The shape and relative intensity of these features provide important insights into the vibrational dynamics of the system, even though quantitative agreement is not achieved.

In conclusion, while the measured and simulated peaks do not completely overlap, the qualitative agreement between the experimental absorbance spectrum and the phonon density of states supports the validity of our proposed hypotheses. The spectral features observed in the MIR region are consistent with multi-phonon absorption processes and are influenced by the limitations of the detectors and the optical thickness of the sample.

6.6 Conclusion

Our measurements provide new insight on the infrared and THz spectral properties of Cu_2O. By comparing our measurements against the calculated phonon spectrum of Cu_2O, we believe that we can explain (for the first time) the MIR absorption features between 100–115 meV and 135–155 meV, i.e. that they are higher order replicas of the Reststrahlen bands. We did not observe any additional features in either MIR or THz absorption spectra of the synthetic or natural samples, which suggests that there are no shallow impurity features in this material.

Chapter 7 Summary

This study addressed synthetic Cu_2O single crystals electrically and optically in several spectral regions with different techniques. This was motived by this material showing great promise for quantum technologies. Cu_2O is known for its unique excitonic properties, holds promise, particularly due to hosting Rydberg excitons that have high principal quantum number. This high excited exciton has a large Bohr radius mean that the excitons are microscale objects, which is interesting because they could be manipulated and transported over longer distances within the material. This is essential for integration of quantum technologies into larger scale system.

Understanding these properties is crucial for harnessing Cu_2O in future quantum applications. A central question driving this research was: why does synthetic Cu_2O exhibit poorer excitonic properties than natural (gemstone) Cu_2O? Or, to put it another way, why are the highest quantum number excitons observed only in natural gemstone material?

Therefore, the primary objective was to investigate the factors contributing to eliminating creation of excitons with high quantum numbers. Scientists question why synthetic Cu_2O doesn't match natural material in exciton quality, despite being purer and showing no X-ray diffraction differences. One hypotheses is that natural crystals form over millions of years, annealing defects, while synthetic growth in hours may leave atomic-scale defects. These defects can create electric fields that distort exciton wave functions, limiting the highest observable quantum number.

This thesis involved a combination of techniques that studying the electrical and optical properties of synthetic Cu_2O single crystal aiming to characterize (Hall measurements) and identify the defect states (PC and FTIR). The study revealed that synthetic Cu_2O suffer from

sub-bandgap defects which could hinder the formation of high excited excitons (reference, Science).

One of the key requirements of this work, discussed in Chapter 4, was optimizing Ohmic contacts on synthetic Cu_2O single crystals to enable accurate electrical characterization and defect analysis. Forming a stable Ohmic contact is crucial for reliable measurements and minimizing the specific contact resistance (ρ_c) allows for more precise assessment of Cu_2O's intrinsic properties, such as conductivity and Hall mobility. Specific contact resistance was studied using a CTLM design, experimenting with different metallization schemes, including Ni-Au, Ti-Au, and Au without an adhesion layer. Systematic testing showed that Au-Cu_2O achieved the most stable contact with the lowest specific contact resistance at ($1.689\times10^{-2}\Omega cm^{-2}$), L_T (7.8 um) and R (217.7 Ω), comparable to literature values and more stable than other schemes.

The successful formation of an Ohmic contact with minimal specific contact resistance could facilitate more precise electrical studies of Cu_2O. The Hall devices in Van der Pauw configuration were fabricated based on this result. The temperature dependent conductivity measurements of synthetic Cu_2O single crystal revealed a special behaviour with two different activation energies (0.2eV and 0.1eV) calculated from fitting dual-exponential functions of the conductivity vs temperature (based on Arrhenius equation). These activation energies correspond to different conduction mechanisms across the temperature range which could indicate the presence of different defect states. This typically suggests that at lower temperatures, carriers may be trapped by shallow defect states requiring a certain activation energy to participate in conduction. At higher temperatures carriers may be excited from deeper defect states corresponding to second higher activation energy. In addition, Hall measurements confirmed that the crystal has a single major electrical carrier with P-type. The carrier concentration confirmed that the material has two acceptors across the temperature range. The Hall mobility was also obtained; it was found to be 10 cm^{-2}/V.s, showing minimal variation across the studied temperature. Phonon scattering and neutral impurity scattering were found to dominate the mechanisms limiting Hall mobility.

Then the same contact metal (Au) was used to fabricate specific device to study and investigate the photoconductivity of Cu_2O. This technique was discussed in detail in Chapter 5, which focuses on identifying defect states using a novel technique which is pulsed wavelength-tuned laser photoconductive spectroscopy. The measurement was taken in the ambient environment. This technique was developed in our lab and has proven to offer significant advantages over traditional absorption spectroscopy like UV-vis. These photoconductivity measurements were performed in a time-resolved manner which was key to distinguishing between different optical process in Cu_2O by analysing the time-dependent photoresponse. We were able to identify certain processes involved in the radiation decay: fast decay followed by slower decay indicating the process of multi trapping and recombination process. One of the unique aspects of this thesis is using this novel technique and the optimized experiment and analysis. This allowed for a comprehensive analysis of material behaviour across tuning wavelength in the range between 800nm and 1500nm. As a result, sub-band defects were detected at 820nm, 900nm, 930nm, 980nm. Some supporting techniques were also applied to assist this result. The method's sensitivity to the sub-band defect states makes it a powerful tool for characterizing semiconductor and designing a faster feedback optimisation loop to track changes due to post growth treatment of crystals.

In conclusion from Chapter 6, our measurements offer new insights into the infrared and THz spectral properties of Cu_2O. By comparing our experimental data with the calculated phonon spectrum, we provide the first explanation for the MIR absorption features observed between 100–115 meV and 135–155 meV, attributing them to higher-order replicas of the Reststrahlen bands. Additionally, the absence of any further features in the MIR or THz absorption spectra of both synthetic and natural samples indicates that shallow impurity levels are not present in this material.

The future work would be focused on the novel technique that has been studied in this thesis - the spectral resolved spectroscopy to pulsed wavelength-tuned laser photoconductivity. The future work focuses on two primary areas within material science: post-growth treatments and defect analysis during fabrication processes. Notably, this

technique operates effectively at ambient temperature, eliminating the need for cryogenic environments, which makes it highly practical and accessible for a wide range of applications.

(i) **Post-Growth Treatments:** The proved sensitivity of this technique to sub-band defect states, combined with its ability to function at ambient temperature, makes it an ideal tool for exploring the effects of various post-growth treatments, such as annealing, doping, and surface passivation. Future studies could systematically investigate how these treatments influence defect states, potentially leading to the development of tailored post-processing techniques to enhance device performance. Understanding the impact of these treatments on defect states will be crucial for optimizing material properties and improving the overall efficiency of the devices.

(ii) **Defect Analysis During Fabrication:** Another significant area for future exploration is to investigate defects introduced during fabrication processes. By analyzing the changes in defect states before and after fabrication, this technique could provide valuable insights into the nature of specific defects introduced, their characteristics, and their potential impact on device properties. The ability to perform these analyses at ambient temperature significantly simplifies the process, allowing for more routine and widespread implementation. Expanding this application beyond material characterization to studying defect states in actual devices, such as solar cells and LEDs, could offer a deeper understanding of the role these defects play in device performance. This knowledge could lead to new strategies for enhancing device efficiency and stability.

Appendix

A. Metallization scheme

Two different metallization schemes involving Ti-Au and Ni-Au layers (10:300nm) were implemented on Cu_2O.

In the first scheme, Ti-Au was used, the CTLM configuration was applied to characterize the contact by applying a DC voltage source. The as-deposited I-V results showed a linear relationship, as depicted in Figure A.1 (a), indicating an Ohmic contact between the metal and Cu_2O. The CTLM used in this study included six different gap spacings on the mask, ranging from 8 µm to 48 µm. This configuration allowed for six separate resistance measurements, each corresponding to a different gap spacing. The results demonstrated that the measured resistance varied with changes in the gap spacing, then applied the correction factors as explained in the main chapter to obtain the linear relationship figure A.1(b). The linear fit to the corrected data yielded the following parameters: (i) the transfer length, L_T, was determined to be 9.65 µm, (ii) the sheet resistance, Rs, was measured at 3.303×10^4 Ω /□, and (iii) the specific contact resistance, ρ_c was found to be 3.075×10^{-2} Ω cm². However, achieving a stable contact was challenging in this case because the metal layer on Cu_2O became unstable. When attempting to alloy it by rapid annealing at 100°C to ensure proper adhesion of the metal to the crystal, the metal layer peeled off.

In the second metallization scheme, Ni-Au (20-300 nm) was deposited on Cu_2O in a CTLM configuration, and the contact was tested. FigureA.1(c) shows as-deposited I-V results were linear. The contact parameters extracted from linear fitting between the total resistance and gap spacing were as follows: the total resistance R_c, was 558.3 Ω, the transfer length L_T, was 7.6 µm, the sheet resistance Rs, was 9.206×10^4 Ω/□, and the specific contact resistance was 5.31×10^{-2}Ω cm² as shown in figureA.1(d). However, similar to the first scheme, the contact peeled off once annealed to alloy the contact.

Given the difficulty of stabilizing these contacts and the higher specific contact resistance observed in both the Ti-Au and Ni-Au schemes, we decided to continue using Au as the contact material looking to its stability and lower specific contact resistance.

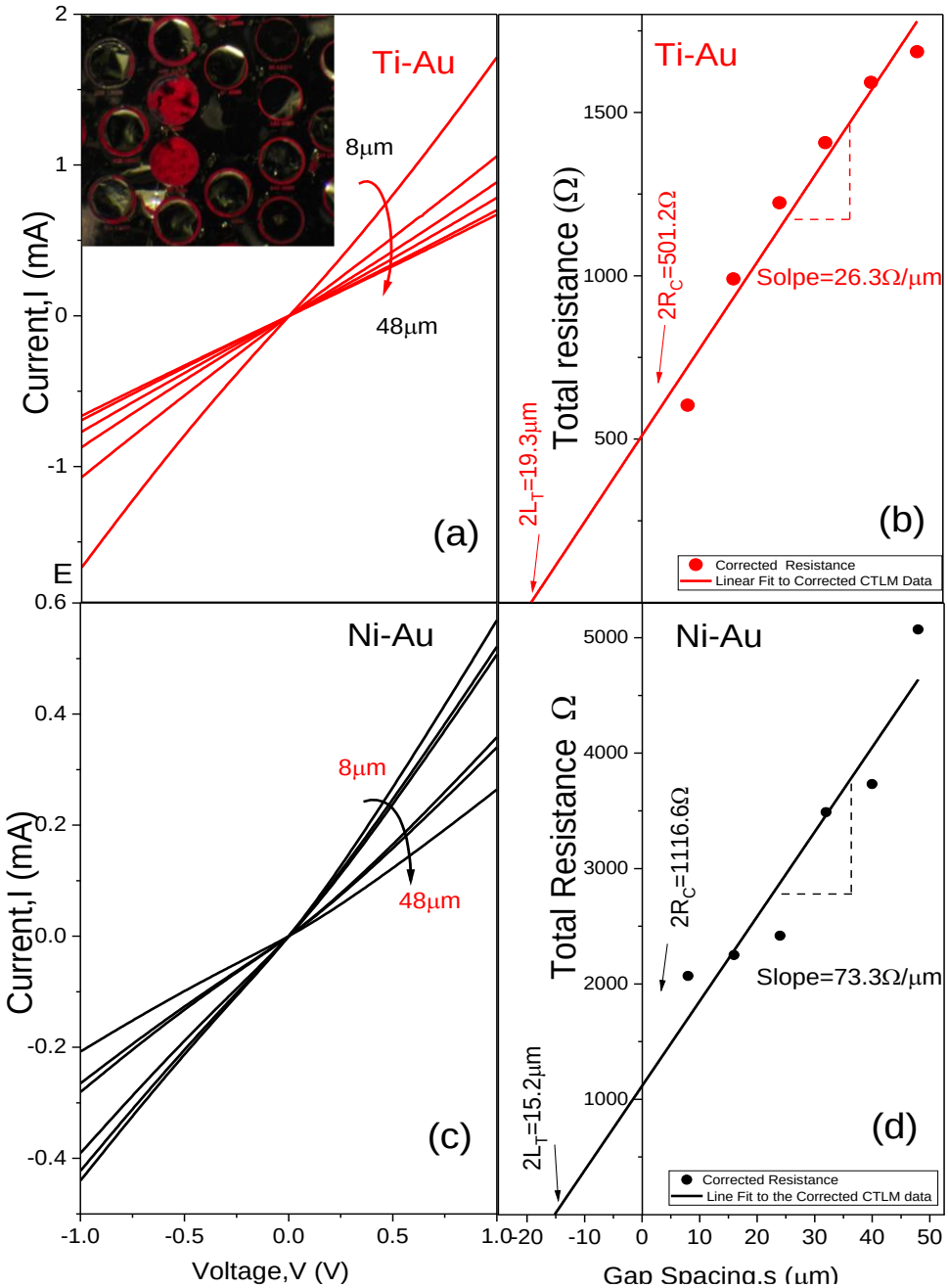

Figure A.1 (a, b) show the characterization of Ti-Au contacts on Cu_2O. (a) depicts the current-voltage (I-V) behaviour as a function of gap spacing, ranging from 8 to 48 μm, indicating Ohmic contact. (b) presents the corrected resistance as a function of gap spacing, with its linear fit which used to determine the contact parameters. (c, d) illustrate the characterization of Ni-Au contacts on Cu_2O. (c) shows the linear I-V relationship, confirming Ohmic contact. (d) displays the corrected resistance versus gap spacing, with linear fitting applied to extract the contact parameters. The inset shows the contact peeled off when annealed.

B- Normalized Photoconductance Spectra of Cu_2O Under Nanosecond-laser pulsed Excitation Measured at Different Biasing at Visible Regime:

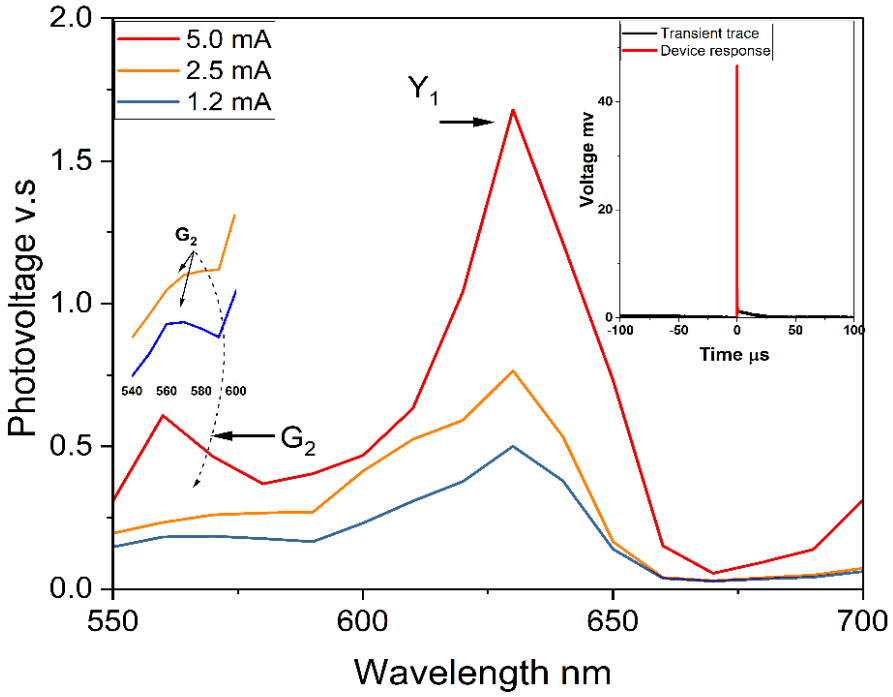

Figure B.1 Spectral behaviour of the photoconductive transient trace for three different bias conditions (1.2, 2.5, and 5 mA). Laser fluctuations at each wavelength were accounted for by normalizing the device response with the reference Si diode response. The inset show the transient trace of 600nm nm the slow response is not notice at this region.

Figure B.1 presents typical photoconductivity spectra of a Cu_2O single crystal in the Vis spectrum region, measured at different electrical bias currents of 1.2 mA, 2.5 mA, and 5.0 mA. This was normalized as demonstrated previously by considering the Si diode as reference and the manufacture data to obtain the device response.

The normalized photoconductivity spectra show two primary peaks, indicated by arrows, corresponding to the green 2P and yellow 1s excitonic states (labelled as G2 and Y1, respectively) [191]. The dominant peak (Y1) is associated with an indirect transition from the ground state to the yellow 1s excitonic state. This transition involves the absorption and subsequent emission of optical phonons, as indicated in Cu_2O material [22]. The G2 is more

pronounced at 5.0mA as increasing the biasing enhanced the spectrum signal compared [192]the other two shown in the inset. These excitonic peaks, have been previously identified within the visible region of Cu_2O spectra. The presence of these peaks is reaffirmed in our study using a time-resolved photoconductivity technique, demonstrating the reliability of this technique in detecting excitonic transitions in Cu_2O.

C Averaging Results for Device Spectrum Measurement

This appendix provides detailed description of the procedures and result related to the device normalized spectrum measurements described in (5.8). The aim is to elaborate on methodological specifics and quantitative finding from the experiment involving spectral analysis.

C.1 Data Collection

The spectral response of the device was recorded as following:

- Spectrum Range: The device response was recorded from 800 nm to 1500 nm across the IR spectrum.
- Repetitions: Each measurement was conducted 20 times, capturing comprehensive data across the specified range.
- Transient Trace Processing: For each wavelength, the transient trace was analysed to determine the device's response. Each wavelength exhibited a unique response profile.
- Background removing: Background noise was removed numerically during post-processing, using a cubic fitting function to simulate and subtract the impedance-related amplitude variation and phase shift caused by the charge carriers generated in the active device.
- Response Types: The resulting transient traces demonstrated varying dynamics, including fast responses followed by slower decay phases. This dynamic behaviour was crucial for understanding the device's photoresponse characteristics (see inset in Figure C.2 & C.3).

- Integration of Response: To quantify the photoresponse at each wavelength, the area under the curve was integrated separately for the fast and slow responses. This integration provided a detailed measure of the total photoresponse spectra exhibited by the device at each point in the spectrum these spectra provided at Figure C.2 for the fast response and Figure C.3 for the decay response.
- Averaging the Spectrum: After processing the individual measurements, the photoresponse spectra obtained from each repetition were averaged. This averaging helped to smooth out anomalies and provide a clearer, more reliable representation of the device's overall spectral performance (Figure C.2 for fast and figure C.3 for the slow).

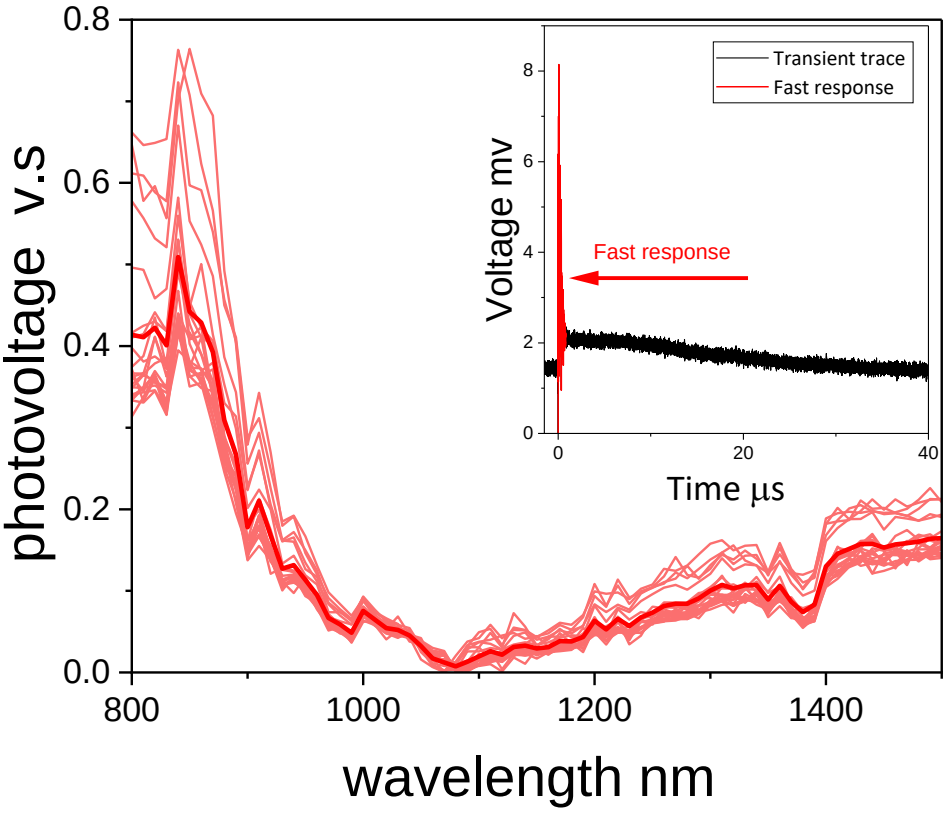

Figure C.2: Unprocessed spectral data of the device's fast response. The light blue spectra represent individual sweeps, with each sweep corresponding to a separate measurement. The dark blue line illustrates the averaged photovoltage. Inset: A transient trace captured at 800 nm, highlighting the

device's initial fast response. The area under the red curve has been integrated to calculate the fast response spectrum.

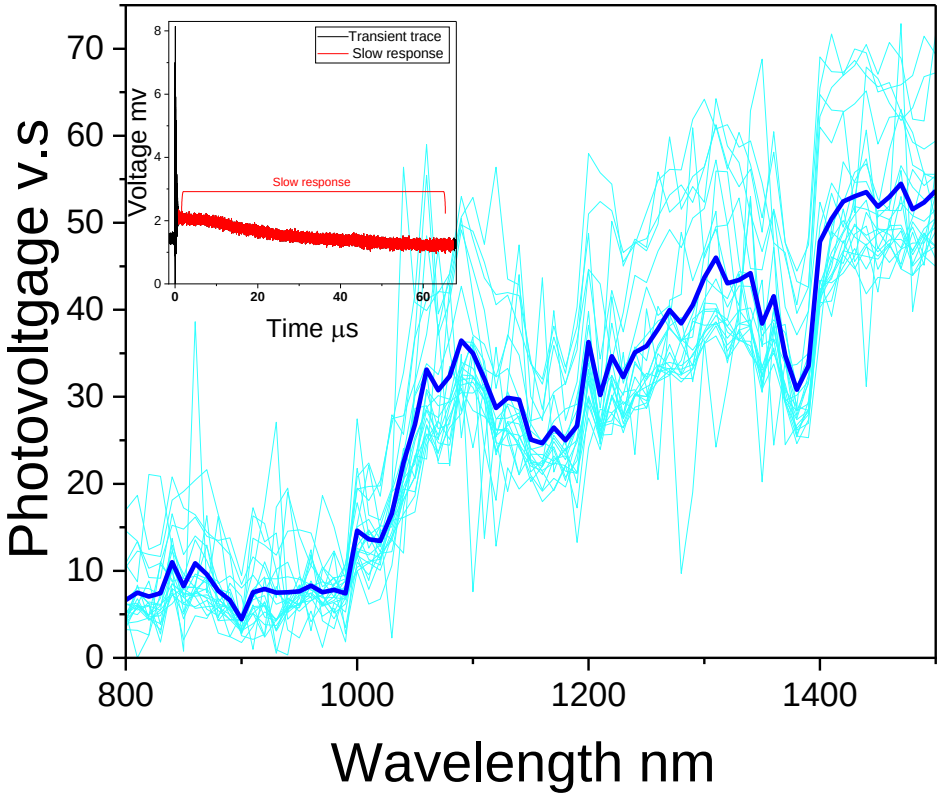

Figure C.3: Unprocessed spectral data of the device's slow response. The light pink spectra represent individual sweeps, with each sweep corresponding to a separate measurement. The dark pink line illustrates the averaged photovoltage. Inset: A transient trace captured at 800 nm, highlighting the device's initial fast response. The area under the red curve has been integrated to calculate the slow response spectrum.

However, some of the time traces were statistically excluded from the averaging as we encountered (<5% of measurement) triggering problems caused a phase jump which manifested as a wobble on the curve when the oscilloscope calculated the average. An example of this is shown in Figure C.4. We used the following statistically robust method to disregard these scans without adding human bias. we calculated the mean and standard deviation of fast and slow response as explained previously then we ignored outliers that were outside the standard deviation and recalculated the mean without the outliers. Figure

C.5 shows the operation of this process for the 22 scans recorded at λ = 940 nm. The red circles highlight scans that have been identified by the algorithm to be outliers. Scan number 13 is the shown in Figure C.4(b).

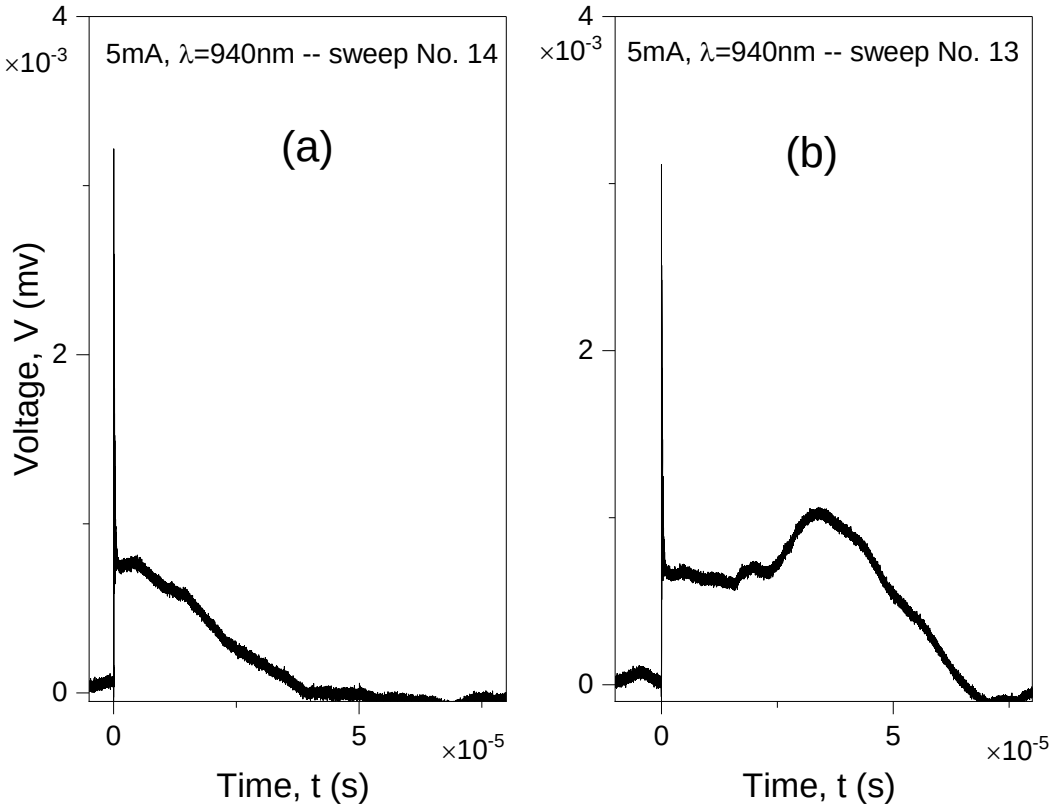

Figure C.4: (a) Typical signal subtraction with fitted cubic background. (b) Bad signal subtraction due to improper cubic fit.

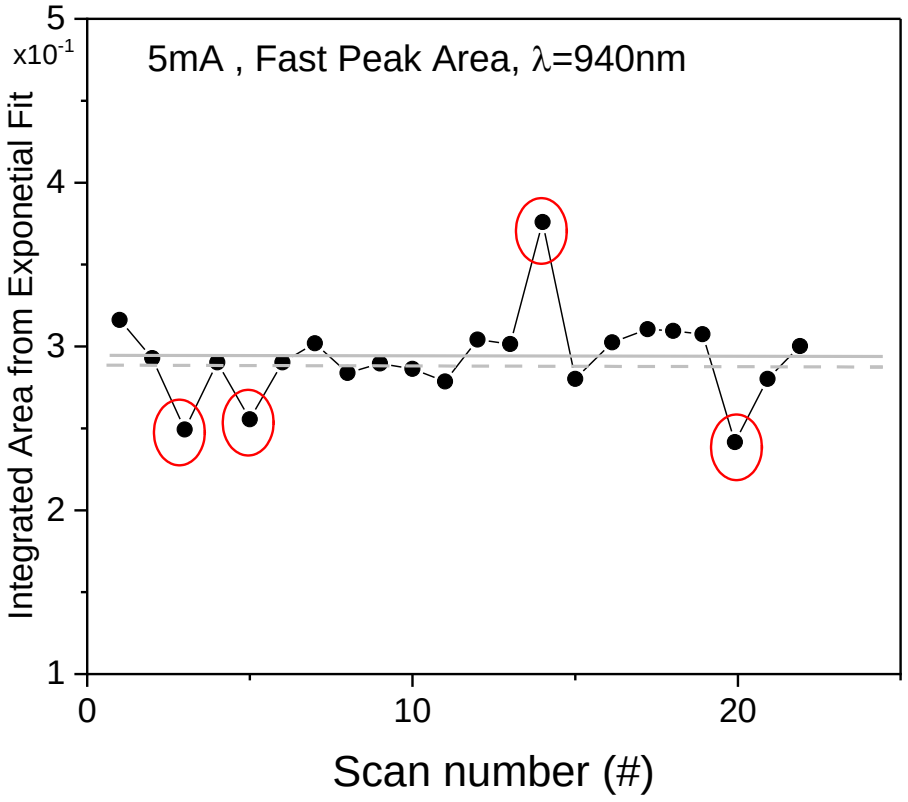

Figure C.5: Comparing the electrical pickup with, and without, the excitation light blocked.

C.2 Calibration Using Reference Diodes

Two types of reference diodes were used:

- **Si Diode for Vis Spectrum:** Employed for calibrating the device response in the visible region.
- **InGaAs Diode for IR Spectrum:** Used for calibrating the device response in the IR region.

Each reference diode was used to measure the pulsed laser intensity as the same time as the device response measured therefore it was repeated 20 times and then the measurements were averaged to obtain a stable reference spectrum for each diode (see Figure C.6 & C.7). For both reference diodes, manufacturer-provided spectral response data were used to identify the detectivity region of both and compare their response trend with

the experimental data. This comparison is crucial for assessing the diode response quality of the laser source itself. And then use this data to calculate the calibration factor.

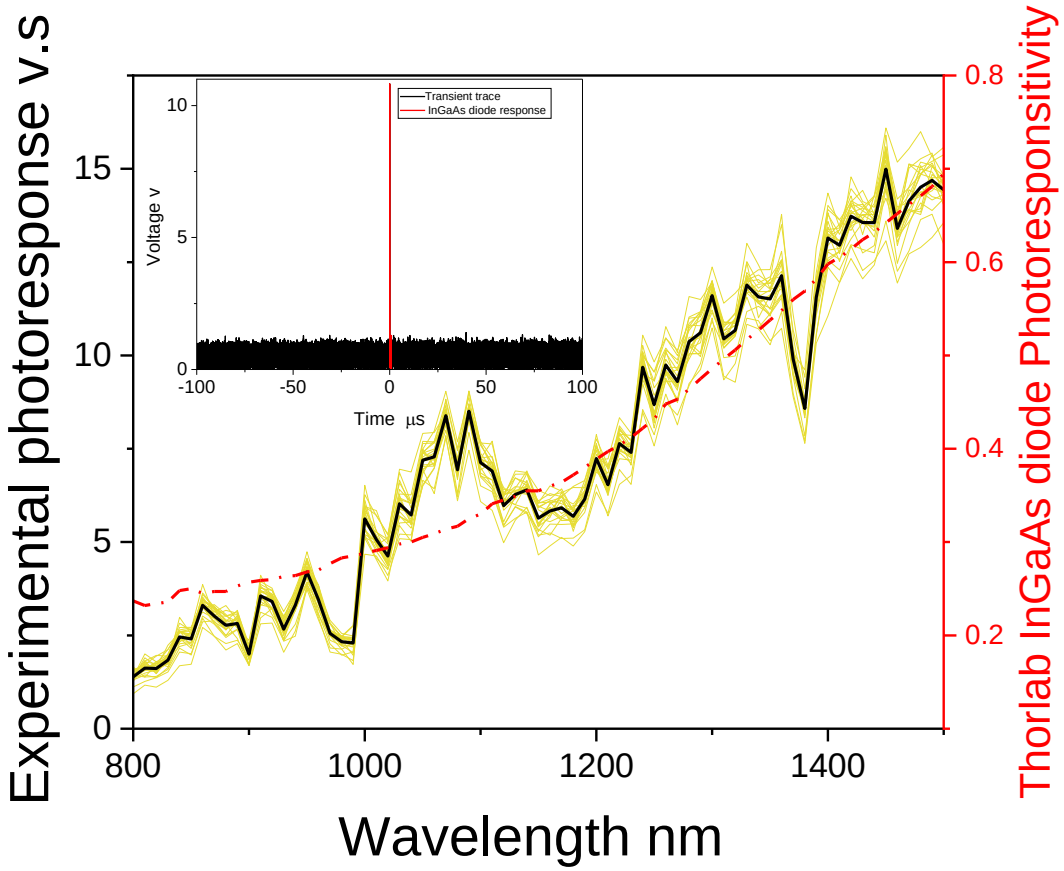

Figure C.6: Photoresponse spectra of InGaAs photodiode over various wavelengths and sweeps. The light-yellow lines represent the individual photoresponse traces from different sweeps, illustrating the variability across measurements. The solid black line is the averaged spectrum, providing a baseline photoresponse. The red dashed line represents the standard photoresponsivity.

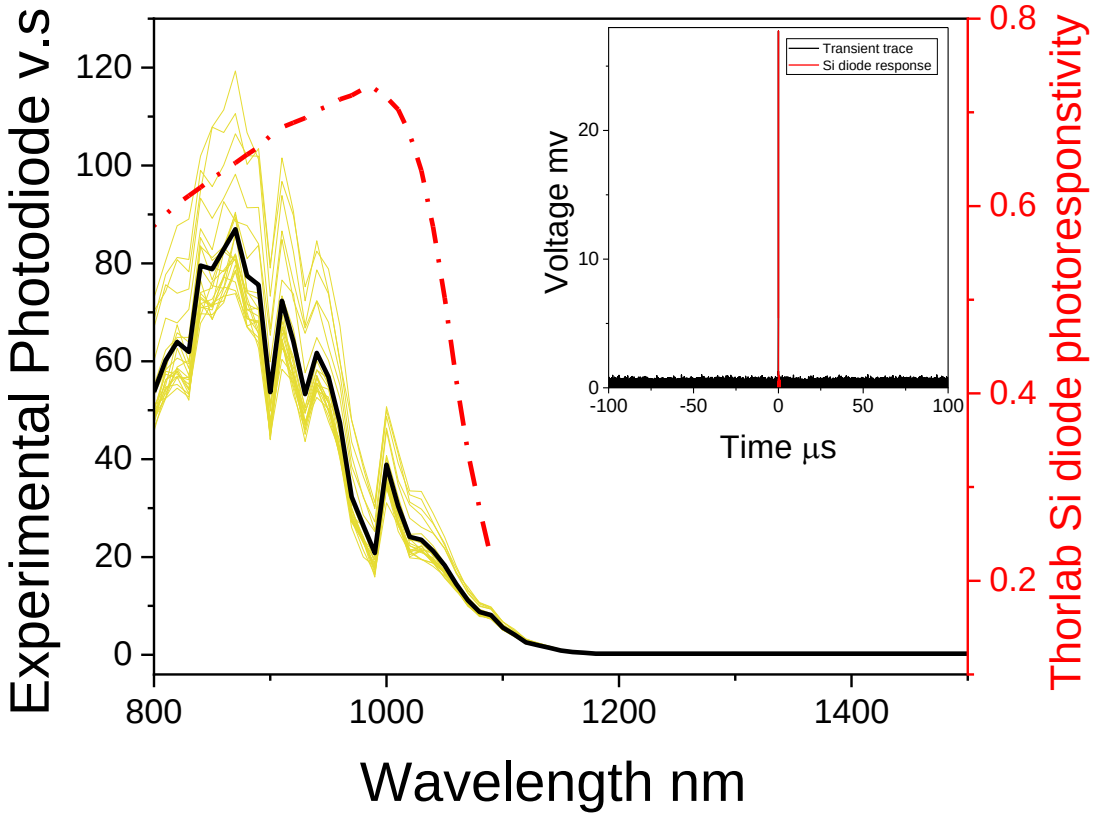

Figure. C.7: Photoresponse spectra of a Si photodiode over various wavelengths and sweeps. The light-yellow lines represent the individual photoresponse traces from different sweeps, illustrating the variability across measurements. The solid black line is the averaged spectrum, providing a baseline photoresponse. The red dashed line represents the standard photoresponsivity curve for the diode, as provided by Thorlabs. In the inset, a transient response trace at 700 nm is shown, with the diode's response to a light pulse highlighted. The area under the red pulse in the inset has been integrated to derive the diode's photoresponse at this specific wavelength.

Reference

[1] "NQTP | UK National Quantum Technologies Programme." https://uknqt.ukri.org/ (accessed Aug. 15, 2024).

[2] "Homepage of Quantum Flagship | Quantum Flagship." https://qt.eu/ (accessed Aug. 15, 2024).

[3] B. C. Barish and R. Weiss, "LIGO and the detection of gravitational waves," *Phys. Today*, vol. 52, no. 10, pp. 44–50, 1999.

[4] M. A. Nielsen and I. L. Chuang, *Quantum computation and quantum information*. Cambridge university press, 2010.

[5] L. K. Grover, "A fast quantum mechanical algorithm for database search," in *Proceedings of the twenty-eighth annual ACM symposium on Theory of computing*, 1996, pp. 212–219.

[6] J. I. Cirac and P. Zoller, "Quantum computations with cold trapped ions," *Phys. Rev. Lett.*, vol. 74, no. 20, p. 4091, 1995.

[7] C. Wang *et al.*, "Towards practical quantum computers: Transmon qubit with a lifetime approaching 0.5 milliseconds," *npj Quantum Inf.*, vol. 8, no. 1, p. 3, 2022.

[8] T. Kazimierczuk, D. Fröhlich, S. Scheel, H. Stolz, and M. Bayer, "Giant Rydberg excitons in the copper oxide Cu 2 O," *Nature*, vol. 514, no. 7522, pp. 343–347, 2014.

[9] A. Browaeys and T. Lahaye, "Many-body physics with individually controlled Rydberg atoms," *Nat. Phys.*, vol. 16, no. 2, pp. 132–142, 2020.

[10] M. Khazali, K. Heshami, and C. Simon, "Single-photon source based on Rydberg exciton blockade," *J. Phys. B At. Mol. Opt. Phys.*, vol. 50, no. 21, p. 215301, 2017.

[11] J. E. Arem, "Color encyclopedia of gemstones," *(No Title)*, 1987.

[12] T. Ito, H. Yamaguchi, K. Okabe, and T. Masumi, "Single-crystal growth and characterization of Cu2O and CuO," *J. Mater. Sci.*, vol. 33, pp. 3555–3566, 1998.

[13] M. A. M. Versteegh *et al.*, "Giant Rydberg excitons in Cu 2 O probed by photoluminescence excitation spectroscopy," *Phys. Rev. B*, vol. 104, no. 24, p. 245206, 2021.

[14] S. A. Lynch *et al.*, "Rydberg excitons in synthetic cuprous oxide Cu 2 O," *Phys. Rev. Mater.*, vol. 5, no. 8, p. 84602, 2021.

[15] K. Zanio, *Semiconductors and semimetals*. Academic Press, 1978.

[16] R. J. Elliott, “Symmetry of excitons in Cu 2 O,” *Phys. Rev.*, vol. 124, no. 2, p. 340, 1961.

[17] C. Uihlein, D. Fröhlich, and R. Kenklies, “Investigation of exciton fine structure in Cu2O,” *Phys. Rev. B*, vol. 23, no. 6, pp. 2731–2740, 1981, doi: 10.1103/PhysRevB.23.2731.

[18] J. B. Grun, M. Sieskind, and S. Nikitine, “Etude spectrophotometrique des spectres continus de Cu2O a diverses temperatures,” *J. Phys. Chem. Solids*, vol. 19, no. 3–4, pp. 189–197, 1961.

[19] T. Ito and T. Masumi, “Detailed Examination of Relaxation Processes of Excitons in Photoluminescence Spectra of Cu 2O,” *J. Phys. Soc. Japan*, vol. 66, no. 7, pp. 2185–2193, Jul. 1997, doi: 10.1143/JPSJ.66.2185.

[20] J. W. Hodby, T. E. Jenkins, C. Schwab, H. Tamura, and D. Trivich, “Cyclotron resonance of electrons and of holes in cuprous oxide, Cu2O,” *J. Phys. C Solid State Phys.*, vol. 9, no. 8, p. 1429, 1976.

[21] A. Goltzené and C. Schwab, “Impurity scattering effect on the cyclotron resonance of carriers in Cu2O,” *Phys. status solidi*, vol. 92, no. 2, pp. 483–487, 1979.

[22] D. W. Snoke, A. J. Shields, and M. Cardona, “Phonon-absorption recombination luminescence of room-temperature excitons in Cu 2 O,” *Phys. Rev. B*, vol. 45, no. 20, p. 11693, 1992.

[23] F. L. Weichman, “Photoconductivity of cuprous oxide in relation to its other semiconducting properties,” *Phys. Rev.*, vol. 117, no. 4, p. 998, 1960.

[24] A. Daunois, J. L. Deiss, and B. Meyer, “Étude spectrophotométrique de l’absorption bleue et violette de Cu2O,” *J. Phys.*, vol. 27, no. 3–4, pp. 142–146, 1966.

[25] X. Nie, S.-H. Wei, and S. B. Zhang, “First-principles study of transparent p-type conductive SrCu 2 O 2 and related compounds,” *Phys. Rev. B*, vol. 65, no. 7, p. 75111, 2002.

[26] T. Ohyama, T. Ogawa, and H. Nakata, “Determination of deformation-potential constants of Cu 2 O by microwave cyclotron resonance,” *Phys. Rev. B*, vol. 56, no. 7, p. 3871, 1997.

[27] F. Bruneval, “Exchange and correlation in the electronic structure of solids, from silicon to cuprous oxide: GW approximation and beyond,” *PhD Thesis*, 2005.

[28] J. P. Hu *et al.*, “On-site interband excitations in resonant inelastic x-ray scattering from Cu 2 O,” *Phys. Rev. B—Condensed Matter Mater. Phys.*, vol. 77, no. 15, p. 155115, 2008.

[29] A. Önsten *et al.*, “Probing the valence band structure of Cu 2 O using high-energy angle-resolved photoelectron spectroscopy,” *Phys. Rev. B—Condensed Matter Mater. Phys.*, vol. 76, no. 11, p. 115127, 2007.

[30] L. Kleinman and K. Mednick, “Self-consistent energy bands of Cu 2 O,” *Phys. Rev. B*, vol. 21, no. 4, p. 1549, 1980.

[31] J. Robertson, “Electronic structure and x-ray near-edge core spectra of Cu 2 O,” *Phys. Rev. B*, vol. 28, no. 6, p. 3378, 1983.

[32] D. Trivich, “Photovoltaic cells and their possible use as power converters for solar energy,” 1953.

[33] Https://www.durham.ac.uk/staff/s-j-clark/, “Professor Stewart Clark.” .

[34] M. M. Beg and S. M. Shapiro, “Study of phonon dispersion relations in cuprous oxide by inelastic neutron scattering,” *Phys. Rev. B*, vol. 13, no. 4, p. 1728, 1976.

[35] M. Ivanda, D. Waasmaier, A. Endriss, J. Ihringer, A. Kirfel, and W. Kiefer, “Low-temperature anomalies of cuprite observed by Raman spectroscopy and x-ray powder diffraction,” *J. Raman Spectrosc.*, vol. 28, no. 7, pp. 487–493, 1997.

[36] Y. Petroff, P. Y. Yu, and Y. R. Shen, “Study of photoluminescence in Cu 2 O,” *Phys. Rev. B*, vol. 12, no. 6, p. 2488, 1975.

[37] V. M. Burlakov, M. Göppert, A. Jolk, A. Dinger, R. Becker, and C. F. Klingshirn, “On a biphononic origin of the 1125 cm− 1 absorption band in cuprous oxide,” *Phys. Lett. A*, vol. 254, no. 1–2, pp. 95–100, 1999.

[38] M. Jörger, T. Fleck, C. Klingshirn, and R. Von Baltz, “Midinfrared properties of cuprous oxide: High-order lattice vibrations and intraexcitonic transitions of the 1 s paraexciton,” *Phys. Rev. B—Condensed Matter Mater. Phys.*, vol. 71, no. 23, p. 235210, 2005.

[39] L. Tertian, D. Hokim, and J. P. Rivière, “Transformations in thin foils of cuprous oxide as observed in an electron microscope,” *J. Phys.*, vol. 39, no. 10, pp. 1135–1139, 1978.

[40] R. D. Schmidt-Whitley, M. Martinez-Clemente, and A. Revcolevschi, “Growth and microstructural control of single crystal cuprous oxide Cu2O,” *J. Cryst. Growth*, vol. 23, no. 2, pp. 113–120, 1974.

[41] R. S. Zucker, “Growth of single crystal cuprous oxide from the melt and luminescence of cuprous oxide,” *J. Electrochem. Soc.*, vol. 112, no. 4, p. 417, 1965.

[42] S. M. Koohpayeh, D. Fort, and J. S. Abell, “The optical floating zone technique: A review of experimental procedures with special reference to oxides,” *Prog. Cryst. Growth Charact. Mater.*, vol. 54, no. 3–4, pp. 121–137, 2008.

[43] A. Neubauer, J. Bœuf, A. Bauer, B. Russ, H. v Löhneysen, and C. Pfleiderer, “Ultra-high vacuum compatible image furnace,” *Rev. Sci. Instrum.*, vol. 82, no. 1, 2011.

[44] J. L. Schmehr, M. Aling, E. Zoghlin, and S. D. Wilson, “High-pressure laser floating zone furnace,” *Rev. Sci. Instrum.*, vol. 90, no. 4, 2019.

[45] I. Nagai, N. Shirakawa, S. Ikeda, R. Iwasaki, H. Nishimura, and M. Kosaka, “Highest conductivity oxide SrMoO3 grown by a floating-zone method under ultralow oxygen partial pressure,” *Appl. Phys. Lett.*, vol. 87, no. 2, 2005.

[46] N. Kikugawa, “Recent Progress of Floating-Zone Techniques for Bulk Single-Crystal Growth,” *Crystals*, vol. 14, no. 6, p. 552, 2024.

[47] R. Hermann, G. Gerbeth, and J. Priede, “Magnetic field controlled floating-zone single crystal growth of intermetallic compounds,” *Eur. Phys. J. Spec. Top.*, vol. 220, no. 1, pp. 227–241, 2013.

[48] K. E. Avers *et al.*, “Electron-beam floating-zone refined UCoGe,” *Phys. Rev. Mater.*, vol. 5, no. 5, p. 54803, 2021.

[49] R. E. De La Rue and F. A. Halden, “Arc-Image Furnace for Growth of Single Crystals,” *Rev. Sci. Instrum.*, vol. 31, no. 1, pp. 35–38, 1960.

[50] J. L. Schmehr and S. D. Wilson, “Active crystal growth techniques for quantum materials,” *Annu. Rev. Mater. Res.*, vol. 47, no. 1, pp. 153–174, 2017.

[51] G. Blankenburg and K. Kassel, “Über die Halbleitereigenschaften des Kupferoxyduls. I Das Herstellungsverfahren unter Berücksichtigung der Stabilitätsbedingungen,” *Ann. Phys.*, vol. 445, no. 4-5, pp. 201–210, 1952.

[52] Y. Ebisuzaki, “Preparation of monocrystalline cuprous oxide,” *J. Appl. Phys.*, vol. 32, no. 10, pp. 2027–2028, 1961.

[53] A. Kinoshita and T. Nakano, “Cu2O crystal growth by hydrothermal technique,” *Jpn. J. Appl. Phys.*, vol. 6, no. 5, p. 656, 1967.

[54] W. S. Brower, “Jr. and HS Parker,” *J. Cryst. Growth*, vol. 8, p. 227, 1971.

[55] D. Trivich and G. P. Pollack, “Preparation of Single Crystals of Cuprous Oxide in an Arc-Image Furnace,” *J. Electrochem. Soc.*, vol. 117, no. 3, p. 344, 1970.

[56] A. F. Wright and J. S. Nelson, “Theory of the copper vacancy in cuprous oxide,” *J. Appl. Phys.*, vol. 92, no. 10, pp. 5849–5851, 2002.

[57] M. Nolan and S. D. Elliott, “Tuning the electronic structure of the transparent conducting oxide Cu2O,” *Thin Solid Films*, vol. 516, no. 7, pp. 1468–1472, 2008.

[58] H. Raebiger, S. Lany, and A. Zunger, “Origins of the p-type nature and cation deficiency in Cu 2 O and related materials,” *Phys. Rev. B*, vol. 76, no. 4, p. 45209,

2007.

[59] A. Soon, X.-Y. Cui, B. Delley, S.-H. Wei, and C. Stampfl, “Native defect-induced multifarious magnetism in nonstoichiometric cuprous oxide: First-principles study of bulk and surface properties of Cu 2− δ O,” *Phys. Rev. B*, vol. 79, no. 3, p. 35205, 2009.

[60] K. B. Chang, L. Frazer, J. J. Schwartz, J. B. Ketterson, and K. R. Poeppelmeier, “Removal of copper vacancies in cuprous oxide single crystals grown by the floating zone method,” *Cryst. Growth Des.*, vol. 13, no. 11, pp. 4914–4922, 2013.

[61] E. J. Mittemeijer and U. Welzel, *Modern diffraction methods*. John Wiley & Sons, 2013.

[62] M. O’Keeffe and W. J. Moore, “Electrical conductivity of monocrystalline cuprous oxide,” *J. Chem. Phys.*, vol. 35, no. 4, pp. 1324–1328, 1961.

[63] W. H. Brattain, “The copper oxide rectifier,” *Rev. Mod. Phys.*, vol. 23, no. 3, p. 203, 1951, doi: 10.1103/RevModPhys.23.203.

[64] S. Lany and A. Zunger, “Anion vacancies as a source of persistent photoconductivity in II-VI and chalcopyrite semiconductors,” *Phys. Rev. B*, vol. 72, no. 3, p. 35215, 2005.

[65] M. Tapiero, J. P. Zielinger, and C. Noguet, “Photomemory effect in Cu2O single crystals. Phenomenology and interpretation,” *Phys. status solidi*, vol. 33, no. 1, pp. 155–166, 1976.

[66] J. P. Zielinger, C. Noguet, and M. Tapiero, “Photomemory effect in Cu2O single crystals kinetics of the excitation and de-excitation processes,” *Phys. status solidi*, vol. 42, no. 1, pp. 91–100, 1977.

[67] F. Biccari, “Defects and Doping in Cu2O,” University of Rome, 2009.

[68] H. Shimada and T. Masumi, “Hall mobility of positive holes in Cu2O,” *J. Phys. Soc. Japan*, vol. 58, no. 5, pp. 1717–1724, 1989.

[69] F. A. Tazenkov, B. A. and Gruzdev, “Positive and negative photomemory in cuprous oxide.,” *Sov. Phys. - Solid State,* vol. 16, p. 460, 1974.

[70] M. Zouaghi, M. Tapiero, J. P. Zielinger, and R. Burgraf, “Hall mobility and hole density in photoactivated Cu2O single crystals,” *Solid State Commun.*, vol. 8, no. 22, pp. 1823–1825, 1970.

[71] T. Masumi, R. K. Ahrenkiel, and F. C. Brown, “Hall mobility of slow electrons in AgCl and the effects of crystal purity,” *Phys. status solidi*, vol. 11, no. 1, pp. 163–174, 1965.

[72] E. Conwell and V. F. Weisskopf, “Theory of impurity scattering in semiconductors,” *Phys. Rev.*, vol. 77, no. 3, p. 388, 1950.

[73] R. C. Hanson, “HALL MOBILITY OF HOLES IN SILVER BROMIDE1,” *J. Phys. Chem.*, vol.

66, no. 12, pp. 2376–2380, 1962.

[74] R. K. Ahrenkiel and R. S. Van Heyningen, “Lifetime and Drift Mobility of Holes in AgBr,” *Phys. Rev.*, vol. 144, no. 2, p. 576, 1966.

[75] T. Kawai, K. Kobayashi, M. Kurita, and Y. Makita, “Drift mobilities of electrons and holes in thallous bromide,” *J. Phys. Soc. Japan*, vol. 30, no. 4, pp. 1101–1105, 1971.

[76] V. N. Dobrovolskii and Y. I. Gritsenko, “Use of the Hall current for investigation of carrier scattering in semiconductors,” *Sov. Physics-Solid State*, vol. 4, no. 10, pp. 2025–2031, 1963.

[77] Y. S. Lee, M. T. Winkler, S. C. Siah, R. Brandt, and T. Buonassisi, “Hall mobility of cuprous oxide thin films deposited by reactive direct-current magnetron sputtering,” *Appl. Phys. Lett.*, vol. 98, no. 19, 2011.

[78] D. E. Hill, “Activation Energy of Holes in Zn-Doped GaAs,” *J. Appl. Phys.*, vol. 41, no. 4, pp. 1815–1818, 1970.

[79] A. L. Mears and R. A. Stradling, “Cyclotron resonance and Hall measurements on the hole carriers in GaAs,” *J. Phys. C Solid State Phys.*, vol. 4, no. 1, p. L22, 1971.

[80] E. Göbel, H. Herzog, M. H. Pilkuhn, and K.-H. Zschauer, “Laser emission due to excitonic recombination processes in high purity GaAs,” *Solid State Commun.*, vol. 13, no. 6, pp. 719–722, 1973.

[81] J. D. Wiley, “Mobility of holes in III-V compounds,” in *Semiconductors and semimetals*, vol. 10, Elsevier, 1975, pp. 91–174.

[82] F. D. Rosi, D. Meyerhofer, and R. V Jensen, “Properties of p-Type GaAs Prepared by Copper Diffusion,” *J. Appl. Phys.*, vol. 31, no. 6, pp. 1105–1108, 1960.

[83] J. Vilms and J. P. Garrett, “The growth and properties of LPE GaAs,” *Solid. State. Electron.*, vol. 15, no. 4, pp. 443–455, 1972.

[84] F. E. Rosztoczy, F. Ermanis, I. Hayashi, and B. Schwartz, “Germanium-Doped Gallium Arsenide,” *J. Appl. Phys.*, vol. 41, no. 1, pp. 264–270, 1970.

[85] O. V Emel’yanenko, N. M. Kolchanova, M. P. Mikhaĭlova, and Y. P. Yakovlev, “The Role of Dmitriı Nikolaevich Nasledov in the Formation and Development of the Physics and Technology of III–V Semiconductors.,” *Semiconductors*, vol. 37, no. 8, 2003.

[86] J. Bloem, A. J. Van der Houven van Oordt, and F. A. Kröger, “A new luminescence emission in Cu2O,” *Physica*, vol. 22, no. 6, pp. 1254–1256, 1956, doi: https://doi.org/10.1016/S0031-8914(56)90217-8.

[87] J. Bloem, “Discussion of some optical and electrical properties of Cu2O,” *Philips Res. Reports*, vol. 13, pp. 167–193, 1958.

[88] N. A. Tolstoi and B. VA, “Luminescence of oxygen vacancies in cuprous oxide,” *Sov. Phys. SOLID STATE, USSR*, vol. 13, no. 5, p. 1135, 1971.

[89] P. Yu, *Fundamentals of semiconductors*. Springer, 2005.

[90] O. Madelung, *Introduction to solid-state theory*, vol. 2. Springer Science & Business Media, 2012.

[91] P. W. Baumeister, “Optical absorption of cuprous oxide,” *Phys. Rev.*, vol. 121, no. 2, p. 359, 1961.

[92] R. J. Elliott, “Intensity of optical absorption by excitons,” *Phys. Rev.*, vol. 108, no. 6, p. 1384, 1957.

[93] M. Fox, *Optical properties of solids*, vol. 3. Oxford university press, 2010.

[94] D. L. Dexter and R. S. Knox, “Excitons Interscience,” *New York*, pp. 52–54, 1965.

[95] J. Ghijsen *et al.*, “Electronic structure of Cu 2 O and CuO,” *Phys. Rev. B*, vol. 38, no. 16, p. 11322, 1988.

[96] A. Jolk, M. Jörger, and C. Klingshirn, “Exciton lifetime, Auger recombination, and exciton transport by calibrated differential absorption spectroscopy in Cu 2 O,” *Phys. Rev. B*, vol. 65, no. 24, p. 245209, 2002.

[97] N. Caswell and P. Y. Yu, “Physical origin of the anomalous temperature dependence of the 1 S yellow exciton luminescence intensity in Cu 2 O,” *Phys. Rev. B*, vol. 25, no. 8, p. 5519, 1982.

[98] J. I. Jang, *Lifetimes of excitons in cuprous oxide*. University of Illinois at Urbana-Champaign, 2005.

[99] M. Hayashi and K. Katsuki, “Hydrogen-like absorption spectrum of cuprous oxide,” *J. Phys. Soc. Japan*, vol. 7, no. 6, pp. 599–603, 1952.

[100] E. F. Gross, “Optical spectrum of excitons in the crystal lattice,” *Nuovo Cim.*, vol. 3, no. Suppl 4, pp. 672–701, 1956.

[101] S. Nikitine, “Experimental investigations of exciton spectra in ionic crystals,” *Philos. Mag.*, vol. 4, no. 37, pp. 1–31, 1959.

[102] D. Fishman, “Excitons in cuprous oxide,” 2008.

[103] J. T. Devreese, *Polarons in ionic crystals and polar semiconductors: Antwerp Advanced Study Institute 1971 on Fröhlich polarons and electron-phonon interaction in polar semiconductors*. North-Holland Publishing Company, 1972.

[104] A. J. Ångström, “I. on the fraunhofer-lines visible in the solar spectrum,” *London, Edinburgh, Dublin Philos. Mag. J. Sci.*, vol. 24, no. 158, pp. 1–11, 1862.

[105] J. J. Balmer, “Notiz über die Spectrallinien des Wasserstoffs,” *Ann. Phys.*, vol. 261, no. 5, pp. 80–87, 1885.

[106] J. R. Rydberg, “XXXIV. On the structure of the line-spectra of the chemical elements,” *London, Edinburgh, Dublin Philos. Mag. J. Sci.*, vol. 29, no. 179, pp. 331–337, 1890.

[107] N. Bohr, “I. On the constitution of atoms and molecules,” *London, Edinburgh, Dublin Philos. Mag. J. Sci.*, vol. 26, no. 151, pp. 1–25, 1913.

[108] B. Höglund and P. G. Mezger, “Hydrogen Emission Line n110→ n109: Detection at 5009 Megahertz in Galactic H II Regions,” *Science (80-.).*, vol. 150, no. 3694, pp. 339–348, 1965.

[109] T. W. Hänsch, “Repetitively pulsed tunable dye laser for high resolution spectroscopy,” *Appl. Opt.*, vol. 11, no. 4, pp. 895–898, 1972.

[110] T. F. Gallagher, “Rydberg atoms,” *Reports Prog. Phys.*, vol. 51, no. 2, p. 143, 1988.

[111] S. Chu, “The manipulation of neutral particles,” *Nobel Lect. Phys.*, vol. 2000, pp. 122–158, 1996.

[112] N. Šibalic and C. S. Adams, “Rydberg Physics, 2399-2891.” IOP Publishing, 2018.

[113] V. Bendkowsky, B. Butscher, J. Nipper, J. P. Shaffer, R. Löw, and T. Pfau, “Observation of ultralong-range Rydberg molecules,” *Nature*, vol. 458, no. 7241, pp. 1005–1008, 2009.

[114] S. Haroche, “Controlling photons in a box and exploring the quantum to classical boundary,” *Ann. Phys.*, vol. 525, no. 10–11, pp. 753–776, 2013.

[115] J. Schmidt *et al.*, “An optogalvanic gas sensor based on Rydberg excitations,” *J. Phys. B At. Mol. Opt. Phys.*, vol. 53, no. 9, p. 94001, 2020.

[116] C. Veit *et al.*, “Pulsed ion microscope to probe quantum gases,” *Phys. Rev. X*, vol. 11, no. 1, p. 11036, 2021.

[117] K. Singer, M. Reetz-Lamour, T. Amthor, L. G. Marcassa, and M. Weidemüller, “Suppression of Excitation and Spectral Broadening Induced by Interactions<? format?> in a Cold Gas of Rydberg Atoms,” *Phys. Rev. Lett.*, vol. 93, no. 16, p. 163001, 2004.

[118] D. Tong *et al.*, “Local blockade of Rydberg excitation in an ultracold gas,” *Phys. Rev. Lett.*, vol. 93, no. 6, p. 63001, 2004.

[119] T. Peyronel *et al.*, “Quantum nonlinear optics with single photons enabled by strongly interacting atoms,” *Nature*, vol. 488, no. 7409, pp. 57–60, 2012.

[120] H. Labuhn *et al.*, “Single-atom addressing in microtraps for quantum-state engineering using Rydberg atoms,” *Phys. Rev. A*, vol. 90, no. 2, p. 23415, 2014.

[121] D. Jaksch, J. I. Cirac, P. Zoller, S. L. Rolston, R. Côté, and M. D. Lukin, “Fast quantum gates for neutral atoms,” *Phys. Rev. Lett.*, vol. 85, no. 10, p. 2208, 2000.

[122] L. Isenhower *et al.*, “Demonstration of a neutral atom controlled-NOT quantum gate,” *Phys. Rev. Lett.*, vol. 104, no. 1, p. 10503, 2010.

[123] A. Neubauer, “Rydberg excitons in cuprous oxide: macroscopic quantum systems coupled to nanoplasmonic and nanophotonic components.” Dissertation, Stuttgart, Universität Stuttgart, 2022, 2022.

[124] N. Sangouard, C. Simon, J. Minář, H. Zbinden, H. De Riedmatten, and N. Gisin, “Long-distance entanglement distribution with single-photon sources,” *Phys. Rev. A*, vol. 76, no. 5, p. 50301, 2007.

[125] E. Knill, R. Laflamme, and G. J. Milburn, “A scheme for efficient quantum computation with linear optics,” *Nature*, vol. 409, no. 6816, pp. 46–52, 2001.

[126] M. Saffman and T. G. Walker, “Creating single-atom and single-photon sources from entangled atomic ensembles,” *Phys. Rev. A*, vol. 66, no. 6, p. 65403, 2002.

[127] M. Pelton *et al.*, “Efficient source of single photons: a single quantum dot in a micropost microcavity,” *Phys. Rev. Lett.*, vol. 89, no. 23, p. 233602, 2002.

[128] J. Claudon *et al.*, “A highly efficient single-photon source based on a quantum dot in a photonic nanowire,” *Nat. Photonics*, vol. 4, no. 3, pp. 174–177, 2010.

[129] G. M. Kavoulakis, Y.-C. Chang, and G. Baym, “Fine structure of excitons in Cu 2 O,” *Phys. Rev. B*, vol. 55, no. 12, p. 7593, 1997.

[130] T. F. Gallagher, “Rydberg atoms,” in *Springer Handbook of Atomic, Molecular, and Optical Physics*, Springer, 1994, pp. 231–240.

[131] A. Gaëtan *et al.*, “Observation of collective excitation of two individual atoms in the Rydberg blockade regime,” *Nat. Phys.*, vol. 5, no. 2, pp. 115–118, 2009.

[132] A. Chernikov *et al.*, “Exciton binding energy and nonhydrogenic Rydberg series in monolayer WS 2,” *Phys. Rev. Lett.*, vol. 113, no. 7, p. 76802, 2014.

[133] D. Christiansen *et al.*, “Phonon sidebands in monolayer transition metal dichalcogenides,” *Phys. Rev. Lett.*, vol. 119, no. 18, p. 187402, 2017.

[134] E. F. Gross and N. A. Karrjew, “Light absorption by cuprous oxide crystal in infrared and visible part of the spectrum,” in *Dokl. Akad. Nauk SSSR*, 1952, vol. 84, p. 471.

[135] J. Heckötter, D. Janas, R. Schwartz, M. Aßmann, and M. Bayer, “Experimental limitation in extending the exciton series in Cu 2 O towards higher principal quantum numbers,” *Phys. Rev. B*, vol. 101, no. 23, p. 235207, 2020.

[136] S. Zielińska-Raczyńska, D. Ziemkiewicz, and G. Czajkowski, “Electro-optical properties

of Rydberg excitons," *Phys. Rev. B*, vol. 94, no. 4, p. 45205, 2016.

[137] P. Rommel *et al.*, "Magneto-Stark effect of yellow excitons in cuprous oxide," *Phys. Rev. B*, vol. 98, no. 8, p. 85206, 2018.

[138] M. Aßmann, J. Thewes, D. Fröhlich, and M. Bayer, "Quantum chaos and breaking of all anti-unitary symmetries in Rydberg excitons," *Nat. Mater.*, vol. 15, no. 7, pp. 741–745, 2016.

[139] S. O. Krüger, H. Stolz, and S. Scheel, "Interaction of charged impurities and Rydberg excitons in cuprous oxide," *Phys. Rev. B*, vol. 101, no. 23, p. 235204, 2020.

[140] M. GmbH, "Substrate Preparation: Cleaning and Adhesion Promotion." [Online]. Available: file:///C:/Users/abela/Downloads/substrate_cleaning_adhesion_photoresist.pdf.

[141] J. H. Klootwijk and C. E. Timmering, "Merits and limitations of circular TLM structures for contact resistance determination for novel III-V HBTs," in *Proceedings of the 2004 International Conference on Microelectronic Test Structures (IEEE Cat. No. 04CH37516)*, 2004, pp. 247–252.

[142] B. Jacobs, M. Kramer, E. J. Geluk, and F. Karouta, "Optimisation of the Ti/Al/Ni/Au ohmic contact on AlGaN/GaN FET structures," *J. Cryst. Growth*, vol. 241, no. 1–2, pp. 15–18, 2002.

[143] D. W. Koon and C. J. Knickerbocker, "What do you measure when you measure resistivity?," *Rev. Sci. Instrum.*, vol. 63, no. 1, pp. 207–210, 1992.

[144] J. Singleton, *Band theory and electronic properties of solids*, vol. 2. OUP Oxford, 2001.

[145] N. I. of S. and T. (NIST). T. H. E. Https://www.nist.gov/pml/engineering-physics-division/popular-links/hall-effect/ and Hall-effect/., "No Title." .

[146] S. M. Sze, Y. Li, and K. K. Ng, *Physics of semiconductor devices*. John wiley & sons, 2021.

[147] "Thorlab website." https://www.thorlabs.com/newgrouppage9.cfm?objectgroup_id=3978.

[148] K. M. Krishnan, *Principles of materials characterization and metrology*. Oxford University Press, 2021.

[149] G. K. Reeves and H. B. Harrison, "Obtaining the specific contact resistance from transmission line model measurements," *IEEE Electron device Lett.*, vol. 3, no. 5, pp. 111–113, 1982.

[150] B. Singh and B. R. Mehta, "Relationship between nature of metal-oxide contacts and resistive switching properties of copper oxide thin film based devices," *Thin Solid*

Films, vol. 569, pp. 35–43, 2014.

[151] W.-Y. Yang and S.-W. Rhee, "Effect of electrode material on the resistance switching of Cu2O film," *Appl. Phys. Lett.*, vol. 91, no. 23, p. 232907, Dec. 2007, doi: 10.1063/1.2822403.

[152] S. Cheng Siah, Y. Seog Lee, Y. Segal, and T. Buonassisi, "Low contact resistivity of metals on nitrogen-doped cuprous oxide (Cu2O) thin-films," *J. Appl. Phys.*, vol. 112, no. 8, p. 84508, 2012.

[153] E. Moons, T. Engelhard, and D. Cahen, "Ohmic contacts to p-CuInSe 2 crystals," *J. Electron. Mater.*, vol. 22, pp. 275–280, 1993.

[154] S. Zee, "Physics of semiconductor devices/In 2 books. Book. 1. Per. from English.-2nd revision. and additional ed," *M. Mir*, 1984.

[155] G. B. Murdoch, M. Greiner, M. G. Helander, Z. B. Wang, and Z. H. Lu, "A comparison of CuO and Cu2O hole-injection layers for low voltage organic devices," *Appl. Phys. Lett.*, vol. 93, no. 8, 2008.

[156] L. C. Olsen, R. C. Bohara, and M. W. Urie, "Explanation for low-efficiency Cu2O Schottky-barrier solar cells," *Appl. Phys. Lett.*, vol. 34, no. 1, pp. 47–49, 1979.

[157] G. S. Marlow and M. B. Das, "The effects of contact size and non-zero metal resistance on the determination of specific contact resistance," *Solid. State. Electron.*, vol. 25, no. 2, pp. 91–94, 1982.

[158] M. A. Omar, *Elementary solid state physics: principles and applications*. Pearson Education India, 1999.

[159] R. A. Keller, "Organic semiconductors: by Y. Okamoto and Walter Brenner. 178 pages, diagrams, 6× 9 in. New York, Reinhold Publishing Corp., 1964. Price, $9.00." Pergamon, 1965.

[160] J. Li *et al.*, "Probing defects in nitrogen-doped Cu2O," *Sci. Rep.*, vol. 4, no. 1, p. 7240, 2014.

[161] W. M. Saslow, *Electricity, magnetism, and light*. Elsevier, 2002.

[162] A. Mittiga, F. Biccari, and C. Malerba, "Intrinsic defects and metastability effects in Cu2O," *Thin Solid Films*, vol. 517, no. 7, pp. 2469–2472, 2009.

[163] S. Ishizuka, S. Kato, T. Maruyama, and K. Akimoto, "Nitrogen doping into Cu2O thin films deposited by reactive radio-frequency magnetron sputtering," *Jpn. J. Appl. Phys.*, vol. 40, no. 4S, p. 2765, 2001.

[164] K. Matsuzaki, K. Nomura, H. Yanagi, T. Kamiya, M. Hirano, and H. Hosono, "Effects of post-annealing on (110) Cu2O epitaxial films and origin of low mobility in Cu2O

thin-film transistor," *Phys. status solidi*, vol. 206, no. 9, pp. 2192–2197, 2009.

[165] G. P. Pollack and D. Trivich, "Photoelectric properties of cuprous oxide," *J. Appl. Phys.*, vol. 46, no. 1, pp. 163–172, 1975.

[166] B. El-Kareh, "Silicon devices and process integration," *New York Springer. doi*, vol. 10, pp. 970–978, 2009.

[167] O. Madelung, "Non-tetrahedrally bonded elements and binary compounds I," *Landolt-börnstein-gr. III Condens. Matter*, 1998.

[168] C. Erginsoy, "Neutral impurity scattering in semiconductors," *Phys. Rev.*, vol. 79, no. 6, p. 1013, 1950.

[169] R. Kužel and F. L. Weichman, "Hole mobility in Cu2O. I. Scattering by lattice vibrations," *Can. J. Phys.*, vol. 48, no. 22, pp. 2643–2656, 1970.

[170] N. M. Gabor, Z. Zhong, K. Bosnick, J. Park, and P. L. McEuen, "Extremely efficient multiple electron-hole pair generation in carbon nanotube photodiodes," *Science (80-.).*, vol. 325, no. 5946, pp. 1367–1371, 2009.

[171] Z. Yin *et al.*, "Single-layer MoS2 phototransistors," *ACS Nano*, vol. 6, no. 1, pp. 74–80, 2012.

[172] R. C. EDEN and B. M. WELCH, "Ultra-high-speed GaAs VLSI: approaches, potential, and progress," in *VLSI Electronics Microstructure Science*, vol. 3, Elsevier, 1982, pp. 109–162.

[173] C. H. Qiu, C. Hoggatt, W. Melton, M. W. Leksono, and J. I. Pankove, "Study of defect states in GaN films by photoconductivity measurement," *Appl. Phys. Lett.*, vol. 66, no. 20, pp. 2712–2714, 1995.

[174] T. Leijtens *et al.*, "Carrier trapping and recombination: the role of defect physics in enhancing the open circuit voltage of metal halide perovskite solar cells," *Energy Environ. Sci.*, vol. 9, no. 11, pp. 3472–3481, 2016.

[175] J. L. Shen, Y. C. Lee, G. W. Shu, W.-C. Chou, and W. Y. Uen, "Observation of persistent photoconductivity in quaternary InGaAsP epitaxial layers," *Semicond. Sci. Technol.*, vol. 17, no. 11, p. L72, 2002.

[176] A. Nagaoka *et al.*, "Comparison of Sb, As, and P doping in Cd-rich CdTe single crystals: Doping properties, persistent photoconductivity, and long-term stability," *Appl. Phys. Lett.*, vol. 116, no. 13, 2020.

[177] A. Dissanayake, M. Elahi, H. X. Jiang, and J. Y. Lin, "Kinetics of persistent photoconductivity in Al 0.3 Ga 0.7 As and Zn 0.3 Cd 0.7 Se semiconductor alloys," *Phys. Rev. B*, vol. 45, no. 24, p. 13996, 1992.

[178] R. D. McConnell and R. Noufi, *Science and technology of thin film superconductors 2*. Springer Science & Business Media, 2012.

[179] "Dr David Morgan." https://www.cardiff.ac.uk/people/view/38478-morgan-david/_recache.

[180] Y. Yang *et al.*, "Annealing time modulated the film microstructures and electrical properties of P-type CuO field effect transistors," *Appl. Surf. Sci.*, vol. 481, pp. 632–636, 2019.

[181] Z. Jin, C. Liu, K. Qi, and X. Cui, "Photo-reduced Cu/CuO nanoclusters on TiO2 nanotube arrays as highly efficient and reusable catalyst," *Sci. Rep.*, vol. 7, no. 1, p. 39695, 2017.

[182] D. Zhang, B. Hu, D. Guan, and Z. Luo, "Essential roles of defects in pure graphene/Cu2O photocatalyst," *Catal. Commun.*, vol. 76, pp. 7–12, 2016.

[183] H. J. Li *et al.*, "Growth behavior and optical properties of N-doped Cu2O films," *Thin Solid Films*, vol. 520, no. 1, pp. 212–216, 2011.

[184] F. A. Akgul, G. Akgul, N. Yildirim, H. E. Unalan, and R. Turan, "Influence of thermal annealing on microstructural, morphological, optical properties and surface electronic structure of copper oxide thin films," *Mater. Chem. Phys.*, vol. 147, no. 3, pp. 987–995, 2014.

[185] S. A. Lynch *et al.*, "Inhomogeneous broadening of phosphorus donor lines in the far-infrared spectra of single-crystalline SiGe," *Phys. Rev. B—Condensed Matter Mater. Phys.*, vol. 82, no. 24, p. 245206, 2010.

[186] J. Tennyson *et al.*, "IUPAC critical evaluation of the rotational–vibrational spectra of water vapor. Part I—Energy levels and transition wavenumbers for H217O and H218O," *J. Quant. Spectrosc. Radiat. Transf.*, vol. 110, no. 9–10, pp. 573–596, 2009.

[187] J. Tennyson *et al.*, "IUPAC critical evaluation of the rotational–vibrational spectra of water vapor, Part III: Energy levels and transition wavenumbers for H216O," *J. Quant. Spectrosc. Radiat. Transf.*, vol. 117, pp. 29–58, 2013.

[188] N. Izairi, M. Shehabi, F. Ajredini, and L. Istrefi, "Investigation of Environmental Pollution by Molecular Aabsorption Spectroscopy," *BALWOIS 2010-Ohrid, Repub. Maced. 29 May 2010*, 2010.

[189] D. O. Scanlon, B. J. Morgan, G. W. Watson, and A. Walsh, "Acceptor levels in p-type Cu 2 O: rationalizing theory and experiment," *Phys. Rev. Lett.*, vol. 103, no. 9, p. 96405, 2009.

[190] G. K. Paul, R. Ghosh, S. K. Bera, S. Bandyopadhyay, T. Sakurai, and K. Akimoto, "Deep level transient spectroscopy of cyanide treated polycrystalline p-Cu2O/n-ZnO solar cell," *Chem. Phys. Lett.*, vol. 463, no. 1–3, pp. 117–120, 2008.

[191] J. Li *et al.*, “Engineering of optically defect free Cu 2 O enabling exciton luminescence at room temperature,” *Opt. Mater. Express*, vol. 3, no. 12, pp. 2072–2077, 2013.

[192] S. Dhara, K. M. Niang, A. J. Flewitt, A. Nathan, and S. A. Lynch, “Photoconductive laser spectroscopy as a method to enhance defect spectral signatures in amorphous oxide semiconductor thin-film transistors,” *Appl. Phys. Lett.*, vol. 114, no. 1, 2019.